THE BORON-RICH

AMORPHOUS MATERIALS

A THESIS
SUBMITTED TO THE DEPARTMENT OF MATERIALS
SCIENCE AND MECHANICAL ENGINEERING
AND THE GRADUATE SCHOOL OF ENGINEERING AND
SCIENCE OF ABDULLAH GUL UNIVERSITY
IN PARTIAL FULFILLMENT OF THE REQUIREMENTS
FOR THE DEGREE OF
DOCTOR OF PHILOSOPHY

By
Ayşegül Özlem KARACAOĞLAN
December 2022

THE BORON-RICH

AMORPHOUS MATERIALS

A THESIS

SUBMITTED TO THE DEPARTMENT OF MATERIALS SCIENCE AND

MECHANICAL ENGINEERING

AND THE GRADUATE SCHOOL OF ENGINEERING AND SCIENCE OF

ABDULLAH GUL UNIVERSITY

IN PARTIAL FULFILLMENT OF THE REQUIREMENTS

FOR THE DEGREE OF

DOCTOR OF PHILOSOPHY

By

Ayşegül Özlem KARACAOĞLAN

December 2022

SCIENTIFIC ETHICS COMPLIANCE

I hereby declare that all information in this document has been obtained in accordance with academic rules and ethical conduct. I also declare that, as required by these rules and conduct, I have fully cited and referenced all materials and results that are not original to this work.

Ayşegül Özlem KARACAOĞLAN

REGULATORY COMPLIANCE

Ph.D. thesis titled "Boron Rich Amorphous Materials" has been prepared in accordance with the Thesis Writing Guidelines of the Abdullah Gül University, Graduate School of Engineering & Science.

Prepared By   Advisor
Ayşegül Özlem KARACAOĞLAN   Prof. Murat DURANDURDU

Head of the Materials Science and Mechanical Engineering Program
Asst. Prof. Çağatay YILMAZ

ACCEPTANCE AND APPROVAL

Ph.D. thesis titled "Boron Rich Amorphous Materials" and prepared by Ayşegül Özlem KARACAOĞLAN has been accepted by the jury in the Materials Science and Mechanical Engineering Graduate Program at Abdullah Gül University, Graduate School of Engineering & Science.

….. /01/2023

JURY   :

Advisor   : Prof. Murat DURANDURDU   ....

Member   : Prof. Mehmet ŞAHİN   ....

Member   : Prof. Serdar ÖNSES   ....

Member   : Prof. Zeki BÜYÜKMUMCU   ....

Member   : Asst. Prof. Fahri ALKAN   ....

APPROVAL:

The acceptance of this Ph.D. thesis has been approved by the decision of the Abdullah Gül University, Graduate School of Engineering & Science, Executive Board dated ….. /….. / 2023 and numbered …………..…… .

……….. /……….. / ………..

Graduate School Dean

Prof. Dr. İrfan ALAN

ABSTRACT

BORON-RICH AMORPHOUS MATERIALS

Ayşegül Özlem KARACAOĞLAN
Ph.D. in Materials Science and Mechanical Engineering
Advisor: Prof. Dr. Murat DURANDURDU

December 2022

In the scope of this thesis, boron-rich amorphous materials having different boron concentrations ($B_{1-x}N_x$, $B_{1-x}O_x$ and $B_{1-x}Si_x$) were created as a result of rapid cooling of their liquid state with the help of an *ab initio* molecular dynamics technique. Their structural, electrical and mechanical properties were exposed in detail. In all boron rich materials, the coordination number of B was found to increase steadily with increasing B content. Similarly N and Si atoms also attained high coordinated motifs with increasing B content. However, the coordination number of O atoms remained null for all compositions. Chemical segregations and hence phase separations were witnessed in most amorphous configurations. The materials with high boron ratios, as expected, consisted of B_{12} icosahedrons. In addition, the formation of nano-sized B_7, B_{10}, B_{14} and B_{16} clusters was observed in some boron-rich compounds. Each computer-generated material exhibited a semiconducting character. The mechanical properties (Bulk, Young and Shear moduli) were perceived to increase with increasing B content. Some amorphous compositions were proposed to be hard materials on the basis of their Vickers hardness estimation.

Keywords: *Boron-rich, amorphous, ab initio, B_{12} molecule, DFT.*

ÖZET

BOR ZENGİNİ AMORF MALZEMELER

Ayşegül Özlem KARACAOĞLAN
Malzeme Bilimi ve Makine Mühendisliği Anabilim Dalı Doktora
Tez Yöneticisi: Prof. Dr. Murat DURANDURDU

Aralık 2022

Bu tez kapsamında, *ab inito* moleküler dinamiği kullanılarak sıvı fazlarının hızlıca soğutulması sonucunda farklı bor oranlarına sahip bor zengini amorf malzemeler ($B_{1-x}N_x$, $B_{1-x}O_x$ ve $B_{1-x}Si_x$) modellenmiştir. Yapısal, elektriksel ve mekanik özellikleri ayrıntılı olarak incelenmiştir. Bor bakımından zengin tüm malzemelerde B'nin koordinasyon sayısının artan B içeriği ile birlikte istikrarlı bir şekilde arttığı bulunmuştur. Benzer şekilde N ve Si atomları da artan B içeriği ile birlikte yüksek koordinasyonlu motifler oluşturmuştur. Fakat O atomlarının koordinasyon sayısı bütün kompozisyonlar için sabit kamıştır. Çoğu amorf modellerinde kimyasal ayrışma ve dolayısıyla faz ayrımları görülmüştür. Yüksek bor oranlarına sahip amorf modeller, beklenildiği gibi, B_{12} ikosahedrallerden oluşmaktadır. Ek olarak, bazı bor-zengini malzemelerde nano-boyutlu B_7, B_{10}, B_{14} and B_{16} kümelerinin oluştuğu bulunmuştur. Her modellenen malzeme yarı iletken özellik göstermektedir. Mekanik özelliklerin (Bulk, Young and Shear modülü) artan B içeriği ile birlikte arttığı bulunmuştur. Bazı amorf kompozisyonların Vickers sertlik tahminlerine dayanarak sert malzemeler olduğu önerilmiştir.

Anahtar Kelimeler: *B-zengini, amorf, ab inito, B_{12} molekülü, DFT.*

Acknowledgements

First and foremost, I would like to express my most appreciation to my supervisor, Prof. Murat DURANDURDU who gracefully and patiently spend his time to lead me with his deep information and intelligence.

Secondly, I would like to present my sincere thanks to other members of my thesis dissertation committee; Prof. Mehmet ŞAHİN, Prof. Serdar ÖNSES, Prof. Zeki BÜYÜKMUMCU and Asst. Prof. Fahri ALKAN, whose insightful guidance and explanations are indispensable.

One of my biggest thanks is to my determined and successful academician friend Asst. Prof. Gamze OKYAY for her encouragement and friendship in my every moment.

Likewise, I would like to convey my heart-felt gratitude to Tevhide Ayça YILDIZ who is with me in every good and bad moment. She is great person and I am very thankful for all her friendship. Every time we worked together was special, I will miss each day.

I would like to state my sincerely thanks to quality group manager at YATAŞ A. Ş., Murat İNAN who were very supportive during my thesis writing term.

I can't pass without thanking my mother and father who has been with me at every moment throughout my life. The fact that they are proud of me is one of my greatest sources of happiness in this life. Your interest and support are invaluable.

I would like to state my special thanks to Gamze Çetin who is a Ph.D. candidate for all her help and support. Good luck with you my dear sister.

Last, but certainly not least my husband who is my soul mate, best friend… One of my biggest thanks to you for your love, patience, commitment and support to me.

TABLE OF CONTENTS

LIST OF FIGURES

LIST OF TABLES

LIST OF ABBREVIATIONS

AIMD   ab initio Molecular Dynamics

B_3Si Silicon Triboride

B_4Si Silicon Tetraboride

BMEOS   Birch-Murnaghan Equation of State

BN   Boron Nitride

BO   Boron Oxide

B-Rich   Boron Rich

BSi   Boron Silicide or Silicon Boride

CG   Conjugate Gradient

CMD   Classical Molecular Dynamics

CPMD   Car-Parrinello Molecular Dynamics

DFT   Density Functional Theory

DZ   Double Zeta

DZP   Double Zeta Polarized

EDOS   Electron Density of States

EOS   Equation of State

GGA   Generalized Gradient Approximation

GO   Geometry Optimization

HF   Hartree-Fock

HK   Hohenberg and Kohn

HOMO   Highest Occupied Molecular Orbital

IBC   Isolated Boundary Condition

KS	Kohn-Sham
LDA	Local Density Approximation
LUMO	Lowest Unoccupied Molecular Orbital
MD	Molecular Dynamics
NAO	Numerical Atomic Orbital
PAW	Projector Augmented Wave
PBC	Periodic Boundary Condition
PBE	Perdew, Burke and Ernzerhof
PCF	Partial Correlation Function
PDF	Pair Distribution Function
PDOS	Partial Electron Density of States
PE	Potential Energy
PES	Potential Energy Surface
PPCF	Partial Pair Correlation Function
PPDF	Partial Pair Distribution Function
PR	Parrinello-Rahman
RDF	Radial Distribution Function
SCF	Self-Consistent Field
SIESTA	Spanish Initiative for Electronic Simulations with Thousand Atoms
TMOs	Transition Metal Oxides
TPSS	Tao, Perdew, Staroverov, and Scuseria

To my dear family

Chapter 1

Introduction

1.1   Importance of Boron and Its Reserves in Turkey

Total boron deposits (B_2O_3) of the world are 1.299.000 thousand tons and Turkey owns the world's biggest boron reserves with 956.000 thousand tons (73.6%), as well as having the most significant boron minerals with high mercantile value and ore quality. The second and third boron deposits of the world are belonging to the USA and Russia, respectively. The distribution of the world boron reserves is sorted by countries in Table 1.1 [1, 2]. The most major global producer countries of boron are Turkey and the USA with a proportion of 56% and of 27%, respectively [3]. Proportion of the world boron production capacity by manufacturers is shown in Fig. 1.1.
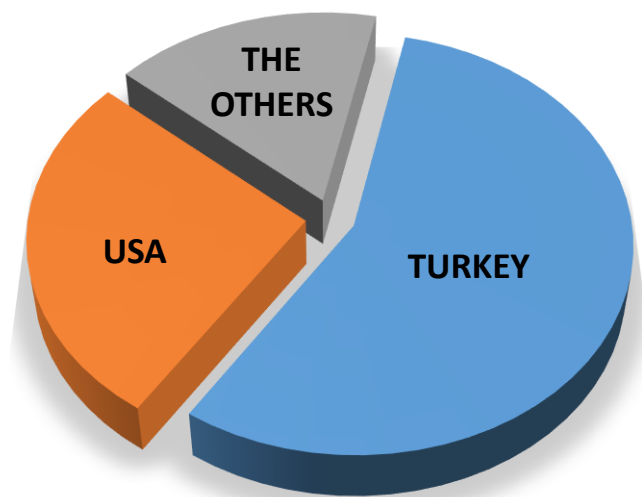
Figure 1.1 Distribution of the world boron production capacity by manufacturers.

Table 1.1 Boron Reserves in the World.

Countries	Reserve Amount (Thousand Ton (Based on B_2O_3))	Distribution (%)
Turkey	956.000	73.6
Russia	100.000	7.7
USA	80.000	6.2
Chile	41.000	3.2
China	36.000	2.8
Peru	22.000	1.7
Serbia	21.000	1.6
Bolivia	19.000	1.5
Kazakhstan	15.000	1.2
Argentina	9.000	0.7
Total	1.299.000	100

The structures of boron minerals involve B_2O_3 in different amounts and are classified according to B_2O_3 content. B_2O_3 content for boron minerals is a significant parameter for industrial applications and Turkey gains extra importance due to the rich in B_2O_3 in the boron minerals. Boron minerals having commercial importance are listed according to their chemical formula and B_2O_3 content in Table 1.2 [4]. Tincal, colemanite and ulexite being rich in terms of B_2O_3 (Tab. 1.2) are the most important boron minerals in Turkey. The biggest tincal ore reserves are found in Eskişehir/Kırka district. Colemanite mineral is found in Emet/Kütahya, Mustafa Kemal Paşa/Bursa and Bigadic/Balıkesir. Ulexite is also located in Emet/Kütahya. As a conclusion, it can be clearly pointed out that boron minerals are of great importance for Turkey and Turkey is the leader for both boron reserves and production capacity in worldwide.

Table 1.2 Boron minerals having commercial importance with the chemical formula and B_2O_3 content [4].

Boron Minerals	Chemical Formula	B_2O_3 content (wt. %)
Boracite (stassfurite)	$Mg_6B_{14}O_{26}C_{12}$	62.2
Sassolite (natural boric acid)	H_3BO_3	56.3
Kernite (rasortie)	$Na_2B_4O_7.4H_2O$	51.0
Colemanite	$Ca_2B_6O_{11}.5H_2O$	50.8
Hydroboracite	$CaMgB_6O_{11}.6H_2O$	50.5
Priceite (pandermite)	$CaB_{10}O_{19}.7H_2O$	49.8
Probertite (kramerite)	$NaCaB_3O_9.5H_2O$	49.6
Tincalconite (mohavite)	$Na_2B_4O_7.5H_2O$	47.8
Ulexite (boronatrocalcite)	$NaCaB_5O_9.8H_2O$	43.0
Szaibelyite (ascharite)	$MgBO_2.20H$	41.4
Tincal (natural borax)	$Na_2B_4O_7.10H_2O$	36.5
Datolite	$CaBSiO_4.OH$	24.9

1.2   What Is Boron Element?

Boron element being the chemical symbol B is positioned in IIIA group of the periodic table. Its atomic number and mass are 5 and 10.811 g/mol, respectively. Additionally, boron is a metalloid element that can show both metallic and non-metallic behavior [5]. For many centuries, boron was known with its formed compounds but not an elemental form. Two French chemists, Louis Joseph GayLussac and Louis Jacques Thenard, (Fig. 1.2 [6]) annunciated the discovery of boron element as new element calling as "bore" [7]. After days of their announcement, English chemist Humphrey Davy (Fig. 1.2 [6]) submitted an article to the Royal Society of London about the discovering of new element referring as "boracium" [8]. On the other hand, boron as an element was qualified by Jöns Jacob Berzelius in 1824 [9]. Lastly, Ezekiel Weintraub, an American chemist, produced the pure boron in 1909 [10].

Figure 1.2 The men who discovered boron as an element: (I) Joseph Louis Gay Lussac, (II) Louis Jacques Thenard, (III) Humphry Davy [6] "Reprinted with permission from Reference [6]. Copyright {1932} American Chemical Society."

Boron is 51st most abundant element in the Earth's crust [11] and is similarly found in water, soil and rocks [12, 13]. In spite of that, boron has high chemical affinity toward other elements and hence, it is not unfortunately found free as an elemental form on the Earth. It can be easily obtained as the oxygen-containing compounds, most especially boric acid and borates [11, 14], for example, boronite ($2Mg_3B_8O_{15} \cdot MgCl_2$), schreckite ($Ca_2B_6O_{11} \cdot 3H_2O$), borax ($Na_2B_4O_7 \cdot 10H_2O$) [14]. The number of discovered boron ore types containing borate, borax, silicoborate have been about 150 up to now. As for the

boron in aqueous solution, it basically consists of the forms of $B(OH)_3$ and $B(OH)_4^-$. $B(OH)_3$ are more predominant in freshwaters whereas $B(OH)_4^-$ exists in intensely alkaline solutions like salty water. In addition, tourmaline is known the most prevalent boron mineral in the Earth's crust and boron is found as $B(OH)_3$ form in this mineral. Besides, the form of $B(OH)_4^-$ of boron fundamentally exists in clay minerals [14].

Apart from naturally occurring forms of boron, it can build divergent compounds having different special properties by reacting with both metal and non-metal elements [5]. Finally, it has also been detected that boron has several isotopes, which are ^8B-^{17}B. Among these isotopes, only ^{10}B, and ^{11}B are innately stable having the proportion of occurrence in nature at 19.9% and 80.1%, correspondingly [15].

1.2.1 The Allotropes of Boron

Although boron can be synthesized in various forms as both crystalline and amorphous, there is no exact information about the number of boron configurations. The phase diagram of boron is illustrated in Fig. 1.3 [16]. In this figure, α and β represent α- and β-rhombohedral and T refers to t-I phase of boron. Among all boron allotropes, it is confirmed that β-rhombohedral (β-R), α-rhombohedral (α-R), β-tetragonal (β-T) and γ-orthorhombic boron are thermodynamically stable [17]. The α-R and β-R structures are well-known crystalline forms of boron. Tetragonal-I (t-I), the former name was β-tetragonal, is also another well-known crystalline form of boron. Besides, there are two crystalline forms of boron synthesizable in special conditions. The first one is tetragonal-II (t-II), called as α-tetragonal [18]. The second one is γ-orthorhombic boron (γ-B) [19], a new high-pressure crystal of γ-B_{28} [20, 21]. As for the amorphous allotropes of boron, the first boron having about 99% impurity was produced by Weintraub in 1909 [22] and two known forms of amorphous boron configurations are available. One of them has a finely fractionated or powder form and the other has a glassy solid form [19]. In addition, apart from these crystalline and amorphous modifications, at least 16 polymorphs, have been published in the previous theoretical investigations but not validated by experiments [17, 23].
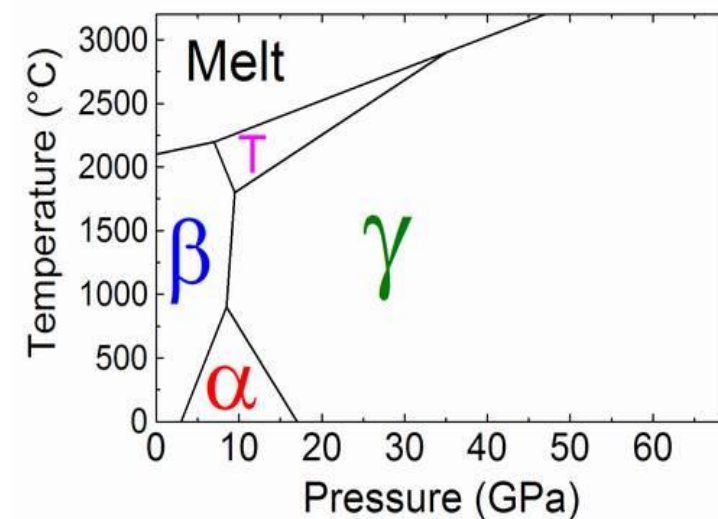
Figure 1.3 The phase diagram of boron [16].

1.2.1.1 α- and β-Rhombohedral Boron

α-R boron has a unit cell of twelve boron atoms (i.e., one icosahedron). The configuration of α-R consists of B_{12} icosahedrons and each B atom is linked to the nearest five B atoms within the same B_{12} molecule (Fig 1.4 (a) [5]). With regard to β-R boron (Fig 1.4 (b) [5], its unit cell is much larger than that of α-R and it has 105-108 B atoms but, it is indeed ideally 105 atoms. One B atom is placed at center of the unit cell. On the other hand, it contains two B_{28} units (i.e., two triply fused icosahedra) (Fig. 1.4 (g) [5]), twelve in the middle of edges and eight icosahedra in the vertices [17].

β-R is thermodynamically accepted as stable at high pressures while α-R is occasionally known as the low temperature structure. Although there have not been any evidences about the transformation from α-R to β-R, the synthesis at different temperatures of these B phases verifies this classification. In other words, α-R can be synthesized if the temperature is less than 1300 K whereas β-R is synthesized only above 1400 K [5].

1.2.1.2 α- and β-Tetrahedral Boron

α-T was proposed and its structure was described in the years of 1943, 1951 and 1958 [24-26] and it was accepted as the first crystalline structure amongst boron allotropes. Twenty years later, in an experimental work it was concluded that only α-R and β-T boron were fabricated in the crystalline form after reaction whereas α-T was not.

5

[27]. This suggestion was supported by another experimental work on tetragonal boron phases and only β-T boron phase was accepted as a crystalline structure in ambient pressure modification in addition to α-and β-R phases [8, 28].

The unit cell of α-T boron [29] (Fig. 1.4 (d) [5]) consists of four B_{12} icosahedrons and two interstitial positions and α-T boron has 50 atoms in the unit cell [5]. Although there has been the description of several different crystal structures for α-T boron in previous studies [28, 30-33], both its real structure and composition have not been fully found answer so far [5].
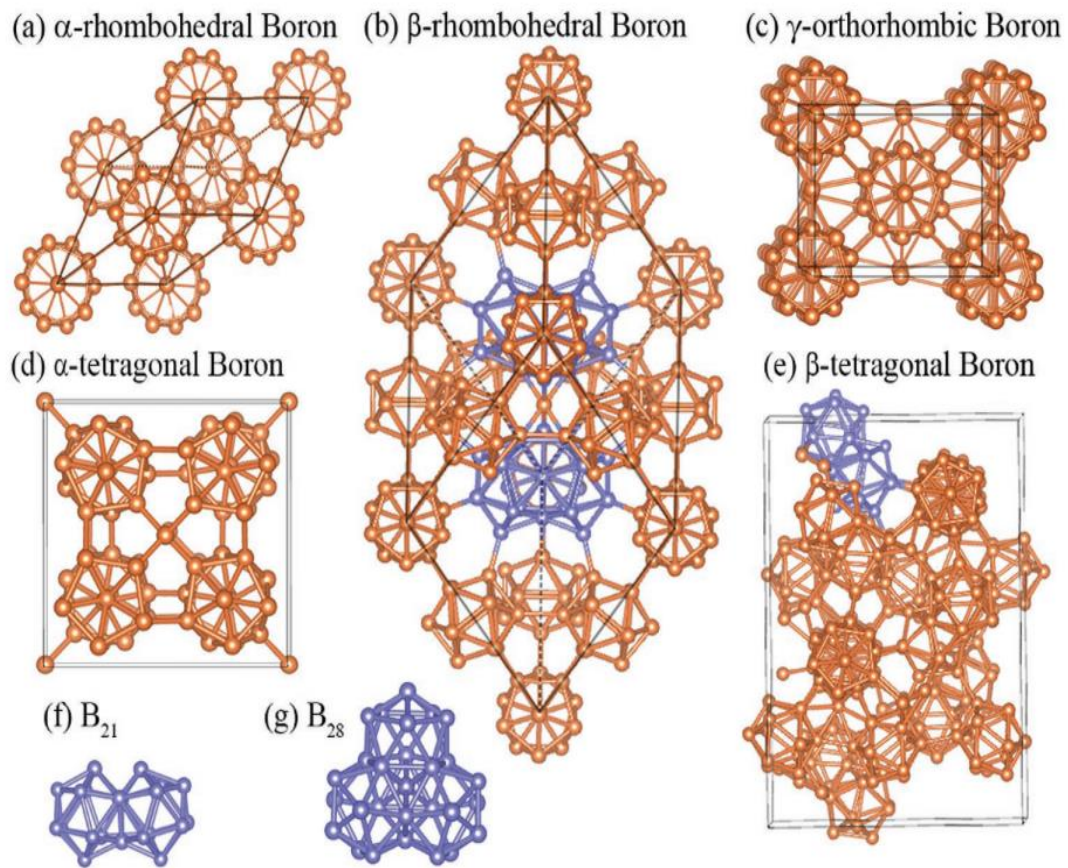
Figure 1.4 The bulk polymorphs of boron allotropes; (a) α-R, (b) β-R, (c) γ-B, (d) α-T, (e) β-T, (f) B_{21} molecule, and (g) B_{28} molecule [5].

As for β-T boron, its crystalline arrangement was first identified in 1979. Its unit cell consists of the B_{21} double-fused icosahedra (Fig. 1.4 (f) [5]), $B_{2.5}$ unit and two B_{12} icosahedra and has 190 atoms [34, 35]. In a different study, it was claimed that the atom number in the unit cell should be 192 due to the uncertain real composition, particularly of the B_{21} units [36].

6

1.2.1.3 γ-Orthorhombic Boron and γ-B$_{28}$

γ-orthorhombic boron was firstly synthesized under a pressure above ~10 GPa and between ~1500°C and 2000°C by Wentorf in 1965 [37]. However, both its chemical composition and structure were not explained exactly. The crystal structure of γ-orthorhombic boron was fully identified by using ab initio calculations [12] and affirmed by using an X-ray diffraction [21, 38]. The unit cell arrangement of γ-orthorhombic phase (Fig. 1.4 (c) [5]) is similar to the NaCl-type framework which contains two icosahedrons and B$_2$ pairs. α-R is stable at low temperatures while β-R sustains its stability at high temperatures. γ-orthorhombic, on the other hand, is stable solely at high pressure and temperature conditions [39, 40].
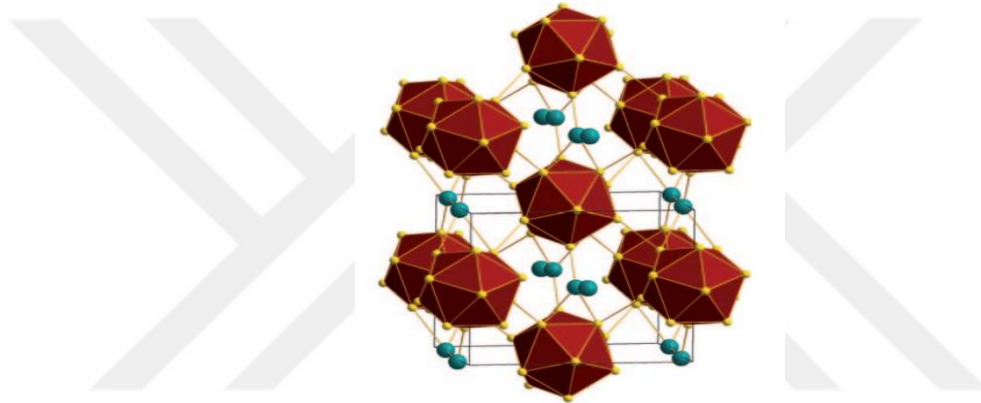
Figure 1.5 The crystal structure of γ-B$_{28}$ phase [5].

About fifteen years ago, γ-B$_{28}$ was reported as a new phase of boron, which was synthesized from β-B at 20 GPa and 2000 K. Additionally, in these researches its structure was depicted via X-ray diffraction [16, 20]. The crystal structure of γ-B$_{28}$ (Fig. 1.5 [5]) resembles to that of α-B that contains six B$_{12}$ icosahedra and B$_2$ pairs.

1.2.1.4 Amorphous Boron

Amorphous boron was first produced by the reaction of boron oxide (B$_2$O$_3$) or boric acid B(OH)$_3$ with potassium, or by electrolysis in the 1800s [41, 42]. Later, in 1892, it was manufactured by the reduction of B$_2$O$_3$ with magnesium. However, it could not be prepared with high purity and was contaminated with different substances like magnesium diborade [43]. The boron having >99% purity was produced in 1909 in a first time [44].

Amorphous boron configurations have B_{12} icosahedrons that are arbitrarily connected to each other with a short-range order [45]. Besides, the amorphous boron powder having impurities shows a brown appearance whereas that of high purity has a black color [46]. The pure or high purity disordered boron could be obtained by using thermal decomposition of B_2H_6 at any temperature less than 1000 °C. In the case of the tempering at 1000 °C, non-crystalline boron converts to β-R [47]. On the other hand, amorphous nanowires having 30-60 nm thickness [48] and fibers [49] can be synthesizable. Similar to the pure or high purity amorphous boron, both amorphous nanowires and fibers transform to β-R nanowires at 1000 °C [47].

1.2.2 Physical and Chemical Natures of Boron

The elemental boron is in the form of solid at room temperature. If boron is not completely pure, its crystal structure has black color while its amorphous form is brown or yellow. Pure amorphous boron has also black color. Boron atoms can be bonded in various different crystal networks which are called as allotropes. The density of crystalline and noncrystalline boron is 2.34 g/cm^3 and 2.37 g/cm^3, correspondingly. Boron element is a relatively inert metalloid as long as it does not contact with the powerful oxidizing agents. When boron grounds with PbF_2 and AgF, in addition, it reacts severely [50].

Boron can be accepted, due to being the smallest of semimetals, as an exceptional element, that is, boron shows both metal and nonmetal characteristics. If boron forms oxides and salts, for instance, B_2O_3 and $B_2(SO_4)_2$, it acts like metals. If boron, on the other hand, forms acids such as H_3BO_3, it behaves like nonmetals.

Boron crystals have high melting/boiling point and great hardness and hence their chemical features are not sufficiently active whereas its amorphous arrangements are more active relative to its crystalline counterparts. Amorphous boron at the room temperature, oxidizes in the air slowly. Boron does not solve in water, ethanol, ether, hydrofluoric acid and hydrochloric acid although it is reacted by concentrated nitric sulfuric acids [14]. Table 1.3 shows the selected physical and chemical features of boron [51, 52].

Table 1.3 The physical and chemical features of boron element [51, 52].

Physical Properties		Chemical Properties	
Atomic weight	10,811 g/mol	Electrochemical	0,1344
Boiling point	3.727 °C	equivalent	g/amp-hr
Melting point	2300 °C	Electronegativity	2,04 Pauling
Thermal expansion	8,3 μm/m.K	Fusion heat	50,2 kJ/mol
coefficient	(at 0 °C)	Ionization potentials;	
Thermal conductivity	0,274 W/cm.K	First potential	8,298 eV
Electrical conductivity	$1,0\ E^{-12}$ μS/cm	Second potential	25,154 eV
Bulk modulus	320 GPa	Third potential	37,93 eV
Physical condition	Solid (at 20 °C, 1 atm)	Valence electron	190 eV
Molar volume	4,68 cm^3/mol	potential	
Vickers hardness	49 GPa		
Fusion enthalpy	22,18 kJ/mol		
Atomization enthalpy	573,2 kJ/mol (at 25 °C)		
Vaporization enthalpy	480 kJ/mol		
Vapor pressure	0,348 Pa (at 300 °C)		
Specific temperature	1,02 J/g.K		

1.3 Boron-Rich Borides

1.3.1 A Brief Overview to Special B-Rich Boron Compounds

The B-rich molecules and solids possess a special importance in both chemistry and industry for their technological applications since these solids have a lot of novel morphological, thermal, electrical and mechanical characters. The configurations of B-rich compounds are identified by subunits of a triangular polyhedron which is named as deltahedra such as icosahedra, tetrahedra and octahedral [5]. Many B-rich materials, in addition, are represented by B_{12} icosahedra and their electronic properties are fundamentally specified with B_{12} icosahedra. For this reason, the electronic character of these solids is pertinent to the number of icosahedrons [53, 54]. The electronic structure of B-rich solids is qualified by three-center bonding, in which the three boron atoms share a common charge pool. It is well known that the bonding charges in the covalently bonded solids are centered betwixt two atoms. Thus, the electronic framework of boron is found

between metallic and covalent bonding and this characteristic renders some of the most extraordinary features in B-rich materials. For instance, B-rich solids having icosahedral units exhibit from insulating materials ($B_{12}P_2$) to conducting materials ($B_{1-x}C_x$) [55]. Besides, B-rich materials have generally high melting point (e.g., T_m for boron carbide (BC) is higher than ∼2600 K) and hence it can be possible to use these solids at very high operation temperatures [56].

Among B-rich solids, BC can be considered as the most extensively investigated material in terms of the thermoelectric applications. BC compound was firstly explored in 1858. Later, B_3C and B_6C were synthesized and identified in 1883 and 1894, correspondingly [57]. B_4C, the stoichiometric formula of BC, was designated in 1934 [58]. After 1950, many investigations on BC were performed, particularly its structures and features. Because of their prominent hardness, high neutron absorption cross-section, low specific weight etc., these materials are presently utilized as a coating for cutting tools, wear resistant refractories and also for ballistic applications such as armor plating [57, 59].

As regards to magnesium diboride (MgB_2), its crystal structure and compound have been known since 1953 [60]. However, the superconducting feature of MgB_2 has been explored in 2001 [61]. Its critical transition temperature is 39 K [61], positioned between the low temperature (i.e., NbTi) and high temperature superconductors (T_c>77 K) [62]. MgB_2 has drawn big attentions due to its outstanding features such as its promising critical current density [63, 64], transport and thermodynamic characteristics [65], doping effect ability [66], pressure effect [67], isotope effect [68] and band structures [68, 69]. With these properties, MgB_2 can be preferred in superconducting cables/devices [70] substituted for expensive ones due to its charming benefits such as small anisotropy, low material cost and simple crystal structure [68, 71].

Calcium hexaboride (CaB_6) can be accepted as another remarkable B-rich material due to its high melting point, high electrical conductivity, chemical stability and hardness. Together with these properties, the most important feature of CaB_6 is its ferromagnetic character [72]. Thanks to being its high conductive and having low work function, CaB_6 is utilized as a hot cathode material. However, if CaB_6 is used at high temperatures, it will oxidize thus deteriorating its properties and shortening its useful life [73]. CaB_6 is also used as high temperature and wear resistant materials, abrasives, surface shielding tools, and an antioxidant in carbon bonded refractories. Lastly, when its power factor is compared with those of thermoelectric materials, for example Bi_2Te_3 and PbTe, it is either

equal to or comparable with them. For this reason, it can be said that CaB_6 is a promising nominee for n-type thermoelectric materials [72].

Lastly, rhenium diboride (ReB_2) was firstly synthesized in 1962 [74]. ReB_2 is a lately accepted ultra-incompressible superhard material class [75] and has been re-explored in hopes of succeeding in high hardness comparable to diamond [76]. An important point for this material is that the preparation process of ReB_2 does not involve high pressure like other hard artificial materials (e. g. c-BN) and therefore it is cheaper to manufacture than others with high pressure production technics but, Re itself is an expensive raw material. ReB_2 can be used in different application areas, for example, cutting tools, wear resistant coatings, etc. [77].

Boron nitrides, boron oxides and silicon borides, which are other special B-rich boron compounds realized within the scope of this thesis, will be pronounced specifically in the next sections.

Briefly, the most common usage areas of boron and boron compounds can be listed as agriculture, construction, metallurgy and materials, chemistry and recently energy. Apart from these usage areas, they have been consumed in numerous fields such as defense industry, glass industry, electronic and computer industry, vision systems, pharmaceutical and cosmetic industry, communication tools, paper industry, protector equipment, sport materials, nuclear industry, automobile industry, textile sector, medicine and aerospace industry [51].

1.3.2 The Properties and Application Fields of Boron-Rich Borides

Properties: Boron-rich (B-rich) borides are in the class of refractory materials having the properties of outstanding hardness, lightweight and extremely stable thermally [78-80]. B-rich compounds exhibit electrically metallic, semimetallic, semiconducting and insulating features. In addition, even ionic conductivity and superconductivity can be observed in B-rich compounds. If their good electrical conductivity combines with low thermal conductivity, B-rich materials can possess good thermoelectrical feature. This feature is preferred because many borides having complicated covalent bonds between boron atoms will be especially attractive materials under high temperatures due to their splendid thermal stability [81].

B-rich compounds have some outstanding physical features which are electrical and thermal conductivity, hardness, Seebeck coefficients and melting point. In here, it should

be highlighted that these physical properties show numerous variations depending upon their source. It is given two reasons for this situation; the first is the challenges related to the production of boron/borides. The second is the problem of compressing non-melting powders consisting of very hard particles and hence, the transport feature measurement and realistic contact becomes difficult [5, 82].

Due to the morphologic complexity of B-rich compounds, numerous new opportunities emerge in order to dope/substitute, affecting the electrical characters of B-rich borides. Borides being the rare-earth metals exhibit a characteristic of either *n*-type or *p*-type semi-conductivity [83].

Application Fields: First of all, it should be mentioned that some of the usage areas of boron compounds will be briefly summarized. The special boron compounds will be described in the next part in details.

Boron can be used as an electronic component in semiconductors. Besides, it can be utilized in ignitor of airbags. Boron fibers are generally used in the aerospace industry and airplane construction as reinforcement component of synthetic materials and light metals. Thanks to the high neutron capture cross-section of boron, ^{10}B works as a neutron capture in the nuclear reactors and the medicine sectors [5].

Boron carbide ceramics having excellent hardness and lightweight can be used as ballistic materials in the personal security areas [84]. Boron carbides also have unique abrasion features even at the high temperatures, so they can serve as sandblasting nozzles or grinding equipment [78]. Composite materials forming of boron carbides and aluminum have good mechanical properties and so, they can be used as engineering materials and high-value building materials [85-87].

Hexagonal boron nitride is the first desired material for crucibles due to its soft structure, high heat conductivity and electrically nonconducting with high chemical resistance. Cubic boron nitride is accepted as the second hardest solid after diamond. Additionally, cubic boron nitride, thanks to excellent oxidation stability, has special application areas [5].

Boron hydrogen materials have been popular in the fields of rocket fuels. Recently, these materials remain on the agenda as hydrogen storage materials such as $NaBH_4$, $LiBH_4$ and H_3NBH_3 for fuel cells [88-91]. Apart from them, there have been special investigations about H_2 uptake characters of the nanotube forms [92] and the hydrogen release is significantly improved in the quaternary hydride $LiB_{0.33}N_{0.67}H_{2.67}$ by simply doping processes [93].

Metal borides are used to harden mechanical parts, tools of sports equipment and turbine/rotor blades that are subjected to extreme stress. Further, due to the high electrical conductivity, chemical resistance and excellent mechanical properties, metal borides can be accepted as functional electrode materials [5]. Metal hexaboride nanowires such as cerium hexaboride (CeB_6) and lanthanum hexaboride (LaB_6) are suggested for high-performance electrical usage areas recently. LaB_6 nanowires are thermos-ionic cathode materials and can be particularly used in electron beam applications. CeB_6 nanowires, similar to LaB_6, can be used as electron emitters in the applications of field-induced emission, thermo-ionic emission, and thermal field-induced emission etc. Moreover, CeB_6 offers potential usages in electronic devices requiring high-performance electron resources [94]. Ferroboron that is a magnetic binary iron alloy forming of boron and iron is used as an alloying agent and hardens steel. Therefore, steels are improved the creep resistance, workability at hot conditions and neutron absorption [95]. Apart from these boron compounds, magnesium diboride gets some attentions because it exhibits superconducting behavior at 39 K (-234 °C) [96].

1.4 A Synoptic to The Materials in The Scope of This Thesis

Throughout this thesis, although the boron compounds studied are boron-rich, general information about boron compounds is given in this section (i.e., both boron-rich phases and non-boron-rich phases).

1.4.1 Boron Nitrides

Boron nitride (BN) is an inorganic ceramic and isostructural to carbon. It can form both sp^2- and sp^3-bonded phases, similar to carbon [97]. BN essentially has four different types of crystal structures; hexagonal (h-BN), rhombohedral (r-BN), cubic (c-BN), and wurtzite (w-BN) and the structural representations of these crystals are illustrated in Fig. 1.6.
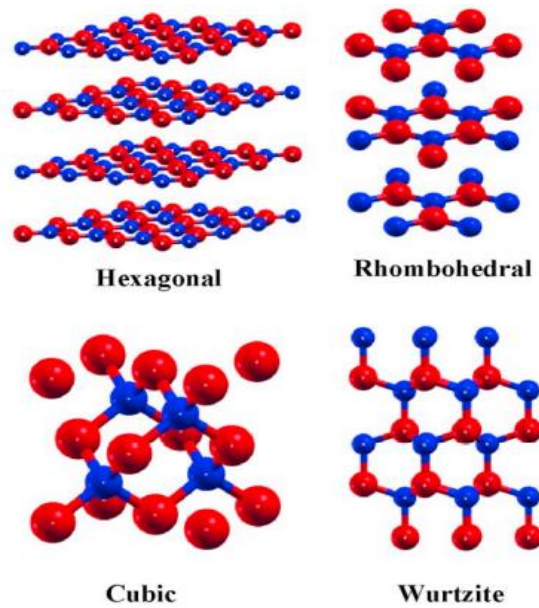
Figure 1.6 The structure illustration of BN crystals.

1.4.1.1. Hexagonal Boron Nitrides

h-BN is a well-studied phase amongst BNs. h-BN consists of layers in analogy to graphite and hence h-BN is generally called as "*white graphite*". In each layer, nitrogen (N) and boron (B) atoms have solid covalent bonds. However, weak van der Waals forces hold the layers together. The two types of different bonding result in a high amount of anisotropy. Furthermore, in addition to the covalent bonds, B-N bonds can exhibit relatively ionic character due to the electronegativity difference between B atoms and N atoms (3.04 for N and 2.04 for B). Consequently, h-BN demonstrates less electrical conductivity in comparison with graphite being semimetal and has higher mechanical hardness owing to its increased interlayer interaction. Because N has higher electronegativity than B, the π-electron is positioned at N and this makes h-BN a semiconductor having a wide forbidden band gap. h-BN retains its structure up to 1000 °C in the air and 1400 °C in vacuum [98].

2D h-BNs can be fabricated by different approaches [99-118], for example, chemical or physical vapor depositions (CVD or PVD), cosegregation process etc. The representation s of CVD and cosegregation techniques are provided in Fig. 1.7 [107] and Fig. 1.8 [117], correspondingly.
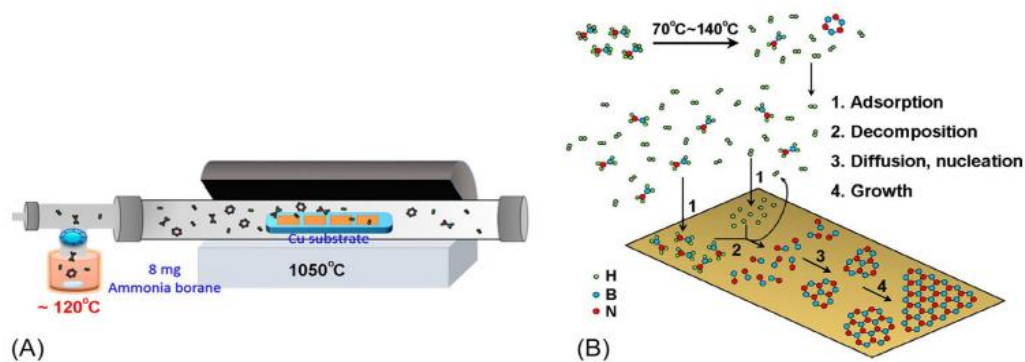
Figure 1.7 Representation of the CVD procedure on a Cu substrate (A) the growth apparatus of h-BN on a Cu substrate (B) [107]
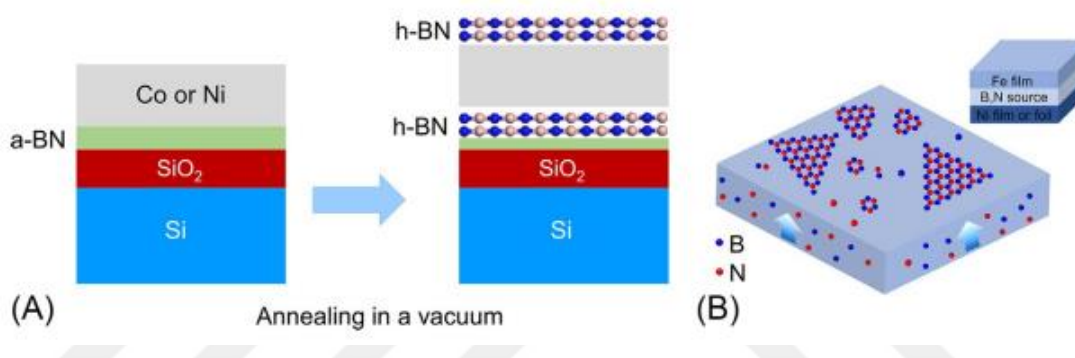
Figure 1.8 (A) Representation of the cosegregation method to produce h-BN layers. (B) The fabrication of h-BN by the vacuum tempering of sandwiched substrata [117].

h-BN films have numerous charming features such as high mechanical strength/elastic modulus excellent inertness, excellent electrical insulation, low dielectric constant, low friction coefficient, a wide optical bandgap and high hardness, temperature stability etc. Due to these attractive characters, h-BN is a promising ceramic in using many diverse application fields [98].

1.4.1.2 Cubic Boron Nitrides

Cubic boron nitride (c-BN) is the second most prevalent phase among BNs. c-BN is first produced from h-BN at the high temperature and pressure (HTHP) application in 1957 [119]. After this year, although much more complicated production technics have been suggested, none of them was not commercially achieved up to 1969 [120].

Thanks to its inimitable features, c-BN has drawn numerous notices as a promising material for many possible application areas. The most prominent feature of c-BN is

doubtlessly its mechanical strength. High electrical resistivity/thermal conductivity, low dielectric constant, wide bandgap, chemical inertness, etc. can be accepted as some of other attracting features of c-BN. Moreover, c-BN has high hardness subsequent to diamond [97]. Its bulk and Young's moduli are also comparable with those of the diamond structure. Although p-type doping is possible for diamond, both n- and p-type impurities are possible for c-BN, significantly affecting its electrical features. c-BN has the zinc blende crystal having sp^3-bonded B atoms and N atoms and it is analogous to diamond. However, c-BN structure possesses one boron face-centered cubic (FCC) cell and one nitrogen FCC cell whereas diamond has two carbon FCC cells. Thanks to all of these and other striking features and the similarities to diamond (see in Tab. 1.4 [98, 120]), c-BN has been a suitable ceramic in various different industrial applications [120].

Table 1.4 The comparison of chemical and physical features of c-BN with diamond [98, 120].

Properties	c-BN	Diamond
Structure	Zinc blende	Diamond
Density (g/cm^3)	3.48	3.52
Bulk modulus (GPa)	367	435
Young modulus (GPa)	800-900	920-1100
Microhardness (GPa)	75-90	80-120
Melting point (K)	3500	4000
Graphitize (K)	>1773	1673-2073
Thermal stability (K)	1573-1673	833-973
Thermal conductivity (kW/m.K)	1.3	2.0
Chemical stability with metal	Better	Bad
Bandgap (eV)	~6.4	5.5
Dopable type	p- and n-type	p-type
Dielectric constant	4.5	5.58

The apparatuses for HTHP synthesis are substantially sophisticated and the c-BN crystals obtained are generally a few millimeters in dimension, which stay too short in most industrial utilizations. c-BN is colorless, c-BN produced by HTHP show a color between yellow and amber (see Fig. 1.9 [121]). This indicates that the crystals between yellow- and amber-color include some impurities. Furthermore, the amber-colored c-BN could be grown by using (Li$_3$BN$_2$ solvent whereas the pale ones could be produced by using Ba$_3$B$_2$N$_4$ solvent [121].

In addition to bulk c-BN crystals, it is possible to produce c-BN thin films. The first thin film forms were synthesized under low pressure in 1979 [122]. After many efforts to produce c-BN thin layers, the succeeded production approaches have been published

since 1990s [123-132], see Fig 1.10, for example, the representation of several plasma-assisted CVD and ion-assisted physical vapor deposition (PVD) methods.
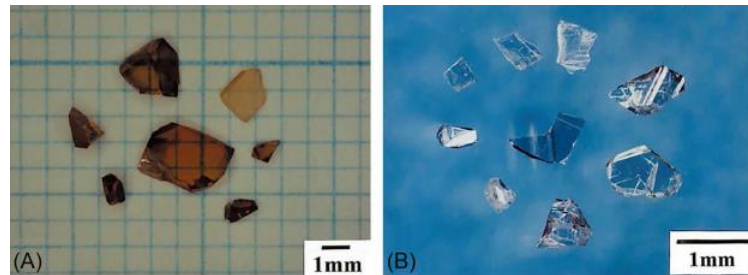
Figure 1.9 c-BN crystals produced by the HTHP technic by using Li₃BN₂ solvent (A) and Ba₃B₂N₄ solvent (B) [121].

Thanks to the high mechanical strength, c-BN is a promising candidate for mechanical applications. Furthermore, bulk and Young's moduli of c-BN have higher values than classical abrasive materials including B_4C and SiC. For this reason, it can be used in abrasive tools. c-BN can be utilized in both grinding and cutting or milling applications. In addition to its mechanical features, as for the electronic nature of c-BN, it is known as the lightest III-V semiconductor and hence, it takes advantage as a good insulator with a wide band gap. c-BN can also have the highest thermal conductivity and this allows that c-BN is exploited as a heat sink in LEDs emitting light, semiconductor lasers and microwave devices at a wide spectrum. c-BN can show both n-type and p-type characters by doping with beryllium and silicone. These semiconductors are used to manufacture p-n junction diodes operating at high temperatures. These kinds of junctions have many different application fields including UV sensors. Lastly, c-BN in electronic devices can be a possible redress to the dire need of smaller, insulating and thermally conductive materials [120].
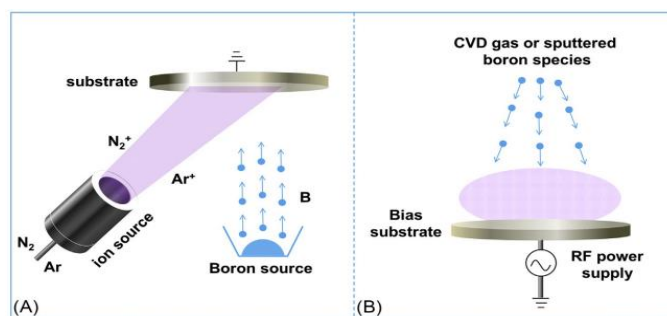
Figure 1.10 Representation of ion-assisted deposition (A) and plasma-assisted deposition (B) [98].

17

1.4.1.3 Rhombohedral Boron Nitrides

Parallel to h-BN, r-BN has a sp^2 bonded crystal. r-BN is generally considered as a hexagonal crystal; however, its primitive cell is a rhombus. r-BN, besides, is structurally, again, analogue to rhombohedral graphite. In many experimental investigation, r-BN does not present adequate size in crystals and cannot be found as a pure structure. Namely, it consists of some h-BN structures. For these reasons, the physical features of r-BN are not known completely. r-BN powders are generally synthesized from turbostratic h-BN at high temperatures [98].

1.4.1.4 Wurtzite Boron Nitrides

Another phase of BNs is wurtzite boron nitride (w-BN). w-BN is composed of sp^3 bonds [98] and is analogous to hexagonal diamond or lonsdaleite [98, 133]. w-BN is synthesized during the HTHP treatment of turbostratic h-BN or r-BN. However it is rarely found in pure arrangement and has a substantial amount of sp^2 bonds. w-BN has a large bandgap with a value of 4.9 eV [134]. Although this wide bandgap insulator has large a Seebeck coefficient, it possesses low electrical conductivity. In addition, w-BN has large thermal conductivity and hence, bulk w-BN is not suitable for the thermoelectric applications [133]. Lastly, it should be emphasized that the physical features of w-BN are not adequately known since the single crystal w-BN has not been manufactured so far.

1.4.2 Boron Oxides

It is possible to classify boron oxides basically in three crystal and/or amorphous phases; boron trioxide (B_2O_3), boron suboxide (B_6O) and boron monoxide (BO).

1.4.2.1 Boron Trioxide

Boron trioxide (B_2O_3) can be named as boria [135] and boric oxide [136]. The high-pressure form of B_2O_3 was first produced in 1959 [137] and the phase diagram showing the lower pressure limits was prepared for production of B_2O_3 structure in 1961 [138].

B_2O_3 is known in three different forms; one of them is amorphous, glassy or vitreous (a-, g- or v-B_2O_3) and the others are crystalline (α- and β-B_2O_3) structures. v-

B_2O_3 is not of a definite melting point and starts to soften at ~325 °C. On the other hand, the crystalline forms of B_2O_3 can be synthesized under high pressures. One of them can be also obtained at atmospheric pressures. The melting points of crystalline forms obtained at high pressure and at atmospheric pressure are 465 °C and 450 °C, respectively. Some physical and chemical features of B_2O_3 are itemized in Tab. 1.5.

Because B_2O_3 has a hygroscopic character, it should be careful to keep way from humidity and/or water. Furthermore, if B_2O_3 is wetted, it reacts exothermally and forms boric acid (H_3BO_3) [139].

Table 1.5 Some physical and chemical properties of B_2O_3.

Properties	B_2O_3
Molecular Weight	69.62 (g/mol)
Melting Point	450-465 °C
Specific Gravity	1.84 gr/cm^3
Heat of Solution (Absorbed)	4.81x10^5 J/kg

The amorphous phase is, by far, the most prevalent investigated among B_2O_3 forms. ν-B_2O_3 is thought to be formed from boroxol rings. In other words, boroxol rings (B_3O_6) (Fig. 1.11) can be defined as rings in which molecular groups consist of interconnected planar triangles of BO_3 and these triangles build up glassy B_2O_3 (ν-B_2O_3) [140, 141]. The substantial morphological alterations are expounded on ν-B_2O_3 which are lastingly compressed from 1 to 5.8 GPa. Previous experimental studies on Raman scattering [142] and nuclear magnetic resonance [143] showed that the increment density of glass is pertinent to the declining amount of boroxol rings. In addition, the increase in glass density is also associated with the transformation from threefold coordinated B atoms to fourfold coordinated B atoms with increasing pressure [142]. The alteration in B atoms coordination (from 3 to 4) can be assumed as probable evidence for presence in the glassy polymorphous systems, which reverberates the two crystalline structures of B_2O_3 mentioned above; α-B_2O_3 and β-B_2O_3.
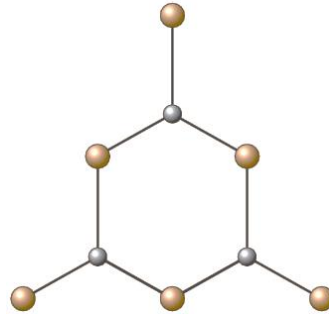
Figure 1.11 The boroxol ring; yellow and grey circles symbolize O and B atoms, correspondingly.

The α phase is a low density of B_2O_3. α-B_2O_3 has a trigonal symmetry and consists of BO_3 triangles. Crystallization of α phase from the molten state at ambient pressure has not been approved kinetically when compared with crystal and liquid densities. For this reason, α-B_2O_3 can be synthesized by annealing the amorphous solid at 200°C and at least 10 kbar for a long time [144, 145]. As for the β phase, it is a high-density form of crystal B_2O_3 and has a tetrahedral symmetry. β-B_2O_3 can be obtained at high pressures and hence, β-B_2O_3 is denser than α-B_2O_3.

B_2O_3 structures are used in specialty glasses and ceramics, refractories, glazes and enamels, chemical reactions and metallurgy applications. Some examples of these applications are given below;

Specialty glasses: Pure B_2O_3 is exploited in the production of specialty glass such as medical glass (ampoules), telescope and optical lenses, electronic glass and ceramic-glass composites. With the use of B_2O_3 glasses, their thermal resistance and mechanical strength increases, their melting temperature decreases and their chemical stability is improved.

Specialty ceramics: By using B_2O_3, it is possible to manufacture the ceramic materials having high heat resistant and mechanical strength.

Refractories: B_2O_3 can be used in producing chemically bonded castable and firebricks requiring resistance to corrosion, abrasion and high temperature.

Glazes and enamels: B_2O_3 improves chemical and scratch resistance and strength of ceramic wares (e.g. porcelain and table wares, floor and wall tiles, enameled appliances). Furthermore, the melting and physical features of these products enhance thanks to B_2O_3.

Chemical reactions: B_2O_3 is exploited as a catalyst in the conversion and production of different organic alloys. Additionally, it can be used in the preparation of metallic borides, boron halides, borate esters and sodium borohydrides.

Metallurgy: At high temperatures, B_2O_3 is accepted as a splendid solvent for metallic oxides. In order to harden steels and to produce alloys with nickel, iron and manganese, B_2O_3 can be used the preparing of especial welding and soldering fluxes. Finally, B_2O_3 is also used to synthesize rare-earth magnets and amorphous metals [139].

1.4.2.2 Boron Suboxide

Crystalline boron suboxide (c-B_6O) being the hardest oxide is known one of the hardest materials. Its Vickers hardness has values of 30-45 GPa [146, 147]. Its crystal has the cubic close packing (ccp) of B_{12} icosahedrons. Due to strongly covalent bonds between atoms and its short interatomic bond lengths, c-B_6O exhibits a series of superior chemical and physical features, for example great hardness, excellent wear resistance, large melting point (1760 °C), high chemical inertness, high thermal conductivity and low mass density [148-151]. Nevertheless, the investigation of both physical and chemical characters of c-B_6O have been interrupted because the procuring of pure and large crystals has some difficulties. For this reason, c-B_6O was suspended from the hardest materials' list [152-155].

B_6O in the crystalline form can be synthesized by the reduction of B_2O_3 with B or by the oxidation $B_6Zn_2O_{11}$ or other oxidants [149-151, 154-157]. In these production technics, c-B_6O is generated at or near ambient pressure and has oxygen deficiencies (B_6O_x, x<0.9) in general. Besides, c-B_6O is of very small grain size (<5μm) and poor crystallinity. On the other hand, the crystal grain size, the crystallinity and the oxygen stoichiometry considerably increase if pressure is applied during the production of c-B_6O [152, 158, 159]. Briefly, the stoichiometric crystalline B_6O material can be only produced under high pressure. Otherwise, in the case of the synthesis of c-B_6O with high temperature and low pressure, it causes the formation of an oxygen deficient compound.

Because of the potential application fields of c-B_6O, it has drawn remarkably attentions and conducted intensive investigations in recent years but the commercial applications have not been determined yet, which is partially related to its low fracture toughness. Additionally, many mechanical features of this material have not completely

comprehended up to now [160]. However, B_6O materials is a good candidate for body-armor materials.

Regarding as amorphous phase of B_6O (a-B_6O), there are different experimental technics to produce a-B_6O such as a reactive radio frequency (RF) magnetron sputtering, a hot-pressing technic, a cathodic (vacuum) arc deposition and an evaporation [161-168].

1.4.2.3 Boron Monoxide

The boron monoxide $(BO)_n$ is generally synthesized with two different forms. The former is the dehydration of subboric acid $(B_2(OH_4))$ [169]. The latter is the reduction of boron trioxide (B_2O_3) with the elemental boron, metal borides/carbides, boron carbide or carbon at temperatures between 850°C-1800°C [170-172]. On the other hand, solid $(BO)_n$ was generated as two different forms, which have white and brown (or amber) color by dehydrating $B_2(OH_4)$ in a previous investigation [169]. In that study, it was observed that $(BO)_n$ having white color is easily soluble in methanol and water whereas that of having brown color dissolves providently in these solvents. On the contrary of the white $(BO)_n$ structure, the brown form is brittle and hard. In the consideration of these observations, two different forms of $(BO)_n$ were identified [169]. The synthesis of $(BO)_n$ having high purity by means of a $B_{(s)}$-$B_2O_{3(l)}$ mixture at a temperature of 1050°C has been completed successfully by another previous study and the glassy $(BO)_n$ having the amber color was obtained with the same production method. Based on the X-ray diffraction pattern, it was concluded that $(BO)_n$ structure exhibited only amorphous character [170].

To determine if the structure has B-B bonds, boron monoxide prepared by means of the hydrolysis of $B_2[N(CH_3)]_2]_4$ involving B-B bonds. In the research, it was concluded that $(BO)_n$ should possess 1 B-B bond for each 2 B atoms such that each B atom should be connected to 2 O atoms. Besides, it was reported that $(BO)_n$ vaporized between 1300°C-1500°C to create B_2O_2 in gaseous form and this was also further proof the existence of B-B bond [173]. Hence, it was proposed two possible three-dimensional configurations comprised from six-membered B_4O_2 or B_3O_3 rings (see in Fig. 1.12 [173]) for $(BO)_n$ [169, 173].
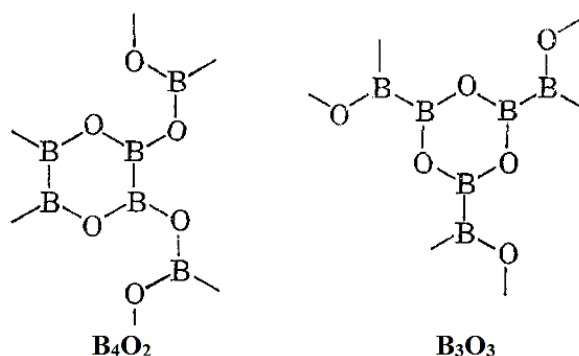
Figure 1.12 B₄O₂ ring and B₃O₃ ring [173].

1.4.3 Silicon Borides or Boron Silicides

Silicon boride or boron silicide (BSi) compounds are in the class of a lightweight ceramics [174]. BSi borides are a charming material and possess a wide range of important industrial applications. BSi materials can be accepted as a promising candidate for future investigations due to its extraordinary features such as a moderate melting point (~1850°C), high hardness, a low specific gravity [175, 176] and excellent electrical conductivity [175]. BSi forming from B polyhedral frameworks, on the other hand, is of exceedingly high chemical stability and high thermal-shock resistance hence BSi is a typical refractory material and generally exploited in devices which can operate at extreme conditions [177-179]. In recent years, boron-doped silicon has also drawn remarkably attention due to its potential superconductivity [180-183]. Unfortunately, the critical temperature increases up to 0.56 K depending on the amount of B concentration [183]. Since 1900s, the extensive studies on the B-Si systems have been conducted. Three different the B-Si materials synthesized at ambient or high-pressure conditions have been proposed in the literature; they are B_3Si (and/or B_4Si), B_6Si and B_nSi (n≥14) [184-186]. Furthermore, an experimental study has been carried out on the amorphous B-Si systems having different stoichiometry.

1.4.3.1 Silicon Triboride and/or Silicon Tetraboride

In 1900, the first original study on the B-Si systems was performed and two different phases of B-Si compounds, SiB_3 and SiB_6, were prepared by using the fusion of elements method [187]. It is possible to say that SiB_3 is divided into two different phases being α-phase and β-phase. α-SiB_3 comprising from B-rich icosahedra was propounded

to be a rhombohedral crystal structure, where Si atoms partly substituted with B atoms in the polar icosahedral sites. For this reason, α-SiB$_3$ has different stoichiometry changing from 2.8 to 4 [188]. α-SiB$_3$ possesses the same configuration with both boron carbide (B$_{12}$C$_2$ or B$_4$C). [179, 189, 190]. α-SiB$_3$ is generally produced by isothermal heating at 1225°C [191]. Although α-SiB$_3$ is rarely synthesized in pure form, it is mostly obtained with SiB$_6$ products [188, 192-196].

β-phase, another structure of SiB$_3$, was first obtained in gallium (Ga) flux at lower temperature (850-1000°C) [197]. β-SiB$_3$ has an orthorhombic crystal system having B atoms engendering regular B$_{12}$ icosahedra. Lastly, it should be pointed out that both α-SiB$_3$ and β-SiB$_3$ are semiconducting ceramics having band gap values of 0.2 eV and 2.0 eV, correspondingly [178].

1.4.3.2 Silicon Hexaboride

Silicon hexaboride (SiB$_6$) crystal was firstly produced after heating B and Si elements in a clay vessel in 1900[187]. In 1956, a cubic phase of SiB$_6$ was proposed by means of the X-ray structure consideration for the first-time [198]. However, in a later study, this crystal phase was claimed to be unstable mechanically [199]. Another SiB$_6$ crystal structure was identified as an orthorhombic phase-based on X-ray diffraction [174, 200]. This crystal has a complex configuration in the orthorhombic unit cell, consisting of about 238 B and 43 Si atoms. Furthermore, the orthorhombic phase of SiB$_6$ includes interconnected icosihexahedra, icosahedra and various isolated B and Si atoms [200]. Based on theoretical research, two other SiB$_6$ crystal structures, namely monoclinic and hexagonal crystals, were proposed as mechanically stable [199]. An interesting point of the research is that monoclinic SiB$_6$ is an indirect bandgap semiconductor (0.41 eV) whereas hexagonal SiB$_6$ has a direct bandgap semiconductor (1.654 eV). This theoretical study also indicates that this new ceramic could be suitable as a refractory material that can operate in extreme situations [199]. Lastly, it should be pointed out that analogue to α-SiB$_3$, the B:Si ratio of 6:1 in SiB$_6$ structure can be changed from SiB$_{5.7}$ to SiB$_{6.1}$ by replacing B or Si atoms at multiple sites [189, 200].

1.4.3.3 The Other Crsytalline Silicon Borides

SiB$_n$ crystals can be obtained by means of the peritectic reaction. In other words, liquid + β-B solid solution = SiB$_n$ at a temperature of 2293 K [201]. SiB$_n$ crystal was, for

the first time, synthesized in a composition of SiB_{14} in 1965 [202] but the value range of n has stayed conflictual up to now. In a former investigation, it was claimed that n value changes between 16 and 26 [203]. After about a decade, it was also propounded that n value ranges from 13.9 and 32.3 in a different study [204]. Ten years later, a wider value span for n was suggested. In this research, the Si-rich solubility limit of SiB_n at a temperature of 1873 K was 5.4% equivalent to $SiB_{17.5}$ structure. The possible highest limit of SiB_n was up to ~60 because the two phase region of $B_{(ss)}+B_nSi$ was thought to be pretty narrow [179].

1.4.3.4 Amorphous Silicon Borides

Amorphous BSi (a-BSi) binary compounds can be produced by using diverse experimental protocols. Amorphous B_nSi_{1-n} ($0 \leq n \leq 1$) configurations were fabricated by radio frequency (rf) plasma decomposition of SiH_4-B_2H_6 gas mixtures [205]. Si-rich a-BSi materials with 0-40% B contents [206] and 1-50% [207] were manufactured by the low-pressure chemical vapor deposition (LPCVD) method at 25°C-700°C [206] and 400°C-520°C [207], correspondingly. As for B-rich a-BSi materials, they were manufactured in the range of 90%-97% by arc-melting or spark plasma sintering procedures [208]. a-BSi films having different Si:B ratios were produced by pulsed laser deposition method. It was proposed that the band gap value of B-rich a-BSi increases with decreasing B concentration [209]. Finally, based on the different previous investigations, it is possible to argue that the oxidation of B and Si in a-BSi alloys is faster than that of crystalline structures when B content is higher [210].

1.5 Motivation of Study

Boron has a great importance for Turkey. Boron appears to have about 230 distinct types of minerals known in nature. The biggest reserves are found in Turkey. The boron minerals found in Turkey possess the maximum quality and more economical fabrication conditions compared to those of the other boron producers in the world. There is a substantial demand for its usages in new fields. Boron will be able to make a great contribution to Turkey's economy.

Thanks to the rapid development in boron chemistry after World War II, there are more than 250 application fields today as raw materials, refined materials and boron

compounds. Boron extraordinarily increases the added-value of the materials. Developing technologies depend on boron and hence the future of boron as a strategic mineral is becoming more and more evident. Consequently, both theoretical and experimental investigations on materials involving boron start to become more and more important. Moreover, a few theoretical investigations have revealed new aspects on new modifications of boron compounds. When comes to B-rich materials, although both crystalline and amorphous forms have been reported, there have been limited investigations on their amorphous phases and hence both their atomic structure and the mechanical and electronic features have not been clarified in details up to now. For this reason, there are two main objects throughout this thesis study: *The first* is to create of B-rich amorphous materials. It is worth stating here that some of the B-rich compounds examined in this thesis have not been previously investigated by any theoretical and experimental studies. *The second* is to explain how the B concentration influences their microstructures and hence their properties.

1.6 Overview

This thesis is structured as follows;

In Chapter 2, the theoretical quantum concepts involving the general information related to the density functional theory are presented.

In Chapter 3, Chapter 4 and Chapter 5, a detailed examination of B-rich amorphous BN (*Chapter 3*), BO (*Chapter 4*) and BSi (*Chapter 5*) with 50-95 at.% B is reported to provide valuable information about their atomistic character and electrical and/or mechanical properties.

In Chapter 6 and Chapter 7, the microstructures and the mechanical and electrical natures of amorphous SiB_3 and amorphous SiB_4 are determined and compared with their crystals.

Finally, in Chapter 8, a discussion and the summary of all results is briefly provided and overall future prospects are mentioned with a few concluding remarks.

Chapter 2

Theoretical Background

In the scope of this thesis, the microstructure, electrical and mechanical properties of B-rich amorphous binary compounds were investigated intensively using a computational approach. The purpose of *"Chapter 2"* is to briefly expound the theoretical methodologies before giving details of the research performed.

2.1 The Density Functional Theory

The density functional theory (DFT) dated back to the initial days of the quantum mechanics, when, in 1926 and 1927 Fermi and Thomas submitted a model for exploring the electronic structure of atoms on the basis of the electron density instead of the wave function [211, 212]. In 1950s, Slater took a considerable step in which the Hartree-Fock (HF) method was simplified by substituting the complex nonlocal Fock operator with a local and single parameter operator including the density [213]. Thus, the approach revolved into a highly effective method for calculating the electronic structure on solids and molecules [214]. In 1964, the density models were turned into a full-fledged theory by Hohenberg and Kohn through their two well-known hypotheses [215]. The first one shows the lowest energy eigenstate of a system as a functional of density. The second one proposes a variational principle, and therefore suggests the path to the *"best"* density, in principle at least: *look for the lowest energy wave function as it has been known in quantum mechanics for decades.* Finally, the basic equations of DFT, which is the last and most important contribution to DFT, were carried out by Kohn and Sham in 1965 [216].

To have a clue of how much improvement has been made in DFT developments, it should go back to 1998, when the Nobel Prize was awarded. In other word, after the vindication of the 1998 Nobel Prize sharing by Kohn who invented the theory [217] and by people who developed the computational methods in quantum chemistry [218]. Since

then, DFT's popularity has continued to grow at an incredible rate. For example, when Burke [219] searched for DFT as a subject in Web of Science, the number of articles was ~1000 in 1996, ~5000 in 2005 and ~8000 in 2010. On the other hand, nowadays, it will not be an exaggeration to describe DFT as a *"par excellence" workhorse* because DFT has been used not only theoreticians but also experimentalists in the combination of computational-experimental papers, while investigating of atomic structure, electronic natures, stability, reactivity and reactions of molecules and polymers and solids [220].

2.1.1 The Schrödinger Equation

To evaluate the electronic structure of any system (atom, molecule or bulk material) and to scrutinize its properties, the electronic wave function must be provided. The wave function of a single-particle system in an external potential might be estimated by solving the single-particle Schrödinger equation. Time-independent Schrödinger equation is specified as follows,

$$\hat{H}|\Psi\rangle = E|\Psi\rangle \tag{2.1}$$

here $\hat{H}$ is Hamiltonian operator and Ψ and E correspond the wave function and energy eigenvalue, correspondingly.

Hamiltonian of a many particles system,

$$\hat{H} = \hat{T} + \hat{V} \tag{2.2}$$

has the kinetic ($\hat{T}$) and potential ($\hat{V}$) energy terms. Two terms in many-body Hamiltonian come from the kinetic energy of electrons and nuclei. On the other hand, the potential energy term has three different type interactions; *nucleus-nucleus, electron-nucleus and electron-electron*. Accordingly, many-body Hamiltonian are composed of five terms as follow,

$$\hat{H} = \hat{T}_e + \hat{T}_n + \hat{V}_{en} + \hat{V}_{ee} + \hat{V}_{nn} \tag{2.3}$$

and the terms can be rewritten explicitly as,

$$\hat{H} = -\sum_i^N \frac{1}{2}\nabla_i^2 - \sum_a^M \frac{1}{2M_a}\nabla_a^2 - \sum_{i,a}^{N,M} \frac{Z_a}{|\vec{r}_i - \vec{R}_a|} + \sum_{i\neq j}^N \frac{1}{|\vec{r}_i - \vec{r}_j|} + \sum_{a\neq b}^M \frac{Z_a Z_b}{|\vec{R}_a - \vec{R}_b|} \tag{2.4}$$

here M_a is the nucleus to electron mass ratio, Z_a refers to the nuclear charge number of nucleus a, and ∇^2 is the Laplacian operator. According to the equation of (2.3), when the system size upsurges, the number of particles will increase and thus too many interactions must be taken account.

2.1.2 Born-Oppenheimer Approximation

The simplification to Hamilton playing a fundamental role in computing the electronic structure was first carried out by Born and Oppenheimer in 1927 [221]. This approximation is based on a big difference between electron and nuclear masses. Nuclei move more slowly because they are ~10^3 times heavier than electrons. Therefore, it can be assumed that nuclei remain stationary with respect to electrons and hence the Hamiltonian

$$\hat{H} = \hat{T}_e + \hat{T}_n + \hat{V}_{en} + \hat{V}_{ee} + \hat{V}_{nn} \tag{2.5}$$

could be rewritten. It can be straightforwardly seen that the second and the fifth terms are directly correlated with nuclei. Because the nuclei are assumed to have a fixed position, their kinetic energy might be ignored and hence, the interaction of the nuclei-nuclei might be considered as a constant. As a result, the electronic Hamiltonian can be stated by the remaining terms as follows;

$$\hat{H}_e = -\sum_i^N \frac{1}{2} \nabla_i^2 - \sum_{i,a}^{N,M} \frac{Z_a}{\left|\vec{r}_a - \vec{R}_a\right|} + \sum_{i \neq j}^N \frac{1}{\left|\vec{r}_i - \vec{r}_j\right|} \tag{2.6}$$

where $\hat{H}_e$ represent the movement of N electrons in a stationary situation of M atomic nuclei. The Schrödinger equation having the electronic Hamiltonian is described as;

$$\hat{H}_e|\Psi_e\rangle = E_e|\Psi_e\rangle \tag{2.7}$$

here Ψ_e represents the electronic wave function which, as electronic energy, depends indirectly on the nuclei positions and explicitly on the electron's positions,

$$\Psi_e = \Psi_e \left(\vec{r} ; \vec{R}_a\right) \qquad E_e = E_e \left(\vec{R}_a\right) \tag{2.8}$$

Consequently, the total energy can be stated as the addition of constant electronic energy and nuclear repulsion. Likewise, the description of the Schrödinger equation involving the nuclear Hamiltonian is as;

$$\hat{H}_n|\Psi_n\rangle = E|\Psi_n\rangle \tag{2.9}$$

here Ψ_n is wave function of nuclei and depends on their coordinates. It expresses the rotation, vibration and translation of a molecule. As for E, it denotes electronic, rotational, vibrational and translational energy.

Within the scope of this subheading, the main problem is to solve the Schrödinger equation for a system with N electrons in an external field. Therefore, the attention should be on the electronic structure problem rather than rotation, vibration and/or translation problems. Namely, from now onward, $\hat{H}$ will represent the electronic Hamilton operator

unless otherwise stated. However, solving the Schrödinger equation by using only $\widehat{H}_e$ is still too difficult for the systems consisting of lots of electrons and consequently, further approaches for many-body systems have been required.

2.1.3 Electron Density

The electron density ρ(r) is an important feature for atoms, molecules and also condensed phases of matters because the principal methodology of DFT is to define a system of interacting electrons as electron density instead of through many-body wave functions. That is, DFT accepts electron charge density $\rho(\vec{r})$ as the fundamental variable to determine the lowest energy eigenstate of multi-electron system. The particle density can be calculated as;

$$\rho(\text{r}) = N \int dr_2 \dots \int dr_N \Psi^*(r_1, r_2, r_3, \dots, r_N)\Psi(r_1, r_2, r_3, \dots, r_N) \qquad (2.10)$$

2.1.4 The Hohenberg-Kohn Theorems

The theorems proposed by Hohenberg and Kohn (HK) in 1964 [215] provide a foundation of the current DFT. Their paper was based on two key conceptions: 1) to introduce the electron density as the fundamental variable and 2) to use the variational method with the aim of finding the ground state density.

For the first section, it is known that the external potential $\upsilon(\vec{r})$ fixes the Hamiltonian for an arbitrary number of electrons. For this reason, the many-particle ground state is completely determined by the number of electrons N and the external potential $\upsilon(\vec{r})$. In the first HK theorems, the electron density is exploited as;

Theorem 1: *"External potential $\upsilon(\vec{r})$ is a unique functional of $\rho(\vec{r})$; apart from a trivial additive constant".*

That is, this theorem states that "*there cannot be two different external potentials for the same ground state density*". Since the external potential defines the many-body Hamiltonian and hence the many-body wave function, all features of a system are identified by its ground state density.

The proof of HK's first theorem starts with the supposal that the electron density cannot uniquely specify the external potential, and beyond that there exist two external potentials, $\upsilon(\vec{r})$ and $\upsilon'(\vec{r})$ for the same ground state density n ($\vec{r}$). Consequently, there

are two different Hamiltonian operators, $\hat{H}$ and $\hat{H}'$ which cause two diverse wave functions Ψ and Ψ'. By studying the variational method;

$$E_0 < \langle\Psi'|\hat{H}|\Psi'\rangle = \langle\Psi'|\hat{H}'|\Psi'\rangle + \langle\Psi'|\hat{H} - \hat{H}'|\Psi'\rangle$$

$$= E_0' + \int \rho(\vec{r})[\upsilon(\vec{r}) - \upsilon'(\vec{r})]d\vec{r} \qquad (2.11)$$

The following equation is obtained by switching primed quantities with the unprimed quantities;

$$E_0' < \langle\Psi|\hat{H}'|\Psi\rangle = \langle\Psi|\hat{H}|\Psi\rangle - \langle\Psi|\hat{H} - \hat{H}'|\Psi\rangle$$

$$= E_0 - \int \rho(\vec{r})[\upsilon(\vec{r}) - \upsilon'(\vec{r})]d\vec{r} \qquad (2.12)$$

Addition of the inequalities 2.11 and 2.12, we get an inconsistent calculation as follow;

$$E_0 + E_0' = E_0' + E_0 \qquad (2.13)$$

This result indicates that there exists only one external potential corresponding to the same electronic density for the lowest eigenstate of a given system. Namely, the ground state electron density, except for an unimportant improver constant, uniquely signifies the external potential.

The second HK statement puts forward that the electron density follows the variational method and is expressed as follows;

Theorem 2: *"Any trial electron density function $\rho'(\vec{r})$ satisfying $\int\rho'(\vec{r})\,d\vec{r} =$*

N will give an energy higher or equal to the true ground state energy"

$$E\,[\rho'(\vec{r})] \geq E\,[\rho(\vec{r})] \qquad (2.14)$$

here $E\,[\rho(\vec{r})]$ corresponds to the energy functional of the ground state electron density.

According to the first HK statement, since it is known that the ground state electron density identifies its particular wave function Ψ, external potential $\upsilon(\vec{r})$ and thus its own Hamiltonian $\hat{H}$, it is possible to say that the trial electron density function $\rho'(\vec{r})$ also identifies its own features for example, Ψ', $\upsilon'(\vec{r})$ and $\hat{H}'$.

$$\langle\Psi'\,|\,\hat{H}\,|\,\Psi'\rangle = \int\rho'(\vec{r})\,\upsilon'(\vec{r})\,d\vec{r} + F\,[\rho'(\vec{r})]$$

$$= E\,[\rho'(\vec{r})] \geq E\,[\rho(\vec{r})]. \qquad (2.15)$$

To sum up, the electron density identifies all features of a system. Besides the energy of a system reaches its lowest value if the electron density corresponds to its true ground state density.

2.1.5 The Kohn-Sham Approximation

HK theorems express that the ground state energy is a functional of $\rho(\vec{r})$ but, there is no information on how to set up unidentified functional $F[\rho(\vec{r})]$ to acquire the energy functional $E[\rho(\vec{r})]$,

$$E[\rho(\vec{r})] = F[\rho(\vec{r})] + \int \rho(\vec{r})V_{Ne}\, d\vec{r} \tag{2.16}$$

One year after the HK theorems were proposed, the applicability of modern DFT was achieved by Kohn and Sham in 1965 [216]. In their research, Kohn and Sham revealed how to approach unknown universal functional $F[\rho(\vec{r})]$. As known, $F[\rho(\vec{r})]$ includes both electron-electron interactions and kinetic energy. This can be written explicitly as the subsequent equation;

$$F[\rho(\vec{r})] = T_s[\rho(\vec{r})] + J[\rho(\vec{r})] + E_{xc}[\rho(\vec{r})] \tag{2.17}$$

here, the right-hand side of the Eq. (2.17) corresponds to the kinetic energy of the non-interacting system, the classical Coulomb interaction, and the exchange-correlation energy, respectively. That is, the sum of the correction in the non-classical electron-electron interactions and in the kinetic energy (due to the interacting electrons).

To calculate the kinetic energy with a decent precision, Kohn and Sham took in consideration of a fictitious non-interacting reference system of electrons that had the same density with the real physical system and released orbital expression for the density. Hereby, it is possible to rewrite the equation of (2.17) as;

$$F[\rho(\vec{r})] = \sum_{i}^{N} \langle \chi_i | -\frac{1}{2}\nabla_i^2 | \chi_i \rangle + \sum_{i}^{N} \langle \chi_i | \frac{1}{2}\frac{\rho(\vec{r}')}{|\vec{r}_i - \vec{r}'|}\, d\vec{r}' | \chi_i \rangle + E_{xc}[\rho(\vec{r})] \tag{2.18}$$

here N represents the number of electrons.

Now on the electron density can be expressed as;

$$\rho = \sum_{i}^{N} \langle \chi_i | \chi_i \rangle \tag{2.19}$$

The reference system consists of non-interacting electrons and hence, its ground state wave function can be indicated-as in the HF approximation-by a single Slater determinant.

$$\Psi_s = \frac{1}{\sqrt{N!}} \begin{pmatrix} \chi_i(\vec{x}_1) & \cdots & \chi_k(\vec{x}_1) \\ \vdots & \ddots & \vdots \\ \chi_i(\vec{x}_N) & \cdots & \chi_k(\vec{x}_N) \end{pmatrix} \tag{2.20}$$

The electron density can be precisely computed by obtaining the orbitals (i.e., χ_i's) that minimalize the energy functional. These orbitals are specified similar to the HF theory. Furthermore, to avoid misunderstanding with the HF orbitals these orbitals are denominated as the Kohn-Sham orbitals (or the KS orbitals for short). Kohn-Sham Hamiltonian or operator

$$h_i^{KS}\chi_i = \varepsilon_i\chi_i \tag{2.21}$$

here the one electron KS operator can be formulated by the following equation;

$$h_i^{KS} = -\frac{1}{2}\nabla_i^2 - \sum \frac{z}{|\vec{r}_i - \vec{r}_j|} + \int \frac{\rho(\vec{r}')}{|\vec{r}_i - \vec{r}'|}\,d\vec{r}' + V_{xc} \tag{2.22}$$

and the exchange-correlation potential (V_{xc}) can be estimated by the functional derivative;

$$V_{xc} = \frac{\delta E_{xc}}{\delta\rho} \tag{2.23}$$

The density must be known to calculate the KS orbitals but, the density can also be found by using the orbitals with the help of Eq. (2.18). In this case, an iterative self-consistent-field (SCF) cycle (see in Fig. 2.1 [222]) should be followed, similar to that of the HF theory. This can be accomplished by first estimating an initial density using orbitals. The KS orbitals as well as the Hamiltonian can be constructed in this way. New density will be obtained by solving the equation and the finding value will be exploited for the subsequent steps. Finally, the acquisition densities converge and become self-consistent with the output density, used to compute the energy.
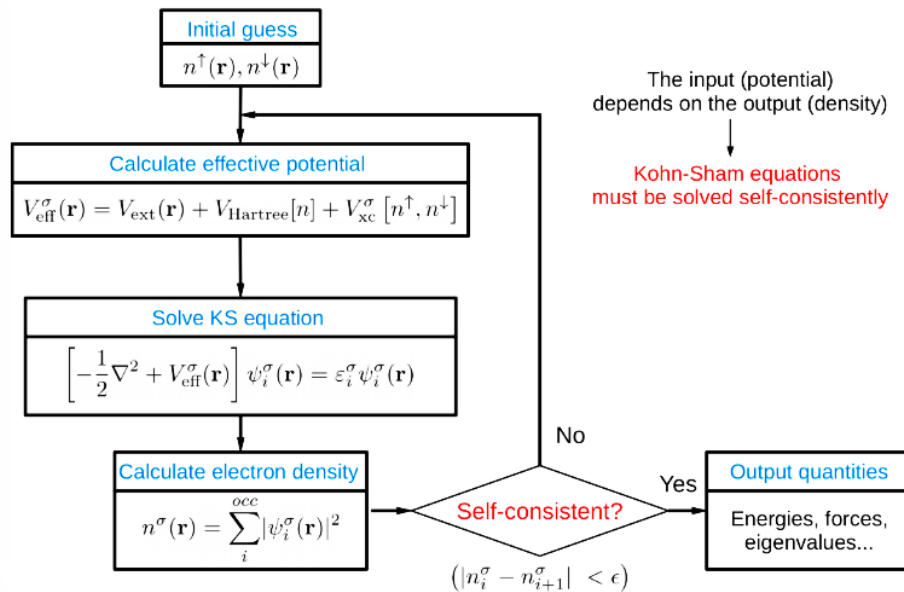
Figure 2.1 The SCF cycle in the DFT [222] Copyright 2021, The Siesta Group Revision c7d47f36.

33

Although there is an obvious common property between the HF and the KS approximations, the HF approach provides an approximate wave function, while that of the KS is in principle precise. The exact energy can be estimated if the exchange-correlation functional in the KS approach is identified. The HF approximation, on other hand, will stay an approximation because it does not consider the effects of electron correlation [223]. The sole problem in the KS-DFT is that the exchange energy-correlation functional is unknown. For unknown exchange energy-correlation functional, several estimations have been offered and some will be considered in the following section.

2.1.6 Exchange Energy-Correlation Functional

The 4th terms in the Eq. of 2.22, as pointed out in the earlier section, can be stated as the functional derivative of the exchange-correlation energy functional with regard to the electron density. $V_{xc}(\vec{r})$ can be found if $E_{xc}[\rho(\vec{r})]$ is identified, yet, the obvious formula of the exchange-correlation energy is not available. While various approaches have been developed for $E_{xc}[\rho(\vec{r})]$, the designing functionals with greater accuracy remains the major challenge in the DFT [224]. A broad array of papers about the development, improvement, tested and comparison of the performance of functionals have been published up to now. The reasons for so many published papers are that the characteristic of functionals is powerfully connected to the precision of calculations and in addition, discrepancies among several DFT methods arise due to the choosing of the functional [225, 226]. In this section, a concise summary will be made about the functionals examined within the scope of thesis.

2.1.6.1 Local Density Approximation

The local density approximation (LDA) can be considered the easiest approach for the exchange-correlation energy functional based on the homogeneous electron gas, which proposed by Kohn and Sham [216]. The energy in the LDA depends only upon the density at a particular point and is stated as below;

$$E_{xc}^{LDA}[\rho(\vec{r})] = \int \rho(\vec{r}) \ \varepsilon_{xc} [\rho(\vec{r})] \ d\vec{r} \qquad (2.24)$$

here, ε_{xc} corresponds to the exchange-correlation energy per electron in a uniform electron gas with electron density $\rho(\vec{r})$. The LDA is of an advantage that the exchange-

correlation functional can be correctly attain via the Slater's Xα model. Hereby, it should be also highlighted that in this model, rather small correlation part in the exchange-correlation functional is ignored.

$$E_{xc}^{LDA}[\rho(\vec{r})] = E_x^{xa}[\rho(\vec{r})] = -\frac{9}{8}\left(\frac{3}{\pi}\right)^{1/3} \alpha \int \rho(\vec{r})^{4/3} d\vec{r} \qquad (2.25)$$

here α is the empirical value. Though the α value is used by Kohn-Sham and Slater as 2/3 and 1, respectively, more corrects result are obtained for both atoms and molecules at values in the range of 2/3 and 1, such as 3/4 [227].

2.1.6.2 Generalized Gradient Approximation

Unlike the LDA, the real molecular system does not have the uniform electron density. Because of this restriction in the LDA, a new approximation named as the generalized gradient approximation (GGA) was developed. The non-uniform nature of electron density is taken into consideration in the GGA and hence, this new approach-because of locally varying density-depends not only on electron density but also on gradient.

$$E_{xc}^{GGA}[\rho(\vec{r})] = \int \rho(\vec{r})\varepsilon_{xc}\left(\rho(\vec{r}), \nabla\rho(\vec{r})\right) d\vec{r} \qquad (2.26)$$

Although the GGA yields improved outcomes than the LDA, particularly for the structural characteristics, both the GGA and the LDA are not successful for the systems that are immensely associated with the electrons (e.g., transition metal oxides (TMOs)) [228]. The functionals suggested by Becke and Perdew (BP86) [229,230] and Perdew, Burke and Ernzerhof (PBE) [231] can be exemplified as commonly used GGAs.

In order to get some information on the chemical accuracy of any system, more recently, the meta-GGA functionals have been put forward by taking a second derivative of the density. The exchange functional by proposed Tao, Perdew, Staroverov, and Scuseria (TPSS) [232], which performs better on properties such as non-covalent interactions, kinetics and thermochemistry, is one of the most popular meta-GGA functionals [233].

2.2 Molecular Dynamics

The first attempts for molecular dynamics (MD) simulations were executed to examine the interactions of hard spheres by Alder and Wainwright in the late 1950s [234,

235]. Stillinger and Rahman, on the other hand, studied the first realistic system (liquid water) in 1974 [236]. The MD simulations is basically hinged on the computation of the equipoise and the transport features of a *classical* many-body system. The *classical* term, in here, refers that the nuclear motion of the particles abides by the laws of Newtonian mechanics. The fact that running an MD simulation is quite similar to an experiment can be explained as follows;

→   In a first step, a model system comprising from N particles is selected.

→   In the next step, the solution of the Newton's equations of motion continues until the system is in equilibrium. In other words, the features of the system do not change with time.

→   Finally, the real measurements are executed.

When we come to an MD program, how it works is briefly explained in a very simple loop below and the MD loop is basically illustrated in Fig. 2.2 [237];

1. The velocities and the initial positions of all particles in the system are determined.

2. The forces acting on the particles are computed.

3. The Newton's equations of motions are taken the integral.

4. The averages of the measured values are computed.
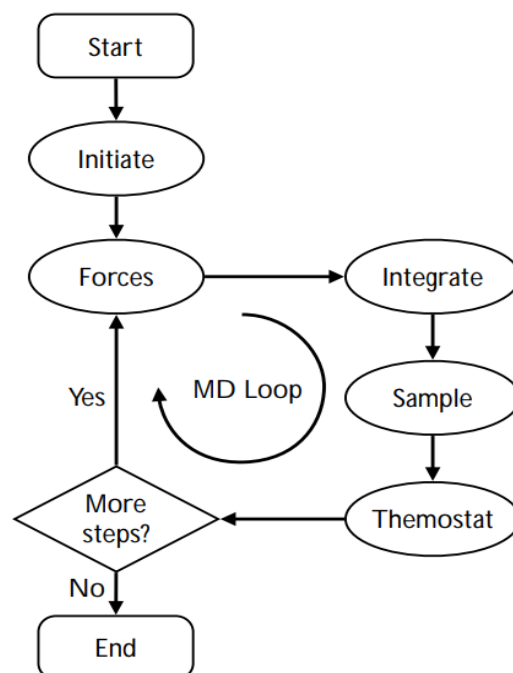
Figure 2.2 The basic MD loop [237].

There are two forms of MD method performed in computer simulations; classic MD (CMD) and ab initio MD from the start (AIMD). Both approaches have some disadvantages and drawbacks as well as advantages.

Since the Parrinello-Rahman MD algorithm seems to be quite successful in regenerating the experimentally monitored phase transformation, it was preferred to use this MD algorithm within the scope of this thesis. The next two sections will first give a brief overview of the CMD and its limitations, followed by a detailed information of the AIMD.

2.2.1 Classical Molecular Dynamics

In the classical molecular dynamics (CMD), the forces are computed from a parametrized potential obtained from either empirical data or first-principles calculations. When compared to the *ab-initio* molecular dynamics, the CMD is fast and also large systems in the order of billions of atoms can be simulated in the CMD. Thus, the simulation of crack propagation, heat transport, grain growth etc. is possible. The achievement of long simulation time in many millions of time steps is also possible for the moderate system sizes; this denotes that relatively long processes such as diffusion can be simulated. Another advantage of the CMD is that, thanks to known potential, it can be modified to examine how alterations in potential affect the physical features of a system. Therefore, a useful model can be obtained to comprehend the underlying mechanics of a system.

Despite its advantages mentioned above, the CMD faces many problems. The first problem is that the empirically fitted forces and potentials exist. The fitting will not become as good as the precise quantum mechanical potential. When fitting the parameters, there will be concessions all the time. It also needs to be decided which features are the most important for the reproduction and which should be fitted to. Another problem is the transferability, as the parameters are fitted to first principles or experimental data for the certain circumstances. Furthermore, when the potential is applied to another circumstance, the fact that how well will stand for this new situation is not well known. Furthermore, when the potential is applied for another circumstance, how prosperously the model will correspond to this new situation is not be known exactly. This implies that, in an unknown configuration, it is difficult to have the knowledge of

how accurate the potential is. For this reason, it can be clearly said that this is a serious drawback/limitation in the CMD since the aim is to estimate the properties of unknowns.

Since most potentials are hinged upon pair and triple interactions, a rapidly increasing number of parameters will be needed to parameterize an alloy consisting of a few elements. On the other hand, as the number of elements upsurges, the number of parameters also increases very rapidly and hence, the fitting process becomes extremely time consuming. One problem in here is that there are many parameters that are interdependent and often do not have enough empirical data to fit. Although the parameters can usually be fitted to *ab-initio* results, will necessitate very expensive calculations.

2.2.2 *Ab-initio* Molecular Dynamics

Ab-initio molecular dynamics (AIMD) possess numerous benefits and highly accurate results compared to CMD. Any parameter does not need to be fit. The only thing that needs to be defined are the atomic number and atomic positions of the elements. The rest will be originated from the fundamental laws of physics.

Due to the difficulties in solving of the numerical equations, AIMD becomes an extremely expensive method. In addition to this limitation, another drawback in AIMD is that many more compelling problems arise because of some recent improvements in the theory.

2.2.2.1 Car-Parrinello Molecular Dynamics

In Car-Parrinello MD (CPMD) calculations, the essential interaction potential is straightforwardly computed using a quantum mechanical electronic structure technique. This combination can be in general implemented easily. For each set of nuclear coordinates, the problem of electronic structure is estimated and the forces acting on atoms are computed by the Hellman-Feynman statement. After that, nuclei are transferred to the next location in as much as the laws of classical mechanics. Finally, the new forces are also computed by a full electronic structure computation. This kind of AIMD is commonly known as "*Born-Oppenheimer dynamics*".

A splendid alternative to this approximation was suggested by Car and Parrinello in 1985 [238]. In this approach, the electronic degrees of freedom are considered as

fictitious classical variables. This system is identified as the extended classical Lagrangian, L$_{ex}$. The Lagrangian is formulated as;

$$L_{ex} = K_N + K_e - E_{pot} + L_{orto} \tag{2.27}$$

If L$_{ex}$ is explicitly rewritten;

$$L_{ex} = \frac{1}{2}\sum_{i=1}^{3N} m_i\, v_i^2 - E[\Psi\,(r_1,\dots,r_{3N})] + \frac{1}{2}\sum_j 2\mu \int dr\, |\dot{\Psi}_J(r)|^2 + L_{orto} \tag{2.28}$$

In the Eq. (2.27) and (2.28), K_N represents the kinetic energy of the nuclei, K_e corresponds the electronic degrees of freedom. E_{pot} relates to the potential energy depending on the position of nuclei and electronic variables. The last term is required to retain the one-electron wave functions orthogonal. If the velocities connected with dynamics based upon Eq. (2.28) are exploited to assign a temperature and are scaled to give T→0, the minimum equilibrium state E will be accomplished. This approximation is referred as CPMD.

2.2.2.2 Parrinello-Rahman Molecular Dynamics

The first version of Parrinello-Rahman (PR) approach (can be called as *"the original Andersen method"*) was introduced by Andersen in 1980 [239]. In this method, it is permitted to alter the size of the simulation cell isotopically by equalizing the computed internal pressure to a desired applied pressure. This is accomplished by acquainting the volume of the simulation box as a new dynamics variable and again by maintaining the periodic boundary conditions. Shortly after the propounding of *"the original Andersen method"*, in 1981, the PR method was generalized by Parrinello and Rahman [240]. In this method, the simulation cell's parameters can alter, more specifically, both the size and shape of the cell can change. This is carried out according to the PR approach as follows.

Let's take account of a general simulation box for MD that fills the entire space by iterating at infinity due to periodic boundary conditions. The MD supercell is identified by the three lattice vectors (**a**, **b**, **c**). The matrix **h** is defined as;

$$\mathbf{h} = (\mathbf{a}, \mathbf{b}, \mathbf{c}) \tag{2.29}$$

here the vectors form the columns of **h** and the location of a particle in the cell, R might be described as below;

$$R = \mathbf{h}S \tag{2.30}$$

where **S** is a vector of the *scaled* position of the particle and the component of **S** is assumed to have values in the range of 0 and 1 inside the cell. The relationship between distances in the *scaled* coordinated and the real coordinates will be defined by means of the metric tensor $G = h^t h$;

$$(R_i - R_j)^2 = (S_i - S_j)^t G(S_i - S_j) \tag{2.31}$$

The fundamental idea of the PR approach is similar to the Andersen dynamics but consider an enhanced Lagrangian. In this system, each component of **h** has classical degrees of freedom whose trajectories are set on by the proper forces. This can be procured by typing the extended Lagrangian system;

$$L_{PR} = \frac{1}{2} \sum_{i=1}^{N} m_i \left(\dot{S}^t G \dot{S}_i \right) - V(r_1, \dots, r_N) + \frac{1}{2} W Tr \left(\dot{h}^t \dot{h} \right) - P_{ext} \Omega \tag{2.32}$$

In here, m_i is the symbol of the mass of i-th particle. *V, W* and P_{ext} are the inter-particle potential, the fictitious mass, the external hydrostatic pressure, respectively. S_i and h^t correspond to a position vector in fractional coordinates for atom i and the transpose of h matrix, correspondingly. Ω is the volume of the simulation box.

The preliminary two terms of Eq. (2.32) describe the Lagrangian for the fixed simulation box. Nonetheless, it should be emphasized that the kinetic energy term in Eq. (2.32) will not coincide with the definite kinetic energy of the particles in the real system as the cell changes over time.

The Euler-Lagrange equations of motion are easily obtained by eq. (2.32);

$$\ddot{S}_i^\alpha = -\frac{1}{m_i} \frac{\partial V}{\partial r_i^\beta} (h^t)_{\beta\alpha}^{-1} - G_{\alpha\beta}^{-1} \dot{G}_{\beta\gamma} \dot{S}_i^\gamma \tag{2.33}$$

$$\ddot{h}_{\alpha\beta} = \frac{1}{W} \left(\pi_{\alpha\gamma} - P_{ext} \delta_{\alpha\gamma} \right) \Omega (h^t)_{\gamma\beta}^{-1} \tag{2.34}$$

where:

$$\pi_{\alpha\gamma} = \frac{1}{\Omega} \left(\sum_i m_i v_i^\alpha v_i^\gamma - \frac{\partial V}{\partial h_{\alpha\delta}} h_{\delta\gamma}^t \right) \tag{2.35}$$

and

$$v_i^\alpha = h_{\alpha\gamma} \dot{S}_i^\gamma \tag{2.36}$$

The Greek letters specify the components of both matrices and vectors. By construing $m_i v_i$ as the momentum of i-th particle, it can be demonstrated that π corresponds with the stress tensor.

$$\frac{\partial V}{\partial h} h^t = \frac{\partial V}{\partial \varepsilon} \tag{2.37}$$

The time deviation of **h** in Eq. 2.34 is due to the instability between P_{ext} and π (π is the instantaneous value of the stress tensor).

The conservative form of the Lagrangian system in Eq. 2.32 is obtained with the help of the constant of motion as below;

$$H = \frac{1}{2}\sum_i m_i v_i^2 + V(r_1, \dots, r_N) + \frac{1}{2}WTr(\dot{h}^t\dot{h}) \tag{2.38}$$

Here, it can be interpreted that $\langle H \rangle$ refers to the enthalpy of the system in physically [241], except for the last term that is insignificant for N in Eq. 2.32.

The key aspect of what is stated under this title is that trajectories created using the PR dynamics yield the mean of thermodynamic measures being equivalent to Gibbs mean in the (N, P, H) statistical ensemble at the thermodynamically limit. In other word, the number of particles, enthalpy and pressure are fixed.

As for W parameter, it deals with the *inertia* of h and it is explicit that the balance feature is not influence by W. The optimal W can be defined as the faster stabilization of the combined cell and ions system. In order to select the optimal W, Andersen proposed that W should be adjusted to gain a relaxation time of the simulation box in the order given in Eq. (2.39);

$$\tau = L/c \tag{2.39}$$

here L is the direct length of the supercell and c corresponds the sound velocity of the system. The typical frequency of the simulation box, in addition, can be estimated by linearizing Eq (2.34). By presuming this frequency as roughly $1/\tau$, the following formula is obtained [241];

$$W = 3 \sum_i m_i/4\pi^2 \tag{2.40}$$

2.2.2.3 Canonical Ensembles Used in Molecular Dynamics

In the simulation, a number of differential equations must be settled with a degree of freedom of each atom. The ensemble theory is utilized to overcome this complexness and describes the characteristic of the whole system. Main ensembles used in the MD simulations are divided into four basic classes; the canonical ensemble, the microcanonical, the grand canonical and the isothermal-isobaric ensembles. A brief explanation of these main ensembles is given in the following sub-titles;

• ***The canonical ensemble:*** This ensemble is symbolized as NVT and the number of atoms, volume and temperate persist constant when interacting the system to a

thermostat. The NVT ensemble is often applied to monitor a system at a certain temperature.

- *The microcanonical ensemble:* The microcanonical ensemble is symbolized as NVE and the number of atoms, volume and total energy are constant. The NVE ensemble is usually preferred to describe the isolated systems. In addition, the NVE ensemble is used in the CMD simulations.

- *The grand canonical ensemble:* The chemical potential and temperature are kept fixed in the grand canonical ensemble (μVT).

- *The isothermal-isobaric ensemble:* This ensemble is symbolized as NPT. During the MD simulation using both barostat and thermostat, pressure and temperature are constant in the NPT ensemble [242, 243]. Most of the experimental investigations are performed under non-isolated, constant pressure and temperature conditions. For this reason, the NPT ensemble is quite useful to create the laboratory conditions. The NPT ensemble also has an importance to calculate the equilibrium features under isobaric conditions [244].

Barostat and thermostat can be used with the different combinations to simulate the behavior of any system; for example, Parrinello-Rahman, Andersen, Langevin and Nosé-Hoover barostats and thermostats. Among them, in the MD simulations the usage of Nosé-Hoover thermostat is mainly preferred.

In order to reach an equilibrium state at the wanted temperature, thermal relaxation time is checked in the Nosé-Hoover. In the case of high relaxation time, the heat flow reduces and thus the system turns into over-damped. If the relaxation time is low in the system, there is a possibility of the fluctuation in temperature.

2.3 Simulation Conditions and Structural Analysis

In this section, an overview of the simulation conditions exploited in the scope in this thesis will be presented. Initially, SIESTA AIMD will briefly be acquainted and then the parameterization of the AIMD simulation code will be outlined. Finally, by giving a brief explanation on the structural analysis technics, this chapter will be completed.

2.3.1 SIESTA

SIESTA is both an approach and a computer program application and is used to carry out efficient electronic structure computations and AIMD simulations of molecules/solids. SIESTA is abbreviation of "*Spanish Initiative for Electronic Simulations with Thousand Atoms*" [245]. SIESTA has some precedencies compared to many other DFT computational tools. It offers superior performance for finite systems such as surfaces, nanotubes, clusters and molecules and can easily overcome computationally demanding systems (i.e., if the system is composed of bigger than 10000 atoms) beyond the reach of plane wave codes. The main advantage of SIESTA, on the other hand, is its N-order scaling algorithm, showing that the CPU time exploited by computations scales linearly with the number of atoms in the simulation box. In this way, SIESTA not only performs very fast simulations by using minimal basis sets, but also gives very correct results by using full zeta and polarized orbitals. Because of these advantages mentioned above, the SIESTA AIMD code was preferred in this thesis to analyze the microstructures and different properties of several B-rich boron compounds.

2.3.2 Pseudopotentials

DFT computations consider the full electron and the nuclei interactions. The pseudopotential approximation is exploited to impair the complexity of the problem. In this approach, an effectual potential having an effect on the valence electrons is considered and the powerful Coulomb interaction with the nuclei and the impacts of the core electrons are ignored. Using the pseudopotential approximation, the DFT calculation can have accurate results because there is a minor impact of the core electrons to the material's energy and also the contribution of the valance electrons is major. This approach is hinged upon the fact that the scattering of the electrons from the nuclei could look like with the weak potential of the valence electrons. Furthermore, an attractive force is exerted on the valence electrons by the nuclei and the wave function of the valance electrons have to be orthogonal to that of the nuclei. The pseudopotential and the corresponding pseudo-wave function of a system exceeding a cut-off radius (r_c) is illustrated in Fig. 2.3 [246]. From this figure, it can be visibly perceived that both the potential and the wave function are not affected.
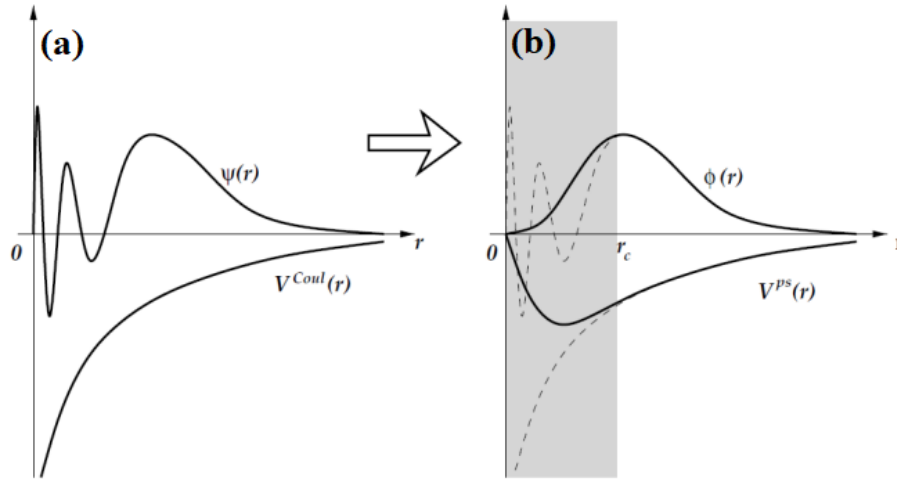
Figure 2.3 The Coulomb potential and the wave function of a system (a) and the pseudopotential and corresponding pseudo-wave function (b) [246].

The pseudopotential technics are employed for the DFT computations. The ultra-soft [247], the projector augmented wave (PAW) [248] and the norm conserving [249] can be given as the examples to the pseudopotential's methods. About the ultra-soft pseudopotential, it has smooth functions and lower cut-off energy. Besides, it gives results accurately. In respect to the PAW pseudopotentials, this method possesses lower cut-of radius in respect to that of the ultra-soft method. Because of the strong Coulomb interaction, the wave functions close to the core region own an oscillating nature. Finally, the norm-protective pseudopotential method is normalized and thus yields the same properties as all electron computations. The wave function in this pseudopotential is in the same norm when compared with all electron calculations both inside and outside the cut-off radius.

The DFT computation is the self-consistent computation. If we elaborate, initially the ground state electron density is predicted. Secondly, the effective potential is attained depending upon the density. Then, by solving the Kohn-Sham equation with the predicted density both the ground state energy and density are found. In the condition that the initial guess is equal to the found density, the computation is completed. Otherwise, another prediction is made and the previous steps are repeated.

In the scope of this thesis, the norm-conserving Troullier-Martins pseudopotentials were employed to determine the ion-electron interaction [250].

2.3.3 Basis Sets

SIESTA is based on the numerical atomic orbital (NAO) basis set. The NAO basis framework is achieved from the numerical solution of the Kohn-Sham equality of the isolated pseudo-atom by means of the Numerov's method (also called as Cowell's method). The fundamental functions are defined via the well-defined spherical harmonic and the alterable radial component for a given orbital. As the designing of NAOs having any shape does not require an addition computational cost, the NAO basis sets are more advantageous than the other basis sets such as plane waves and grids. In addition, NAOs can be easily localized to annihilate the long-range interactions, resulting in better scaling. On the other hand, the additional angular symmetry must be defined via artificial polarization functions since the solid does not have the actual spherical symmetry. In the simulations throughout this thesis, either double-ζ (DZ) or double-ζ plus polarized (DZP) basis sets were chosen to define the valance states of all atoms.

2.3.4 Periodic Boundary Conditions

In the MD simulations, a system is identified by a simulation box with a size established by the simulations conditions. Two different types of the boundary conditions exist in general; the isolated boundary condition (IBC) and the periodic boundary conditions (PBC). The IBC is particularly useful for the clusters and molecules whereas the PBC is applicable for the liquids and bulk solids [242].

The PBCs (see in Fig. 2.4 [251]) must eliminate the effects of surface and also should permit to the analysis of finite systems. If PBC is identified in the simulation, the particles are positioned in a box surrounded by their replicas. As a result, the interaction between the particles depicts the interaction between their images in the neighboring boxes as well [252].
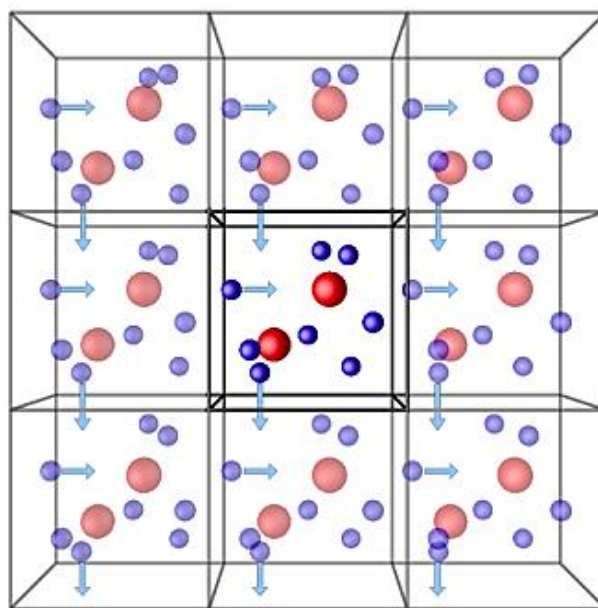
Figure 2.4 The schematic illustration of the PBC [251].

2.3.5 Geometry Optimization

In this thesis, the geometry optimization (GO) was carried out to relax the final structure with a conjugate gradient (CG) variable cell approach which is based on the independent variation of unit cell parameters and atomic positions. The system was thought to be optimized as soon as the maximum force on the atoms reached the force tolerance criterion of 0.01eV/Å. If the convergence or force criteria cannot be reached with the CG method, it is also preferable to use the PR method to relax the final structure.

2.3.6 The Pair Distribution Function

The pair distribution function (PDF) which is an important structural characteristic is symbolized as $g(r)$ and is also named as the partial correlation function (PCF) or radial distribution function (RDF). When taking in consideration a homogenous distribution of the atoms and molecules in space, the $g(r)$ offers the likelihood of finding an atom at the distance of r from a selected atom (see in Fig. 2.5 [251]).
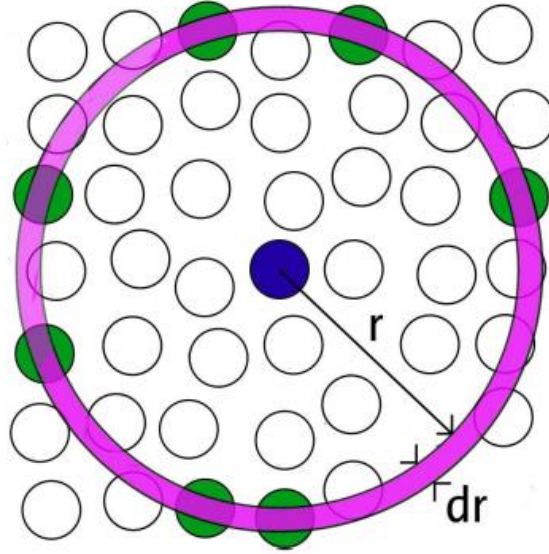
Figure 2.5 The space discretization for the evaluation of the PDF [251].

By dividing the volume into shells (*dr*), there is a possibility of computation the atom numbers, dn(*r*), at a distance between *r* and *r+dr* from a particular atom;

$$dn(r) = \frac{N}{V}g(r)4\pi^2 dr \tag{2.41}$$

where *N*, *V* and g(*r*) correspond to the atom numbers and the model volume, respectively.

From Eq. (2.41), the volume of the shell having the thickness of *dr* can be calculated approximately as follow;

$$V_{shell} = \frac{4}{3}\pi(r + dr)^3 - \frac{4}{3}\pi r^3 \approx 4\pi r^2 dr \tag{2.42}$$

If the species is two or more, then the PDF g$_{\alpha\beta}$(r) can be found as;

$$g_{\alpha\beta}(r) = \frac{dn_{\alpha\beta}(r)}{4\pi r^2 dr \rho_\alpha} \tag{2.43}$$

In here,

$$\rho_\alpha = \frac{V}{N_\alpha} = \frac{V}{Nxc_\alpha} \tag{2.44}$$

here c_α is the composition of atomic species α.

2.3.7 Equation of State

Equation of state (EOS) for a solid defines its behavior under alterations in tension or compression and can be briefly described as the relationship between functions such as energy (E), temperature (T), volume (V), pressure (P) or specific heat.

The easiest *isothermal* EOS of a solid is its bulk modulus (K), a measure of the capability of a material to resistant the alterations in volume under external pressure. The equilibrium bulk modulus K_0 of a solid is as below;

$$K_0 = -V \left(\frac{\partial P}{\partial V}\right)_T \tag{2.45}$$

where $\partial P/\partial V$ is the partial derivative of pressure with regard to volume. In addition, a dimensionless parameter K_0' is the first derivative of K_0 with respect to pressure and is expressed as follow;

$$K_0' = \left(\frac{\partial K_0}{\partial P}\right)_T \tag{2.46}$$

where P is the pressure and P as a function of volume can be formulated as;

$$P(V) = -\left(\frac{\partial E}{\partial V}\right)_S \tag{2.47}$$

If the bulk modulus is reformed by using the Eq. (2.47);

$$K(V) = V \left(\frac{\partial^2 E}{\partial V^2}\right)_{T,S} \tag{2.48}$$

Our final relaxations were presented at a temperature of 0 K in the AIMD simulations and hence the Gibbs free energy defined in below is enthalpy at 0 K;

$$H(V) = E(V) + P(V).V \tag{2.49}$$

The 3rd order Birch-Murnaghan EOS (BMEOS) based on the study of Francis Dominic Murnaghan published in 1944 [253] was first introduced by Albert Francis Birch [254]. BMEOS is the relation between the applied pressure and the volume of a solid and the equation of the 3rd order BMEOS is as;

$$E(V) = E_0 + \frac{9V_0 K_0}{16}\left\{\left[\left(\frac{V_0}{V}\right)^{\frac{2}{3}} - 1\right]^3 K_0' + \left[\left(\frac{V_0}{V}\right)^{\frac{2}{3}} - 1\right]^2 \left[6 - 4\left(\frac{V_0}{V}\right)^{\frac{2}{3}}\right]\right\} \tag{2.50}$$

where $K' = dK/dP$ (P is pressure) and the subscript "0" means the equilibrium values.

Once more with the using of Eq. (2.47), P(V) 3rd order BMEOS can be derived as follow;

$$P(V) = \frac{3K_0}{2}\left[\left(\frac{V_0}{V}\right)^{\frac{7}{3}} - \left(\frac{V_0}{V}\right)^{\frac{5}{3}}\right]\left\{1 + \frac{3}{4}(K_0' - 4)\left[\left(\frac{V_0}{V}\right)^{\frac{2}{3}} - 1\right]\right\} \tag{2.51}$$

By fitting the 3rd order BMEOS to these, both the enthalpy and the *K* value can be simply calculated as soon as the pressure-volume values for the system are procured.

2.3.8 Bond Properties

Throughout this thesis, the bond length distribution between 1st neighbor atoms, the distribution of bond angles in the simulation cell and the average 1st coordination numbers were computed for all simulated structures.

2.3.9 Electronic Properties

In order to determine the electronic structure of both ordered and disordered phases, the electron density of states (EDOS) is utilized. EDOS is the number of a single-particle state at a particular energy level which allows the occupation of electrons and can be formulated as;

$$\rho_{EDOS}(E) = \frac{1}{N_f} \sum_{i=1}^{N_f} \delta(E - \varepsilon_i) \tag{2.52}$$

here, N_f represents the total number of occupied electronic states and ε_i corresponds the energy eigenvalues. With the EDOS calculations, it is possible the detection of the Fermi level and band gap, a knowledge on both valance and conduction bands and the comprehension of the electron conduction mechanism in the solid phases.

2.3.10 Mechanical Properties

The mechanical properties of ordered and disordered phases investigated in the scope of this thesis were also calculated by using the classic mechanical equations.

Young's modulus or elasticity modulus (E) is defined as the opposition of a material to elastic distortion under loading, and it is calculated by applying a uniaxial stress to the principal axes of the solid structures. During the stress application, both the cell's vectors and the atomic positions are optimized. From the slope of stress (σ) – strain (ε) curve; E can be easily estimated as;

$$E = \frac{\sigma_{axial}}{\varepsilon_{axial}} \tag{2.53}$$

It is possible to calculate the Poisson's ratio of a material subjected to a uniaxial stress along the principal axes (x, y and z);

$$\nu_{ij} = -\frac{\Delta L_i/L_i}{\Delta L_j/L_j} \tag{2.54}$$

Here, i denotes the transfer strain direction while j signifies the applied strain direction. Ls are the length of the supercell's vectors along the principal axes. Therefore, we employ a uniaxial stress along the principal axis of each model and observe the

changes along transfer directions to estimate Poisson's ratio. In this way, we perceive six different values for Poisson's ratio from the best linear fit. The average value of ν is estimated.

If the K and E are calculated by the Eq. (2.50) and (2.53), correspondingly then the Poisson's ratio can be also found in a second way using the following definition;

$$\nu = \frac{1}{2} - \frac{E}{6K} \tag{2.55}$$

Similarly, if the K and ν_{ij} are calculated by the Eq. (2.50) and (2.54), respectively then the Young modulus can be provided in a second way as;

$$E = 3K(1 - 2\nu) \tag{2.56}$$

Shear modulus (μ), also referred as the modulus of rigidity, characterizing the opposition to plastic distortion is calculated with the knowledge of E and ν with the following formulation;

$$\mu = \frac{E}{2(1 + \nu)} \tag{2.57}$$

The Vicker's hardness (H$_v$) values are also calculated using the next four empirical equations [255-258];

$$H_v = 0.151\,\mu \tag{2.58}$$

$$H_v = 2\left(\frac{\mu}{n^2}\right)^{0.585} - 3 \tag{2.59}$$

$$H_v = 0.92\left(\frac{1}{n}\right)^{1.137}(\mu)^{0.708} \tag{2.60}$$

$$H_v = 0.0635\,E \tag{2.61}$$

In addition to the mechanical parameters mentioned above, the microhardness value (*H*) of some amorphous models can also be calculated by using next equation [259];

$$H = \frac{(1-2\nu)E}{6\,(1+\nu)} \tag{2.62}$$

Finally, the brittle-ductile characteristic of any solid can be classified by means of either the Pugh's ratio (n) or Poisson's ratio. The critical value is defined to be 1.75 for n. If n is bigger than 1.75, a solid shows the ductile character. Otherwise, n is smaller than 1.75, the solid exhibits the brittle character. In addition, if the Poisson ratio is bigger than 0.26, a solid is ductile, if not, it shows brittle feature [260, 261].

$$n = K/\mu \tag{2.63}$$

Chapter 3

Hard Boron Rich Boron Nitride Nanoglasses

The work presented in this chapter is published in A. Ö. Çetin Karacaoğlan, M.Durandurdu, Journal of American Ceramic Society 2018, 101(5), 1929-1939.

3.1 Introduction

Boron Nitride (BN) is an important ceramic and has received considerable attentions due to its excellent optical, electrical, and mechanical properties such as high thermal conductivity, high strength, high temperature stability, low dielectric constant, wide band gap, n- and p-type dupability, lubricity, the capability of hydrogen uptake etc. [262-277]. Therefore, it has various advanced technological applications ranging from cosmetic products to flexible nanoelectronics.

BN was first synthesized in the form of a hexagonal structure (h-BN) in 1840 [278]. Being a two-dimensional (2D) layered structure with sp^2 hybridization, it is the most stable form at ambient conditions. Another well-known 2D structured BN has the rhombohedral symmetry (r-BN) [279]. The high temperature and pressure treatments of h-BN and r-BN yield three-dimensional (3D) zinc-blende cubic (c-BN) and/or wurtzite (w-BN) structures having sp^3 hybridization [280-296]. Both BN phases are considered as a superhard material.

Boron (B) rich nitrides are new materials of interest and possess high hardness, and high thermal and chemical stabilities. Therefore, they can be used in advanced electronics as well [274, 297]. Several B subnitrides such as $B_{13}N_2$, $B_{50}N_2$, B_6N, B_4N etc. [274, 297-302] have been proposed to date. They have been commonly synthesized under the high-pressure treatments of B/BN melts. The structure and/or thermodynamic stability of some of these B subnitrides have not been well established yet. The $B_{13}N_2$ and $B_{50}N_2$ phases have a 3D structure and are believed to consist of distorted B_{12} icosahedrons connected

by N-B-N atomic chains, and inter-icosahedral B-B bonds [274, 297, 299, 300]. The existence of B_6N still remains mystery [303].

Amorphous BN (a-BN) is another interesting form of BN and can be prepared using different experimental techniques such as ball milling technique, very high frequency plasma chemical vapor deposition etc. [304, 305]. The short-range order of a-BN is predominantly due to sp^2 hybridization [304-306]. It consists of randomly oriented h-BN-like nanosheets and it is almost free from chemical disorder (no homopolar bonds) [306].

B rich a-BN or hydrogenated B rich a-BN materials are of interest as well and have been investigated in several experiments [272, 307-309]. Yet most of these studies primarily focused on their physical properties, in particular, their electronic structures and did not provide solid information about their short-range order and some of their mechanical properties in details. On the basis of the X-ray diffraction spectra [308], different local structures were proposed for B rich a-BN depending on B content. For high B concentrations, the amorphous materials were predicted to have a random network of icosahedra. For the films with B contents less than 80 at.%, the icosahedrons were separated and the h-BN like structure was emerged [308].

In this work, we use ab initio molecular dynamics simulations to model B rich B_xN_{1-x} ($0.55 \leq x \leq 0.95$) amorphous materials and to explore their local structure, electronic structure and mechanical properties. We reveal, for the first time, some remarkable features of these amorphous systems. The observation of B:BN phase separations, a content induced structural phase transformation in the BN rich domains, the formation of a cage-like B_{16} molecule, high hardness of some amorphous alloys are important outcomes of the present study.

3.2 Computational Method

All simulations were performed by the SIESTA *density functional theory* (*DFT*) *code* [310]. We used the Becke gradient exchange functional [229] and Lee, Yang, and Parr correlation functional [311] to evaluate the exchange correlation energy and the Troullier and Martins approach to construct norm-conserving nonlocal pseudopotentials [250]. The simulations were done at Γ points using the DZP basis. We set the time step of each molecular dynamics simulation 1.0 fs. We adopted the structure

of liquid $B_{0.5}N_{0.5}$ having 216 atoms (108 N and 108 B) at 3300 K [306] as a starting structure and substituted randomly N atom by B atom until we had a certain amount of B concentration ($\sim$55 %-95 %). The initial configurations were subjected to high temperatures and thermalized at 2500 K ($\sim$95 at.% B)-3300 K ($\sim$55 at.% B) for at least 50.0 ps and then they were quenched to 300 K in $\sim$150.0-300.0 ps. All these simulations were performed within the NPT (isothermal–isobaric) ensemble. We applied the velocity scaling method and the Parrinelo–Rahman technique [240] to control temperature and pressure, respectively. Yet during the thermalization and quenching procedures, no shear deformations were allowed. The resulting models at 300 K were optimized using the NPH (isobaric-isenthalpic) ensemble until the maximum force is less than 0.02 eV/Å. The VESTA [312] and ISAACS [251] programs were used to visualize and analyze the amorphous models, separately.

3.3 Results

3.3.1 Structural Properties

In order to understand the nature of bonding for each atomic species and to identify the microstructure of the amorphous configurations, we primarily study their partial pair distribution functions (PPDFs) and present some of them in Fig. 3.1. The PPDFs exhibit the typical characteristics of an amorphous network for all compositions such that they have a well-defined first neighbor peak and the lack of long-range correlations. As predictable, we observe drastic changes in the distributions with increasing boron concentration: the intensity of the first B-B peak increases slowly while that of the second B-B peak decreases.
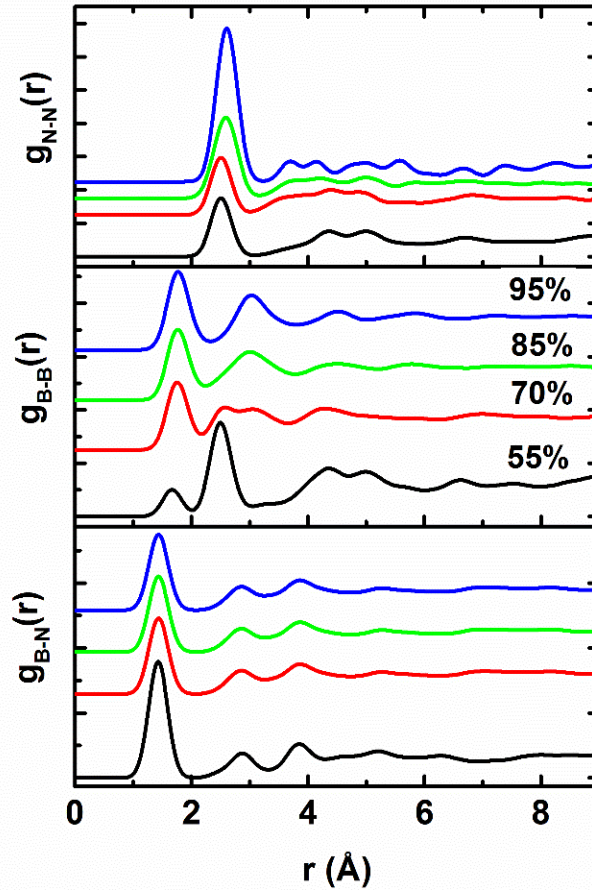
Figure 3.1 Partial pair distribution functions at some B concentrations.

Figure 3.2 shows the variation of the first peak position of the B-N, B-B and N-N correlations as a function of B concentration. The average B-N bond distance is projected to be 1.43 Å at 55 % B content, which is indeed pretty close to the sp^2 bond length of 1.44 Å reported for h-BN [313]. The B-N bond separation remains almost unchanged up to 70 at. % B at which point it begins to rise and reaches a value of 1.53 Å at 80 % B content. After this concentration, it exhibits a small fluctuation around this value. It should be noteworthy here that the mean B-N bond separation (1.53 Å) at 80 % and higher B concentrations is rather parallel to the sp^3 bond distance of 1.54 Å reported for c-BN [313]. The first peak of the B-B bond correlation for 55 at. % B is located at 1.67 Å and increases progressively to a value of ~1.77 Å up to 80 at. % B. After which, it remains almost null. The B-B bond length, ~1.77 Å, is relatively comparable with 178-1.80 Å formed in the liquid B and a-B [314, 315]. In the model having 55 at.% B, the N-N distance is positioned at 2.50 Å. This value is pretty close to the N-N separation of 2.50 Å originated in h-BN [313] and 2.56 Å found in c-BN [313]. With increasing B content, the N-N distance also increases, but this increase is not too drastic (~1.2 %). A visual

review of the structures as shown in Figure 3.3 reveals that N atoms somehow prefer forming BN domains rather than being homogeneously distributed in the amorphous structures for high boron contents. Therefore, they can be classified as BN nanoscale domains in the amorphous networks. This observation can be interpreted as the occurrence of BN:B nanoscale phase separations in the models and is particularly important since it reveals that these materials can serve as nanoglass ceramics. From the PPDFs, one can also see that the models present no N-N homopolar (wrong) bonds.
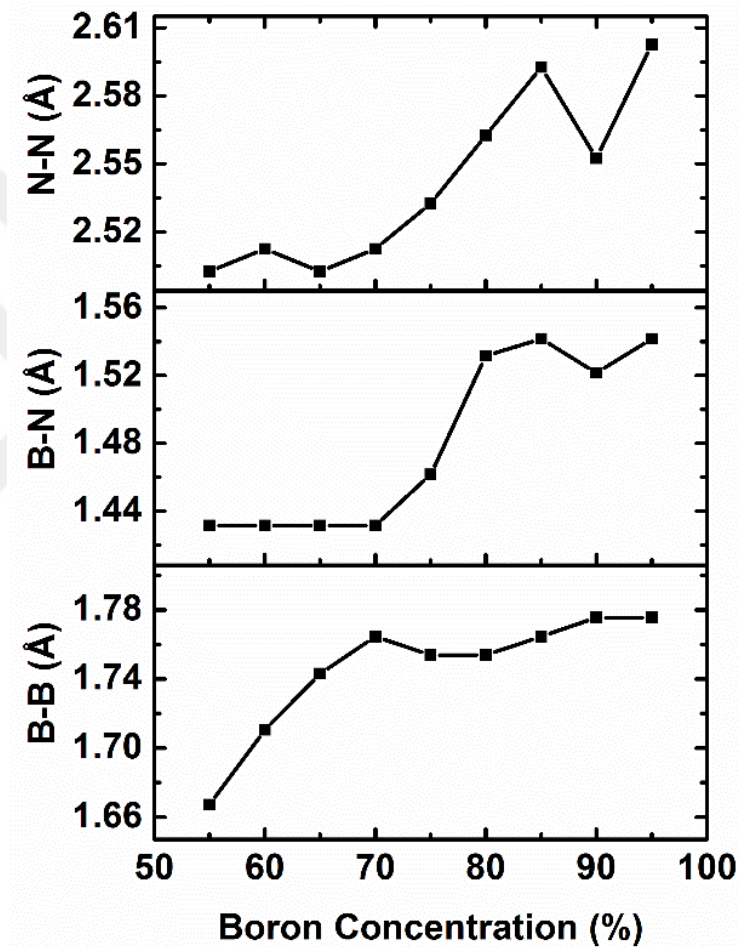
Figure 3.2 Variation in B–N, B–B and N–N separations as a function of B content.
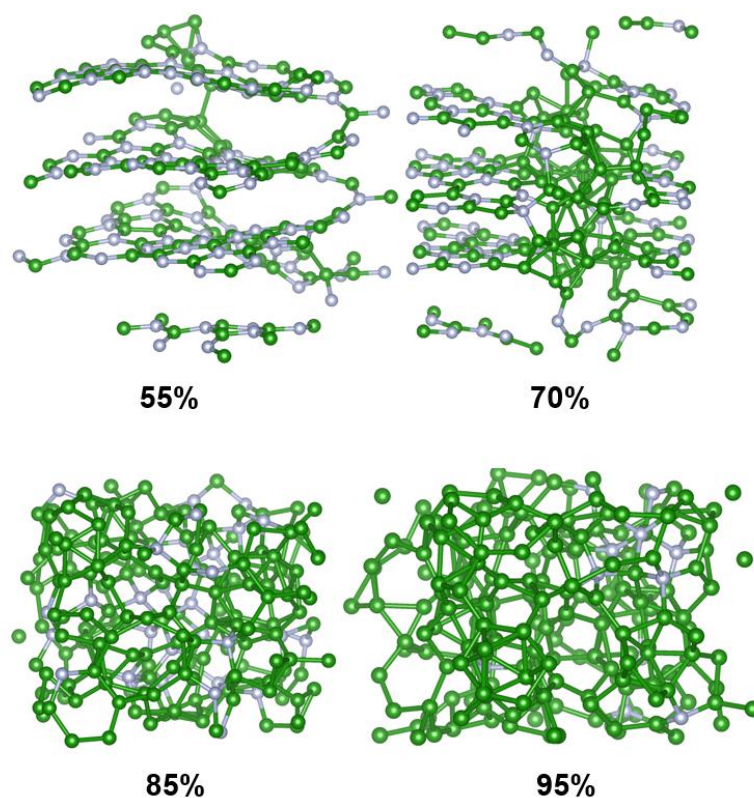
Figure 3.3 Ball stick representation of some amorphous models.

Total and partial coordination numbers are estimated by using the first minimum of the PPDFs (1.94-2.05 Å for the B-N distribution and 1.96-2.27 Å for the B-B correlation depending on B contents). The N-average coordination number is around 3 up to 70 at. % B as illustrated in Fig. 3.4, suggesting the dominated sp^2 hybridization in these amorphous alloys, in agreement with the experimental prediction [308]. At 75% B concentration, the N-coordination number rapidly rises and becomes 3.36. At this content, some of the N atoms form sp^3 hybridization. At 80% and higher B contents, almost all N atoms present sp^3 hybridization. This observation discloses the fact that there is a structural phase change from a 2D-like arrangement to a 3D-like arrangement in the BN rich regions. It should be noted here that in all amorphous alloys modeled, no fivefold or higher coordinated N atoms are traced. At low B contents, the mean coordination number of B is estimated to be 3.02 and it linearly increases to 5.88 at 95% B concentration. This value is indeed comparable with the average coordination number of pure a-B.
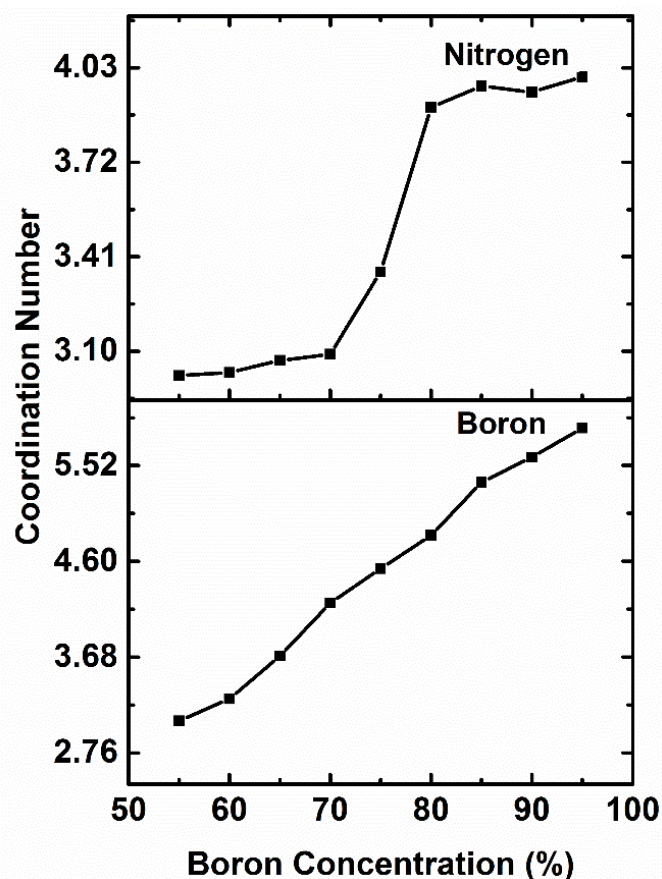
Figure 3.4 Modification of partial coordination numbers as a function of B content.

To have additional information about the microstructure of the amorphous systems, we study the coordination distribution of the models and present our findings in Fig. 3.5. As seen from the figure, threefold-coordinated B configurations drastically decrease while sixfold coordinated B structures severally increase with increasing B content. Fourfold and fivefold and fourfold coordinated arrangements initially increase, reach a maximum at 80 % B concentration and then decrease. Sevenfold coordination also forms in the models and become noticeable beyond 80% B content. For N atoms, the picture is very naive: there are only threefold and fourfold coordinated configurations. While one drops, the other one rises drastically between 70% and 80% concentrations.
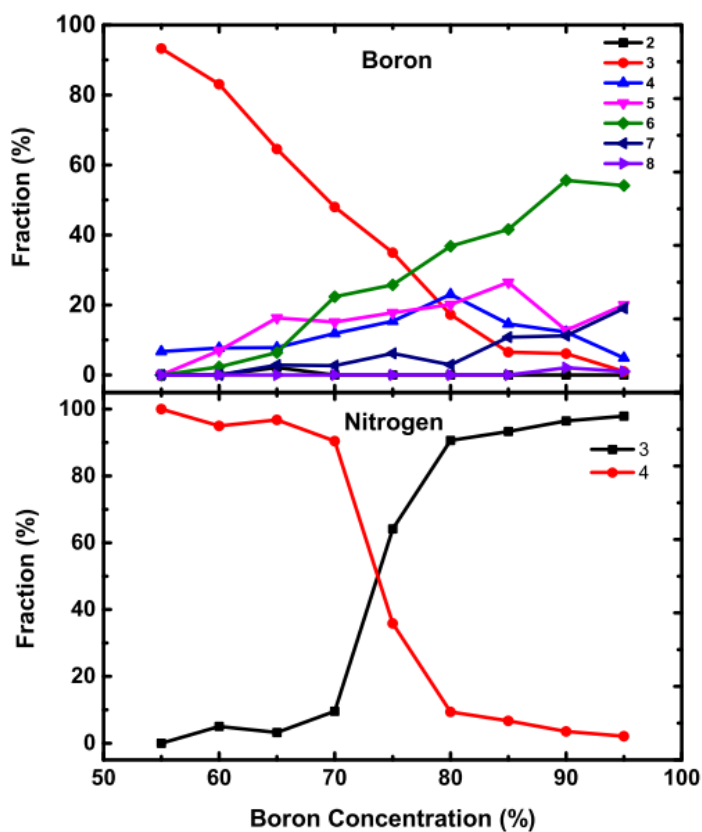
Figure 3.5 Coordination distribution of B and N atoms as a function of B concentration.

In addition to the PPDFs and coordination number investigations, we perform the bond angle distribution analysis to have detailed information about the atomic structure of a-BNs. The B-N-B and N-B-N angle distributions of some models are shown in Fig. 3.6. The main peak of the B-N-B and N-B-N angles is located at around 120°, suggesting the h-BN-like short-range order up to 75 at. % B at which point it shifts around 117°. At 80% B concentration, the main peak for both angle distributions is placed near 105°-111° that are pretty close to the tetrahedral angle of 109.5°, supporting a structural modification from a 2D h-BN like short-range order to a 3D c-BN or w-BN like short-range order in the BN rich regions. When the B-B-B angles are concerned, at 55% B content it has a broad distribution ranging from 57° to 156° and has many peaks. At 60% B concentration, the distribution has two peaks at around 60° and 110° and they become stronger with increasing B contents. These angles are indeed comparable with the angles of 60° and 108° originated from the intra-icosahedral bonds of the pentagonal pyramids (the quasimolecular B_{12} icosahedron). The general shape of the B-B-B angle distribution

function at high B concentrations is actually quite similar to what has been reported for α-B and liquid B.
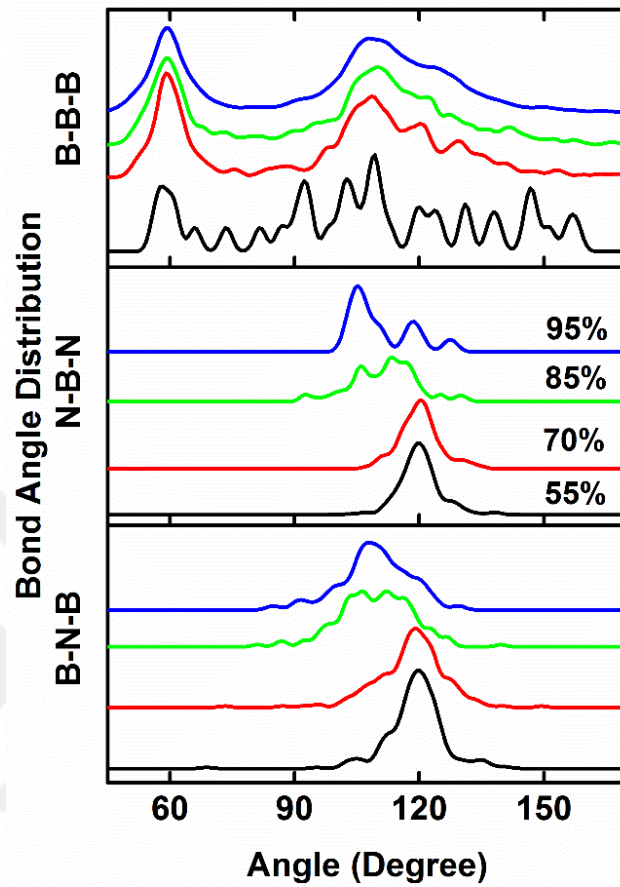
Figure 3.6 Bond angle distribution functions.

The Voronoi polyhedral approach [316] can be used to have additional information about the structures at the atomistic level. In this approach, a polyhedron is symbolized by indices $<n_3, n_4, n_5, n_6,…>$. Here n_i and Σn_i correspond to the number of i-edge faces of polyhedron and its total coordination number, respectively. The main building unit of crystalline and amorphous B and B rich materials is commonly the quasimolecular B_{12} icosahedron that consists of ideal pentagonal pyramids. The Voronoi polyhedrons with the $< 2,2,2,0 >$ and $< 2,3,0,0 >$ indices correspond to the ideal and defective pentagonal pyramids, respectively. Consequently, we specifically focus on them and present their variation as a function of B concentration in Fig. 3.7.
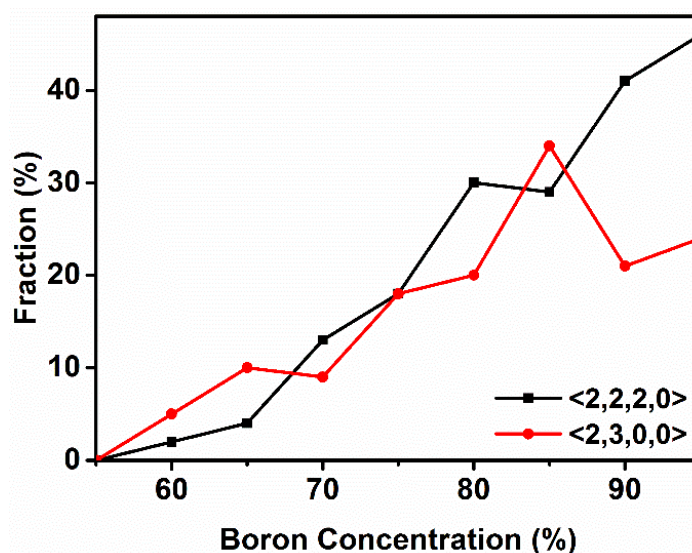
Figure 3.7 Fraction of ideal < 2,2,2,0 > and defective < 2,3,0,0 > pentagonal pyramids.

A noticeable number of these polyhedrons first appear at 65% B content and increases continuously thereafter. In order to see whether these significant amount of ideal or defective pyramidal clusters produce any B_{12} icosahedron, we visualize the models carefully using the Vesta program and find that the first complete B_{12} molecule forms at 70% B content. In addition to the quasimolecular B_{12} icosahedron, at 75 % and higher B concentrations, we discover, for the first time, the presence of a cage-like B_{16} molecule (see Figure 3.8) in the amorphous networks. Such a molecule has not been reported in any previous investigations. The B_{16} molecule consists of ideal pentagonal pyramids and incomplete or defective hexagonal pyramids. In the amorphous structures, each B atom of this molecule is sixfold coordinated and the B-B bond lengths range from 1.6 to 1.8 Å. We should note there that the B_{16} molecule does not develop in pure a-B model. Therefore, a kind of interaction(s) in B-N systems must be responsible for the formation of this molecule.

In order to see whether an isolated B_{16} molecule (each B atom is five-fold coordinated) is stable, we performed an additional investigation such that B_{16} cluster extracted from the amorphous network was placed in a large simulation box (breaking periodic boundary conditions) and its atomic coordinates were optimized using a conjugate gradient technique and 256 special k-points for the Brillouin zone integration. As shown in Fig. 3.8, the cluster underwent a severe deformation and hence, we reached a conclusion that the isolated B_{16} cluster was unstable.
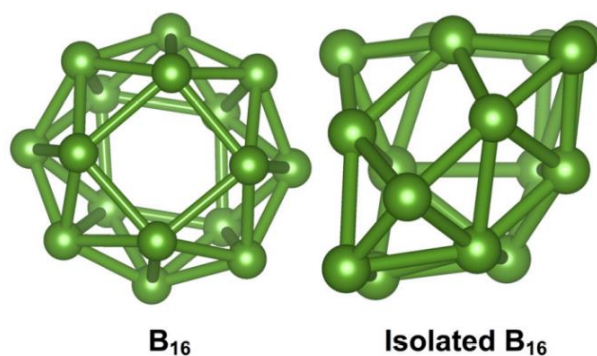
Figure 3.8 B₁₆ cluster formed in the amorphous alloys and the isolated B₁₆ molecule after relaxation.

3.3.2 Electronic Properties

The crystalline and amorphous forms of BN have various high tech applications, especially in the semiconductor technology. Therefore, it is important to identify the electronic structure of the amorphous alloys proposed in this study. Figure 3.9 shows the modification of the HOMO-LUMO band gap energy as a function of B concentration. As understood from the figure, a 10% change in the stoichiometry results in a drastic closure of the band gap energy. Between 60% and 95% B concentrations, although the gap fluctuates, it is approaches the theoretical band gap value (0.3 eV) of a pure a-B model. It should be pointed out here that the insufficiency of the DFT-GGA approaches to describe the excited states yields an underestimation in the band gap energies. Consequently, the theoretical band gap energies are not comparable with the experimental band gaps as shown in Fig. 3.9. Yet, in spite of the different values, one can see almost similar trend in the variation of the theoretical and experimental band gap energy [308] with changing B content (Fig. 3.9).
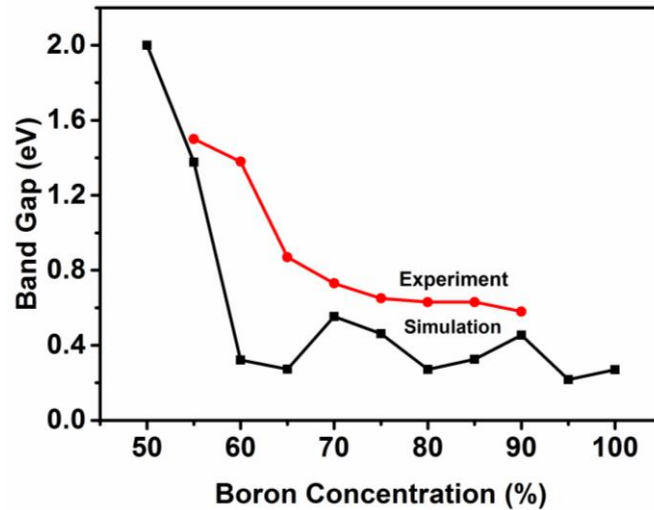
Figure 3.9 Variation in band gap energy as a function of B content. The experimental data were extracted from Ref. [48]. There are some uncertainness B contents since the experimental samples have some O and C impurities.

3.3.3 Mechanical Properties

In order to predict the mechanical properties of the amorphous models, we first study their energy as a function of volume and fit the data to the 3rd order BMEOS in Eq. 2.50. From the fit, we predict K (indicates the compressibility) for each material and present our data in Fig. 3.10.
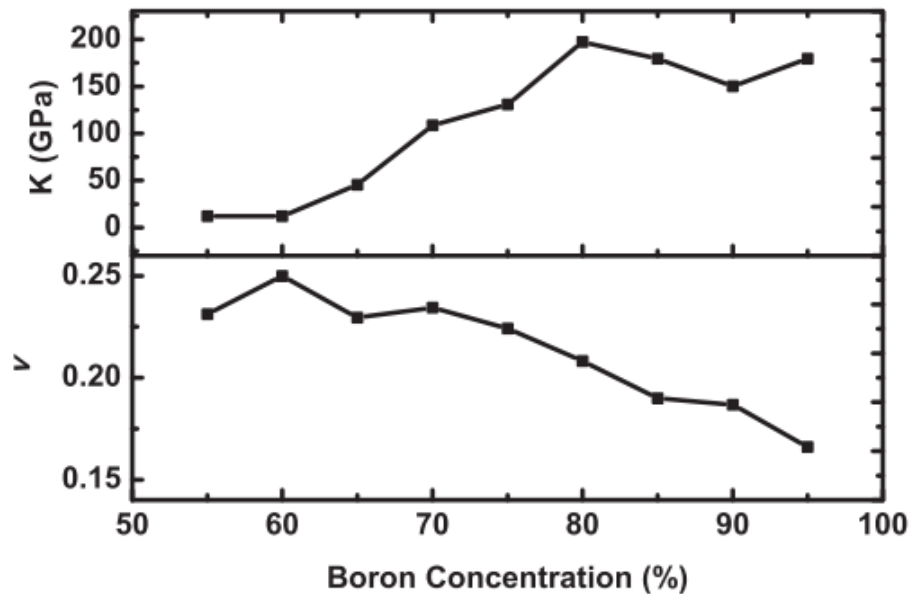
Figure 3.10 Variation in bulk modulus (K) and Poisson's ratio (v) as a function of B content.

The K of the network for 55 at. % B is equal to about 12 GPa, which is indeed less than the h-BN bulk modulus of ~32-36 GPa [288, 317]. This might be due the disorder nature of the models and randomly oriented hexagonal nanosheets in the amorphous networks. As expected, with increasing B content, K increases gradually and has a peak value of about 200 GPa at 80% B content, and then slightly decreases. At the peak value, the amorphous network has the largest BN domains with sp^3 hybridization, relative to the other networks. The K value of c-BN and w-BN is 390 and 375 GPa [318, 319], respectively while it is about 200 GPa for the $B_{13}N_2$ phase [320] and the B crystals [21, 321-325]. Consequently, the predicted K values are noticeably less than that of the 3D structured BN crystals, but they are comparable with that of B polymorphs and that of B subnitrides.

Using Eq. (2.54), the Poisson ratio of each materials is also calculated. In here it should be pointed out that the uniaxial compression generally results in an expansion in the transfer directions. This behavior is defined by the Poisson ratio that is explained as the negative ratio of transfer strain in the i direction developing from an applied strain in the j direction. The Poisson ratio averaged over three directions as a function of B content is provided in Fig. 3.10 as well. At 55% B content, it is estimated to be about 0.23, which is indeed close to 0.21 reported for h-BN [326]. As the B content is increased, the Poisson ratio decreases linearly, as anticipated, due to the gradual structural modification from a 2D structure to a 3D structure and reaches a minimum value of 0.16. This value is fairly close to 0.15 measured for c-BN [327] and 0.11-0.13 [323-325] predicted for the B polymorphs.

We can simply calculate Young's modulus (E) using both Eq. (2.53) and Eq. (2.56). Young's modulus computed using the both equations is given in Fig. 3.11. As seen from the figure, both approaches yield the same trend with some fluctuations. Young's modulus gradually changes from ~20 GPa to ~350 GPa. The experimental Young's modulus of a-BN:H is 47 $\pm$ 5 GPa [328], moderately higher than our prediction for the low B contents. The value, 350 GPa estimated for high B concentrations, is noticeably smaller than 445-550 GPa found for the B crystals [323-325], 587 $\pm$ 30 GPa estimated for the thick c-BN film [327], 847 GPa predicted for the bulk polycrystalline material [329], and 909 GPa reported for the single crystal c-BN [330].
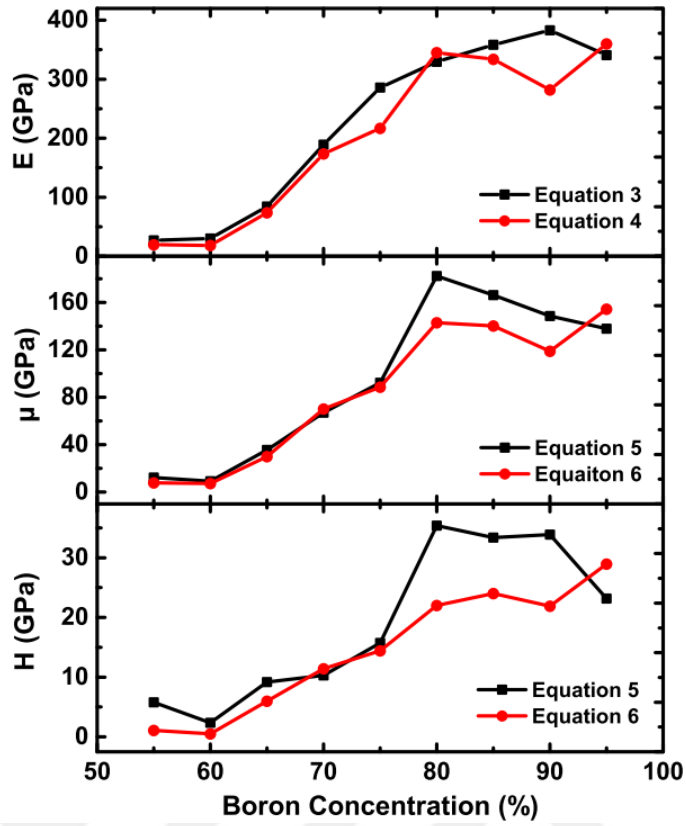
Figure 3.11 Young's Modulus (E), Shear modulus (l) and Vickers hardness (H) as a function of B content. Shear moduli obtained using Equations (5) and (6) are used to estimate the Vickers hardness.

In order to estimate shear modulus (μ), we applied shear stresses on the simulation cells. After a full relaxation, we determined the shear stresses and shear strains and then calculated shear modulus using the next equation;

$$\mu = \frac{shear\ stress}{shear\ strain} = \frac{\sigma_{ij}}{\frac{\Delta L_i}{L_j}}\ (i \neq j) \tag{3.1}$$

Alternatively shear modulus can also be projected using the Eq. (2.57). The shear modulus estimated using both equations is also provided in Fig. 3.11 and changes from about 8.0 GPa to 155 GPa. The shear modulus computed for the high B concentrations is closer to 197-236 GPa measured for the B crystals [323-325], but it is considerably less than the shear modulus of c-BN (312-378 GP) [329,331,332].

We finally compute the Vickers hardness using Chen's equation (Eq. 2.59) [256]. The variation of the hardness shown in Fig. 3.11 reveals that at 80% and higher B concentrations, the Vickers hardness is greater than 20 GPa, implying that these amorphous alloys can be considered as a hard material. Yet the hardness values estimated are less than ~40 GPa projected for B crystals [333].

3.4 Discussion

Our simulations expose some remarkable features of the B rich a-BN materials. The first interesting observation is the occurrence of BN:B phase separations in these networks. Even at low boron concentrations, the model mainly has h-BN-like structure and the excess B atoms are aggregated to one side of the model and produce B rich region(s), as illustrated in Fig. 3.3. The excess B atoms principally connect randomly distributed and oriented h-BN like nanosheets to form a 3D-like structure. The observation of such phase separations is actually quite important because it proposes that these systems can serve as nanoglass materials.

We also observe the occurrence of a 2D-to-3D phase transformation in the BN rich regions by simply changing B concentration. Such a structural phase transformation meaningfully improves the mechanical properties of the amorphous networks (Fig. 3.9). The Vickers hardness of some alloys reaches a value larger than 20 GPa, offering that they have potential to serve as a hard material. Yet we need to underline here that due to the linear fitting, we do definitely expect some errors in our predicted Poisson's ratios, Young's moduli and shear moduli and hence the Vickers hardness. Careful experimental studies are indeed desirable to reveal their accurate mechanical properties.

Another interesting finding is the formation of a small cage like B_{16} molecule that does not exist in pure a-B. Consequently, we believe that interaction of B-N atoms is responsible for the formation of the B_{16} molecule. Although the isolated B_{16} molecule (each B atoms is fivefold coordinated) is found to be not stable i.e. it undergoes a drastic deformation, it might be stabilize by functionalizing it with some elements or molecules. Therefore, further investigations are certainly needed to provide more information about this simple molecule and its properties. Additionally at present we do not know whether the B_{16} molecule is unique for only B-N systems or it can also form in other B rich amorphous materials such BC, BSi etc. Therefore, further studies are absolutely desirable to shed some light onto this issue.

Experimental investigations have applied the plasma chemical vapor deposition, ion-beam deposition, spin coating process etc. to produce B rich a-BN films. Yet in these studies [307-309], possible B:BN phase separations have not been discussed. It is likely that these techniques did not allow the formation of such separations or the samples had such phase separations, but they might be too small to be clearly identified by the current

experimental techniques. Here we will suggest the traditional experimental technique to manufacture B rich a-BN alloys having B:BN phase separations such that they can serve as *nanoglass* ceramics. As mentioned above, there exist several B rich BN crystalline phases such as $B_{13}N_2$, $B_{50}N_2$, B_6N, etc. They are generally prepared from B/BN melts at high-temperature and pressure conditions. At very high temperatures, B rich BN systems are known to form mixtures of phases of B and BN, signifying that the observation of the phase separations in the present work is physical. We believe that the same experimental procedure can be applied to fabricate the B rich amorphous materials with phase separations if and only if significantly fast quenching rates are applied to suppress the crystallization. Note that depending on quenching rates, different structured amorphous materials having different size of amorphous or amorphous-crystalline domains for the same composition can be prepared. Additionally the application of pressure to the melts can drop the 2D-to-3D phase modification to lower B concentrations such that the materials can have larger BN domains having sp^3 hybridization. Controlling the size of domains in the amorphous alloys and their local structure can have significant impacts on their electronic structure (band gap engineering) and mechanical properties. Therefore these materials can offer a wide range of applications in semiconductor technology.

Finally we need to stress here that all these findings are based on the 216 atoms amorphous models. For real systems, macroscopic phase separations can take place instead of nanoseparations, the 2D-to-3D phase transformation in the BN rich regions can occur at a different B content, and the formation of a complete quasimolecular B_{12} icosahedron can form at a distinct B concentration. Therefore, for real systems all properties of these amorphous alloys can differ from the estimated ones in the present study.

3.5 Conclusions

We have generated, for the first time, B rich a-B_xN_{1-x} ($0.55{\leq}x{\leq}0.95$) models by using ab initio MD simulations and recovered their local structure, mechanical properties, and electronic structures. As perceived in B/BN melts, we notice clear BN:B phase separations in all amorphous networks. This observation means that these amorphous materials can serve as a *nanoglass* ceramic. Two types of hybridizations are observed in the BN rich domains depending on B concentrations. Below 70 at. % B, sp^2 hybridization

is dominated and the short-range order of the amorphous networks is similar to that of the 2D h-BN structure. The sp^2 and sp^3 hybridizations form between 70 at. % B and 80 at. % B. At higher B concentrations, sp^3 hybridization with a frequency of ~90-98% is perceived in the amorphous configurations as seen in the c-BN or w-BN crystals. Consequently, a phase transformation from the 2D structure to the 3D structure in the BN rich domains is proposed. In the B rich regions, we find that 60 % B concentration is significant enough to produce the ideal and defective pentagonal pyramids and 70 % B content is adequate to observe a complete B_{12} molecule. In addition to the B_{12} molecule, the formation of a cage-like B_{16} molecule is, for the first time, observed in some amorphous alloys. Yet we find that the isolated B_{16} molecule is not stable. Some of these B rich amorphous materials possess a high Vickers harness and hence they can be used as a hard material. The electronic structure calculations suggest that all amorphous materials are semiconductor. We also speculate that B rich BN *nanoglasses* can be synthesized from fast quenching of B/BN melts.

Chapter 4

Boron-Rich Amorphous Boron Oxides from Ab initio Simulations

The work presented in this chapter is submitted in A. Ö. Çetin Karacaoğlan, M.Durandurdu, Journal of Non-Crystalline Solids 2023, 604, 122130.

4.1 Introduction

The development of novel materials plays an important continuing role in the progression of the advanced technology. These novel materials can be classified as the corrosion-, erosion-, oxidation- and wear-resistant material systems [161]. Especially the wear-resistant materials/composites have drawn remarkably attention due to both the increasing production demand in efficiency and the stimulation of new potential application areas [334]. The wear-resistant systems are generally qualified by high fracture toughness and high hardness. For this reason, these systems must be in the class of extremely-hard materials or super-hard materials [334]. The two known hardest materials are diamond and cubic boron nitride (c-BN), respectively. Diamond can be used many applications requiring the extreme wear resistance. Besides, c-BN can be also use of many areas if high chemical stability is necessary. However, these materials have some disadvantages in advanced technology implementations. To make clarify, it is not possible to use the diamond as a cutting tool for ferrous alloys at high temperatures and c-BN is weaken with the increase in temperature and transforms to its hexagonal form (h-BN). In order to overcome these difficulties, tremendous investigations have been performed to produce new superhard materials for the industrial applications [158, 159, 335-337]. On the other hand, the ultra-hard or hard materials having the commercial importance are mostly composed of light elements and hence boron rich (B-rich) compounds are good candidates [334] because they have short interatomic bond lengths and strongly covalent bonds [5, 147] and these characteristics yield to outstanding

chemical (high chemical inertness), physical (high hardness, low mass density, high thermal conductivity) and mechanical (excellent wear resistance) features [147, 338, 339]. In summary, B-rich compounds with these features have a remarkable importance for the nuclear industry [340], thermoelectric applications [341, 342], catalysis [343] and hydrogen storage [344, 345] and so, they are strategic materials.

Among B-rich compounds, boron suboxides (B_xO, $x>1$) have a great attention in the technologic areas due to their promising and outstanding properties such as high hardness, low density, high tensile strength, semi-conductivity, high chemical stability and large bulk moduli. B_2O phase has a special place as an "unsymmetrical" analogue of carbon [152, 346-348]. Even though the high temperature/pressure syntheses of B_2O in both graphite-like [152, 347] and diamond-like [347] was discussed, the later studies propounded that these phases of B_2O are not stable and that could not be reproduced [349, 350]. Apart from B_2O structure, B_xO phases having different stoichiometry ($x=$ 4, 6, 7, 8, 10, 12, 16, 18, 20, 22 and 26) were also synthesized and analyzed [155, 156, 346]. Amongst these structures, however, B_6O has gotten a special attention and is the most extensively investigated one because it is accepted as a hardest material after diamond and c-BN. B_6O crystallizes in two structures, namely, α-B_6O [153] and β-B_6O [351, 352]. α-B_6O has an α-boron (α-B) crystal structure that can be represented by an oxygen-stuffed phase of α-B [351]. α-B_6O can be described as a cubic close packing (ccp, ABCABC… stacking) of the icosahedral B_{12} unit with two oxygen atoms occupying all octahedral spaces in it [351]. Besides, the crystal structure of α-B_6O is closely associated with that of boron carbide (c-BC) as well [5]. α-B_6O, as in c-BC, has a wide composition range resulting from the non-complete filling at the oxygen atom positions between the icosahedral B_{12} units. On the other hand, β-B_6O, the new phase of B_6O, was asserted with both theoretical and experimental studies [351, 352]. β-B_6O, similar to α-B_6O, is derived from *β*-B phase with an oxygen-stuffed in it and is based on a hexagonal close packing (hcp, ABAB… stacking) [351]. It was shown that most properties (volume, hardness, elastic moduli and DFT band gaps) of α- and β-B_6O structures are very similar each other [351].

In addition to the crystalline forms, amorphous boron suboxides (a-B_xO) can be fabricated with different experimental protocols, for example, a hot pressing, a reactive radio frequency (RF) magnetron sputtering, an evaporation and a cathodic arc deposition [161-167]. Additionally, *ab initio* molecular dynamics (AIMD) [353-355] and classical molecular dynamics (MD) [165] simulations were executed to shed lights on some of a-

B_xO compounds. The main focus on these experimental and theoretical studies was the mechanical (specifically hardness) and electrical properties of a-B_xO. Apart from these investigations, a high-pressure study reported that the B_6O structure transformed from the crystal phase to an amorphous phase comprising of glassy boron (a-B) and amorphous boron trioxide (a-B_2O_3) upon pressure release [356]. Furthermore, the shear-induced amorphization was observed in B_6O during the nanoindentation process [357]. Later, the amorphization of B_6O was theoretically scrutinized by using an *ab initio* dynamic simulation [358].

Most experimental and theoretical investigations in the literature are related to c-B_6O and there have been limited studies on the amorphous forms and hence their atomic structures and electrical and mechanical properties have not yet been explained in details. The present work is based on AIMD simulations and has two main objectives: the first one is the creation of B-rich amorphous boron oxides (a-B_xO_{1-x}, $0.5 \leq x \leq 95$, some of which have not been investigated before) and the second one is to shed some lights onto the influence of B concentration on their local structure and mechanical characters.

4.2 Methodology

All AIMD calculations of B-rich a-B_xO_{1-x} ($0.5 \leq x \leq 0.95$) were carried out via SIESTA code that is based on the density functional theory (DFT) [310] with the generalized gradient approximations (GGA) as parameterized by Lee, Yang and Parr (LYP) for exchange–correlation functions [229, 311]. The calculations were performed at the Γ-point of the Brillouin zone (BZ) and double-zeta (DZ) was used as the basis sets. The pseudopotential for B- and O-atoms was generated by using the Troullier and Martins scheme [250]. AIMD simulations were executed within the isothermal–isobaric ensemble. The velocity scaling and the Parrinello-Rahman methodologies [240] were preferred to control temperature and pressure, respectively. Each AIMD time step was selected to be 1.0 fs. The starting configuration was a BN melt having almost no chemical disorder and a mean coordination number of about 3.0. In the first step, a-$B_{50}O_{50}$ structure was constructed from the BN melt by replacing N atoms with O atoms (100 B atoms and 100 O atoms). In order to create other B-rich B_xO_{1-x} phases ($0.55 \leq x \leq 0.95$), B atoms were randomly substituted with O atoms until the structure reached to the projected B concentration. Thuswise, ten different networks were generated to be simulated. Then,

the supercells were exposed to an initial temperature which was determined roughly from BO phase diagram [349] and it is in the range of 3000 K (50 at.% B)-2500 K (95 at.% B). In our earlier work on B_6O [354], the simulation time of 40 ps was found to be enough to have an equilibrated melt. Nonetheless in the present study, the $B_{50}O_{50}$ system was thermalized for 150 ps at different temperatures 2500-3000K and the structure at 40 ps and 150 ps was compared. The partial pair distribution functions (PPDFs) shown in Fig. 4.1 reveal no significant topological difference between these two structures. For the structure at 40 ps, the mean coordination number of B and O atoms was found to be 3.06 and 1.96, respectively and for the structure at 150 ps, the average coordination number of B and O atoms was determined to be 3.07 and 1.95, correspondingly. Due to no significant difference in the first coordination shell of the structure at 40 ps and 150 ps, the other compositions were equilibrated for 40 ps at their initial temperature. These configurations were then quenched to the room temperature (300 K) in ~200-250 ps. The final structures at 300 K were relaxed by using a conjugate gradient (CG) approximation until the maximum force on atoms is smaller than 0.01 eV/Å. All amorphous networks were visualized by means of VESTA software [312]. Lastly, the crystalline B_2O, B_2O_3 and B_6O structures were studied for compression purposes.
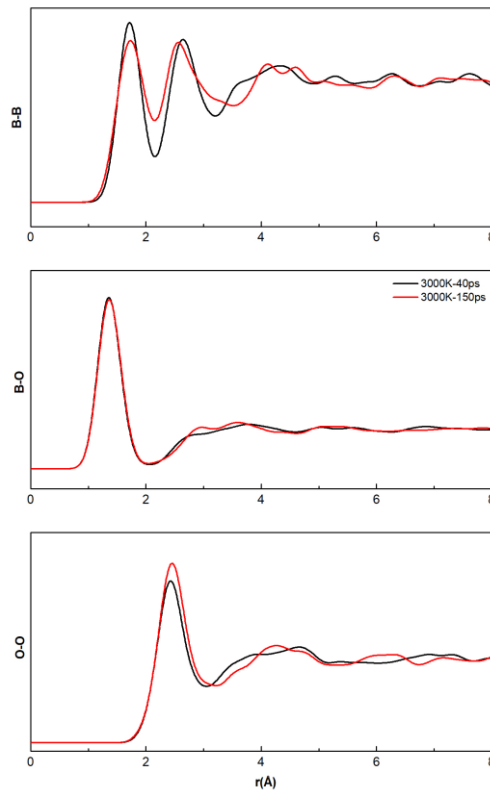
Figure 4.1 The PPDFs of the $B_{50}O_{50}$ system thermalized for 40 ps and 150 ps at 3000K.

4.3 Results

4.3.1 Local Structure

In order to assess the primary structural descriptions of each amorphous model, PPDFs are elucidated as a first step of our analysis and some examples are plotted in Fig. 4.2. The B-B, B-O and O-O correlations for all B contents exhibit a clear well-defined first peak, which is the main character of an amorphous structure.
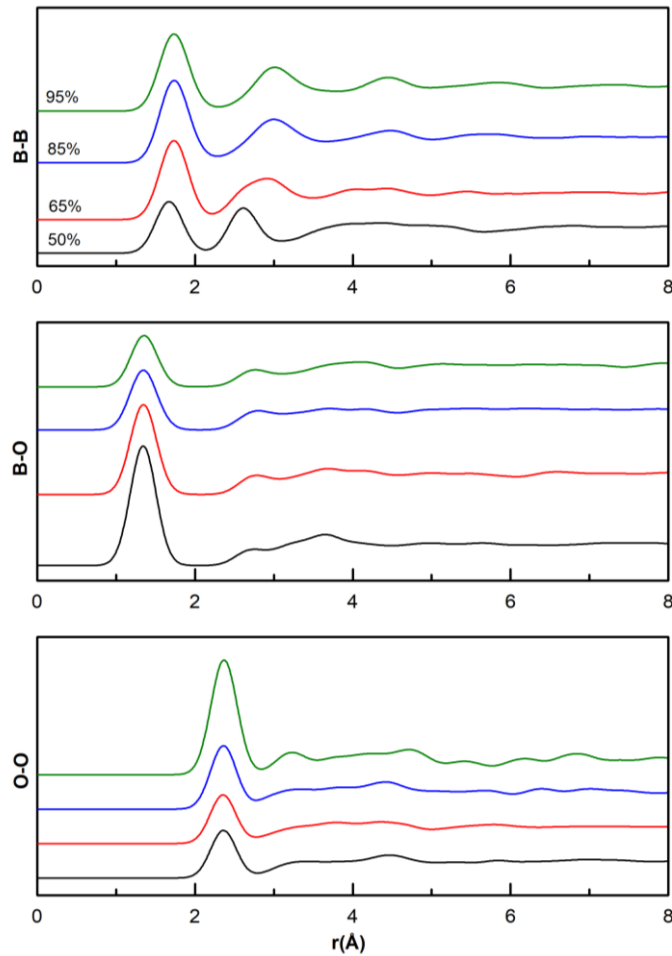
Figure 4.2 The PPDFs of a-B_xO_{1-x} at some B concentrations.

In the aim of the understanding of the effects of B concentration on the average bond lengths of the simulated materials, the peak position of first B-B and B-O coordination shell (r_{ij}) of all models are perceived and presented along with the available data in the literature in Table 4.1. The mean B-B bond length increases with increasing B content and it is in the range of 1.67-1.76 Å. The range predicted is well-comparable with the previous experimental and theoretical results of 1.68-1.86 [151, 359-362] (Table 4.1).

Additionally, for high B content materials, the average B-B bond separation is in a good accordance with 1.78 and 1.80 Å in a-B [45, 363]. On the other hand, the mean B-O bond length is projected to be between 1.34-1.37 Å. Subsequently, one can see that B concentration has practically no impact on this bond separation. This is due to the fact that the coordination number of O atoms remains almost the same for all compositions (see below). The B-O bond length (1.34-1.37 Å) predicted is parallel to 1.34-1.35 Å in c-B_2O_3 [364, 365] but it is considerably shorter than 1.43-1.50 Å in c-B_6O [151, 354, 361, 362]. This shortening conceivably denotes the polymerization of the B-O units and the formation of B_3O_2 type local structures in the simulated amorphous configurations. Lastly, the O-O bonding does not form in all models.

Table 4.1 The shortest distances r_{ij} (i,j are types of atoms) between atoms for all amorphous models.

r_{ij}	r_{BB}	r_{BO}	r_{OO}	Theoretical/ Experimental	References
Phase					
Amorphous					
$B_{50}O_{50}$	1.67	1.34	2.36	Theoretical	*This study*
$B_{55}O_{45}$	1.72	1.35	2.36	Theoretical	*This study*
$B_{60}O_{40}$	1.73	1.35	2.37	Theoretical	*This study*
$B_{65}O_{35}$	1.73	1.34	2.35	Theoretical	*This study*
$B_{70}O_{30}$	1.74	1.35	2.36	Theoretical	*This study*
$B_{75}O_{25}$	1.73	1.34	2.36	Theoretical	*This study*
$B_{80}O_{20}$	1.72	1.35	2.36	Theoretical	*This study*
$B_{85}O_{15}$	1.73	1.34	2.36	Theoretical	*This study*
$B_{90}O_{10}$	1.76	1.37	2.38	Theoretical	*This study*
$B_{95}O_5$	1.73	1.35	2.36	Theoretical	*This study*
B	1.78			Theoretical	[353]
	1.80			Experimental	[45]
B_6O	1.75	1.37		Theoretical	[354]
Crystal	1.68	1.37	2.41	Theoretical	*This study*
B_2O	1.75	1.58	2.57	Theoretical	[426]
	1.75-1.86	1.35-1.39		Theoretical	[360]
	2.54	1.34	2.37	Theoretical	*This study*
	2.75	1.35	2.60	Theoretical	[364]
		1.37-1.46		Theoretical	[365]
B_2O_3	1.76	1.50	3.31	Theoretical	*This study*
	1.70-.1.81	1.50	3.01	Theoretical	[361]
	1.68-1.83	1.46-.1.48	3.00-3.03	Experimental	[151]
B_6O		1.43-1.46	3.05-3.08	Experimental	[362]

In the next step, we define another important parameter, the mean coordination number, to offer an additional description of the local structure of the amorphous

networks at the atomistic level. The average coordination number of B- and O-atoms are determined by using the first minimum of the related PPDFs as the interatomic distance between each pair of atoms (i.e., cut-off radii, 2.14-2.30 Å for the B-B pair and 2.01-2.09 Å for the B-O pair depending upon the B content) and their variation as a function of B concentration is depicted in Fig. 4.3. The average coordination of B atom radically changes from 3.18 to 5.62 with increasing B/O ratio. The mean coordination of B atom at low B contents is comparable with 3.0 in c-B_2O and c-B_2O_3 while between 70-95 at.% B, it is close to 6 as in c-B_6O, c-B and a-B [54]. Perhaps the most extraordinary observation is unaffected O-coordination; it is about 2 for all compositions. Among the BO materials, O-atoms in B_2O_3 (glass or crystal) are twofold coordinated while they are threefold coordinated in c-B_6O. This finding provides an additional support for B-O polymerization in all amorphous network.
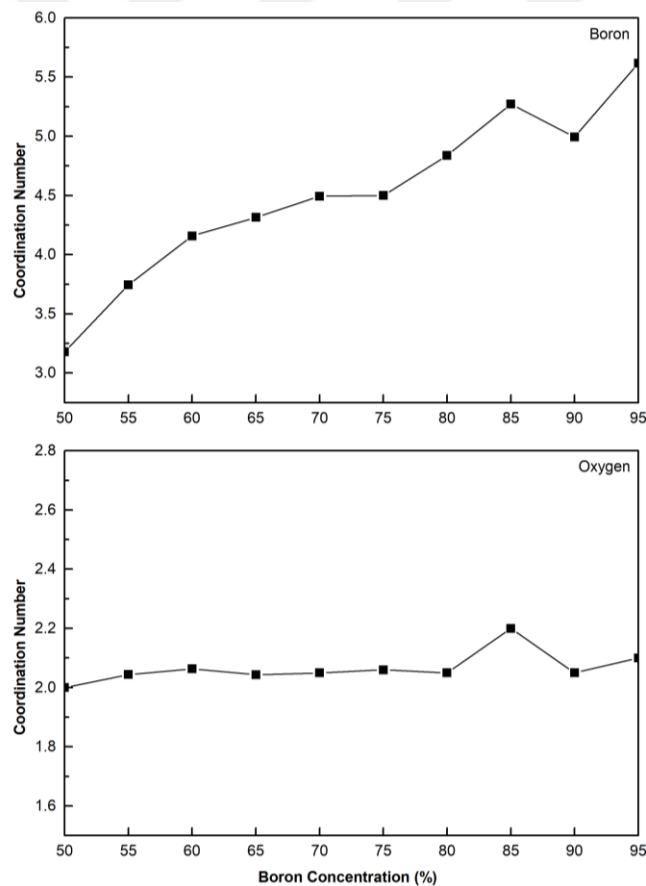
Figure 4.3 The modifications in average coordination number of B- and O-atoms as a function of B content.

In order to have particularly knowledge regarding the atomic structure of the models, we investigate the coordination distribution of the amorphous models and our

results are illustrated in Fig. 4.4. As B concentration rises, the fraction of threefold coordinated B atoms importantly declines from 81% to ~5% whilst that of sixfold coordinated B atoms alters from 3% to ~55% (see in Fig. 4.4). The frequency of fourfold and fivefold coordinated motifs of B atoms increases with increasing B content as well. Lastly, a trivial amount of sevenfold coordinated B atoms develops in some amorphous models. As for O atoms, the models have a large fraction of twofold and a small fraction of threefold coordinated motifs.
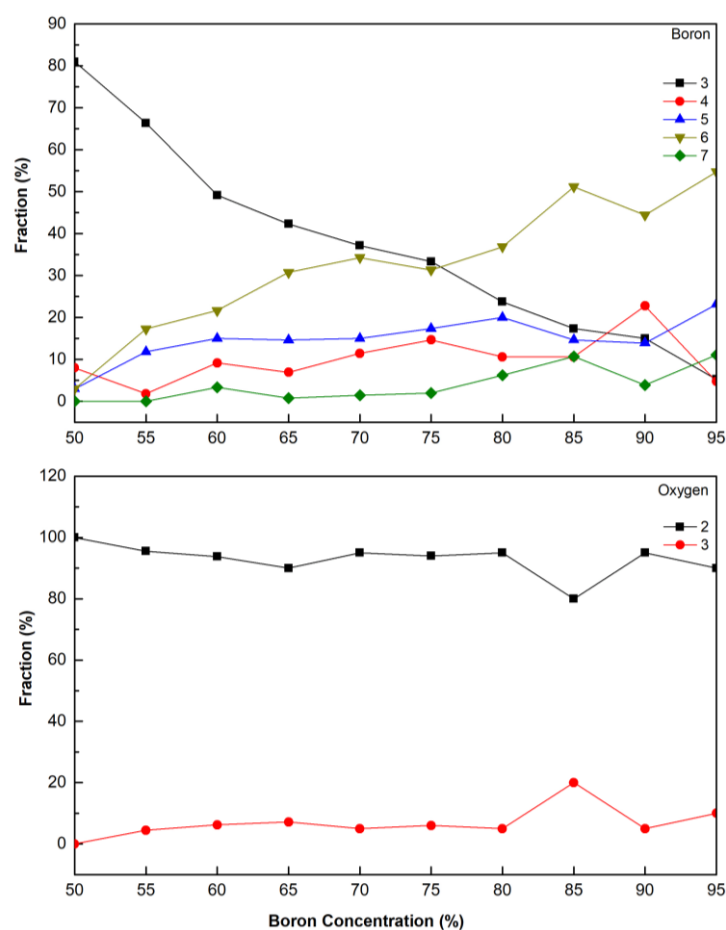
Figure 4.4 The coordination distributions of B and O atoms as a function of B concentrations.

The Voronoi polyhedron analysis [366, 367] can shed some lights on the sorts of cluster formed around B atom. A Voronoi polyhedron can be constructed by connecting perpendicular bisectors between a central atom and all of its neighboring atoms and is identified by the topological Voronoi index $(n_3, n_4, n_5,...)$, where n_i is the number of i-edge faces of a polyhedron around certain atom and Σn_i represents the total coordination

number of the corresponding polyhedron. We focus on certain polyhedra having high frequencies, especially, produced by B_{12} icosahedra. The B_{12} icosahedron that is a key unit of most B/B-rich materials in both the crystalline and amorphous forms consist of the pentagonal-pyramid structure (B_6). In the Voronoi analysis, the pentagonal-pyramid-like structures can form in the way of complete or incomplete (or defective). The complete pentagonal-pyramid-like clusters are represented by <2, 2, 2, 0> type index while the incomplete or defective ones are described by <2, 3, 0, 0>. The fraction of these indices for B atoms is shown in Fig. 4.5. Note that even a-$B_{50}O_{50}$ has a small amount of these clusters and with increasing B content their fraction drastically increases, implying that they have a strong tendency to form B_{12} molecules.
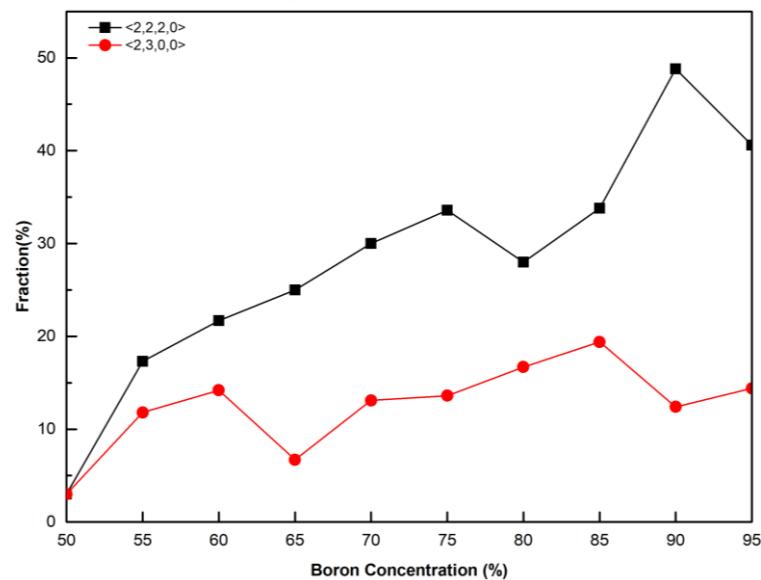
Figure 4.5 The fractions of <2, 2, 2, 0>, <2, 3, 0, 0> and <4, 0, 0, 0> type indices as a function of B content.

All computer-generated configurations were visualized and the ball-stick representation of some of which is presented in Fig. 4.6. One can see the occurrence of chemical segregations and the formation of a possible B-rich and O-rich regions (B:B_2O_3 phase separations). Indeed, in high pressure experiment on B_6O, the formation of a-B_6O was recovered upon pressure release and the recovered sample consists of a-B_2O_3 and a-B domains, parallel to our observation [356].
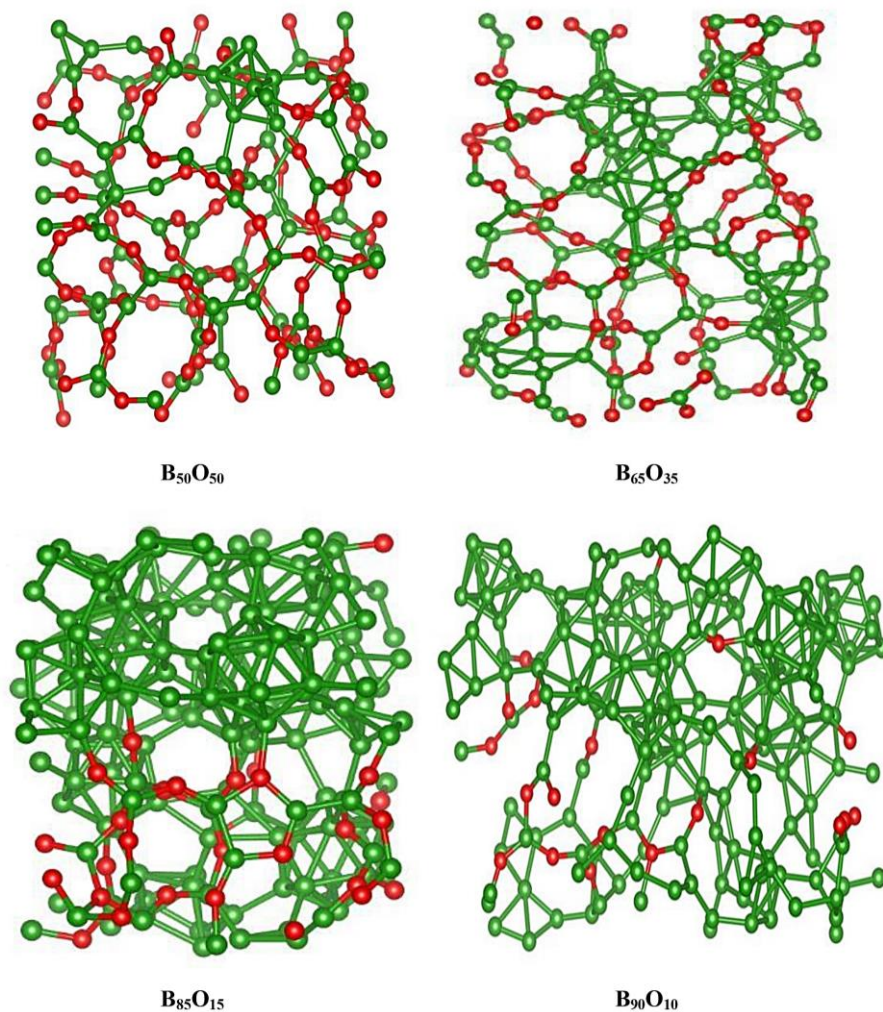
Figure 4.6 The ball-stick representations of the simulated amorphous networks.

We further calculate the bond angle distributions (BADs) for each amorphous network and some of them are plotted in Fig. 4.7. When the B-B-B angles are considered, as for 50% and 55% B contents, the B-B-B angles show a broad distribution changing from about 88º-140º but a sharp peak at about 60º appears in the distribution. In addition to this angle, another sharp peak at ~107º develops at 60% and higher B concentrations. These two angles are indeed originated from the bonds of the pentagonal pyramids like motifs. By considering the B-O-B angles, all BADs demonstrate an expansive distribution in the range of ~108º-170º but have a noticeable main around 135°, parallel to that of c-B_2O_3. The O-B-O angles in the simulated models possess a main peak at around 120º, similar to those of B_2O and B_2O_3 crystals.
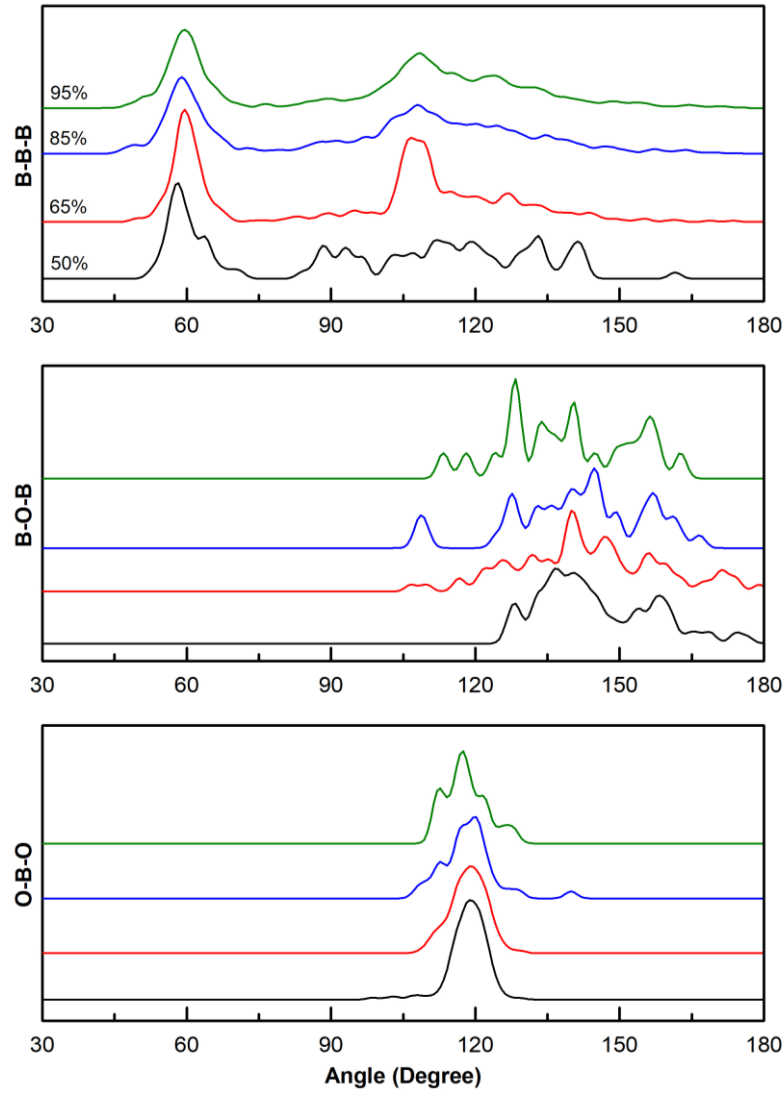
Figure 4.7 BADs in some B contents.

4.3.2 Mechanical Properties

The applications of an engineering material in technology requires the knowledge about its mechanical characteristics. For this reason, we consider the mechanical features of each amorphous configuration in details. We first probe the bulk modulus (K) that can be readily calculated by fitting the energy (E)-volume (V) correlation to the 3rd order BMEOS (Eq. 2.50).

The alteration of K as a function of B content is illustrated in Fig. 4.8 and given in Table 4.2 as well. For comparison purpose, the accessible data in the literature are also provided in the same table. The K value of the amorphous materials drastically changes from ~21 GPa to ~182 GPa. This increasing trend in bulk modulus is thought to be

originated from the development of more B_{12} molecules at high B contents in the systems. At low B contents, the K values predicted are comparable with the experimental or theoretical values of ~10-18 GPa in a-B_2O_3 [368] and c-B_2O_3 [349] and 24 GPa in c-B_2O [359]. Our estimations beyond 80% B concentrations are approximately overlapped with the previous experimental and theoretical findings of 106 GPa for a-B_6O [354] and 109-272 GPa for a-BO_x (x: 0.02– 0.28) [164]. Moreover, the K value at 95% B content is ~182.4 GPa, comparable with 213 GPa (experimental) [322] and 193 GPa (theoretical) in c-B [369].

Table 4.2 Bulk (K), young (E) and shear (μ) moduli, poisson ratios (ν) and Pugh's ratio (n). K, E, μ and H$_v$ are in the unit of GPa.

	K	*ν*	*E*	*μ*	*n*	*H$_v$*	**References**
Phase							
Amorphous							
$B_{50}O_{50}$	33.2	0.35	29.2	10.8	3.068	-0.83-1.86	*This study*
$B_{55}O_{45}$	21.3	0.32	23.0	8.7	2.444	-0.51-1.54	*This study*
$B_{60}O_{40}$	32.6	0.26	46.6	18.5	1.768	2.66-3.79	*This study*
$B_{65}O_{35}$	25.3	0.25	38.3	15.3	1.651	4.12-5.40	*This study*
$B_{70}O_{30}$	59.9	0.26	85.2	33.7	1.776	5.70-7.09	*This study*
$B_{75}O_{25}$	77.6	0.26	112.2	44.6	1.741	7.72-9.27	*This study*
$B_{80}O_{20}$	87.3	0.22	145.6	59.6	1.465	8.99-10.97	*This study*
$B_{85}O_{15}$	119.7	0.22	199.6	81.7	1.465	12.33-13.81	*This study*
$B_{90}O_{10}$	150.4	0.21	260.9	107.7	1.397	16.27-17.90	*This study*
$B_{95}O_5$	182.4	0.22	311.9	128.4	1.421	19.19-19.81	*This study*
B_6O	106	0.18	203	86		13-18	[354]
B_2O_3	10						[368]
BO_x*	109-272	0.2					[164]
Crystal							
B_2O	24	0.68					[426]
B_2O_3	10-18						[349]
						1.5±5	[374]
B_6O	181-300		470-540	206-227			[339, 351, 370, 372, 373]
	209.4-246	0.15	480-507.8	208-223.1		38-38.2	[351,361]
						33-36	[334]
						45	[147]
B_xO**						32-60	[375]
Boron	213		470			35	[322]
	193						[369]

*BO_x thin films; x: 0.02– 0.28,
**B_xO ; x:2, 4, 6, 7, 8, 10, 12, 18, 20, 22.
Ref. 351, 354, 361, 369, 372, 373, 426 are theoretical works,
Ref. 147, 322, 334, 339, 370 are experimental works.

Poisson's ratio of a material subjected to a uniaxial stress is calculated with Eq. 2.54. The average value of ν is given in Fig. 4.8. ν shows a decreasing trend and change

from ~0.35-0.21 that are in coherent with the values of 0.15, 0.18 and 0.2 for c-B_6O [361], a-B_6O [354] and a-BO_x (x: 0.02– 0.28) [164], respectively. It should be noted here that because of the fitting, some errors in Poisson's ratio predicted are expected.
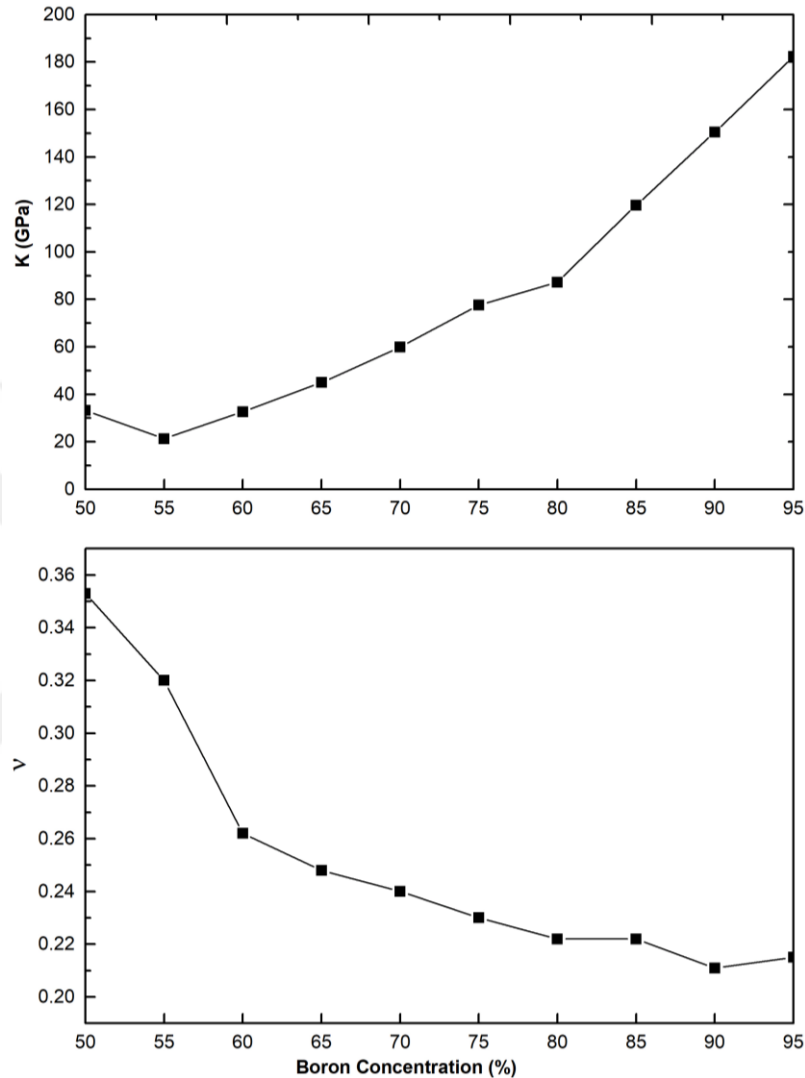
Figure 4.8 Variation in bulk modulus (K) and Poisson ratio (ν) as a function of B concentration.

Young's modulus (E) is calculated using Eq. 2.56. It tends to increase overall from 23 to 312 GPa (see Fig. 4.9 and Table 4.2), indicating that the materials become less elastic with increasing B concentration. Our estimated value for a-$B_{85}O_{15}$ (~200 GPa) is parallel to the theoretical result of ~203 GPa in a-B_6O [354]. However, the reported experimental and theoretical E values for c-B_6O (470-540 GPa) [339, 361, 370, 371] and c-B (470 GPa) [161] (Table 4.2) are very much higher than our findings.
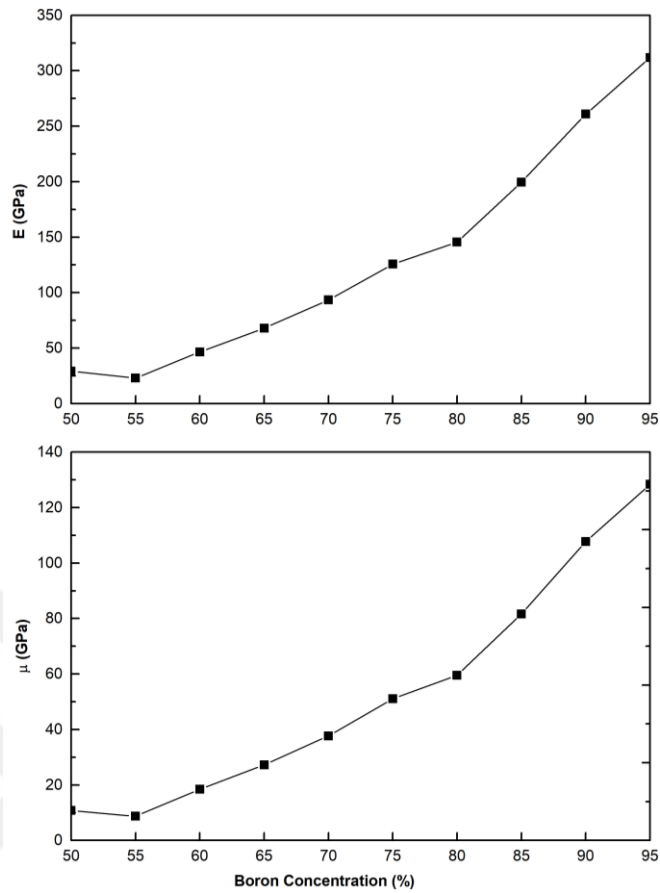
Figure 4.9 Variation in young (E) and shear (μ) modulus vs B content.

Since we acquire E and ν values, shear modulus (μ) can be easily computed with Eq. 2.57. Shear modulus of the simulated amorphous models increases from ~9 GPa to ~128 GPa (see Fig. 4.9) with increasing B content. The calculated value of a-$B_{85}O_{15}$ (~82 GPa) is again analogue to that of a-B_6O (~86 GPa) [354] computed in the earlier theoretical work. Yet, the estimated μ values for c-B_6O (206-227 GPa) structure in the previous works [339, 351, 365, 370, 372, 373] are also highly bigger than those of our μ result (Table II). The smaller result in the amorphous forms signifies that they have more a flexible structure than the crystalline forms.

In addition to these mechanical parameters, we evaluate the Vicker's hardness (H_v) using the four different empirical equations (Eq. 2.58-2.61) [255-258]. The results obtained from these equations are exposed in Fig. 4.10. The hardness shows an increasing trend and is in the range about 1.3 to 19.8 GPa. Our predictions to certain B content are comparable with the previous experimental result of 1.5±5 GPa for c-B_2O_3 structure [374], but are noticeably less than the previous experimental results of 32-60 GPa for c-

B$_x$O (x:2, 4, 6, 7, 8, 10, 12, 18, 20, 22), c-B$_6$O and c-B [147, 322, 334, 351, 369, 375]. We should note here that the negative values obtained is due to the limitation of equation VI (see Ref. 257 for more information)
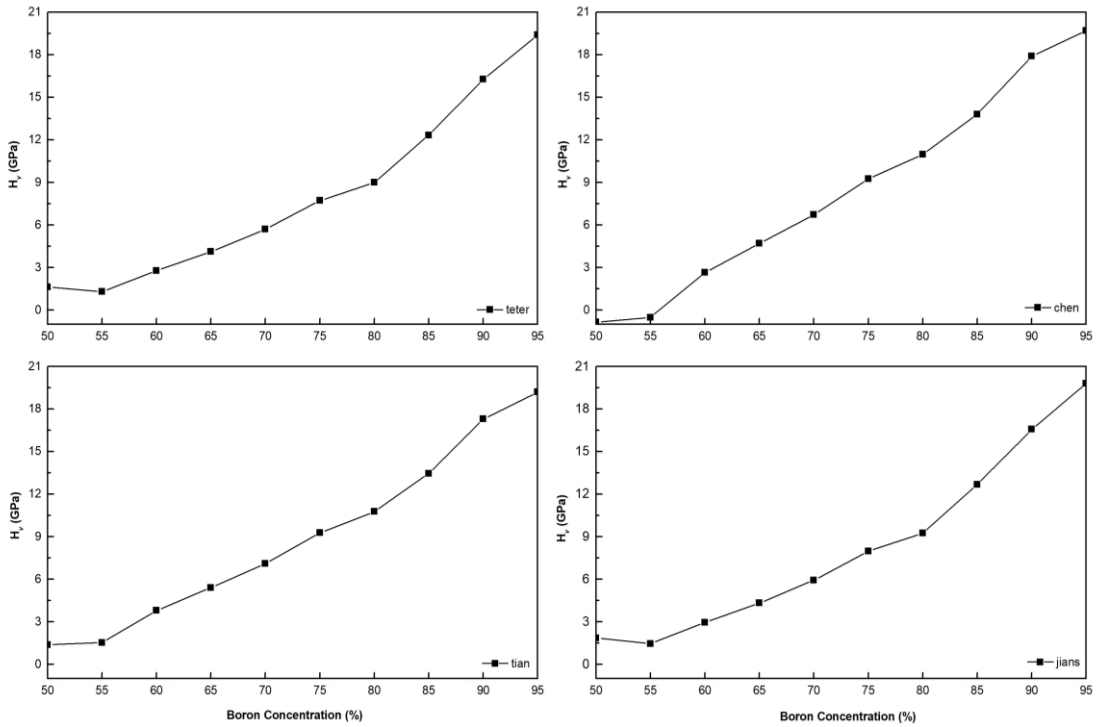
Figure 4.10 B concentration dependence of Vickers hardness (*H*).

In addition to the Vicker's hardness, the microhardness value (H) of each model is also calculated by using Eq. 2.62 [259] and illustrated in Fig. 4.11. The H value of the models changes from 1.05 GPa to 24.4 GPa depending on B concentration. We find no data in the literature to compare our estimations.
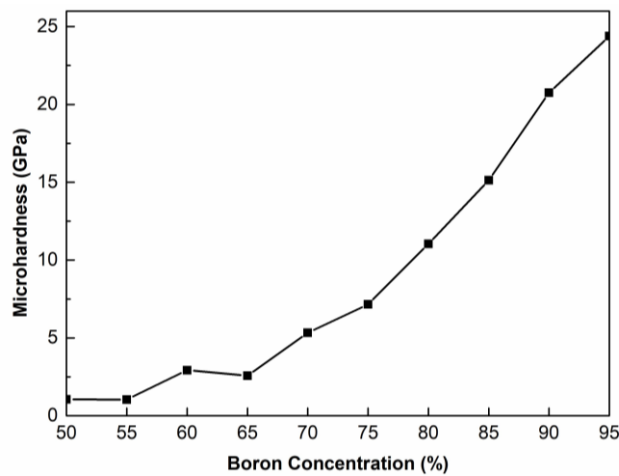
Figure 4.11 B concentration dependence of the alterations in microhardness (*H$_v$*).

Lastly, the determining of brittle-ductile characteristic of any material has a big importance in the advanced technological applications. This characteristic can be specified by two different ways, Poisson's ratio and Pugh's ratio (n) [260, 261]. 1.75 is believed as the critical value for n. If n is smaller (bigger) than the critical value, the material presents the brittle (ductile) feature. On the other hand, if the Poisson's ratio is less (higher) than 0.26, the material exhibits brittle (ductile) character. For some amorphous materials, the values of n and ν (Table 4.2) are in the range of 1.768-3.068 and 0.26-0.35, correspondingly. Consequently, it can be expressed that the B-rich amorphous materials up to 70-75% concentration show a ductile character while the others exhibit a brittle feature.
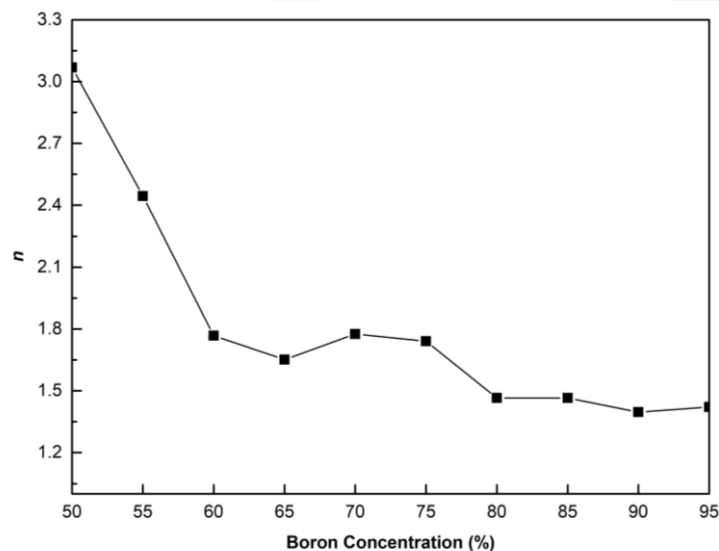
Figure 4.12 Variation in Pugh's ratio (n) vs B content.

4.4 Discussion

An extensive investigation on B-rich a-B_xO_{1-x} ($0.5 \leq x \leq 0.95$) materials is carried out to expose their features and several remarkable observations are exposed. First one is that coordination number of O atoms almost independent on the compotation while that of B atoms steadily increases from 3.18 to 5.62. The local structure around O atoms is found to be fairly parallel to that of B_2O_3 consisting of twofold coordinated O-atoms. The second one is the occurrence of chemical segregation in all disordered networks, resulting in possible B:B_2O_3 phase separations. Indeed, a pressure-induced amorphization was observed in c-B_6O on decompression and resulting a-B_6O consists of a-B_2O_3 and a-B

domains, validating our finding. Yet unlike a-B_2O_3, boroxol rings are not observed in our models. The formation of such rings has not been discussed in the earlier work on a-B_xO [162-167, 353-355] as well. It is known that the formation of the rings requires a long simulation time. We simulate $B_{50}O_{50}$ more than 150 ps at different temperatures as mention in the method section but we do not observe a drastic structural change between the configuration at 40 ps and 150 ps and detect the formation boroxol rings in the structure. Here we can speculate some possibilities for no existing rings in the models: i) It might possible that the compositions studied do not allow to the development of such rings, ii) it is also likely that even 150 ps is not enough for the development of boroxol rings for the compositions simulated and iii) it is possible that the size of the simulation box is not large enough, namely the size of B_2O_3 domains are not large enough for the development of the rings. Probably a machine-learning potential on a larger system for a long simulation time can clarify this issue.

As the B concentration increases, the coordination number of B atom increases and B atoms have a strong tendency to form pentagonal pyramid-like structures and hence B_{12} icosahedrons. Their formation has a dramatic influence on the mechanical properties. Namely they increase with increasing B content, in agreement with the previous investigation on a-B_xO. Yet when the mechanical properties of amorphous network are compared with the crystalline counterpart, a radical decrease in the mechanical properties is detected in the amorphous forms. This is probably due to the formation of soft B_2O_3-like regions in the models.

Within the limitation of DFT and approximation used to estimate the mechanical properties of the amorphous model, our simulation also reveals a region whether there is a ductile-to brittle transition in the amorphous materials, which corresponds to 70-75% B concentrations. We should note here that Pugh's ratio approach was proposed for polycrystalline materials while Poisson ratio approach was proposed for metallic glasses and hence there might be some uncertainties for composition at which the transition occurs.

4.5 Conclusions

One of the most commonly studied materials appears to be boron oxides. These materials, especially boron suboxides, have the present world-wide attention due to their high bulk modulus and high indentation hardness. For this reason, we have generated the amorphous B_xO_{1-x}, ($0.5 \leq x \leq 95$) configurations by means of AIMD simulations and their microstructure and mechanical features have been scrutinized. The mean B-coordination increases from 3.18 to 5.62 but the mean O-coordination remains almost null and about 2 as in B_2O_3. $B:B_2O_3$ phase separations are observed in all materials modelled. Moreover, the mechanical properties of our B-rich boron oxides have been discussed. The bulk modulus of the models is found to be between ~21-182 GPa. The Vicker's hardness is estimated to be in the range of -0.51-19.81 GPa. The amorphous materials (B_xO_{1-x}, $x \geq 80$) are classified as hard materials. Within the limitations of DFT and approaches used, we speculate that there is a ductile-to-brittle transition at around 70-75% B contents.

Chapter 5

Possible Boron-Rich Amorphous Silicon Borides from Ab initio Simulations

The work presented in this chapter is submitted in A. Ö. Çetin Karacaoğlan, M.Durandurdu, Journal of Molecular Modelling.

5.1 Introduction

The boron-silicon (BSi) binary compounds have drawn substantial attentions for many years. The existence of these compounds was recognized more than one century ago. However, there are still unknows and controversies about them. The first reports dated back to the study of Moissan and Stocks in 1900's in which silicon triboride (c-SiB$_3$) and silicon hexaboride (c-SiB$_6$) were ferreted out in the crystalline form by the technic of fusion of elements [187] but no information was provided about their crystal structure. Later, c-SiB$_3$, as a single crystal phase having a tetragonal symmetry, was affirmed with the hot-pressing method between 1873 K and 2073 K by Samsanov and Latisheva in 1955 [376]. In 1956, Zhuravkev proposed that c-SiB$_6$ had a structure resembling to the cubic compound of CaB$_6$ [198]. However, the later investigations on SiB$_6$ did not validate the cubic crystal and as an alternative they proposed an orthorhombic structure [174, 200, 377-379]. The crystalline silicon tetraboride (c-SiB$_4$), a more well-known B-Si binary compound, was fabricated in different experiments in 1960 [192, 193, 196]. Yet, the presence a cubic form of c-SiB$_4$ and its quality and impurities were questioned in other studies [188, 194, 380]. In spite of a few published data [376, 381,382], the physical and mechanical properties remained unknown until 1989 at which Tremblay and Angers discovered an interesting and effective technic to produce SiB$_4$ powders [383] and revealed its physical (porosity, specific density and microstructural aspects) and mechanical properties (elastic modulus, flexural strength and Vickers microhardness) in details. [384]. In summary, there are three different types in

the phase diagram of B-rich crystal binary compounds, which are referred as c-SiB$_3$ (and/or SiB$_4$), c-SiB$_6$ and c-SiB$_n$ [385].

B-rich molecules or solids have an importance significance in Physics, Chemistry and Materials Science due to their remarkable properties. The main characteristic of icosahedral B-rich systems, for example, B$_4$C, SiB$_3$, B$_6$O, SiB$_3$ etc. [150, 153, 386-388] is composed of the α-rhombohedral phase of B (α-B$_{12}$) and their arrangements [55, 389]. These solids show superb thermoelectric performance and resists to high melting temperatures up to 2400 ℃ [55]. For this reason, they are referred as very stable refractory materials having high melting temperatures [389]. Moreover, they have a low mass density, splendid hardness, good chemical inertness, adjustable semiconducting aspects, high elasticity modulus, high mechanical strength and high stability in oxygen [390-393].

Both Si-rich and B-rich noncrystalline solids can be easily synthesized. The first amorphous semiconducting B$_n$Si$_{1-n}$ ($0 \leq n \leq 1$) alloys were prepared by the rf (radio frequency) plasma decomposition of SiH$_4$-B$_2$H$_6$ gas mixtures in 1979 [205]. In this research, the infrared vibrational modes, the optical absorption, the electrical conductivity, the spin resonance and the hydrogen content (between 10% and 45% hydrogen) of these films were analyzed [205]. In 1983, amorphous B-Si alloys with 0-40% B concentrations were generated by low pressure chemical vapor deposition (LPCVD) technique and their thermal oxidation was examined [394]. In a different experiment (in 1993), amorphous B$_n$Si$_{1-n}$ ($0 \leq n \leq 1$) thin films were easily produced by the LPCVD method as well and the impacts of Si incorporation on their structural modifications were explored [395]. Si-rich disordered BSi alloys with 1-50 at. % B were produced by the LPCVD and the change in optical band gap was studied [396]. A few years later, the same group prepared Si-rich amorphous BSi materials with 0-25 at. % B and their oxidation at temperatures of 25-600°C were qualitatively explored [210]. B-rich BSi compounds having 90-97% B contents were fabricated by the arc-melting and spark plasma sintering and the thermoelectric properties and the effects of phase composition and microstructure on the thermoelectric properties were explored [208]. In the last study, B-rich B-Si films by the pulsed laser deposition (PLD) technique with different B/Si ratios were prepared and the change in band gap energy was projected from the optical absorption spectrum of the films [209]. The authors deduced an increase in the band gap with decreasing B concentration [209].

According to our literature review, *amorphous BSi binary compounds* (B_nSi_{1-n}, $0.5 \leq n \leq 0.95$) are still one of inadequately known B-involving solids as semiconductors and refractory materials because no extensive investigation has carried out to understand their structure at the atomistic level and their electronic and mechanical properties so far. This paper reports a detailed examination of B-rich amorphous SiB with 50-95 at. % B to provide valuable information about their features.

5.2 Computational Method

In order to create B-rich amorphous models, the density functional theory (DFT) based *ab initio* molecular dynamics (AIMD) simulations were used [310]. The pseudopotentials were due to the Troullier-Martins approach [250]. The DZ basis sets were selected for the valance electrons and the Γ point was chosen to sample the Brillion zone. The exchange correlation energy was estimated via the Perdew Burke Ernzerhof (PBE) generalized gradient approximation (GGA) [231]. To execute AIMD simulations, the NPT (i.e., isothermal-isobaric) ensemble was preferred. The velocity scaling method was used to control temperature and the Parrinello-Rahman technique [240] with the fictitious mass of 20.0 $Ry.fs^2$ was used to control pressure. In MD simulation, a small-time step is more desirable to accurately sample highest frequency motion; its typical value is 1.0 fs and hence in the current study this typical value was used. Since a 200 atoms model is fair enough to capture the short-range order of amorphous networks, we used a 200 atoms the BN melt having almost no chemical disorder as starting structure and contracted our $B_{0.5}Si_{0.5}$ configuration (100 B atoms and 100 Si atoms) by replacing N atoms with Si atoms. Then B atoms was randomly substituted with Si atoms until the structure reached to certain B contents. In this way, we created ten different configurations ranging from 50% to 95% B contents. Each initial structure was thermalized at a different temperature according to BSi phase diagram [397]. The lowest temperature (1800 K) was applied to 50% B content while the highest one (2300 K) was applied to 95% B content for 30 ps. The melts were then slowly quenched to the room temperature in 75.0-100.0 ps. By using the conjugate gradient method, the final structures at 300 K were optimized such that the greatest forces on atoms are smaller than 0.01 eV/Å. In addition to these amorphous configurations, we also studied c-SiB$_3$ and c-SiB$_4$ to compare their features with those of the amorphous models. In order to accurately

estimate the band gap energy of the amorphous structures, we performed the GGA+U calculations. In order to evaluate the Hubbard potential U, we focused on the $B_{50}Si_{50}$ model because the band gap was estimated about 0.8 eV for the $B_{50}Si_{50}$ thin film [209] The Hubbard potentials U=8.0 eV for B-p state and U=7.0 eV for Si-p state were found to produce about 0.8 eV band gap energy for our $B_{50}Si_{50}$ model and hence we used these two parameters for all other amorphous configurations to predict their electronic structure.

5.3   Results

5.3.1 Atomic Structure

5.3.1.1 The Partial Pair Distribution Functions (PPDFs)

First, we probe the amorphous configurations using the partial pair distribution functions (PPDFs) since PPDFs can offer valuable information about their microstructure. The PPDFs of some models generated are depicted in Fig. 5.1. All PPDFs exhibit classic characteristics of an amorphous network such that they all show a well-defined short-range correlation but not long-range ones. In order to reveal the influence of B content on the average B-B, B-Si and Si-Si bond separations, the position of first maximum peak in all correlations is studied and plotted in Fig. 5.2.
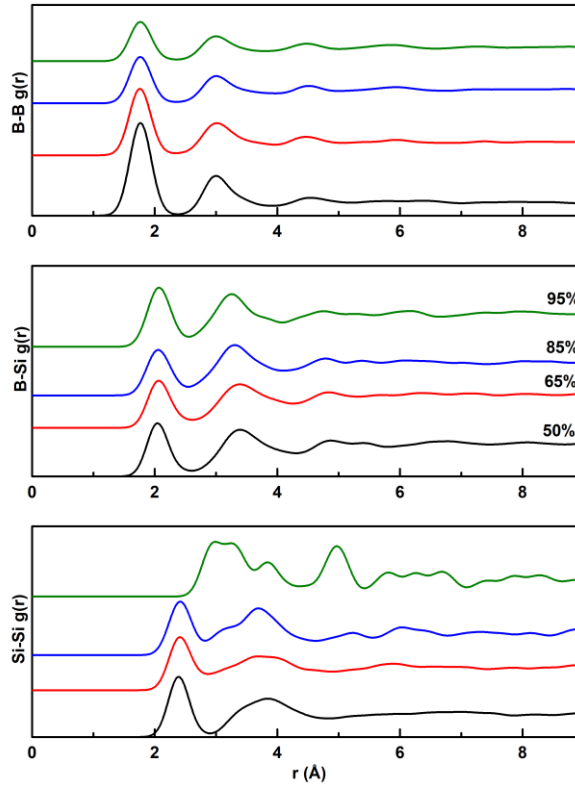
Figure 5.1 The partial pair distribution functions (PPDFs) of some computer-generated BSi amorphous models. It should be noted that Si-Si bonds do not form in a-B$_{95}$Si$_5$.

The B-B bond length is projected to be in the range 1.76 to 1.77 Å, implying that the change in B/Si composition has almost no effect on this bond length. For c-SiB$_3$ and c-SiB$_4$, the B-B bond separation is computed to be 1.77 Å and 1.82 Å, respectively. When the previous experimental and theoretical studies on the crystalline BSi materials are considered, the estimated range for B-B bond is well-comparable with the values of 1.75-1.90 Å in c-SiB$_{2.5}$ (the monoclinic symmetry) [398], 1.74-1.92 Å in c-SiB$_3$ (the triclinic symmetry) [398], 1.792 Å in c-SiB$_3$ (the orthorhombic symmetry) [178], 1.84 Å in c-B$_{2.89}$Si [188] and 1.77-1.85 Å in c-SiB$_6$ [200]. The average B-Si bond distance slightly fluctuates between 2.04 Å and 2.07 Å, again suggesting no strong influence of B content on this bond length as well. The B-Si bond length is computed to be 1.99 Å for c- SiB$_3$ and 2.01 Å for c-SiB$_4$. Our predictions are quite comparable with the earlier experimental and theoretical results of 2.02-2.22 Å in c-SiB$_{2.5}$ (the monoclinic symmetry) [398], 2.00-2.22 Å in c-SiB$_3$ (the triclinic symmetry) [398], 2.02-2.17 Å in c-SiB$_6$ [200] and 2.002 Å in c-B$_{2.89}$Si [188]. As regards to the mean Si-Si bond separation, it is in the range 2.38 to 2.42 Å. The change in this bond distance is again is not too drastic. The average Si-Si

90

bond length from our simulation is 2.57 Å for c-SiB$_3$ and 2.15 Å for c-SiB$_4$. The Si-Si bond separation obtained in the present work is slightly longer than 2.33 Å in c-SiB$_{2.5}$ (the monoclinic symmetry) [398], 2.36 Å in c-SiB$_3$ (the triclinic symmetry) [398], 2.12-2.21 Å in c-SiB$_6$ [200], 2.35-2.36 Å in c-Si [399]. We should note here that there is no Si-Si bonding at 95% B content and hence the peak in the PPDFs around 3 Å corresponds to the second neighbor coordination shell.
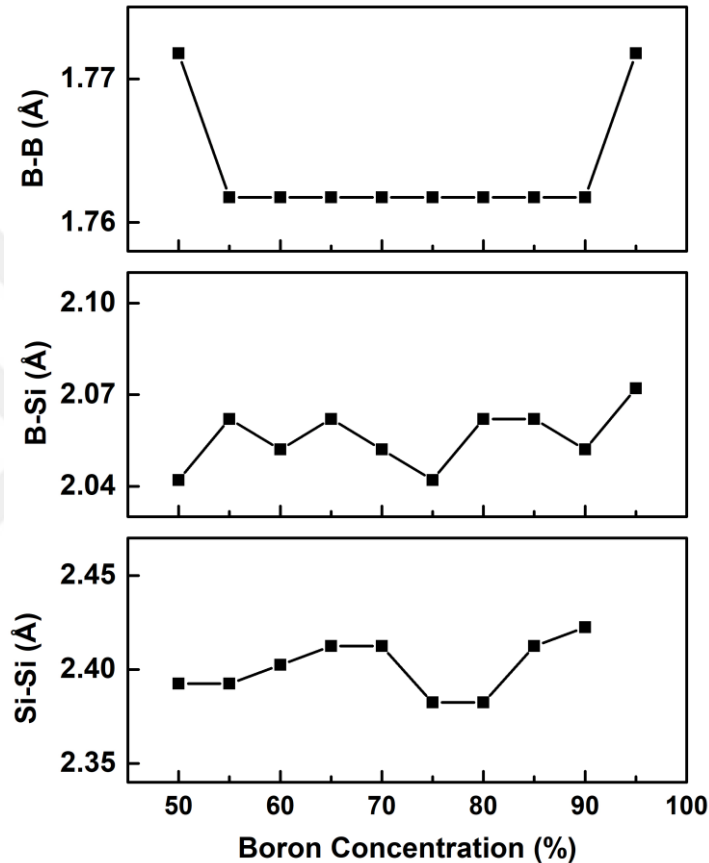
Figure 5.2 The computed bond length of B-B, B-Si and Si-Si pairs vs B concentration.

5.3.1.2 The Coordination Number

The mean coordination numbers are indeed one of the key parameters for amorphous materials. By using the first minimum of PPDFs (2.34-2.37 Å for the B-B pair, 2.54-2.62 Å for the B-Si pair and 2.82-3.02 Å for the Si-Si pair depending upon B concentration), the coordination numbers are estimated and their variation as a function of B content is illustrated in Fig. 5.3. The trend in B and Si coordination is similar and they increase with increasing B/Si composition. The coordination for B atom changes

from 5.49 to 6.18 while that of Si atom changes from 4.29 to 5.6 with increasing B content. We should note that the value of 6.18 for B atom is comparable with 6.3 in amorphous B [389]. We also note here that the mean coordination number of B atom in amorphous SiB_3 and SiB_4, about 5.8, is comparable with 6 in their crystalline counterpart. Additionally, the average coordination number (about 4.6) of Si atom in a-SiB_3 is close to 5.0 in c-SiB_3 while the noticeable deviation in Si coordination (4.7) is observed in the amorphous SiB_4 phase compared to 3.3 in c-SiB_4.
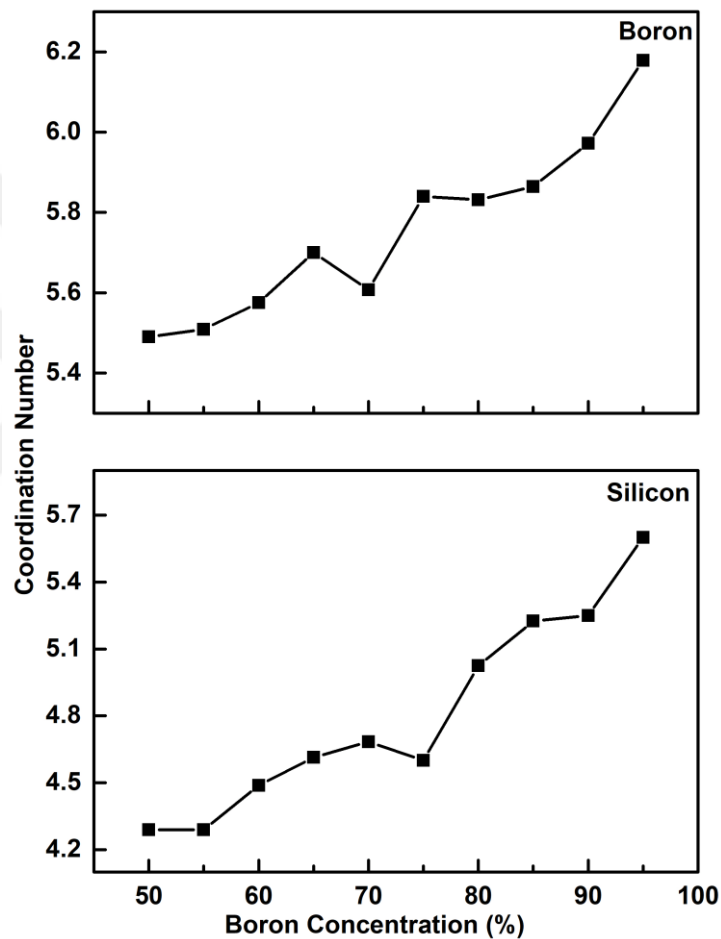
Figure 5.3 B content dependence of average coordination number of B and Si atoms.

At 50% B content, the structure consists of mainly fourfold coordinated Si atoms (77.0%) and sixfold coordinated B atoms (56.0%). The fraction of fivefold and sixfold coordinated Si atoms is ~12% and 8%, correspondingly. These higher coordinated Si atoms mainly involve pentagonal-like configurations. On the other hand, the frequency of fourfold and fivefold coordinated B atoms is about 16.0% and 22.0%, respectively.

The tetrahedral coordination of B and Si atoms decreases with increasing B/Si composition but it does not diminish even at the highest B concentration. Parallel to this decrease, the fraction of 5- and 6-fold coordinated motifs for Si atom increases gradually whilst fivefold coordination for B atoms decreases. Some models also present negligible amount of 3-fold and 8-fold coordinated Si atoms (Fig. 5.4).
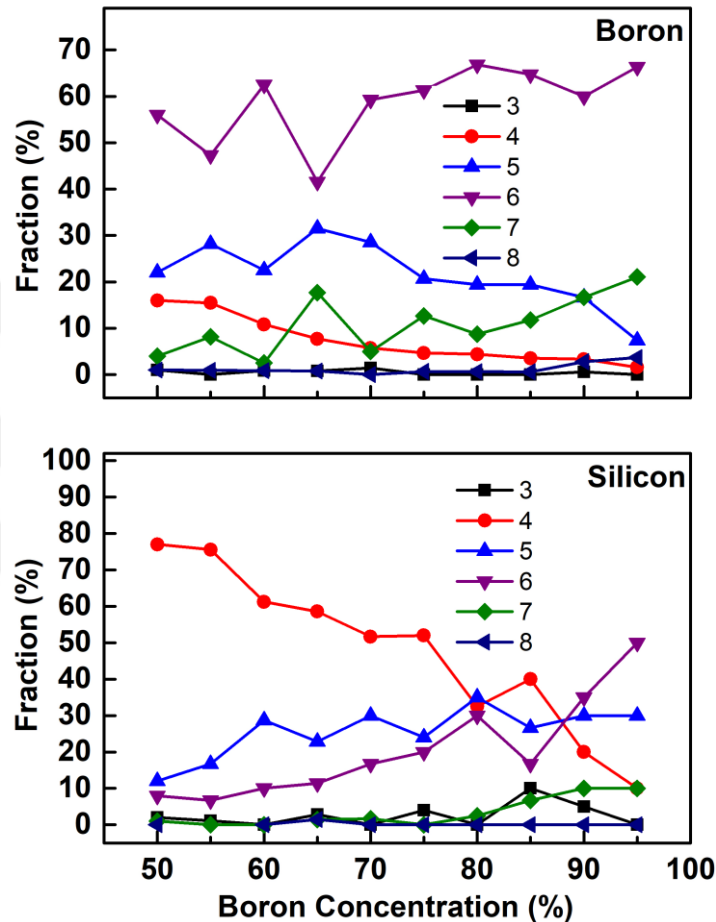
Figure 5.4 The coordination distributions of B and Si atoms as a function of B concentrations.

5.3.1.3 The Bond Angle Distribution

In order to shed additional lights on the atomic structure of amorphous B_nSi_{1-n} configurations, a bond angle distribution examination is carried out and the B-B-B, B-Si-B, Si-B-Si and Si-Si-Si distributions are illustrated in Fig. 5.5.
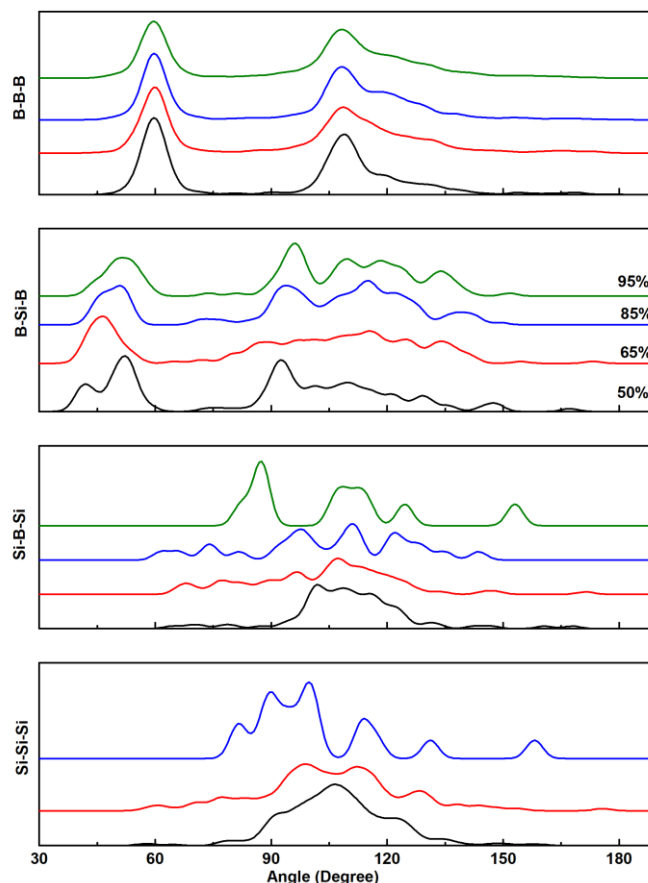
Figure 5.5 The bond angle distributions functions in some B contents.

There are two main peaks located at ~60° and ~108° related to the B-B-B angles for all compositions, which are a result of the intra-icosahedral bonds of the pentagonal pyramids (i.e., B_{12} molecules), similar to those of pure amorphous or crystalline B structures. For the Si-B-Si angle distributions, a broad peak located around 111°, close to the tetrahedral angle of 109.5° up to 80% B content, suggesting some signature of tetrahedral character in these amorphous networks. Yet beyond 80% B content, this character diminishes due to the formation of higher coordinated motifs around Si-atoms. Indeed, the Si-Si-Si angle distribution also shows similar trend as in the Si-B-Si distribution. B-Si-B angles, on the other hand, produce the most complex distribution because of differently coordinated Si atoms involving both tetrahedral and pentagonal pyramids-like motifs.

5.3.1.4 The Voronoi Analysis

The Voronoi polyhedron investigation [366, 367] can offer useful information regarding the types of clusters formed around each atom and hence about the amorphous models. In this method, a polyhedron is indicated in the way of $<n_3, n_4, n_5, n_6, ...>$ type indices. In here, n_i and Σn_i are the number of i-edge faces of a polyhedron and its total coordination number, correspondingly. In order to identify Voronoi polyhedrons, the first minimum of PPDFs was used as a cutoff radius. The key structure of amorphous and crystalline B and B-rich materials is mostly the quasi-molecular B_{12} icosahedrons formed by the pentagonal pyramids. In the Voronoi analysis, the pentagonal pyramid-like motifs can be represented by $<2,2,2,0>$ index. In B based amorphous materials, incomplete pentagonal pyramid-like clusters can also form and can be denoted by $<2,3,0,0>$ index. Therefore, we mainly focus on these two indices and analysis their variation (Fig. 5.6). With reference to B atoms, the fraction of $<2,2,2,0>$ type polyhedrons increases gradually with increasing B content as expected and parallel to this increase, the frequency of $<2,3,0,0>$ type index decreases slowly but they still exist at the highest B content and have a fraction of ~7%.
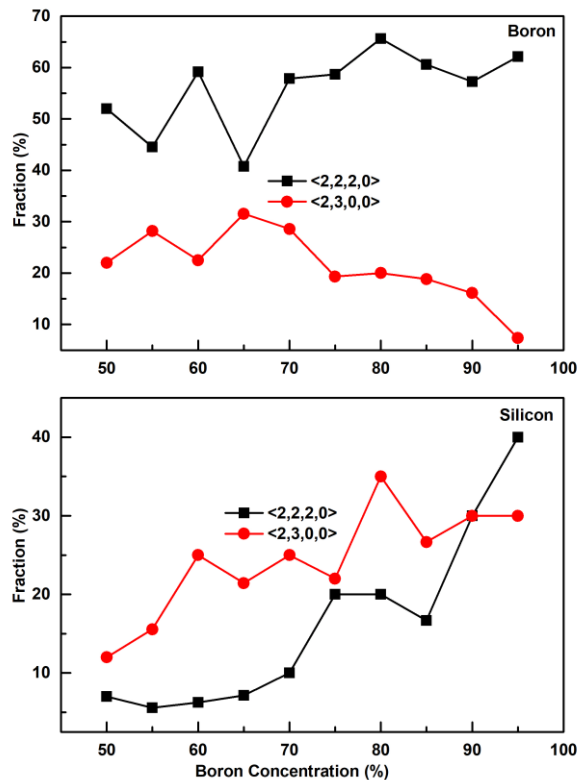
Figure 5.6 B content dependence of $<2,2,2,0>$ and $<2,3,0,0>$ indices that correspond to ideal and incomplete pentagonal pyramid-like motifs, respectively.

The computer-generated models are visualized via the VESTA program [312] and the models are shown in Fig 5.7.
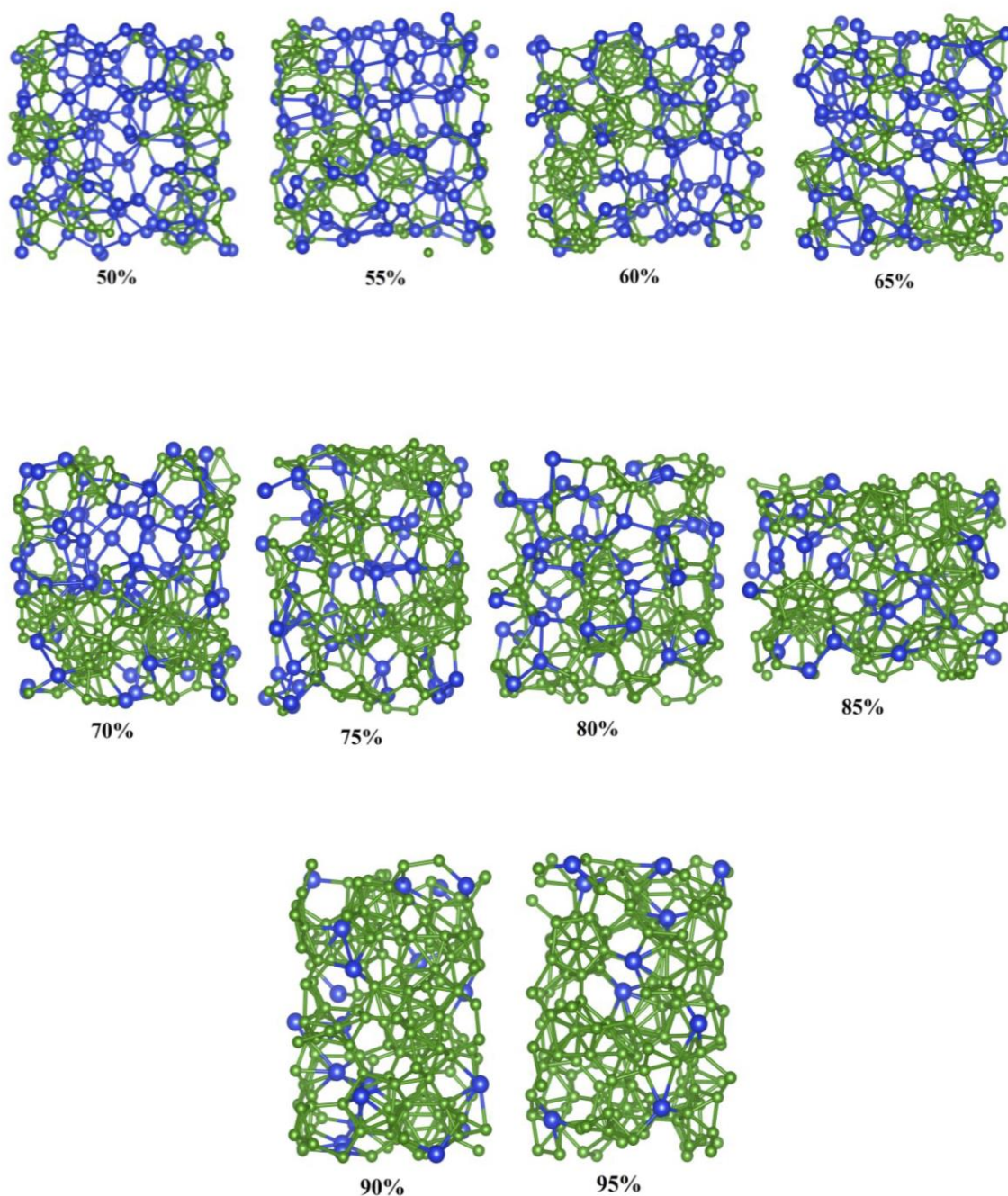
Figure 5.7 Ball-stick representation of modelled noncrystalline configurations.

By means of Voronoi analyses and visualizations, we observe the formation of the complete B_{12} and $B_{11}Si$ icosahedrons (see Fig. 5.8) and the development of B_{10}, B_{13} and B_{14} molecules in some models.
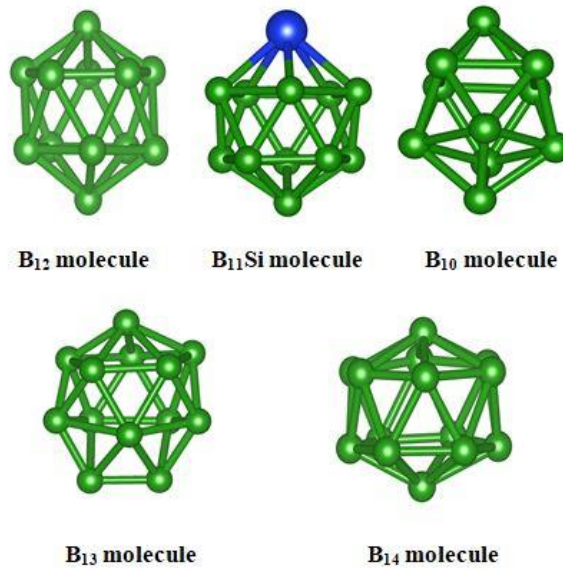
Figure 5.8 Cage-like clusters formed in the amorphous BSi systems.

5.3.2 The Electronic Properties

The amorphous and crystalline BSi materials can have important technological applications, in particular in the semiconducting technology. For this reason, determining their electronic structure is essential. Fig. 5.9 depicts the variation of HOMO-LUMO band gap energy predicted using GGA+U calculations as a function of B content. The band gap does not show a clear trend but fluctuates between 0.81 and 1.12 eV, comparable with 0.5-1.0 eV reported for B:Si thin films [209].
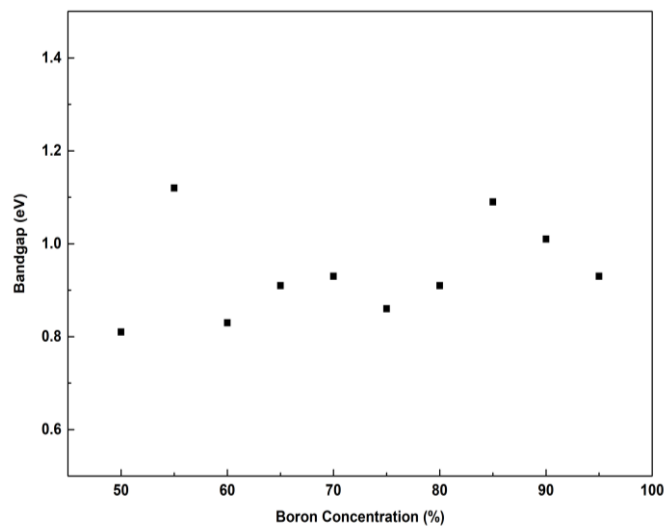
Figure 5.9 B content dependence of forbidden energy band gap based on GGA+U calculations.

5.3.3 The Mechanical Properties

For the functional applications of a material, it is necessary to identify its mechanical characteristics. For this reason, we consider the mechanical features of each amorphous configuration in details. We first probe the bulk modulus (K) that can be readily calculated by fitting the energy (E)-volume (V) correlation (Fig. 5.10) to the 3rd order BMEOS (Eq. 2.50).
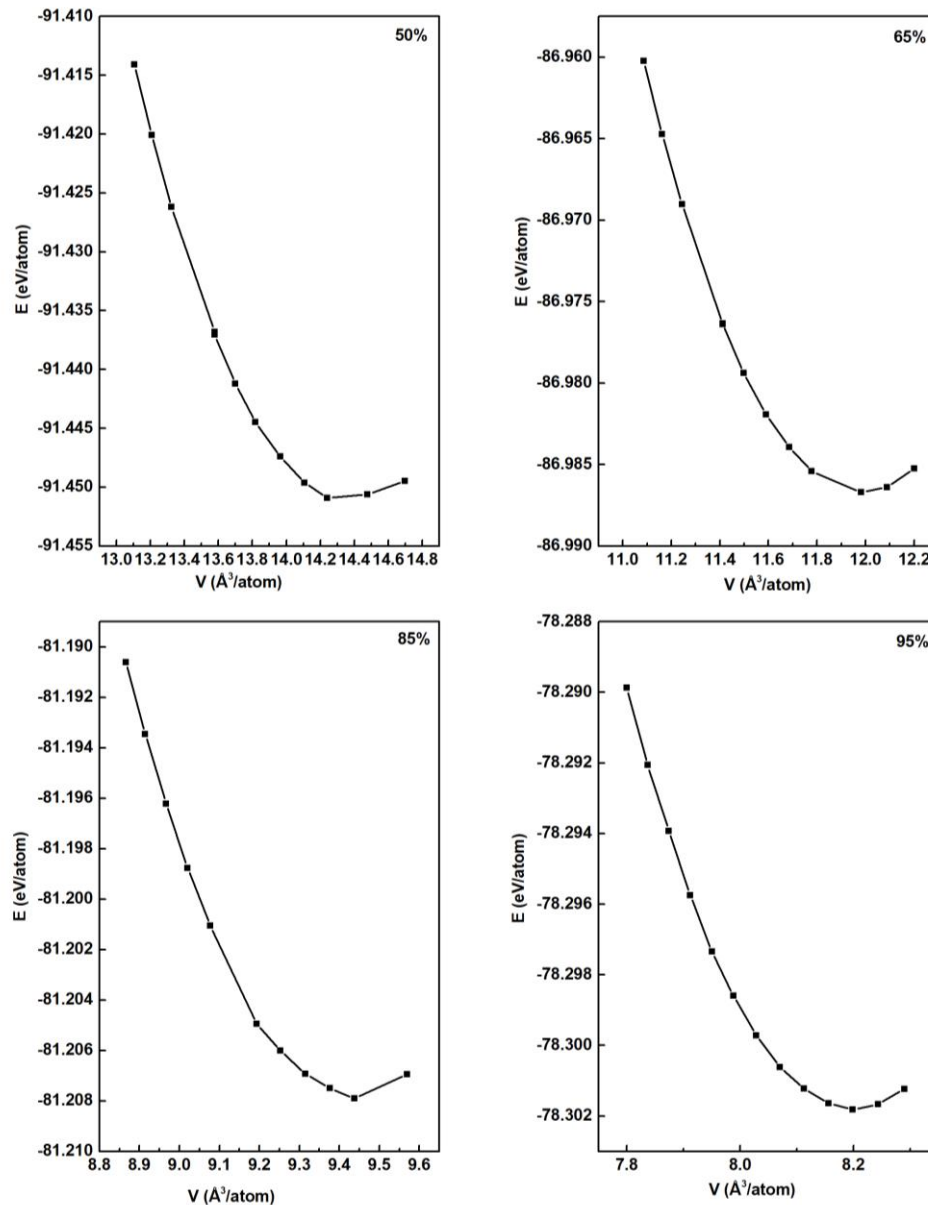
Figure 5.10 Energy-volume relation of some BSi amorphous models.

The computed K values as a function of B concentration are illustrated in Fig. 5.11 and given in Table I as well. For comparison, available data in the literature are also

provided in the same table. The K value of the amorphous materials drastically changes from ~90 GPa to ~182 GPa with increasing B content, as expected to due to the formation of more B_{12} molecules in the system. The bulk modulus of c-SiB_3 and c-SiB_4 is also computed and found to be ~159 GPa and ~161 GPa, respectively, which are approximately overlapped with the earlier theoretical results of about 121.1-183.5 GPa for c-SiB_3, c-SiB_4, c-SiB_6 and c-SiB_{36} [199]. For the amorphous form of c-SiB_3 and c-SiB_4, a slight reduction in K value (see Table I) is observed due to their disordered nature. It should be noted here that the computed bulk modulus of the amorphous materials with high B contents seems to be reasonably comparable with that of pure B crystals (α-, β-, γ- and tetragonal forms) having K≈ 200 GPa [21, 322-324].
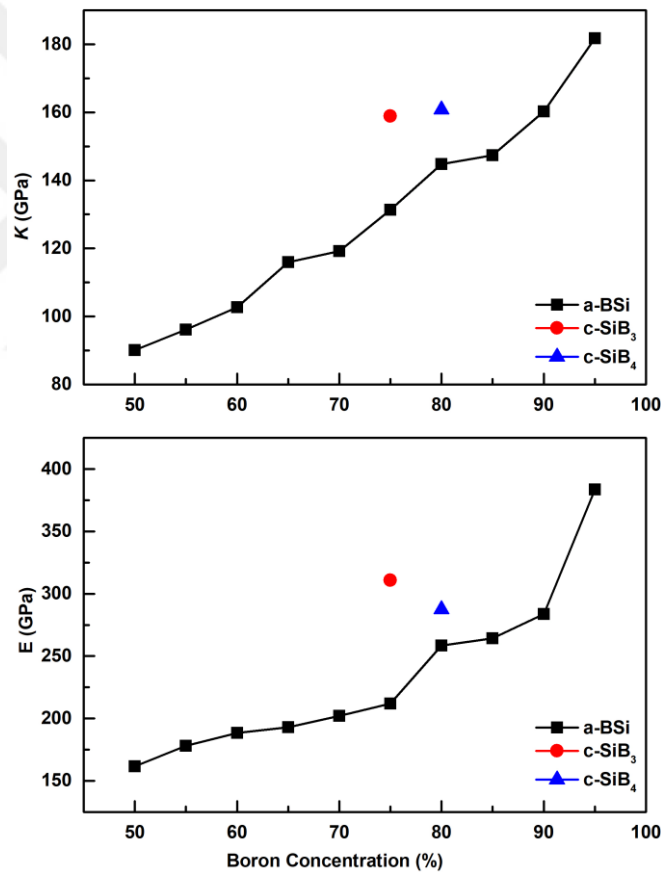
Figure 5.11 Change in bulk (K) and Young (E) moduli as a function of B concentration.

In order to predict Young modulus (E), a uniaxial stress along the principle axes of the modeled amorphous materials and the crystalline phases is applied and their atomic coordinates and simulation cell vectors are relaxed. Then the stress-strain relation is

studied and from the slope of the relation. Young modulus (E) is obtained from Eq. (2.53) and depicted in Fig. 5.11. Young modulus increases from ~162 to 384 GPa with increasing B content, indicating that the materials become less elastic at high B contents. Young modulus of c-SiB$_3$ and c-SiB$_4$ is calculated as ~311 GPa and ~288 GPa, respectively. The estimated values are, as seen in Table I, parallel to the results of ~150-359 GPa in c-SiB$_3$, c-SiB$_6$ and c-SiB$_{36}$ [199].

Table 5.1 Bulk (K), Young (E) and shear (μ) moduli, Poisson ratios (ν), Pugh's ratio (*n*) and Vicker's hardness (H). K, E, μ and H are in the unit of GPa.

Phase	*K*	*E*	*ν*	*μ*	*n*	*References*
a-B$_{50}$Si$_{50}$	90.1	161.6	0.2	67.3	1.339	This study
a-B$_{55}$Si$_{45}$	96.1	178.1	0.191	74.8	1.285	This study
a-B$_{60}$Si$_{40}$	102.7	188.5	0.194	78.9	1.301	This study
a-B$_{65}$Si$_{35}$	115.9	192.9	0.223	78.9	1.469	This study
a-B$_{70}$Si$_{30}$	119.2	201.9	0.217	82.9	1.436	This study
a-B$_{75}$Si$_{25}$	131.4	211.8	0.231	86.0	1.528	This study
a-B$_{80}$Si$_{20}$	144.8	258.5	0.203	107.5	1.348	This study
a-B$_{85}$Si$_{15}$	147.4	264.3	0.201	110	1.339	This study
a-B$_{90}$Si$_{10}$	160.3	283.7	0.205	117.7	1.362	This study
a-B$_{95}$Si$_5$	181.8	383.6	0.148	167	1.089	This study
c-B$_{75}$Si$_{25}$	159	310.8	0.17	132.4	1.2	This study
c-B$_{80}$Si$_{20}$	161	288	0.214	119.6		This study
c-SiB$_3$	171.2	310.8	0.20	129.8	1.32	[199]
c-SiB$_4$		280				[382]
	172.1	150	0.35	55.4	3.11	[199]
c-SiB$_6$	179.2	358.8	0.17	153.8	1.17	[199]
	81.24					[400]
c-SiB$_6$-81	121.1	163.8	0.27	64.3	1.88	[199]
c-SiB$_{36}$	183.5	358.1	0.17	152.4	1.20	[199]
c-Boron	185-231.5					[21, 322-324]
		445-550	0.11-0.13	197-236		[323-325]

Knowing E and K allow us to calculate Poisson ratio (ν) using Eq. (2.55). As seen from Fig. 5.12, ν shows a fluctuant tendency (~0.19-0.23) up to 90 % at B and then it drastically decreases to ~0.15 at 95% B ratio. ν is estimated to be 0.17 for c-SiB$_3$ and 0.2 for c-SiB$_4$. From Table 5.1, it can be seen that the estimated values of ν for the crystalline and amorphous structures are coherent with 0.17-0.35 in c-SiB$_3$, c-SiB$_6$ and c-SiB$_{36}$ [199, 400]. Additionally, the value (0.148) is quite close to 0.11-0.13 in B crystals [323-325].
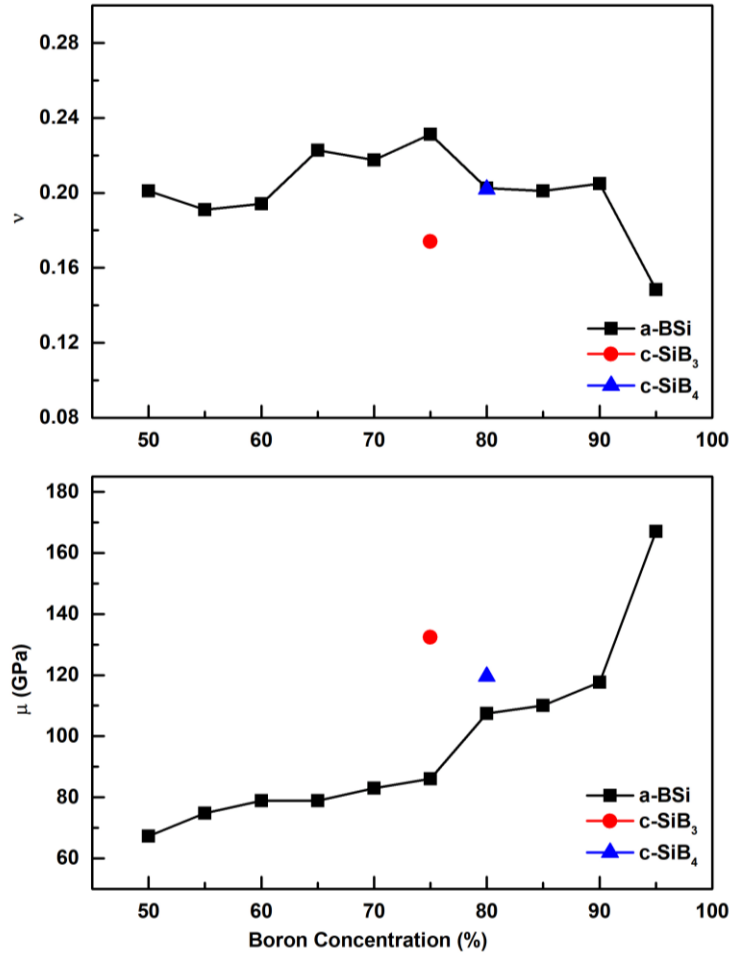
Figure 5.12 Variation in Poisson's ration (ν) and shear modulus (μ) vs B content.

Since we acquire E and ν values, shear modulus (μ) can be easily computed with Eq. (2.57). Shear modulus of the simulated amorphous models possesses a steady increase from ~67 GPa to 167 GPa (see Fig. 5.12) with increasing B content. We estimate μ to be ~132 GPa for c-SiB$_3$, ~120 GPa for c-SiB$_4$. The calculated values are again close to ~55-154 GPa reported for B-rich BSi crystals [322]. On the other hand, the maximum value is noticeably less than ~197-236 GPa in the crystalline B phases [323, 324, 400]. The smaller result in the amorphous forms signifies that they have more a flexible structure than the crystalline forms.

In addition to these mechanical parameters, we finally evaluate the Vicker's hardness (H) using the three different empirical equations (Eq. 2.58-2.60) [255-257]. The results obtained from these equations are given in the Fig. 5.13. The hardness shows an undulate trend but a sudden jump at 95% B concentration. The computed *H* value for our B-rich disordered configurations is estimated to be in the range 10 to 33 GPa.

Additionally, the H value for c-SiB$_3$ and c-SiB$_4$ is computed to be 20-25 GPa and 18.1-20.2 GPa, respectively. Our estimations are in an excellent agreement with the previous experimental and theoretical results of 23-27 GPa estimated for the crystals (23-27 GPa) [382, 384]. Yet the maximum hardness predicted is noticeably less than 42-50 GPa reported for B crystals [16, 20].
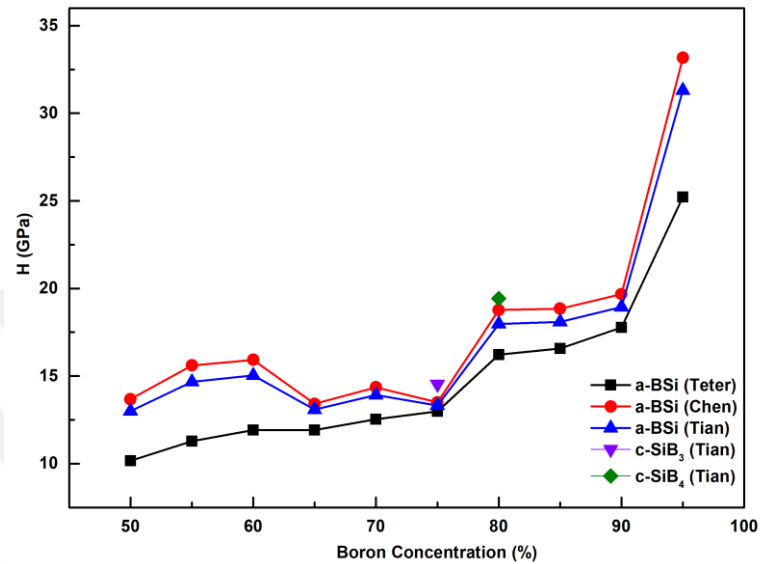
Figure 5.13 B concentration dependence of Vickers hardness (H).

The brittle-ductile characteristic of any solid can be classified by means of either the Pugh's ratio (n) or Poisson's ratio [260, 261]. The critical value is equal to 1.75 for n. If n is bigger than 1.75, a solid shows the ductile character. Otherwise, $n<1.75$, the solid exhibits the brittle character. In addition, if the Poisson ratio is bigger than 0.26, a solid is ductile, if not, it shows brittle feature [260, 261]. n and ν values for our B-rich amorphous BSi systems are estimated to be in the range of 1.09-1.53 and 0.191-0.231, respectively, so one can clearly say that our configurations display a brittle character as it should be in ceramic materials.

5.4 Discussion

The B$_{12}$ molecule is the main building unit of B phases and B-rich materials and are observed in all compositions including B$_{50}$Si$_{50}$ in the present work. This might not be surprising because an experimental investigation reported that a low B content about 17% is enough for the development of B$_{12}$ icosahedra in BSi materials. The present

investigation reveals an outstanding feature of B-rich amorphous BSi solids, namely the formation of ideal $B_{11}Si$ icosahedron(s) in addition to B_{12} molecules in all amorphous structures. The ideal $B_{11}Si$ icosahedron does not form in any crystalline BSi phases. The development of ideal $B_{11}Si$ molecules or pentagonal pyramid-like motifs around Si atoms leads to higher mean coordination for Si atoms and a different local arrangement around them in the amorphous configurations compared to the crystals. It should be noted that $B_{11}C$ molecules (in which C atom is sixfold coordinated) do exist in the amorphous and crystalline forms of B_4C and hence the observation of high coordinated Si in the amorphous models is unsurprising.

It appears that B atoms have a strong affinity to form pentagonal pyramid-like topologies. This results in B-rich and Si-rich regions in all amorphous models except $B_{95}Si_5$, namely, the occurrence of B:Si phase separations in these amorphous configurations.

We observe the formation of some uncommon cage-like clusters such as B_{10}, B_{13} and B_{14} in some amorphous network. The B_{10} molecule was perceived in an amorphous BAs model. The others, on the other hand, have not been reported in any B based materials. Since we did not observe the formation of these unusual molecules in our previous simulations on pure amorphous B, we think that the phase separation (B:Si) provides a driving force their formation in amorphous BSi materials. Yet further theoretical studies on a large system, probably using a machine learning potential, are necessary to clarify this matter.

With increasing B content, as a result of the formation of more pentagonal pyramids and hence B_{12} molecules, the mechanical properties of BSi systems are drastically improved and at high B contents, some mechanical properties of amorphous BSi become comparable with those of B crystals. Consequently, the modelled amorphous materials can be categorized as hard materials because their Vicker's hardness is greater than 10 GPa (any material having the hardness of 10 GPa can be classified as a hard solid).

Lastly, when the electronic behavior is considered, all amorphous networks show a semiconducting behavior. Subsequently, they can serve as thermoelectric materials and can substitute the crystalline materials that cannot be easily synthesized. Easy production of amorphous materials might provide some advantages over crystalline phases fabricated at certain stoichiometries.

5.5 Conclusions

Amorphous $B_n Si_{1-n}$, $(0.5 \leq n \leq 95)$ configurations are generated by using AIMD simulations and their local structure, electronic properties and mechanical features have been investigated and compared with the available data in the literature. The changing B/Si content has almost no effect on the mean bond lengths but the average coordination number changes from 5.5 to 6.2 for B atoms and from 4.3 to 5.6 for Si atoms. The strong tendency of B atoms to arrange themselves in pentagonal pyramid-like configurations yields Si:B phase separations in the amorphous networks. Most pentagonal pyramid-like motifs lead to the formation of B_{12} and $B_{11}Si$ molecules. The $B_{11}Si$ icosahedrons do not exist in any SiB crystalline phases. The formation of $B_{11}Si$ icosahedrons yields a different local structure in amorphous structures than the crsytals. When the electronic behavior has been discussed, all amorphous compositions can be classified as semiconducting materials having a band gap energy of 0.81-1.12 eV. The bulk modulus of B-rich amorphous silicon borides is calculated to be in the range ~90 GPa to 182 GPa. The Vickers hardness increases with increasing B content and reaches values of 25-33 GPa at 95% B concentration. Due to their electrical and mechanical properties, these materials can be potential candidates for refractory materials and can substitute the crystalline phases that cannot easily be fabricated.

Chapter 6

Amorphous Silicon Triboride: A First Principles Study

The work presented in this chapter is published in A. Ö. Çetin Karacaoğlan, M. Durandurdu, Journal of Non-Crystalline Solids 2020, 536, 119995.

6.1 Introduction

Boron (B), a III-A group element, is a trivalent metalloid showing both metal and non-metal characteristics and has drawn considerable attention due to its unique/complex structures and properties [5]. B can have a rich variety of compounds [5] and form a strong covalent bond with other elements because of sp2 hybridization and its small radius [401, 402]. B compounds such as BN, BC, BO, BMg, and BSi are extensively used as engineering materials for various purposes more than a century because of their interesting and unusual properties [403-405]. Among these compounds, silicon borides or boron silicides (BSi) have drawn considerable attention on superconductivity in the thermoelectric devices [200, 403, 404, 406]. Moissan and Stock performed the first original study on BSi systems in 1900 [187] and were able to prepare two different crystalline borides, silicon triboride (c-SiB3) and silicon hexaboride (c-SiB6), by fusion of the elements. In 1955, Samsonov and Latysheva were able to fabricate the c-SiB_3 single phase by means of the hot pressing at temperatures of 1873–2073 K [376]. According to Samsonov and Latysheva's study [376], c-SiB_3 was available if the samples contained between 21 mol% and 27 mol% of Si. The invariant reaction for the SiB_3 crystal was also reported in the literature [201, 407]. In a different study, β-SiB_3 was proposed as the alternative orthorhombic phase of SiB_3 [178]. Noncrystalline SiB materials having a wide range of B and Si concentrations were synthesized using different experimental protocols [205-210]. Amorphous B_xSi_{1-x} $(0 \leq x \leq 1)$ systems were produced by radio frequency (rf) plasma decomposition of silane-diborane gas mixtures [205]. Si-rich amorphous SiB

binary compounds having B content ranging from 0 to 40% at various temperatures between 25–700 °C [206] and from 1% to 50% at temperatures of 400-520 °C were fabricated by low pressure chemical vapor deposition (LPCVD) method [207]. Besides, amorphous BSi films with Si/B atomic ratios of 1/9, 2/8, 3/7, 4/6 and 5/5 were manufactured by pulsed laser deposition process [209]. B-rich SiB materials having B concentration in the range of 90.0-97.0% were synthesized by arc-melting and spark plasma sintering protocol [208]. As expected, the optical band gap of B-rich amorphous SiB materials increases with decreasing B content [209]. It appears that when B concentration is higher, the oxidation of Si and B components in the amorphous SiB alloys is faster in compared to both Si and B crystals [210]. Boron rich amorphous SiB systems have suitable properties such as high hardness and high-temperature stability and hence are expected to have applications as high-temperature thermoelectric materials [203, 205]. However, a clear atomistic level description of these alloys is not available in the literature. In order to better understand these materials, perhaps as a first step, the amorphous form of the SiB crystals should be modelled and compared with its crystalline counterpart whose the structure and properties are known. To our knowledge, the amorphous state of SiB_3 (a-SiB_3) has not been investigated so far. The aim of the present work is to determine the microstructure and the mechanical and electrical features of a-SiB_3, to associate them with those of the crystal and to make some contributions to the literature. In particular, we would like reveal whether the amorphous state is as useful as the crystal and offers some practical applications in technology.

6.2 Computational method

The molecular dynamics (MD) calculations were achieved by the SIESTA *ab initio* code [310] that is based on the density functional theory (DFT). The pseudopotentials were established by the Troullier–Martins scheme [250]. The double zeta basis set was chosen for the valence electrons and the Γ point was used for the Brillion zone integration. The exchange correlation energy was due to the PBE-GGA method [231]. The isothermal-isobaric (NPT) ensemble was constituted to perform the MD simulations. Each MD time was set to 1.0 fs. The temperature applied was controlled by the velocity scaling and the volume of the supercell at ambient pressure was adjusted by the Parrinello–Rahman technique [240] having a fictitious mass of 20.0 $Ry.fs^2$. Our

simulation box had randomly distributed 200 atoms (150 B atoms and 50 Si atoms) and its initial density was 2.0219 g/cm^3. The supercell was subjected to a temperature of 2000 K for around 40 ps. The density of the system increased to a value of 2.2198 g/cm^3 in less than 5.0 ps and it fluctuated slightly between 2.1717 and 2.2198 g/cm^3 in the rest of the simulation time at 2000 K. The melt was then slowly quenched to 300 K by using a cooling rate of 2.0×1012K/s. At room temperature, it was additionally equilibrated for 2.0 ps and the resulting structure was optimized using a conjugate gradient method. For the optimization, the force criterion was set to be 0.02 eV/Å. The density of the relaxed amorphous phase was 2.2941 g/cm^3, which is marginally less than 2.4341 g/cm^3 predicted for the crystal, as expected because most amorphous states have a lower density than their crystalline counterparts. Our value for the crystal is slightly less than the experimental prediction of 2.47 g/cm^3 [398] and the theoretical value of 2.45 g/cm^3 [408] based on a plane wave calculation.

6.3 Results

6.3.1 Atomic structure

The microstructure of the ordered and disordered SiB$_3$ phases illustrated in Fig. 6.1 is firstly compared by the partial pair distribution function (PPDF) analysis given in Fig. 6.2. The first neighbor B-B separation of the amorphous model is located at 1.76 Å that is fairly close to 1.77 Å in the crystal. Additionally, this value is comparable with experimental result of 1.78 Å reported for amorphous B [314]. The second peak of the B-B correlation is positioned at 2.97 Å, which is again objectively parallel to 2.95 Å in the crystal and 3.02 Å in amorphous B [314]. Consequently, based on these results, we can propose that the distribution of B-atoms in the noncrystalline state is comparable with that of B-atoms in the crystal and even in amorphous B.
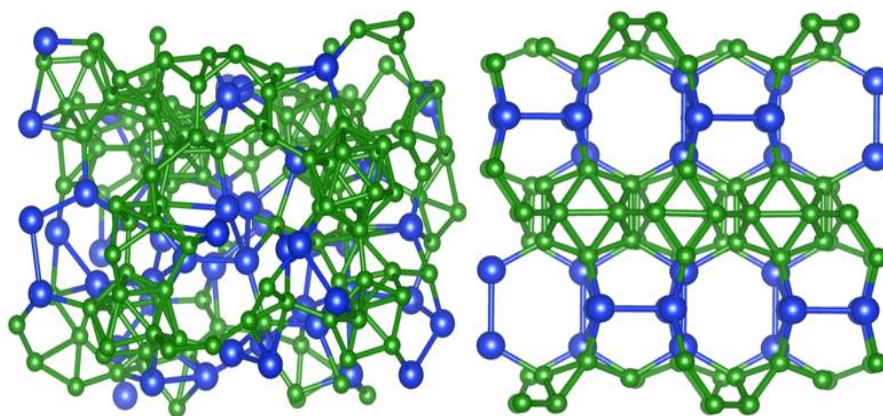
Figure 6.1 Amorphous and crystalline SiB₃ structure, respectively.

The first two peaks of B-Si pair of a-SiB$_3$ are at 2.04 Å and 3.34 Å, respectively. They are again analogous to 1.99 Å and 3.34 Å in the crystalline phase. Our B-Si distance is also akin to the experimental values of 1.89–1.94 Å reported for the Si$_3$B crystal [409]. The Si-Si bond distance is estimated to be 2.38 Å for a-SiB$_3$ and 2.57 Å for c-SiB$_3$. So, an obvious decrease in the Si-Si bond separation is perceived by amorphization, which might be the indication of the formation of different type of Si motifs in both phases.
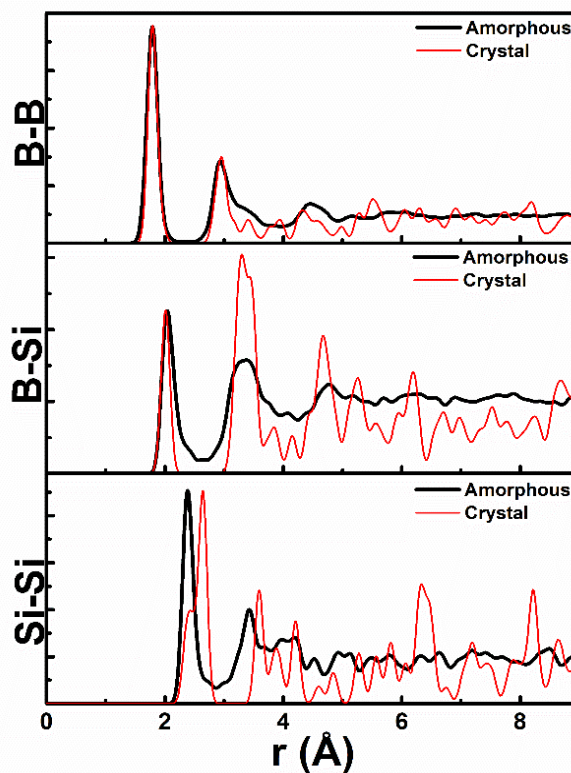
Figure 6.2 Partial pair correlation functions (PPDFs) of c-SiB₃ and a-SiB₃, which are plotted using Gaussian smoothing factor of 0.05. Also, to clearly compare both structures, the intensity of PPDFs of the crystal is scaled.

In order to determine the type of configurations formed in the short range order of both phases, we estimate their partial coordination numbers using the first minimum (B-B = 2.35 Å, B-Si = 2.62 Å, Si-Si = 2.88 Å for the amorphous and B-B = 2.37 Å, B-Si = 2.62 Å, Si-Si = 2.78 Å for the crystal) of the PPDFs. The mean coordination number of B and Si atoms in the amorphous state is found as 5.8 and 4.6, respectively, which are very close to 6.0 (B atoms) and 5.0 (Si atoms) in the crystal. As shown in the Fig. 6.3, the most common unit for B atoms is sixfold-coordination with a frequency of about 61%. The fraction of fivefold- and sevenfold-coordination for B atoms is 20.7% and 12.7%, correspondingly. On the other hand, the most privileged motif for Si atoms is fourfold-coordination having a frequency of 52%. Si atoms present a nonnegligible amount of fivefold-(24%) and sixfold-(20%) coordination as well. Accordingly, one can see here that Si atoms have a tendency to form fourfold instead of fivefold coordination. The coordination analysis provides useful information at the atomistic level but does not offer a depth understanding of the local structure of the amorphous network. Such an understanding can be attainable by the chemical environmental analysis. Table 6.1 presents the chemical distribution of each species. According to the Table 6.1, $B-B_6$ (27.33%) and $B-B_5Si$ (26.67%) type of clusters are the key units around B atoms in a-SiB_3. Indeed, they are the main building motifs of the crystal having frequencies of 33.33% and 66.67%, respectively. In addition to them, a visible number of $B-B_7$, $B-B_3Si_2$ and $B-B_4Si$ motifs is perceived in the amorphous configuration. Thus, it can be concluded here that the formation of $B-B_5Si$ is less favorable in the amorphous state than in the crystal and approximately 50% of B atoms in the noncrystalline network have the arrangements, analogous to those of the crystal. For Si atoms, $Si-BSi_3$ (24%) and $Si-B_2Si_2$ (16%) units are found as the most dominated ones in the a-SiB_3 model. Besides, $Si-B_3Si_2$, $Si-B_3Si_3$, $Si-B_4Si$ and $Si-B_4Si_2$ type of structures having a low fraction are also presented in the disordered structure. On the other hand, c-SiB_3 consists of only $Si-B_2Si_3$ type of motif and such a motif does indeed barely exist in the amorphous network, implying that the chemical environment of Si atoms in a-SiB_3 does not coincide with that of c-SiB_3. On the basis of these findings, one can conclude here that although the average coordination of a-SiB_3 is comparable with that of the crystal, its local structure marginally resembles to that of the crystal.
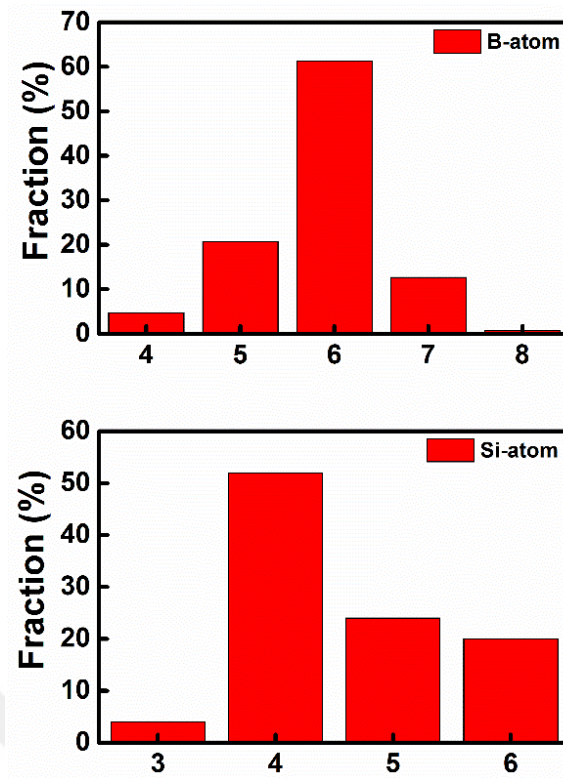
Figure 6.3 Coordination distribution in a-SiB$_3$.

Table 6.1 Chemical distribution in a-SiB$_3$. CN represents the total coordination number.

C.N.	B atom		C.N.	Si atom	
3	B$_2$Si	0.67%	3	B$_2$Si	2.00%
4	B$_3$Si	2.00%	4	BSi$_3$	24.00%
4	B$_4$	1.33%	4	B$_2$Si$_2$	16.00%
4	Si$_4$	0.67%	4	B$_3$Si	2.00%
5	BSi$_4$	1.33%	4	B$_4$	4.00%
5	B$_2$Si$_3$	1.33%	5	BSi$_4$	2.00%
5	B$_3$Si$_2$	8.67%	5	B$_2$Si$_3$	4.00%
5	B$_4$Si	8.00%	5	B$_3$Si$_2$	10.00%
5	B$_5$	2.00%	5	B$_4$Si	8.00%
6	B$_3$Si$_3$	2.00%	5	B$_5$	2.00%
6	B$_4$Si$_2$	5.33%	5	Si$_5$	2.00%
6	B$_5$Si	26.67%	6	B$_3$Si$_3$	8.00%
6	B$_6$	27.33%	6	B$_4$Si$_2$	6.00%
7	B$_6$Si	2.00%	6	B$_5$Si	2.00%
7	B$_7$	10.00%	6	B$_6$	2.00%
8	B$_7$Si	0.67%	7	B$_3$Si$_4$	2.00%
			7	B$_5$Si$_2$	4.00%

In order to reveal similarities/distinctions between two phases in details, we perform the Voronoi polyhedral investigation. The cutoff radii used in the coordination and chemical distribution analyses are adopted for this investigation as well. A Voronoi

polyhedron, a three dimensional solid figure having many plane faces, is symbolized by indices $\langle l3, l4, l5, l6, \ldots\rangle$ where li represents the number of i-edge faces of a polyhedron and Σ li is its total coordination number. In the crystal, B atoms form just one type of cluster represented by $\langle 2,2,2,0\rangle$ index, which is the pentagonal pyramid-like unit. In the amorphous state, B atoms structure largely in the $\langle 2,2,2,0\rangle$ type of configuration with a fraction of 59% as well. Additionally, an incomplete pentagonal pyramid-like unit having $\langle 2,3,0,0\rangle$ (19%) index appear in the amorphous phase. Consequently, most B-atoms form a polyhedron similar to one formed in the crystal. On the other hand, Si atoms create only $\langle 2,3,0,0\rangle$ type polyhedron in the crystal while they construct the $\langle 2,2,2,0\rangle$ (20%), $\langle 2,3,0,0\rangle$ (22%) and $\langle 4,0,0,0\rangle$ (46%) kind of arrangements in the amorphous network. So, tetrahedral configuration appears to be the dominated one for Si atoms. Perhaps, the most interesting finding is the presence of a nonnegligible amount the pentagonal pyramid-like units $\langle 2,2,2,0\rangle$ around Si-atoms in the amorphous state. A close analysis reveals that the pentagonal pyramid-like configurations of B and Si atoms lead to the formation of the B_{12}, $B_{11}Si$ and B_{10} molecules (see Fig. 6.4) in the noncrystalline state. It should be noted that last two molecules are not presented in the crystal.

B_{12} molecule   **$B_{11}Si$ molecule**   **B_{10} molecule**
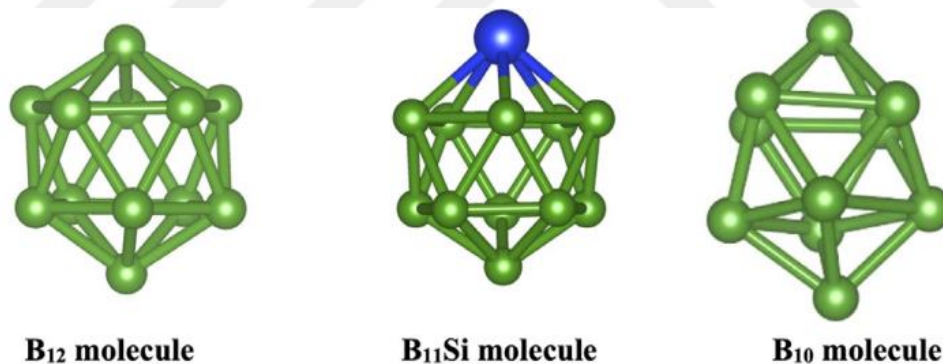
Figure 6.4 B_{12}, $B_{11}Si$ and B_{10} molecules formed in a-SiB_3.

Bond angle distribution examination given in Fig. 6.5 might provide extra information about the model at the atomistic level. The analysis exposes apparent differences between two forms of SiB_3 considering their atomic structure. The most noticeable difference is the presence of a broad Si-B-Si distribution in a-SiB_3 contrary to the crystalline state. The B-B-B distribution has two principal peaks at around 60° and 107° for both amorphous and crystal structures. These angles are due to the intraicosahedral bonds of the pentagonal pyramids (B_{12} icosahedrons). The B-Si-B angles for the amorphous model produce a broad distribution changing from 40° to 150°, quite

different than sole angle of around 117° in the crystal. It should be noted that this distribution is someway similar to that of the B-B-B angles since some Si atoms have a trend to create the pentagonal pyramid-like structures. The amorphous system has a wide Si-Si-Si angle distribution ranging from 50° to 150° while the crystalline phase has three peaks at 60°, 90° and 120°. All these findings support only partial similarities, particularly around B atoms, in both phases of SiB$_3$.
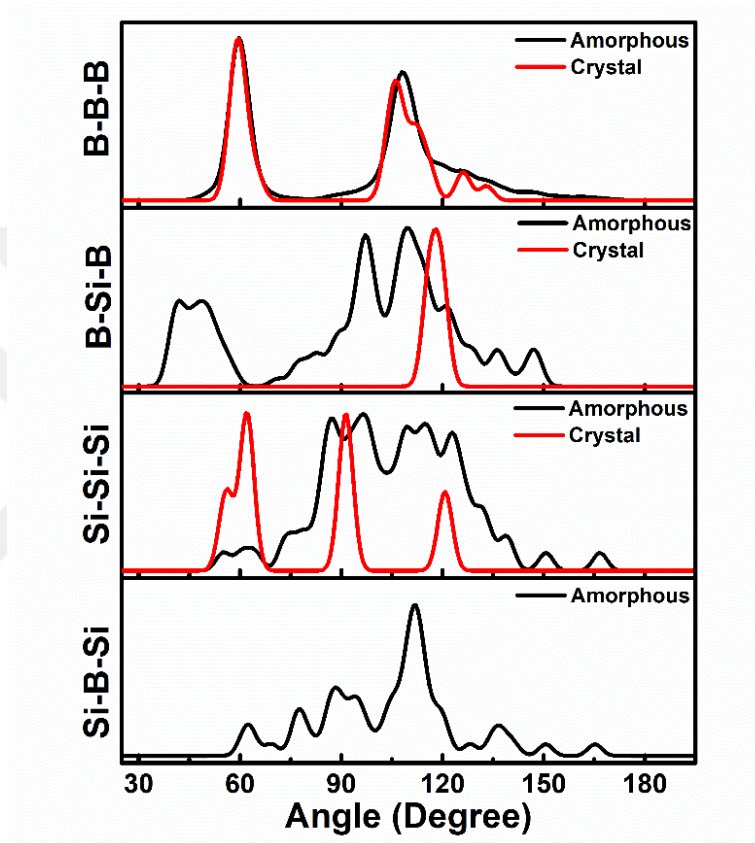
Figure 6.5 Bond angle distribution of a-SiB$_3$ and c-SiB$_3$.

6.3.2 Electrical properties

c-SiB$_3$ is a semiconducting material having a GGA band gap of about 1.4 eV [408]. In order to see how amorphization affects on the electronic structure of SiB$_3$ and to uncover if the amorphous form can serve as an electronic material, we study its electron density of states (EDOS) and partial electron density of states (PDOS) and compare them with those of the crystal. The EDOS of the amorphous and crystalline phases is depicted in Fig. 6.6. According to the EDOS analysis, both structures exhibit a semiconducting

behavior. The HOMO-LUMO band gap energy of the amorphous and crystalline states is found to be 0.2 eV and 1.86 eV (that is slightly higher than the GGA result of 1.4 eV [408]), correspondingly. The gap value predicted for amorphous phase appears to be reasonable considering the experimental values of 0.5–0.75 eV reported for B-rich amorphous BSi materials [209] in spite of underestimation of the band gap in DFT-GGA simulations. PDOS given in Fig. 6.6 can offer more information regarding the electronic structure. Fig. 6.6 reveals that the most dominant states for both conduction and valence bands are B-p electrons, similar to what has been reported in the earlier study [199], while the other states have a minimal effect to the bands near the Fermi level.
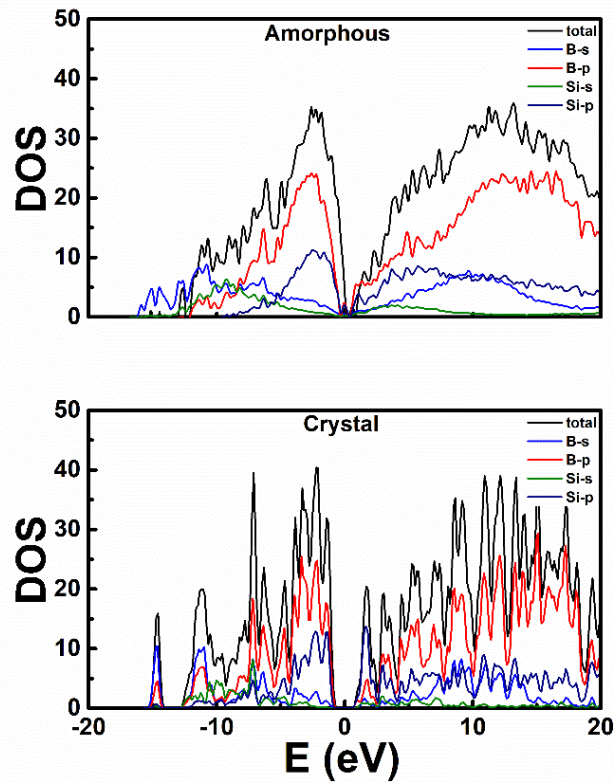
Figure 6.6 Total and partial electron density of states.

6.3.3 Mechanical properties

The practical applications of a material commonly require the knowledge on its mechanical properties. In this section we study the mechanical properties of both structures of SiB_3 and compare them in details. Firstly, we focus on the bulk modulus (K) which can be easily estimated by fitting the energy (E)-volume (V) relation of the amorphous and crystalline phases (Fig. 6.7) to the 3rd order BMEOS (Eq. 2.50). The K

value is found to be ~131 GPa for the amorphous network and ~159 GPa for the crystal. Consequently, a slight decrease in bulk modulus is experienced in SiB$_3$ by amorphization, which is anticipated because of the disordered nature of a-SiB$_3$. Our K value is found to be comparable with 171.2 GPa estimated for c-SiB$_3$ [199].
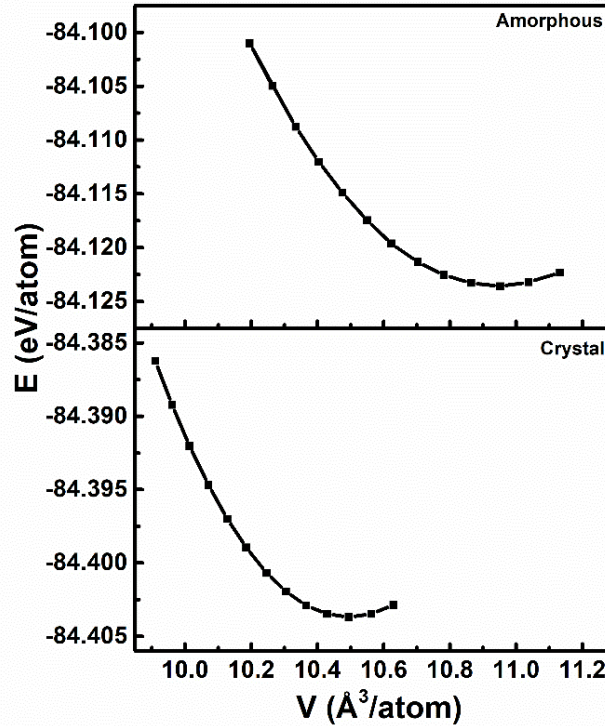
Figure 6.7 Energy as a function of volume

In order to estimate Young's modulus (E), defined as the resistance of a material to elastic deformation under loading, a uniaxial stress is applied along the principle axes (x, y and z) of the SiB$_3$ phases while the other stress components are set to be zero. Both the simulation cell parameters and the atomic coordinates are permitted to relax. From the stress (σ) – strain (ε) relation (Eq. (2.53)), the average E is calculated as 310.8 GPa for the crystal and 211.8 GPa for the amorphous network. The Young modulus of the amorphous phase is noticeably smaller than the crystal meaning that the amorphous form is more elastic than the crystal. We should point out here that our value for c-SiB$_3$ precisely overlaps with the earlier theoretical prediction [199].

Using the equation (2.55), the Poisson ratio is projected to be as 0.23 for the amorphous phase and 0.17 for the crystal, close to the earlier estimation of 0.2 [199].

We calculate shear modulus (μ) (Eq. (2.57)), the modulus of rigidity, representing the resistance to plastic deformation, to be around 86 GPa for a-SiB$_3$ and 132.4 GPa for the crystal, comparable with the previous theoretical result of 129.8 GPa [199]. Note that the smaller μ value of the amorphous form indicates that it is more flexible than the crystal.

By using three different equations (Eq. 2.58-2.60) [255-257], the Vickers hardness is predicted to be 13.3-14.2 GPa for the amorphous state and 20-25 GPa for the crystal. So, one can see that amorphization leads to a substantial decrease in the Vickers hardness. From the Pugh's ratio (Eq. (2.63)), it is possible to predict the brittle or ductile behavior of a material. 1.75 is accepted as a critical value for n. If n is bigger than 1.75, the material is classified as a ductile solid. If n is smaller than 1.75, it is classified as a brittle solid. *n* is calculated as 1.53 for a-SiB$_3$ and 1.2 for c-SiB$_3$. Subsequently, both phases present a brittle character but the amorphous form will show better performance of resistance to stress cracking than the crystal since the higher Pugh's ratio means less brittleness.

6.4 Conclusions

The microstructure, electronic structure and mechanical features of an a-SiB3 network created using ab initio MD calculations are compared with those of the crystalline phase. In the amorphous state, Si and B atoms have the mean coordination numbers of 5.8 and 4.6, correspondingly, comparable with 6.0 (B atom) and 5.0 (Si atom) in the crystal. The local structure of a-SiB$_3$ is found to be partially parallel to that of the crystal. Specifically, partial structural similarities around B atoms are observed in both phases of SiB$_3$. However, such similarities are not detected around Si-atoms. The occurrence of B$_{12}$, B$_{11}$Si and B$_{10}$ molecules is observed in a-SiB$_3$ but the last two do not form in the crystal. a-SiB$_3$ presents a semiconducting behavior but its energy band gap is noticeably less than that of the crystal. The bulk modulus is projected to be 131 GPa for the amorphous configuration and 159 GPa for the crystalline state. The Vickers hardness of a-SiB$_3$ is calculated to be around 13–15 GPa, less than 20–25 GPa estimated for the crystal. So amorphization significantly influences the atomic structure, electronic properties and mechanical features of SiB$_3$. Yet, different preparation techniques such as irradiation, mechanical milling, and high pressure (some B rich materials can transform to amorphous state at high pressure) might lead to an amorphous network with a distinct local structure and of course the distinct microstructure may result in different electrical

and mechanical properties. Therefore, additionally studies using different preparation protocols are needed to better understand a-SiB$_3$.

Chapter 7

A First Principles Study of Amorphous and Crystalline Silicon Tetraboride

7.1 Introduction

In 1900s, the first inventive work on boron-silicon (BSi) systems was carried out [187] and two different crystalline borides, which are c-SiB$_3$ and c-SiB$_6$ (c represents crystal), were synthesized by technic of fusion of elements [187]. In 1955, c-SiB$_3$ was fabricated by the use of hot pressing method at a temperature ranging from 1873 to 2073 K. Different studies [380, 410, 411] also provided supporting evidence on the formation of c-SiB$_3$. However, the existence of c-SiB$_3$ was questioned in other studies [412-414] and instead the accessibility of c-SiB$_4$ compound was proposed [192, 194, 196, 383, 393, 415, 416].According to Ref. 416, c-SiB$_3$ was never detected and the material assigned as c-SiB$_3$ in some of earlier studies was indeed c-SiB$_4$. c-SiB$_4$ could be synthesized by using different techniques such as solid-state reaction from Si and B powders [376, 412], solid-vapor reactions of silicon metal with BCl$_3$ or BH$_3$ and of boron metal with SiX$_4$ (X represents any halogen) [413], vapor phase reactions in the systems [414, 417]. High purity c-SiB$_4$, was produced by the solid-phase reaction between Si and B crystalline powders at a temperature of 1250-1350 °C in argon phase and the removing excess Si from the resulting product by a purification treatment with chlorine vapours at 430 °C [383]. Recently the stability of diamond-like SiB$_4$ was investigated [400].

Amorphous BSi binary compounds with a wide range of B and Si contents as both B-rich and Si-rich were fabricated by using various experimental procedures. Some of these production processes are radio frequency (rf) plasma decomposition system of SiH$_4$-B$_2$H$_6$ gas blending [205], pulsed laser deposition method [209], the low pressure

chemical vapor deposition (LPCVD) technic [207] and arc-melting and spark plasma sintering procedures [208]. As to optical band gap of B-rich amorphous BSi materials, the band gap value was reported to increase with increasing Si concentration [209].

Although there are some studies on the crystalline phases of SiB compounds, the atomic structure of amorphous BSi compounds and some of their properties currently remain unknown. In order to make more clear comprehension and observation about these noncrystalline binary systems, it is indeed necessary to first simulate amorphous configuration of the known BSi crystalline states and then to analogize their differences/similarities in details. To the best of our knowledge, there has not been any attempt to investigate amorphous SiB_4 (a-SiB_4) up to now. The aim of this research is to reveal the atomic structure and the mechanical and electrical properties of a-SiB_4 and to compare them with those of the crystal.

7.2 Methodology

To generate an amorphous model and to study its properties, SIESTA *ab initio* code [310] within the pseudopotential approach [250] and the Perdew, Burke and Ernzerhof generalized gradient approximation (GGA) [231] was used. The double zeta (DZ) basis sets for the valence electrons and the Γ point for the Brillion zone were adopted. The NPT ensemble was chosen to carry out molecular dynamics (MD) simulations having a time step of 1.0 fs. The velocity scaling and Parrinello-Rahman [240] techniques were used to control temperature and pressure, respectively. We used three different configurations as initial structures (the B_4N melt (model 1, an amorphous B_4C configuration (model 2) and the B_2C_2N melt (model 3)) to reveal the importance of the starting structure. From these structures we created 200 atoms B_4Si configurations by replacing N and C by Si atoms. Each structure was thermally equilibrated at 2000 K for 35.0 ps. After that, these melts were analysed by the partial pair correlation functions (PPCFs) provided in Figure 7.1. As can be seen from the figure, each melt presents roughly similar PPCFs (Si-Si correlation shows a large fluctuation, probably due to a low concentration of Si atoms [418], suggesting that 35.0 ps is long enough to yield a similar final configuration at 2000 K for each starting structure. Therefore, we chose the B_4N melt and progressively quenched to 300 K in a period of about 170.0 ps. Finally, the simulation box was relaxed till the highest force was less than 0.02 eV/Å. The Vesta Program was used to visualize

the structures [312]. The coordination and the lattice parameters of the SiB$_4$ crystal (conventional standard) were obtained from Ref. 419 and a supercell having 360-atoms was contracted and relaxed with the conjugate gradient technique. The relaxed lattice parameters $a=b=6.27$ Å and $c=12.65$ Å are comparable with the experimental results of $a=b=6.33$ Å and $c=12.74$ Å [193] and plane wave calculation predictions of $a=b=6.21$ Å and $c=12.46706$ Å [419] and $a=b=6.31$ Å and $c=12.71$ Å [199].
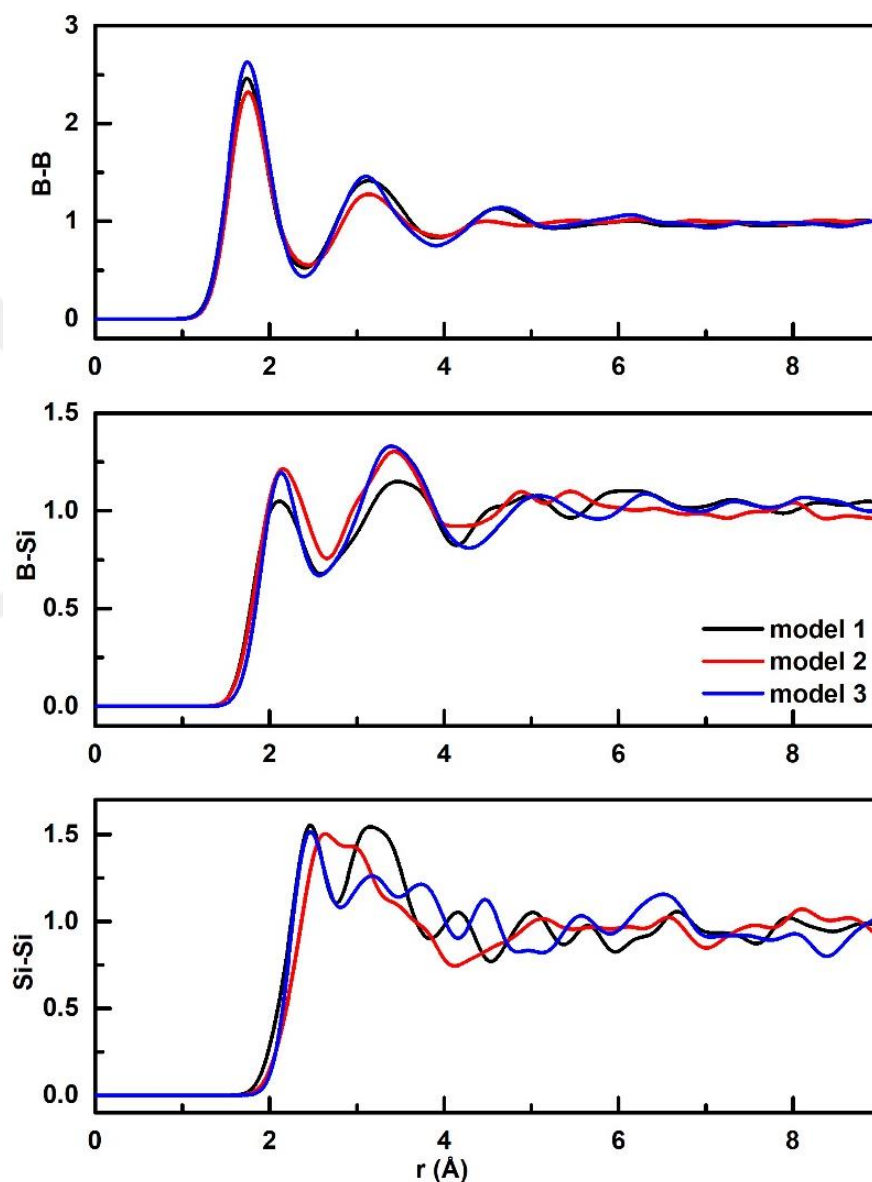
Figure 7.1 Partial pair distribution functions (PPCFs) of three different configurations at 2000 K.

7.3 Results

7.3.1 Atomic Structure

PPCFs for a-SiB$_4$ and c-SiB$_4$, which can shed considerable light on their local structure (see Fig. 7.2), are depicted in Fig. 7.3. As to Fig. 7.3, B-B distribution function reveals some parallelisms between the disordered and ordered modifications of SiB$_4$. The first and second peaks of B-B separation for the a-SiB$_4$ model are positioned at 1.77 Å and 3.01 Å, correspondingly, which are slightly less than 1.82 Å and 3.15 Å found in c-SiB$_4$. So, a slight shortening is experienced in B-B bond length in the amorphous state. It should be noted here that the B-B bond distance estimated in the present work is quite comparable with the experimental value of 1.773 Å in c-SiB$_6$ [420] and theoretical results of 1.67-1.82 Å reported for SiB binary compounds [199]. The B-Si average bond length for a-SiB$_4$ and c-SiB$_4$ is 2.06 Å and 2.01 Å, respectively, which are parallel to each other and to the previous theoretical prediction of 1.995 Å in the diamond-like SiB$_4$ structure [400]. The second peak is positioned at 3.32 Å for the amorphous network and 3.16 Å for the crystal. Note that they are quite off from each other. Also, the Si-Si mean bond length in a-SiB$_4$ is 2.37 Å, noticeably larger than 2.15 Å in the crystalline state, which is probably associated with the formation of higher coordinated Si motifs in the amorphous network (see below). The second Si-Si peak is projected to be 3.63 Å for the amorphous network and 3.61 Å for the crystal.
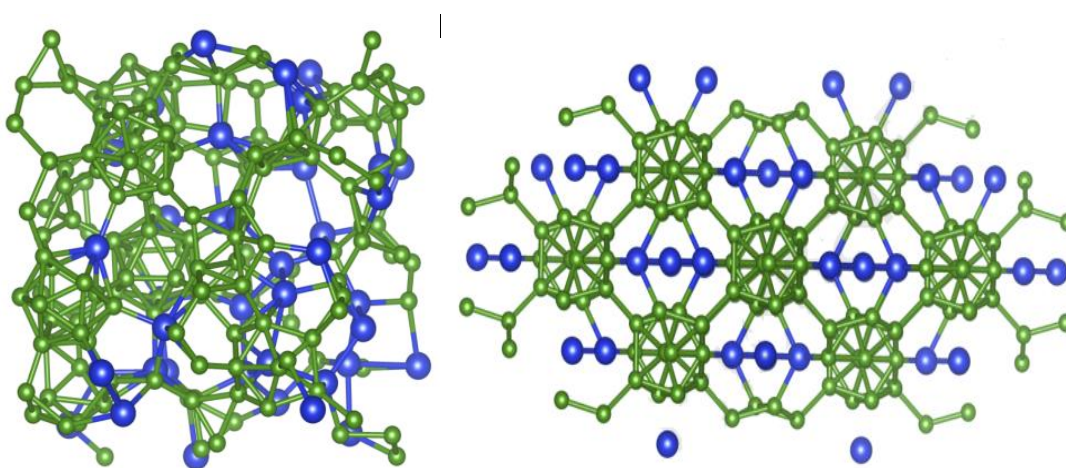
Figure 7.2 The ball-stick representation of a-SiB$_4$ and c-SiB$_4$, respectively.
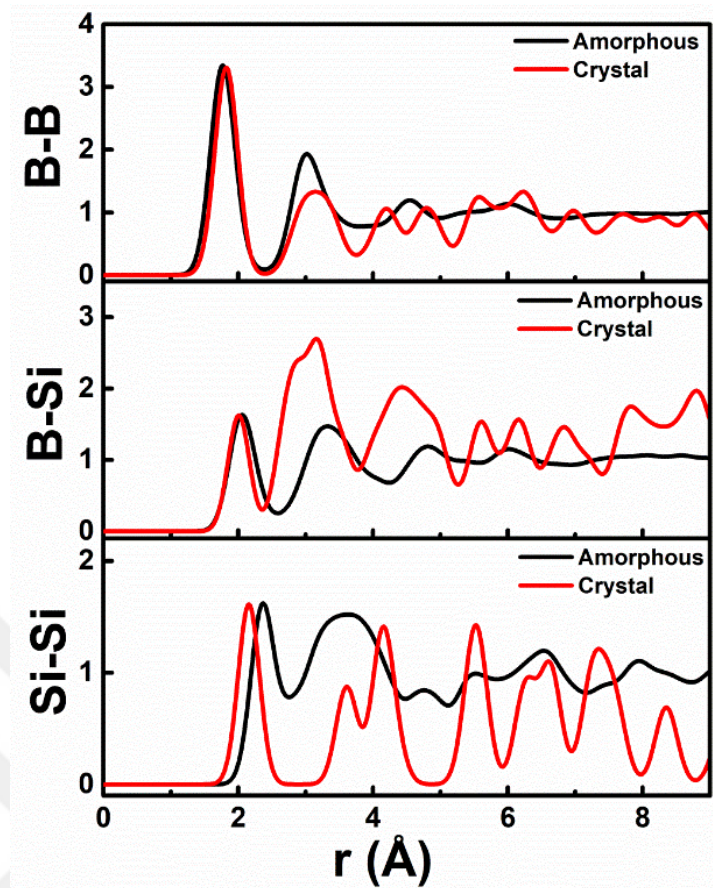
Figure 7.3 PPCFs of a-SiB₄ and c-SiB₄.

The total and mean coordination number of both phases and their chemical environmental distribution are premeditated by using the first minimum value of the PPCFs (B-B=2.38 Å, B-Si=2.58 Å, Si-Si=2.75 Å for the disordered model and B-B=2.39 Å, B-Si=2.35 Å, Si-Si=2.89 Å for the ordered structure). The partial coordination number for B atoms in the amorphous configuration is found to be 5.8 that is very parallel to 6.0 in the crystal. However, the mean coordination number of Si atoms for the amorphous and crystal is determined to be 4.7 and 3.3, respectively. So, an obvious increase in Si coordination is induced by amorphization. To have more information about the structure at the atomistic level, the coordination distribution of B and Si atoms for a-SiB₄ is depicted in Fig. 7.4. According to Fig. 7.4, the most dominated clusters for B atoms are the sixfold coordinated ones (~67%) followed by fivefold (18%) and sevenfold (10%) coordinated units. The crystal contains only sixfold coordination for B-atoms. For Si atoms, the most privilege unit is five-fold coordination (37.5%). Besides, Si atoms form threefold- (10%), fourfold- (30%) and sixfold- (22.5%) coordinated configurations. The crystal consists of only twofold (33.33%) and fourfold (66.67%) Si atoms. The chemical

environmental distributions of B atom and Si atom in a-SiB$_4$ showed in Table 7.1 provide more information about the systems. As seen from the table, the most prepotent clusters around B atoms are B-B$_6$ (29.38%) and B-B$_5$Si (28.75%) type units, representing the ideal pentagonal pyramid-like structures. Furthermore, B-B$_3$Si$_2$, B-B$_4$Si and B-B$_4$Si$_2$ type motifs with a small fraction of 7.5% exist in the noncrystalline configuration. In fact, the main building units for B atoms in c-SiB$_4$ are B-B$_6$ (50%) and B-B$_5$Si (50%) type clusters and hence the chemical environment of about 58% of B-atoms in the amorphous network is parallel to that of B-atoms in the crystal. On the other hand, the chemical environmental distribution of Si atoms in the amorphous state is more complex than that of Si atoms in c-SiB$_4$. c-SiB$_4$ has only two type clusters: Si-B$_3$Si (66.67%) and Si-Si$_2$ (33.33%) and both do not exist in our a-SiB$_4$ model. As to a-SiB$_4$, Si-B$_6$ (17.5%) and Si-B$_2$Si$_2$ (15%) type motifs are two leading ones. In addition to them, Si-B$_4$ (10%), Si-B$_4$Si (7.5%), Si-B$_3$ (10%), Si-B$_3$Si (10%) and Si-B$_2$Si (10%) type clusters are presented in the amorphous state. These analyses reveal that the local structure and chemical environment around Si atoms in two forms of SiB$_4$ are significantly different from each other.
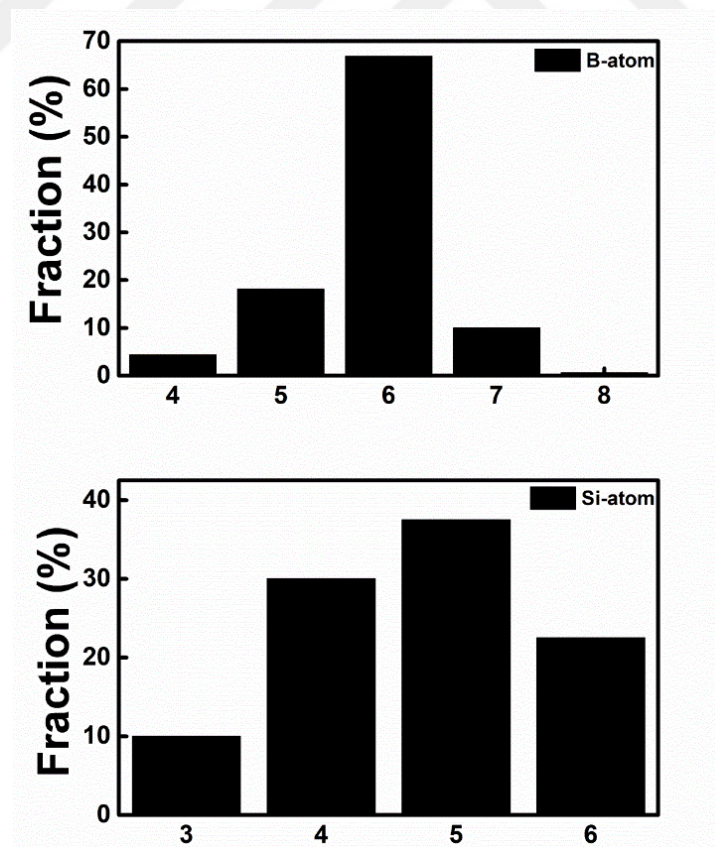
Figure 7.4 The coordination distribution in the amorphous model.

Table 7.1 Chemical distribution in the disordered SiB$_4$ structure.

B atom		Si atom	
B$_6$	29.38%	B$_6$	17.50%
B$_5$Si	28.75%	B$_2$Si$_2$	15.00%
B$_4$Si	7.50%	B$_4$	10.00%
B$_4$Si$_2$	7.50%	B$_3$	10.00%
B$_3$Si$_2$	7.50%	B$_3$Si	10.00%
B$_7$	5.62%	B$_2$Si	10.00%
B$_3$Si	2.50%	B$_4$Si	7.50%
B$_5$	2.50%	BSi$_3$	5.00%
B$_3$Si$_3$	1.88%	B$_5$	5.00%
BSi$_3$	1.88%	B$_3$Si$_2$	5.00%
B$_6$Si	1.88%	BSi$_2$	2.50%
B$_5$Si$_2$	0.62%	B$_5$Si	2.50%
B$_4$	0.62%		
B$_8$	0.62%		
B$_2$Si$_3$	0.62%		
B$_2$Si$_2$	0.62%		

In order to have more comprehensive knowledge about the types of clusters formed in these systems, we also carry out the Voronoi polyhedra analysis. A Voronoi polyhedron is denoted by the indices $<k_3, k_4, k_5, k_6, \ldots>$, where k_i and Σk_i are the numeral of i-edge faces of the polyhedron and its coordination number, correspondingly. For B atoms, only one type cluster, pentagonal pyramid, forms in the crystal and is represented by $< 2, 2, 2, 0 >$ (100%) index. On the other hand, B atoms in a-SiB$_4$ exhibit 11 dissimilar polyhedra and the most widely distributed ones are $< 2, 2, 2, 0 >$ (~66%) and $< 2, 3, 0, 0 >$ (18%) type clusters. Here the $< 2, 3, 0, 0 >$ index can be identified as incomplete pentagonal pyramid-like units. So, these observations provide additional support the similarities around B atoms in both forms of SiB$_4$. The most interesting finding is that Si atoms in the noncrystalline network have a tendency to form significant amounts of pentagonal like configurations, namely $< 2, 2, 2, 0 >$ (15%) and $< 2, 3, 0, 0 >$ (35 %). Additionally, noticeable amounts of $< 4, 0, 0, 0 >$ (25 %) and $< 0, 6, 0, 0 >$ (10%) type motifs form in a-SiB$_4$. Yet none of them exist in c-SiB$_4$.

It should be pointed out here that the ideal and incomplete pentagonal pyramid-like motifs for B and Si atoms in a-SiB$_4$ cause the formation of B$_{12}$ and B$_{11}$Si icosahedrons and B$_{x<12}$ type molecules (see Fig. 7.5). Note that B$_{11}$Si molecules do not happen in c-SiB$_4$ but B$_{11}$C icosahedrons form in amorphous/crystalline B$_4$C materials [421-423].
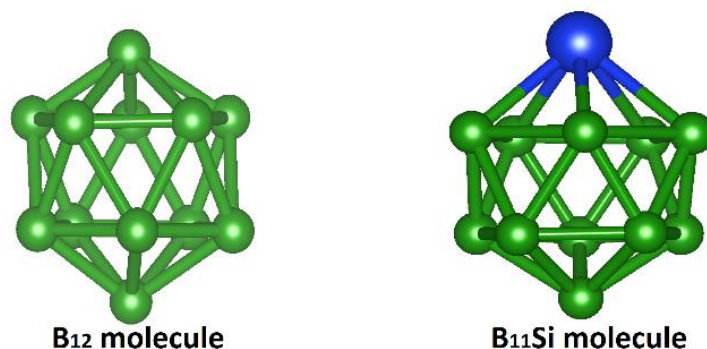
Figure 7.5 B$_{12}$ and B$_{11}$Si molecules formed in a-SiB$_4$.

In order to get extra information about the local structure of these two phases at the atomistic level, we also perform the bond angle distribution analysis given in Fig. 7.6. The distribution reveals some significant differences/similarities between the amorphous and crystalline SiB$_4$ phases. Si-B-Si angles do not form in the crystal but are presented in the amorphous state and have a wide distribution. The B-B-B angle distribution of both phases are generally in good accordance with each other, again providing firm evidence on resemblances around B atoms in two forms of SiB$_4$. When the B-Si-B distribution is considered, both structures show a different distribution such that c-SiB$_4$ has only one peak at 116° while a-SiB$_4$ has a distribution similar to the B-B-B angles because of the formation of B$_{11}$Si molecules or Si-B$_x$ type motifs in the noncrystalline model. In the Si-Si-Si angle distribution, the amorphous model exhibits a broad distribution changing from ~70° and ~150° because of higher coordinated Si atoms but the ordered structure has a sole peak at ~180° due to Si-Si-Si chains.
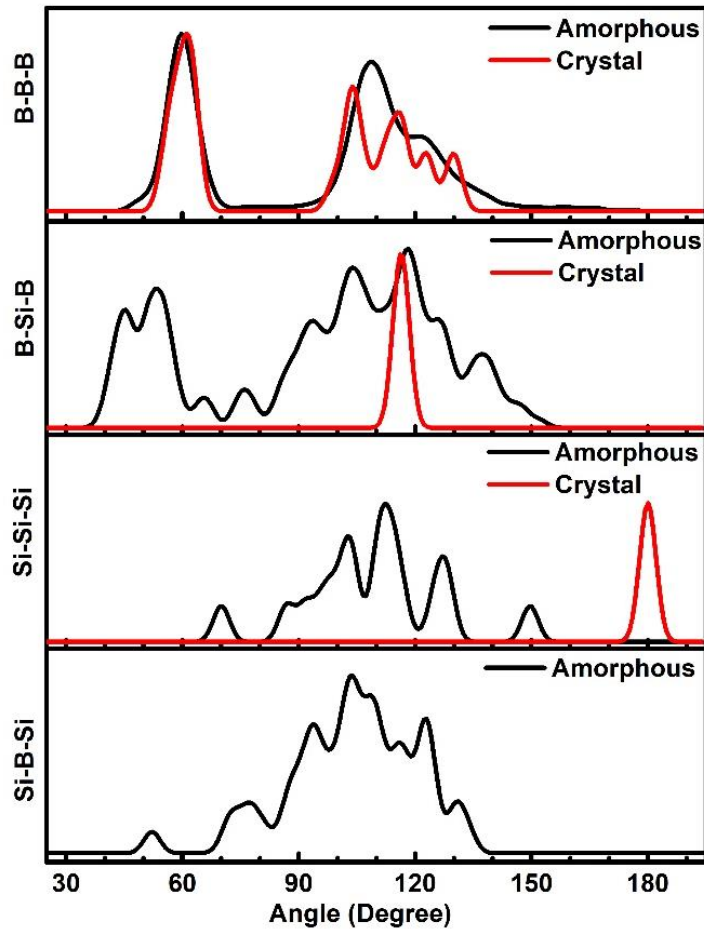
Figure 7.6 The bond angle distribution of a-SiB₄ and c-SiB₄.

7.3.2 Electronic Structure

The electronic structure of both SiB_4 phases are probed by the electron density of states (EDOS) and partial density of states (PDOS). They are illustrated in Fig. 7.7. Both phases exhibit a semiconducting behavior. The forbidden band gap energy is calculated to be around 0.16 eV (amorphous) and 0.88 eV (crystal). Yet our prediction is inconsistent with Ref. 199 in which no band gap is reported for c-SiB_4. On the other hand, according to the previous experimental investigation, the forbidden bandgap of B-rich amorphous Si-B thin films ranges from 0.5 to 1.2 eV [209]. Therefore, our estimation for the amorphous form is in acceptable limits considering the underestimation of band gap energy in DFT-GGA calculations. In order to have specific information about their electronic structure, the PDOS analysis is carried out as well. B-p state is the most preponderant effect on the valance and conduction bands, consisting with the previous theoretical investigation on c-SiB_4 [199]. B-s and Si-p states offer some contributions to

the valance and conduction bands as well while Si-*s* state has the minimal impact on both bands near the Fermi level.
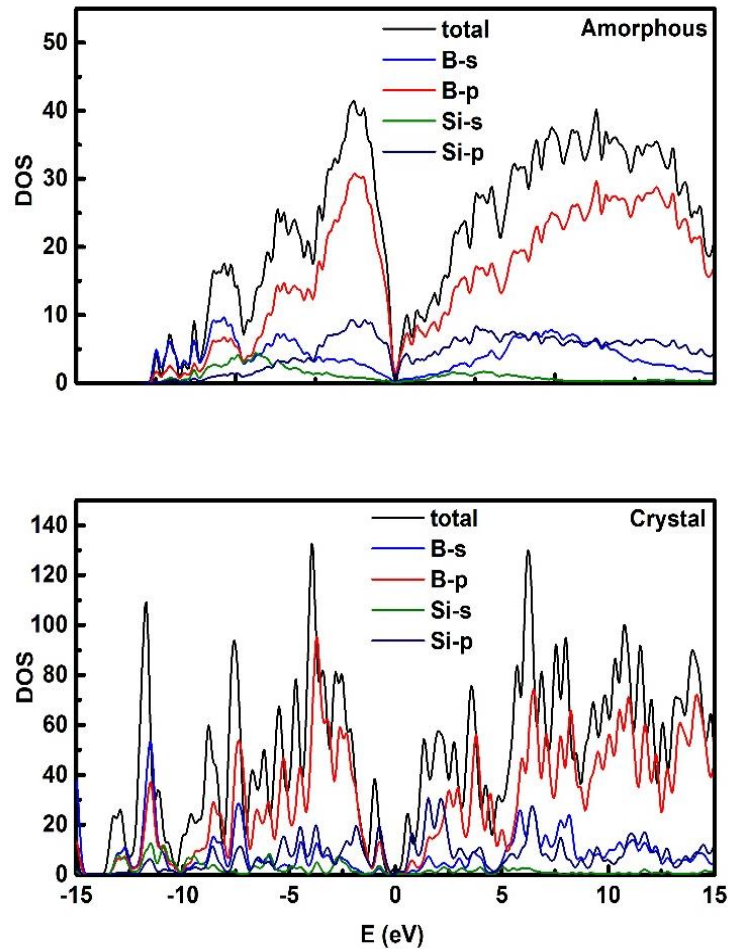
Figure 7.7 Total and partial electron density of states.

7.3.3 Mechanical Properties

The mechanical properties of both phases calculated and the available data in the literature are given in Table 2. As can be seen from the table and discussed below, our results are comparable with some of the earlier theoretical and experimental predictions.
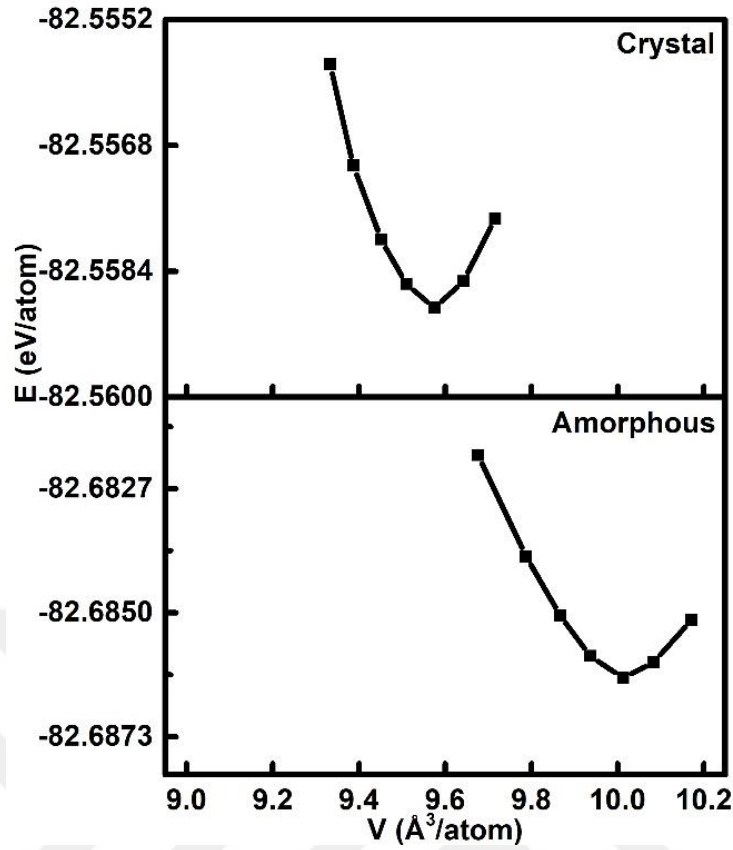
Figure 7.8 The energy of a-SiB₄ and c-SiB₄ as a function of volume.

In order to figure out the bulk modulus (K), we scrutinize the energy (E) – volume (V) relation of both SiB₄ phases (see Fig. 7.8) and fit our data to the 3rd order BMEOS (Eq. 2.50). *K* is computed to be ~151 GPa for the disordered state and ~161 GPa for the ordered one, which are comparable with ~136-172 GPa reported in the other theoretical analysis on c-SiB₄ [199, 419].

The most fascinating finding from Fig. 7.8 is that the amorphous form is energetically more favourable than the crystal, in a contrast to common expectation. The relative energy difference between two forms of SiB₄ is predicted to be 0.127 eV/atom. Here we also calculate the formation energy of each structure using the following relation,

$$\Delta E_{form} = E_{total}\big(Si_x B_y\big) - [x E_{total}(Si) + y E_{total}(B)] \tag{7.1}$$

For the crystal, the energy is estimated to be about -0.27 eV/atom, comparable with -0.24 eV/atom reported in Ref. 419. For the amorphous form, the energy is estimated -0.39 eV/atom, again suggesting that the amorphous form is more favourable.

Table 7.2 The calculated bulk modulus (K in GPa), young modulus (E in GPa), Poisson's ratios (v), shear modulus (μ in GPa), Pugh's ratio (*n*) and Vicker's hardness (H in GPa) of a-SiB₄ and c-SiB₄ compounds.

Phase	K	E	v	μ	n	H	References
a-SiB₄	150.59	258.46	0.214	106.454	1.415	16.075 (Eq. VI)	This study
						17.449 (Eq. VII)	This study
						16.895 (Eq. VIII)	This study
						18.06 (Eq. VI)	This study
c-SiB₄	160.86	287.54	0.202	119.602	1.345	20.222 (Eq. VII)	This study
						19.43 (Eq. VIII)	This study
			0.3655	24.0			[400]
	136-140		0.21	86-114			[312]
	172.1	150.0	0.35	55.4	1.32		[193]
		280				27.0	[423]
						32.6	[256]

Since we can easily calculate Young modulus (E) from σ (stress) and ε (strain) relation (Eq. (2.53)), namely, a-SiB₄ and c-SiB₄ are exposed to a uniaxial stress along their principle axes (*x*, *y* and *z*) and their σ-ε relation is monitored. By using the best linear fitting line, three different values for Young modulus are estimated. The mean Young modulus is computed to be ~258 GPa for a-SiB₄ and ~288 GPa for c-SiB₄, which are parallel to the previous experimental result of 280 GPa for the crystal [382] but higher than the theoretical result of 150 GPa [199].

Using the Eq. (2.55), the Poisson ratio (*v*) for the a-SiB₄ and c-SiB₄ are conjectured to be around 0.214 GPa and 0.202, respectively, in good agreement with 0.21 [419]. Yet they are very off from the previous theoretical value of 0.35 [199] calculated for c-SiB₄ and 0.3655 [400] estimated for the diamond like SiB₄.

The shear modulus (μ) (Eq. 2.57) is computed to be 106.5 GPa (amorphous) and 119.6 GPa (crystal), very close to the theoretical values of 86-114 GPa [419]. However, they are not comparable with the previous result of 55.4 GPa (c-SiB₄) [199] and 24 GPa (diamond-like SiB₄) [400]. Such a different result might be expected for diamond-like SiB₄ phase because of its different chemistry and structure (fourfold coordination) but the origin noticeable difference between Ref. 199 and 419 for c-SiB₄ is not clear.

By means of three different equations (Eq. 2.58-2.60) [255-257], the Vickers hardness (H) is estimated to be 16.1-17.4 GPa for the noncrystalline configuration and 18.1-20.2 GPa for the crystalline compound. Our results are noticeably less than the experimental result of 27 GPa [382] and theoretical value of 32.6 GPa [424]. It should be pointed out that the Vickers hardness slightly decreases in the amorphous state but it can still be considered as a hard material.

7.4 Discussion

Perhaps the most unusual finding is that the amorphous form of SiB_4 is energetically more favorable than the crystal. Two possible scenarios can be considered for this abnormal case. The first one is that the simulation parameters used in the present study might be not good enough to capture the relative energy difference between these two phases. Such a situation is probable but we do not see such an unusual behavior for SiB_3 (the crystal has lower energy then the amorphous). Consequently, such a finding in SiB_3 might weaken the first possibility. The second one is that the crystal structure of SiB_4 was not correctly identified. This is likely. Indeed, B and B-rich materials have a complex structure that cannot be easily identified. Therefore, new experimental studies might be necessary to confirm/determine the crystal structure of SiB_4. The observation of noticeable differences around Si atoms in both forms of SiB_4 might strengthen the second possibility.

According to our calculation, a-SiB_4 can be classified as a narrow band gap semiconductor and can be used as infrared detectors or thermoelectrics. Yet depending on preparation techniques, this material can show different transport properties as shown in the Si-B systems [425].

7.5 Conclusions

In order to reveal the microstructure and the electronic and mechanical properties of a-SiB_4 and to compare them with those of the crystalline state, an a-SiB_4 network is simulated by using an ab initio technique. In both forms of SiB_4, the mean coordination number of B atoms is found to be analogous but that of Si atoms is noticeably different because Si atoms form higher coordinated configurations in the amorphous state, relative

to the crystal. We observe the formation of pentagonal-like structures around Si atoms and $B_{11}Si$ type molecules, which do not form in c-SiB$_4$. a-SiB$_4$ offers a semiconducting feature but its energy band gap is quite smaller than that of the crystal. Bulk modulus is calculated to be around 151 (a-SiB$_4$) and 161 GPa (c-SiB$_4$). The Vickers hardness is found to be around 16-17 GPa for the noncrystalline model and to be 18-20 GPa for the crystal structure. The most fascinating finding is that the amorphous form has lower energy then the crystalline form. This brings a question "Was the crystalline structure of SiB$_4$ correctly identified?"

Chapter 8

Conclusions and Future Prospects

8.1 Conclusions

In the scope of this thesis, DFT calculations were performed by using *ab initio* molecular dynamics simulations to investigate both atomic configurations and the electronic and mechanical properties of B-rich amorphous networks.

In Chapter 3, we studied B-rich a-BN (B_xN_{1-x}, $0.55 \leq x \leq 0.95$) materials and observed BN:B phase separations in some compositions. For low B contents, sp^2 hybridization was found to be dominant in BN-rich regions while for higher B contents, both sp^2 and sp^3 hybridizations were perceived. On the other hand, in B rich regions, ideal and incomplete pentagonal pyramid-likes structures and hence B_{12} icosahedrons were found to form. A cage-like B_{16} molecule was, for the first time, observed in some amorphous materials. B-rich a-BN materials were predicted to be semiconductor. Due to the change in the mean coordination number, the mechanical properties were found to increase with increasing B content.

In Chapter 4, a-BO (B_xO_{1-x}, $0.5 \leq x \leq 95$) materials were modeled and their properties were investigated. The B coordination increased gradually with the increase of B content but the O-coordination remained constant. Similar to a-BNs, phase separations (B:B_2O_3) were witnessed. An improvement in the mechanical properties of amorphous silicon borides was perceived with increasing B concentration. Some amorphous compounds were proposed to be hard materials. A possible ductile-to-brittle transition was speculated between 70 and 75% B concentrations.

In Chapter 5, B-rich a-SiB (B_nSi_{1-n}, $0.5 \leq n \leq 95$) were studied. The coordination number of both B and Si was found to increase gradually with increasing B content. The formation of B_{12} and $B_{11}Si$ icosahedrons was observed in all amorphous materials studied. It should be noted here that $B_{11}Si$ icosahedrons form in only amorphous configurations not in crystalline silicon borides. Amorphous silicon borides were proposed to be

semiconducting materials based on GGA+U calculations. The mechanical properties of amorphous silicon borides were significantly improved at high B contents.

In Chapter 6, both amorphous and crystalline forms of SiB_3 were explored and the local structure around Si atoms was found to be different in both forms, leading to different mechanical and electrical properties. In the amorphous form, the formation of B_{12}, $B_{11}Si$ and B_{10} molecules were observed.

In Chapter 7, the crystalline and amorphous structures of SiB_4 were compared. In this compound, the local structure around Si atoms was found to be different as well. The most remarkable finding is that the amorphous structure was found to be energetically more favorable than the crystal. Both structures were semiconductor but had a very different band gap value.

8.2 Societal Impact and Contribution to Global Sustainability

Materials science will play a critical role in the utilizing of finite resources in the world with their uttermost potential. Sustainability in the scope of materials may indicate to the technology that permits the manufacturing of energy from waste materials or the advancement of new sustainable processes and materials. In this regard, boron has an important position in the context of sustainable materials by helping of the reducing of green-gas emissions or the preserving environment. Boron has been having very wide range application fields like detergent, ceramic, glass etc. The interest and demand for boron are increasing day by day in consequence of the developments in both industrial technologies and activities. Due to both the increasing demand to boron and the importance of sustainability with increasing environmental awareness, there have been experimental and theoretical studies on the global sustainability of the industrial productions comprising of boron elements from cradle to gate.

In recent years, boron-rich amorphous materials have acquired remarkable attentions because some might offer potentials to solve some current global issues related to environmental pollution, health and energy crises. The amorphous materials studied in the context of this thesis show a semiconducting behavior and hence they can be a good candidate for semiconductor technology. Consequently, these materials might be used in the development of renewable energy such as in solar, wind or hydro powers.

In Turkey's 2023 Vision, it is emphasized that Turkey should be a country that produces advanced technology. Turkey has the largest boron reserve share in the world. Therefore, it is recommended that Turkey will be the world leader in the production of boron-based new generation ceramics. This thesis is parallel with the Turkey's 2023 Vision and will have valuable contributions to this Vision.

Additionally, this thesis will be helpful in optimizing boron processing conditions and guiding experimental research in this field for determining the right production conditions, choosing the right composition ratios, setting up experimental protocols, saving energy, saving materials etc.

Finally, the articles emerging from the investigations demonstrated here are listed in the "Curriculum vitae" section at the end of this thesis.

8.3 Future Prospects

The physical and chemical properties of the materials studied in this thesis might be altered in different conditions. In the first scenario, doping procedures can be considered, which is known to have the significant effects on the properties of a material. In a future study, the influence of doping on these amorphous materials with metallic or nonmetallic elements such as carbon, nitrogen, aluminum, magnesium etc. can be investigated and the properties of these amorphous systems might be improved. In the second scenario, the preparation techniques or conditions can be considered. It is known that the materials prepared at high temperature and pressure conditions can show a different structure and hence properties, relative to one prepared at ambient pressure condition. Consequently, the preparation of these materials at different pressure treatments can improve their properties. Lastly, the high-pressure behavior of these amorphous materials at room temperature or high temperatures can be investigated since it is known that pressure can lead to a high-density amorphous phase, quite different than the amorphous configurations prepared at ambient pressure condition.

BIBLIOGRAPHY

[1]   A. Çolak, B. Laratte, B. Elevli, and S. Çoruh, "Abiotic Depletion of Boron: An Update Characterization Factors for CML 2002 and ReCiPe." Minerals, 12(4), 435-435 (2022).

[2]   U.S. Geological Survey. Mineral Commodity Summaries; U.S. Governement Publishing Office: Reston, VA, USA. Available online: https://pubs.er.usgs.gov/publication/mcs2021.

[3]   ETI Maden. Bor Sektör Raporu. 2020. Available online: https://www.etimaden.gov.tr/storage/2021/Bor_Sektor_Raporu_2020.pdf.

[4]   P. A. Lyday, "Boron." US Geological Survey Minerals Yearbook, 13.1-13.10 (2000).

[5]   B. Albert, and H. Hillebrecht, "Boron: elementary challenge for experimenters and theoreticians." Angewandte Chemie International Edition 48(46), 8640-8668 (2009).

[6]   M. E. Weeks, "The discovery of the elements. XII. Other elements isolated with the aid of potassium and sodium: Beryllium, boron, silicon, and aluminum." Journal of Chemical Education, 9(8), 1386-1412 (1932).

[7]   J. L. Gay-Lussac, and L. J. Thénard, "Sur la décomposition et la recomposition de l'acide boracique." Annales de Chimie et de Physique, 68, 169-174 (1808).

[8]   H. Davy, "XXXIV. Electrochemical researches on the decomposition of the earths; with observations on the metals obtained from the alkaline earths, and on the amalgam procured from ammonia." The Philosophical Magazine, 32(127), 193-223 (1808).

[9]   J. J. Berzelius, "Untersuchungen über die Flussspathsäure und deren merkwürdigsten Verbindungen." Annalen der Physik, 77(6), 169-230 (1824).

[10]   E. Weintraub, "Preparation and properties of pure boron." Transactions of the American Electrochemical Society, 16, 165-184 (1909).

[11]   Ş. G. Özkan, T. D. Tombal, İ. K. Ünver, and A. E. OSMANLIOĞLU, "Bor bileşiklerinin özellikleri, üretimi, kullanımı ve nükleer reaktör teknolojisinde önemi." Journal of Boron, 1(2), 86-95 (2016).

[12] W. G. Woods, "An introduction to boron: history, sources, uses, and chemistry." Environmental health perspectives, 102(suppl 7), 5-11 (1994).

[13] S. A. Etimine, "ETİMADEN," Available online: http://www.etimine.com/ (6 April 2022).

[14] Y. Zhu, J. Cai, N. S. Hosmane, and Y. Zhang, "Introduction: basic concept of boron and its physical and chemical properties." In Fundamentals and Applications of Boron Chemistry, Elsevier, 1-57 (2022).

[15] "Atomic Weights and Isotopic Compositions for All Elements." National Institute of Standards and Technology. Retrieved 21 September 2008.

[16] A. R. Oganov, J. Chen, C. Gatti, Y. Ma, Y. Ma, C. W. Glass, ... and V. L. Solozhenko, "Ionic high-pressure form of elemental boron." Nature, 457(7231), 863-867 (2009).

[17] X. Sun, X. Liu, J. Yin, J. Yu, Y. Li, Y. Hang, ... and W. Guo, "Two-dimensional boron crystals: structural stability, tunable properties, fabrications and applications." Advanced Functional Materials, 27(19), 1603300-1603300 (2017).

[18] A. F. Holleman, "Lehrbuch der anorganischen Chemie." Walter de Gruyter GmbH & Co KG, (2019).

[19] E. Wiberg, A. F. Holleman, and N. Wiberg, "Inorganic chemistry." Academic press (2001).

[20] V. L. Solozhenko, O. O. Kurakevych, and A. R. Oganov, "On the hardness of a new boron phase, orthorhombic γ-B28." Journal of superhard materials, 30(6), 428-429 (2008).

[21] E. Y. Zarechnaya, L. Dubrovinsky, N. Dubrovinskaia, Y. Filinchuk, D. Chernyshov, V. Dmitriev, ... and S. I. Simak, "Superhard semiconducting optically transparent high pressure phase of boron." Physical Review Letters, 102(18), 185501 (2009).

[22] E. Weintraub, "Preparation and properties of pure boron." Transactions of the American Electrochemical Society, 16, 165-184 (1909).

[23] A. J. Mannix, X. F. Zhou, B. Kiraly, J. D. Wood, D. Alducin, B. D. Myers, ... and N. P. Guisinger, "Synthesis of borophenes: Anisotropic, two-dimensional boron polymorphs." Science, 350(6267), 1513-1516 (2015).

[24] A. W. Laubengayer, D. T. Hurd, A. E. Newkirk, and J. L. Hoard, "Boron. I. Preparation and properties of pure crystalline boron." Journal of the American Chemical Society, 65(10), 1924-1931 (1943).

[25] J. L. Hoard, S. Geller, S., and R. E. Hughes, "On The Structure Of Elementary Boron1." Journal of the American Chemical Society, 73(4), 1892-1893 (1951).

[26] J. L. Hoard, R. E. Hughes, and D. E. Sands, "The structure of tetragonal boron1." Journal of the American Chemical Society, 80(17), 4507-4515 (1958).

[27] K. Ploog, and E. Amberger, "Kohlenstoff-induzierte gitter beim bor: I-tetragonales (B12) 4B2C und (B12) 4B2C2." Journal of the Less Common Metals, 23(1), 33-42 (1971).

[28] K. Ploog, H. Schmidt, E. Amberger, G. Will, and K. H. Kossobutzki, "B48B2C2 und B48B2N2, zwei Nichtmetallboride mit der Struktur des sog. I tetragonalen Bors." Journal of the Less Common Metals, 29(2), 161-169 (1972).

[29] C. P. Talley, S. La Placa, and B. Post, "A new polymorph of boron." Acta Crystallographica, 13(3), 271-272 (1960).

[30] A. F. Holleman, "Lehrbuch der anorganischen Chemie." Walter de Gruyter GmbH & Co KG (2019).

[31] N. N. Greenwood, A. Earnshaw, and K. Hückmann, "Chemie der elemente." Weinheim: VcH Vol. 1, (1988).

[32] G. Will, and K. Ploog, "Crystal structure of I-tetragonal boron." Nature, 251(5474), 406-408 (1974).

[33] G. Will, G., and K. H. Kossobutzki, "X-ray diffraction analysis of B50C2 and B50N2 crystal-lizing in the "tetragonal" boron lattice." Journal of the Less Common Metals, 47, 33-38 (1976).

[34] M. Vlasse, R. Naslain, J. S. Kasper, and K. Ploog, "Crystal structure of tetragonal boron related to α-AlB12." Journal of Solid State Chemistry, 28(3), 289-301 (1979).

[35] M. Vlasse, R. Naslain, J. S. Kasper, and K. Ploog, "The crystal structure of tetragonal boron." Journal of the Less Common Metals, 67(1), 1-6 (1979).

[36] J. Donohue, "Structures of the Elements." Wiley (1974).

[37] R. H. Wentorf Jr, "Boron: another form." Science, 147(3653), 49-50 (1965).

[38] E. Y. Zarechnaya, L. Dubrovinsky, N. Dubrovinskaia, N. Miyajima, Y. Filinchuk, D. Chernyshov, and V. Dmitriev, "Synthesis of an orthorhombic high pressure boron phase." Science and Technology of Advanced Materials, 9, 044209-044209 (2009).

[39] G. Parakhonskiy, N. Dubrovinskaia, E. Bykova, R. Wirth, and L. Dubrovinsky, "Experimental pressure-temperature phase diagram of boron: resolving the long-standing enigma." Scientific reports, 1(1), 1-7 (2011).

[40] A. Masago, K. Shirai, and H. Katayama-Yoshida, "Crystal stability of α-and β-boron." Physical Review B, 73(10), 104102-104102 (2006).

[41] J. L. Gay-Lussac, and L. J. baron Thénard, "Recherches physico-chimiques: faites sur la pile, sur la préparation chimique et les propriétés du Potassium et du Sodium; sur la décomposition de l'acide boracique; sur les acides fluorique, muriatique oxigéné; sur l'action chimique de la lumière; sur l'analyse végétale et animale, etc... Tome second." Deterville, 2 (1811).

[42] H. Davy, Gilb. Ann., 73, 16 (1810).

[43] H. Moissan, "Étude du Bore Amorphe." Annales de Chimie et de Physique, 6, 296-320 (1895).

[44] E. Weintraub, "Preparation and properties of pure boron." Transactions of the American Electrochemical Society, 16, 165–184 (1909)

[45] R. G. Delaplane, U. Dahlborg, W. S. Howells, and T. Lundström, "A neutron diffraction study of amorphous boron using a pulsed source." Journal of Non-Crystalline Solids, 106(1-3), 66-69 (1988).

[46] R. A. Lidin, "Inorganic substances handbook." Begell House, New York (1996).

[47] J. S. Gillespie Jr, "Crystallization of massive amorphous boron." Journal of the American Chemical Society, 88(11), 2423-2425 (1966).

[48] Y. Q. Wang, and X. F. Duan, "Crystalline boron nanowires." Applied physics letters, 82(2), 272-274 (2003).

[49] S. Johansson, J. Å. Schweitz, H. Westberg, and M. Boman, "Microfabrication of three-dimensional boron structures by laser chemical processing." Journal of applied physics, 72(12), 5956-5963 (1992).

[50] Y. Kar, N. Şen, N., and A. Demirbaş, "Boron minerals in Turkey, their application areas and importance for the country's economy." Minerals & Energy-Raw Materials Report, 20(3-4), 2-10 (2006).

[51] BOREN Ulusal Bor Araştırma Enstitüsü 2016, Available online: http://www.boren.gov.tr/tr/bor/bor-elementi

[52] E. E. Yegül, "Bor zenginleştirme tesislerinde ara ürün tenörlerinin arttırılması için yöntemlerin incelenmesi." Yüksek Lisans Tezi, Hacettepe Üniversitesi Fen Bilimleri Enstitüsü, Ankara, (2007).

[53] H. Werheit, "On the electronic transport properties of boron carbide." In The physics and chemistry of carbides, nitrides and borides Springer, Dordrecht, 185, 677-690 (1990).

[54] R. Franz, and H. Werheit, "Influence of the Jahn-Teller effect on the electronic band structure of boron-rich solids containing B12 icosahedra." In AIP Conference Proceedings, American Institute of Physics, 231(1), 29-36 (1991, July).

[55] D. Emin, "Icosahedral boron-rich solids." Physics Today, 40(1), 55-62 (1987).

[56] H. Werheit, "Boron-rich solids: a chance for high-efficiency high-temperature thermoelectric energy conversion." Materials Science and Engineering: B, 29(1-3), 228-232 (1995).

[57] F. Thevenot, "Boron carbide—a comprehensive review." Journal of the European Ceramic society, 6(4), 205-225 (1990).

[58] R. R. Ridgway, "Boron carbide: A new crystalline abrasive and wear-resisting product." Transactions of The Electrochemical Society, 66(1), 117-133 (1934).

[59] J. L. Watts, "Controlled synthesis of boron carbide using solution-based techniques." Doctoral dissertation, Queensland University of Technology (2018).

[60] V. Russell, R. Hirst, F. A. Kanda, and A. J. King, "An X-ray study of the magnesium borides." Acta Crystallographica, 6(11-12), 870-870 (1953).

[61] J. Nagamatsu, N. Nakagawa, T. Muranaka, Y. Zenitani, and J. Akimitsu, "Superconductivity at 39 K in magnesium diboride."Nature, 410(6824), 63-64 (2001).

[62] M. Rafieazad, Ö. BALCI, A. C. A. R. Selçuk, and M. Somer, "Review on magnesium diboride (MgB2) as excellent superconductor: Effects of the production techniques on the superconducting properties." Journal of Boron, 2(2), 87-96 (2017).

[63] J. M. An, and W. E. Pickett, "Superconductivity of MgB 2: covalent bonds driven metallic." Physical Review Letters, 86(19), 4366-4369 (2001).

[64] Y. Bugoslavsky, G. K. Perkins, X. Qi, L. F. Cohen, and A. D. Caplin, "Vortex dynamics in superconducting MgB2 and prospects for applications." Nature, 410(6828), 563-565 (2001).

[65] D. K. Finnemore, J. E. Ostenson, S. L. Bud'Ko, G. Lapertot, and P. C. Canfield, "Thermodynamic and transport properties of superconducting Mg 10 B 2." Physical Review Letters, 86(11), 2420-2422 (2001).

[66] J. S. Slusky, N. Rogado, K. A. Regan, M. A. Hayward, P. Khalifah, T. He, ... and R. J. Cava, "Loss of superconductivity with the addition of Al to MgB2 and a structural transition in Mg1-x AlxB2." Nature, 410(6826), 343-345 (2001).

[67] M. Monteverde, M. Nunez-Regueiro, N. Rogado, K. A. Regan, M. A. Hayward, T. He, ... and R. J. Cava, "Pressure dependence of the superconducting transition temperature of magnesium diboride." Science, 292(5514), 75-77 (2001).

[68] S. L. Bud'Ko, G. Lapertot, C. Petrovic, C. E. Cunningham, N. Anderson, and P. C. Canfield, "Boron isotope effect in superconducting MgB 2." Physical Review Letters, 86(9), 1877-1880 (2001).

[69] J. Kortus, I. I. Mazin, K. D. Belashchenko, V. P. Antropov, and L. L. Boyer, L. L. "Superconductivity of metallic boron in MgB 2." Physical Review Letters, 86(20), 4656-4659 (2001).

[70] T. Tan, "Application of superconducting magnesium diboride (MGB2) in superconducting radio frequency cavities." Ph.D Thesis, Temple University, Philadelphia (2015).

[71] C. Buzea, and T. Yamashita, "Review of the superconducting properties of MgB2." Superconductor Science and Technology, 14(11), R115-R146 (2001).

[72] Calcium hexaboride, Available online: https://en.wikipedia.org/wiki/Calcium_hexaboride#cite_note-2

[73] Z. Li, Z. R. Li, and H. Meng, H. "Organic light-emitting materials and devices." CRC press (2006).

[74] S. J. La Placa, and B. Post, "The crystal structure of rhenium diboride." Acta Crystallographica, 15(2), 97-99 (1962).

[75] L. Yan-Ling, Z. Guo-Hua, and Z. Zhi, "All-electron study of ultra-incompressible superhard material ReB2: structural and electronic properties." Chinese Physics B, 18(10), 4437-4442 (2009).

[76] H. Y. Chung, M. B. Weinberger, J. B. Levine, A. Kavner, J. M. Yang, S. H. Tolbert, and R. B. Kaner, R. B. "Synthesis of ultra-incompressible superhard rhenium diboride at ambient pressure." Science, 316(5823), 436-439 (2007).

[77] Rhenium Diboride (ReB2), Available online: https://www.reade.com/products/rhenium-diboride-reb2

[78] R. Telle, "Boride–eine neue Hartstoffgeneration?." Chemie in unserer Zeit, 22(3), 93-99 (1988).

[79]   R. Riedel, "Novel ultrahard materials." Advanced Materials, 6(7-8), 549-560 (1994).

[80]   M. Herrmann, H. Klemm, C. Schubert, and R. Riedel, "Handbook of ceramic hard materials." Weinheim: Wiley-VCH, 2, 749-801 (2000).

[81]   H. J. Sterzel, "Thermoelectrically active materials and generators containing them." U.S. Patent No. 6,444,894. Washington, DC: U.S. Patent and Trademark Office (2002).

[82]   H. Werheit, P. Runow, and H. G. Leis, "On boron-suboxide surface layers and surface states of β-rhombohedral boron." Physica Status Solidi (a), 2(3), K125-K129 (1970).

[83]   K. A. Gschneidner, J. C. Bunzli, and V. Pecharsky, "Handbook on the Physics and Chemistry of Rare Earths", Elsevier, Amsterdam, 38, 106-173 (2008).

[84]   M. L. Wilkins, "Use of boron compounds in lightweight armor." In Boron and refractory borides Springer, Berlin, Heidelberg 633-648 (1977).

[85]   D. C. Halverson, A. J. Pyzik, and I. A. Aksay, "Processing and Microstructural Characterization of B4C-AI Cermets." In Proceedings of the 9th Annual Conference on Composites and Advanced Ceramic Materials: Ceramic Engineering and Science Proceedings Hoboken, NJ, USA: John Wiley & Sons, Inc., 6, 736-744, (1985, January).

[86]   A. J. Pyzik, and D. R. Beaman, "Al-B-C Phase Development and Effects on Mechanical Properties of B4C/Al-Derived Composites." Journal of the American Ceramic Society, 78(2), 305-312 (1995).

[87]   J. C. Viala, G. Gonzales, and J. Bouix, "Composition and lattice parameters of a new aluminium-rich borocarbide." Journal of materials science letters, 11(10), 711-714 (1992).

[88]   L. Schlapbach, and A. Züttel, "Hydrogen-storage materials for mobile applications." Nature, 414(6861), 353-358 (2001).

[89]   A. Züttel, A. Borgschulte, S. I. Orimo, "Tetrahydroborates as new hydrogen storage materials." Scripta Materialia, 56(10), 823-828 (2007).

[90]   T. B. Marder, "Will we soon be fueling our automobiles with ammonia–borane?." Angewandte Chemie International Edition, 46(43), 8116-8118, (2007).

[91]   C. W. Yoon, P. J. Carroll, and L. G. Sneddon, "Ammonia triborane: a new synthesis, structural determinations, and hydrolytic hydrogen-release properties." Journal of the American Chemical Society, 131(2), 855-864 (2009).

[92]   S. H. Lim, J. Luo, W. Ji, and J. Lin, "Synthesis of boron nitride nanotubes and its hydrogen uptake." Catalysis Today, 120(3-4), 346-350 (2007).

[93]   F. E. Pinkerton, M. S. Meyer, G. P. Meisner, and M. P. Balogh, "Improved hydrogen release from LiB0. 33N0. 67H2. 67 with noble metal additions." The Journal of Physical Chemistry B, 110(15), 7967-7974 (2006).

[94]   H. Zhang, Q. Zhang, J. Tang, and L. C. Qin, "Single-crystalline CeB6 nanowires." Journal of the American Chemical Society, 127(22), 8002-8003 (2005).

[95]   Ferro Boron, Available online: https://www.americanelements.com/ferro-boron-11108-67-1

[96]   J. Nagamatsu, N. Nakagawa, T. Muranaka, Y. Zenitani, and J. Akimitsu, "Superconductivity at 39 K in magnesium diboride." Nature, 410(6824), 63-64 (2001).

[97]   N. Izyumskaya, D. O. Demchenko, S. Das, Ü. Özgür, V. Avrutin, and H. Morkoç, "Recent development of boron nitride towards electronic applications." Advanced Electronic Materials, 3(5), 1600485-1600485 (2017).

[98]   X. Zhang, and J. Meng, "Recent progress of boron nitrides." Ultra-Wide Bandgap Semiconductor Materials, 347-419 (2019).

[99]   D. Pacile, J. C. Meyer, Ç. Ö. Girit, and A. J. A. P. L. Zettl, "The two-dimensional phase of boron nitride: Few-atomic-layer sheets and suspended membranes." Applied Physics Letters, 92(13), 133107-133107 (2008).

[100] R. V. Gorbachev, I. Riaz, R. R. Nair, R. Jalil, L. Britnell, B. D. Belle, ... and P. Blake, "Hunting for monolayer boron nitride: optical and Raman signatures." Small, 7(4), 465-468 (2011).

[101] L. H. Li, Y. Chen, G. Behan, H. Zhang, M. Petravic, and A. M. Glushenkov, "Large-scale mechanical peeling of boron nitride nanosheets by low-energy ball milling." Journal of materials chemistry, 21(32), 11862-11866 (2011).

[102] W. Q. Han, L. Wu, Y. Zhu, K. Watanabe, and T. Taniguchi, "Structure of chemically derived mono-and few-atomic-layer boron nitride sheets." Applied Physics Letters, 93(22), 223103-223103 (2008).

[103] Y. Lin, T. V. Williams, T. B. Xu, W. Cao, H. E. Elsayed-Ali, and J. W. Connell, "Aqueous dispersions of few-layered and monolayered hexagonal boron nitride nanosheets from sonication-assisted hydrolysis: critical role of water." The Journal of Physical Chemistry C, 115(6), 2679-2685 (2011).

[104] K. G. Zhou, N. N. Mao, H. X. Wang, Y. Peng, Y., and H. L. Zhang, "A mixed-solvent strategy for efficient exfoliation of inorganic graphene analogues." Angewandte Chemie, 123(46), 11031-11034 (2011).

[105] L. Song, L. Ci, H. Lu, P. B. Sorokin, C. Jin, J. Ni, ... and P. M. Ajayan, "Large scale growth and characterization of atomic hexagonal boron nitride layers." Nano letters, 10(8), 3209-3215 (2010).

[106] Y. Shi, C. Hamsen, X. Jia, K. K. Kim, A. Reina, M. Hofmann,... and J. Kong, "Synthesis of few-layer hexagonal boron nitride thin film by chemical vapor deposition." Nano letters, 10(10), 4134-4139 (2010).

[107] R. J. Chang, X. Wang, S. Wang, Y. Sheng, B. Porter, H. Bhaskaran, and J. H. Warner, "Growth of large single-crystalline monolayer hexagonal boron nitride by oxide-assisted chemical vapor deposition." Chemistry of Materials, 29(15), 6252-6260 (2017).

[108] K. M. Kim, C. Y. Eugene, and Y. Kim, "Mapping protein receptor–ligand interactions via in vivo chemical crosslinking, affinity purification, and differential mass spectrometry." Methods, 56(2), 161-165 (2012).

[109] J. C. Koepke, J. D. Wood, Y. Chen, S. W. Schmucker, X. Liu, N. N. Chang, ... and J. W. Lyding, "Role of pressure in the growth of hexagonal boron nitride thin films from ammonia-borane." Chemistry of Materials, 28(12), 4169-4179 (2016).

[110] S. Behura, P. Nguyen, S. Che, R. Debbarma, and V. Berry, "Large-area, transfer-free, oxide-assisted synthesis of hexagonal boron nitride films and their heterostructures with MoS2 and WS2." Journal of the American Chemical Society, 137(40), 13060-13065 (2015).

[111] K. H. Lee, H. J. Shin, B. Kumar, H. S. Kim, J. Lee, R. Bhatia, ... and S. W. Kim, "Nanocrystalline-Graphene-Tailored Hexagonal Boron Nitride Thin Films." Angewandte Chemie, 126(43), 11677-11681 (2014).

[112] H. Wang, X. Zhang, J. Meng, Z. Yin, X. Liu, Y. Zhao, and L. Zhang, "Controlled growth of few-layer hexagonal boron nitride on copper foils using ion beam sputtering deposition." Small, 11(13), 1542-1547 (2015).

[113] H. Wang, X. Zhang, H. Liu, Z. Yin, J. Meng, J. Xia, ... and J. You, "Synthesis of Large-Sized Single-Crystal Hexagonal Boron Nitride Domains on Nickel Foils by Ion Beam Sputtering Deposition." Advanced materials, 27(48), 8109-8115 (2015).

[114] J. H. Meng, X. W. Zhang, H. Liu, Z. G. Yin, D. G. Wang, Y. Wang, ... and J. L. Wu, "Synthesis of atomic layers of hybridized h-BNC by depositing h-BN on graphene via ion beam sputtering." Applied Physics Letters, 109(17), 173106-173106 (2016).

[115] M. Xu, D. Fujita, H. Chen, and N. Hanagata, "Formation of monolayer and few-layer hexagonal boron nitride nanosheets via surface segregation." Nanoscale, 3(7), 2854-2858 (2011).

[116] S. Suzuki, R. M. Pallares, and H. Hibino, "Growth of atomically thin hexagonal boron nitride films by diffusion through a metal film and precipitation." Journal of Physics D: Applied Physics, 45(38), 385304-385304 (2012).

[117] C. Zhang, L. Fu, S. Zhao, Y. Zhou, H. Peng, and Z. Liu, "Controllable Co-segregation Synthesis of wafer-scale hexagonal boron nitride thin films." Advanced Materials, 26(11), 1776-1781 (2014).

[118] S. Sonde, A. Dolocan, N. Lu, C. Corbet, M. J. Kim, E. Tutuc, ... and L. Colombo, "Ultrathin, wafer-scale hexagonal boron nitride on dielectric surfaces by diffusion and segregation mechanism." 2D Materials, 4(2), 025052-025052 (2017).

[119] R. H. Wentorf Jr, "Cubic form of boron nitride." The Journal of Chemical Physics, 26(4), 956-956 (1957).

[120] Cubic Boron Nitride and Its Applications, Available online: https://nanografi.com/blog/cubic-boron-nitride-and-its-applications/

[121] T. Taniguchi, and S. Yamaoka, "Spontaneous nucleation of cubic boron nitride single crystal by temperature gradient method under high pressure." Journal of crystal growth, 222(3), 549-557 (2001).

[122] M. Sokołowski, "Deposition of wurtzite type boron nitride layers by reactive pulse plasma crystallization." Journal of Crystal Growth, 46(1), 136-138 (1979).

[123] W. Dworschak, K. Jung, and H. Ehrhardt, "Growth of cubic boron nitride coatings in a magnetic field enhanced rf glow discharge." Diamond and Related Materials, 3(4-6), 337-340 (1994).

[124] W. J. Zhang, C. Y. Chan, K. M. Chan, I. Bello, Y. Lifshitz, and S. T. Lee, "Deposition of large-area, high-quality cubic boron nitride films by ECR-enhanced microwave-plasma CVD." Applied Physics A, 76(6), 953-955 (2003).

[125] H. Yang, C. Iwamoto, and T. Yoshida, "High-quality cBN thin films prepared by plasma chemical vapor deposition with time-dependent biasing technique." Thin solid films, 407(1-2), 67-71 (2002).

[126] S. Matsumoto, and W. Zhang, "High-rate deposition of high-quality, thick cubic boron nitride films by bias-assisted DC jet plasma chemical vapor deposition." Japanese Journal of Applied Physics, 39(5B), L442-L444 (2000).

[127] T. A. Friedmann, P. B. Mirkarimi, D. L. Medlin, K. F. McCarty, E. J. Klaus, D. R. Boehme, ... and J. C. Barbour, "Ion-assisted pulsed laser deposition of cubic boron nitride films." Journal of applied physics, 76(5), 3088-3101 (1994).

[128] H. Hofsäss, H. Feldermann, M. Sebastian, and C. Ronning, "Thresholds for the phase formation of cubic boron nitride thin films." Physical Review B, 55(19), 13230-13233 (1997).

[129] J. Hahn, M. Friedrich, R. Pintaske, M. Schaller, N. Kahl, D. R. T. Zahn, and F. Richter, "Cubic boron nitride films by dc and rf magnetron sputtering: Layer characterization and process diagnostics." Diamond and related materials, 5(10), 1103-1112 (1996).

[130] K. Hirama, Y. Taniyasu, S. I. Karimoto, Y. Krockenberger, and H. Yamamoto, "Single-crystal cubic boron nitride thin films grown by ion-beam-assisted molecular beam epitaxy." Applied Physics Letters, 104(9), 092113-092113 (2014).

[131] J. Pascallon, V. Stambouli, S. Ilias, D. Bouchier, G. Nouet, F Silva, and A. Gicquel, "Microstructure of c-BN thin films deposited on diamond films." Diamond and related materials, 8(2-5), 325-330 (1999).

[132] N. Deyneka, X. W. Zhang, H. G. Boyen, P. Ziemann, and F. Banhart, "Growth of cubic boron nitride films on Si by ion beam assisted deposition at the high temperatures." Diamond and related materials, 13(3), 473-481 (2004).

[133] V. Sharma, H. L. Kagdada, P. K. Jha, P. Śpiewak, and K. J. Kurzydłowski, "Thermal transport properties of boron nitride based materials: A review." Renewable and Sustainable Energy Reviews, 120, 109622-109622 (2020).

[134] K. T. Park, K. Terakura, and N. Hamada, "Band-structure calculations for boron nitrides with three different crystal structures." Journal of Physics C: Solid State Physics, 20(9), 1241-1251 (1987).

[135] I. Vishnevetsky, and M. Epstein, "Solar carbothermic reduction of alumina, magnesia and boria under vacuum." Solar Energy, 111, 236-251 (2015).

[136] L. McCulloch, "A crystalline boric oxide." Journal of the American Chemical Society, 59(12), 2650-2652 (1937).

[137] F. Dachille, and R. Roy, "A New High-pressure Form of B2O3 and Inferences on Cation Coordination from Infrared Spectroscopy." Journal of the American Ceramic Society, 42(2), 78-80 (1959).

[138] J. D. Mackenzie, and W. F. Claussen, "Crystallization and phase relations of boron trioxide at high pressures." Journal of the American Ceramic Society, 44(2), 79-81 (1961).

[139] Boric Oxide, Available online: https://www.borax.com/BoraxCorp/media/Borax-Main/Resources/Data-Sheets/boric-oxide.pdf?ext=.pdf

[140] A. K. Hassan, L. M. Torell, L. Börjesson, and H. Doweidar, "Structural changes of B 2 O 3 through the liquid-glass transition range: A Raman-scattering study." Physical Review B, 45(22), 12797-12805 (1992).

[141] P. Umari, and A. Pasquarello, "Fraction of boroxol rings in vitreous boron oxide from a first-principles analysis of Raman and NMR spectra." Physical review letters, 95(13), 137401-137401 (2005).

[142] V. V. Brazhkin, I. Farnan, K. I. Funakoshi, M. Kanzaki, Y. Katayama, A. G. Lyapin, and H. Saitoh, "Structural transformations and anomalous viscosity in the B 2 O 3 melt under high pressure." Physical review letters, 105(11), 115701-115701 (2010).

[143] G. Carini Jr, E. Gilioli, G. Tripodo, and C. Vasi, "Structural changes and elastic characteristics of permanently densified vitreous B 2 O 3." Physical Review B, 84(2), 024207-024207 (2011).

[144] M. J. Aziz, E. Nygren, J. F. Hays, and D. Turnbull, "Crystal growth kinetics of boron oxide under pressure." Journal of applied physics, 57(6), 2233-2242 (1985).

[145] G. E. Gurr, P. W. Montgomery, C. D. Knutson, and B. T. Gorres, "The crystal structure of trigonal diboron trioxide." Acta Crystallographica Section B: Structural Crystallography and Crystal Chemistry, 26(7), 906-915 (1970).

[146] P. F. McMillan, "New materials from high-pressure experiments." Nature materials, 1(1), 19-25 (2002).

[147] D. He, Y. Zhao, L. Daemen, J. Qian, T. D. Shen, and T. W. Zerda, "Boron suboxide: As hard as cubic boron nitride." Applied Physics Letters, 81(4), 643-645 (2002).

[148] S. Lee, S. W. Kim, D. M. Bylander, and L. Kleinman, "Crystal structure, formation enthalpy, and energy bands of B 6 O." Physical Review B, 44(8), 3550-3554 (1991).

[149] H. F. Rizzo, W. C. Simmons, and H. O. Bielstein, "The existence and formation of the solid B 6 O." Journal of the Electrochemical Society, 109(11), 1079-1082 (1962).

[150] T. Lundstro, and Y. G. Andreev, "Superhard boron-rich borides and studies of the BCN system." Materials Science and Engineering: A, 209(1-2), 16-22 (1996).

[151] T. Lundström, "Structure and bulk modulus of high-strength boron compounds." Journal of Solid state chemistry, 133(1), 88-92 (1997).

[152] H. T. Hall, and L. A. Compton, "Group IV analogs and high pressure, high temperature synthesis of B2O." Inorganic Chemistry, 4(8), 1213-1216 (1965).

[153] H. Hubert, B. Devouard, L. A. Garvie, M. O'Keeffe, P. R. Buseck, W. T. Petuskey, and P. F. McMillan, "Icosahedral packing of B12 icosahedra in boron suboxide (B6O)." Nature, 391(6665), 376-378 (1998).

[154] A. R. Badzian, "Superhard material comparable in hardness to diamond." Applied physics letters, 53(25), 2495-2497 (1988).

[155] V. Srikanth, R. Roy, E. K. Graham, and D. E. Voigt, "BxO: phases present at high pressure and temperature." Journal of the American Ceramic Society, 74(12), 3145-3147 (1991).

[156] X. Liu, X. Zhao, W. Hou, and W. Su, "A new route for the synthesis of boron suboxide B7O." Journal of alloys and compounds, 223(1), L7-L9 (1995).

[157] M. Olofsson, and T. Lundström, "Synthesis and structure of non-stoichiometric B6O." Journal of alloys and compounds, 257(1-2), 91-95 (1997).

[158] H. Hubert, L. A. Garvie, B. Devouard, P. R. Buseck, W. T. Petuskey, and P. F. McMillan, "High-pressure, high-temperature synthesis and characterization of boron suboxide (B6O)." Chemistry of materials, 10(6), 1530-1537 (1998).

[159] I. S. Gladkaya, T. I. Dyuzheva, E. A. Ekimov, N. A. Nikolaev, and N. A. Bendeliani, "Crystal growth at high pressure and the problem of characterization of the interstitial phases in the B–C–O system." Journal of alloys and compounds, 329(1-2), 153-156 (2001).

[160] R. Machaka, B. W. Mwakikunga, E. Manikandan, T. E. Derry, I. Sigalas, and M. Herrmann, "Mechanical and structural properties of fluorine-ion-implanted boron suboxide." Advances in Materials Science and Engineering (2012).

[161] S. M. Gorbatkin, R. L. Rhoades, T. Y. Tsui, and W. C. Oliver, "Hard boron oxide thin-film deposition using electron cyclotron resonance microwave plasmas." Applied physics letters, 65(21), 2672-2674 (1994).

[162] C. Doughty, S. M. Gorbatkin, T. Y. Tsui, G. M. Pharr, and D. L. Medlin, "Hard boron–suboxide-based films deposited in a sputter-sourced, high-density plasma deposition system." Journal of Vacuum Science & Technology A: Vacuum, Surfaces, and Films, 15(5), 2623-2626 (1997).

[163] C. C. Klepper, R. C. Hazelton, E. J. Yadlowsky, E. P. Carlson, M. D. Keitz, J. M. Williams, ... and D. B. Poker, "Amorphous boron coatings produced with vacuum arc deposition technology." Journal of Vacuum Science & Technology A: Vacuum, Surfaces, and Films, 20(3), 725-732 (2002).

[164] D. Music, J. M. Schneider, V. Kugler, S. Nakao, P. Jin, M. Östblom, ... and U. Helmersson, "Synthesis and mechanical properties of boron suboxide thin films." Journal of Vacuum Science & Technology A: Vacuum, Surfaces, and Films, 20(2), 335-337 (2002).

[165] D. Music, U. Kreissig, V. Chirita, J. M. Schneider, and U. Helmersson, "Elastic modulus of amorphous boron suboxide thin films studied by theoretical and experimental methods." Journal of applied physics, 93(2), 940-944 (2003).

[166] D. Music, V. M. Kugler, Z. Czigány, A. Flink, O. Werner, J .M. Schneider, ... and U. Helmersson, "Role of carbon in boron suboxide thin films." Journal of Vacuum Science & Technology A: Vacuum, Surfaces, and Films, 21(4), 1355-1358 (2003).

[167] D. Music, U. Kreissig, Z. S. Czigány, U. Helmersson, and J. M. Schneider, "Elastic modulus-density relationship for amorphous boron suboxide thin films." Applied Physics A, 76(2), 269-271 (2003).

[168] D. Li, and W. Y. Ching, "Electronic structure and optical properties of the B12O2 crystal." Physical Review B, 54(3), 1451-1454 (1996).

[169] T. Wartik, and E. F. Apple, "A new modification of boron monoxide." Journal of the American Chemical Society, 77(23), 6400-6401 (1955).

[170] F. A. Kanda, A. J. King, V. A. Russell, and W. Katz, "Preparation of boron monoxide at high temperatures." Journal of the American Chemical Society, 78(7), 1509-1510 (1956).

[171] N. P. Nies, and G. W. Campbell, "Inorganic boron-oxygen chemistry." Boron, metallo-boron compounds, and boranes, (53), 231 (1964).

[172] R. J. BROTHERTON, and A. L. McCLOSKEY, "Hydrolyses of Some Boron-Nitrogen Derivatives." Advances in Chemistry 131-138 (1964).

[173] A. L. McCloskey, R. J. Brotherton, and J. L. Boone, "The Preparation of Boron Monoxide and its Conversion to Diboron Tetrachloride1." Journal of the American Chemical Society, 83(23), 4750-4754 (1961).

[174] C. F. Cline, "An investigation of the compound silicon boride (SiB6)." Journal of The Electrochemical Society, 106(4), 322-325 (1959).

[175] N. Takashima, Y. Azuma, and J .I. Matsushita, "High-temperature thermoelectric properties of silicon boride ceramics as a smart material." MRS Online Proceedings Library (OPL), 604, 233-238 (1999).

[176] S. Tanaka, N. Fukushima, J. I. Matsushita, T. Akatsu, K. Niihara, and E. Yasuda, "Mechanical properties of SiB6 addition of carbon sintered body." In Smart Materials, 4234, 346-354 (2001, April).

[177] H. F. Rizzo, B. C. Weber, and M. A. Schwartz, "Refractory Compositions Based on Silicon-Boron Oxygen Reactions." Journal of the American Ceramic Society, 43(10), 497-504 (1960).

[178] J. R. Salvador, D. Bilc, S. D. Mahanti, and M. G. Kanatzidis, "Stabilization of β-SiB3 from Liquid Ga: A Boron-Rich Binary Semiconductor Resistant to High-Temperature Air Oxidation." Angewandte Chemie International Edition, 42(17), 1929-1932 (2003).

[179] Y. Imai, M. Mukaida, M. Ueda, and A. Watanabe, "Band-calculation of the electronic densities of states and the total energies of boron–silicon system." Journal of alloys and compounds, 347(1-2), 244-251 (2002).

[180] E. Bustarret, C. Marcenat, P. Achatz, J. Kačmarčik, F. Lévy, A. Huxley, ... and J. Boulmer, "Superconductivity in doped cubic silicon." Nature, 444(7118), 465-468 (2006).

[181] K. Kádas, L. Vitos, and R. Ahuja, "Theoretical evidence of a superconducting transition in doped silicon and germanium driven by a variation of chemical composition." Applied Physics Letters, 92(5), 052505-052505 (2008).

[182] X. Blase, E. Bustarret, C. Chapelier, T. Klein, and C. Marcenat, "Superconducting group-IV semiconductors." Nature materials, 8(5), 375-382 (2009).

[183] C. Marcenat, J. Kačmarčík, R. Piquerel, P. Achatz, G. Prudon, C. Dubois, ... and D. Débarre, "Low-temperature transition to a superconducting phase in boron-doped silicon films grown on (001)-oriented silicon wafers." Physical Review B, 81(2), 020501-020501 (2010).

[184] A. I. Zaitsev, and A. A. Kodentsov, "Thermodynamic properties and phase equilibria in the Si-B system." Journal of phase equilibria, 22(2), 126-135 (2001).

[185] R. W. Olesinski, and G. J. Abbaschian, "The B− Si (boron-silicon) system." Bulletin of alloy phase diagrams, 5(5), 478-484 (1984).

[186] M. A. Imam, J. S. Young, and R. G. Reddy, "Determination of Thermodynamic Properties of Si-B Alloys." Metallurgical and Materials Transactions B, 50(2), 981-990 (2019).

[187] H. Moissan, and A. Stock, "Preparation and properties of two silicon borides: SiB3 and SiB6." Comptes rendus de l'Académie des Sciences, 131, 139-143 (1900).

[188] B. Magnusson, and C. Brosset, "The Crystal Structure of B 2.8 Si." Acta Chemica Scandinavica, 16, 449-455 (1962).

[189] T. L. Aselage, "The coexistence of silicon borides with boron-saturated silicon: Metastability of SiB3." Journal of materials research, 13(7), 1786-1794 (1998).

[190] T. L. Aselage, and D. R. Tallant, "Association of broad icosahedral Raman bands with substitutional disorder in SiB 3 and boron carbide." Physical review B, 57(5), 2675-2678 (1998).

[191] X. Liang, A. Bergara, Y. Xie, L. Wang, R. Sun, Y. Gao, ... and Y. Tian, "Prediction of superconductivity in pressure-induced new silicon boride phases." Physical Review B, 101(1), 014112-014112 (2020).

[192] C. Brosset, and B. Magnusson, "The silicon-boron system." Nature, 187(4731), 54-55 (1960).

[193] V. I. Matkovich, "A new form of boron silicide, B4Si." Acta Crystallographica, 13(8), 679-680 (1960).

[194] H. F. Rizzo, and L. R. Bidwell, "Formation and structure of SiB4." Journal of the American Ceramic Society, 43(10), 550-552 (1960).

[195] E. Colton, "Preparation of tetraboron silicide, B4Si." Journal of the American Chemical Society, 82(4), 1002-1002 (1960).

[196] C. F. Cline, and D. E. Sands, "A new silicon boride, SiB4." Nature, 185(4711), 456-456 (1960).

[197] J. R. Salvador, D. Bilc, S. D. Mahanti, and M. G. Kanatzidis, "Stabilization of β-SiB3 from Liquid Ga: A Boron-Rich Binary Semiconductor Resistant to High-Temperature Air Oxidation." Angewandte Chemie International Edition, 42(17), 1929-1932 (2003).

[198] N. N. Zhuravlev, "X-ray determination of the structure of SiB." Kristallografiya, 1(6), 666-668 (1956).

[199] B. Zhang, L. Wu, and Z. Li, "Predicted structural evolution and detailed insight into configuration correlation, mechanical properties of silicon–boron binary compounds." Rsc Advances, 7(26), 16109-16118 (2017).

[200] M. Vlasse, G. A. Slack, M. Garbauskas, J. S. Kasper, and J. C. Viala, "The crystal structure of SiB6." Journal of solid state chemistry, 63(1), 31-45 (1986).

[201] J. Wu, W. Ma, D. Tang, B. Jia, B. Yang, D. Liu, and Y. Dai, "Thermodynamic description of Si-B binary system." Procedia Engineering, 31, 297-301 (2012).

[202] R. F. Giese Jr, J. Economy, and V. I. Matkovich, "Interstitial derivatives of β boron." Zeitschrift für Kristallographie, 122(1-2), 144-147 (1965).

[203] B. Armas, G. Male, D. Salanoubat, C. Chatillon, and M. Allibert, "Determination of the boron-rich side of the B-Si phase diagram." Journal of the less common metals, 82, 245-254 (1981).

[204] T. B. Massalski, H. Okamoto, P. R. Subramanian, and L. Kacprzak, "Binary alloy phase diagrams." ASM International, 28-9 (1990).

[205] C. C. Tsai, "Characterization of amorphous semiconducting silicon-boron alloys prepared by plasma decomposition." Physical Review B, 19(4), 2041-2055 (1979).

[206] W. M. Lau, R. Yang, B. Y. Tong, and S. K. Wong, "Thermal oxidation of amorphous silicon-boron alloy." MRS Online Proceedings Library (OPL), 105, 163-168 (1987).

[207] G. R. Yang, Y. P. Zhao, and B .Y. Tong, "Studying low-pressure chemical vapor deposition a-Si: B alloys by optical spectroscopy." Journal of Vacuum Science & Technology A: Vacuum, Surfaces, and Films, 16(4), 2267-2271 (1998).

[208] L. Chen, T. Goto, J. Li, and T. Hirai, "Synthesis and thermoelectric properties of boron-rich silicon borides." Materials Transactions, JIM, 37(5), 1182-1185 (1996).

[209] M. Takeda, M. Ichimura, H. Yamaguchi, Y. Sakairi, and K. Kimura, "Preparation of boron–silicon thin film by pulsed laser deposition and its properties." Journal of Solid State Chemistry, 154(1), 141-144 (2000).

[210] G. R. Yang, Y. P. Zhao, M. Abburi, S. Dabral, and B. Y. Tong, "Comparison of low-temperature oxidation of crystalline Si and B with a-Si: B alloy: An x-ray

photoelectron spectroscopy study." Journal of Vacuum Science & Technology A: Vacuum, Surfaces, and Films, 15(2), 279-283 (1997).

[211] E. Fermi, "Statistical method of investigating electrons in atoms." Zeitschrift für Physik, (48), 73-79 (1928).

[212] L. H. Thomas, "The calculation of atomic fields." In Mathematical proceedings of the Cambridge philosophical society, 23(5), 542-548 (1927).

[213] J. C. Slater, "A simplification of the Hartree-Fock method." Physical review, 81(3), 385-390 (1951).

[214] S. Liu, "Conceptual Density Functional Theory: Towards a New Chemical Reactivity Theory." John Wiley & Sons (2022).

[215] P. Hohenberg, and W. Kohn, "Inhomogeneous electron gas." Physical review, 136(3B), B864-B871 (1964).

[216] W. Kohn, and L. J. Sham, "Self-consistent equations including exchange and correlation effects." Physical review, 140(4A), A1133-A1138 (1965).

[217] W. Kohn, "Nobel Lecture: Electronic structure of matter—wave functions and density functionals." Reviews of Modern Physics, 71(5), 1253-1266 (1999).

[218] J. A. Pople, "Nobel lecture: Quantum chemical models." Reviews of Modern Physics, 71(5), 1267-1274 (1999).

[219] K. Burke, "Perspective on density functional theory." The Journal of chemical physics, 136(15), 150901-150901 (2012).

[220] W. Koch, and M. C. Holthausen, "A chemist's guide to density functional theory." John Wiley & Sons (2015).

[221] M. Born, and J. R. Oppenheimer, "1. Zur Quantentheorie der Molekeln." Annalen der Physik, 389(20), 457-484 (1927).

[222] The self-consistent-field cycle, Available online: https://docs.siesta-project.org/projects/siesta/tutorials/basic/scf-convergence/

[223] E. Lewars, "Introduction to the theory and applications of molecular and quantum mechanics", Computational chemistry, 318 (2011).

[224] P. W. Atkins, and R. S. Friedman, "Molecular quantum mechanics." Oxford university press (2011).

[225] F. Jensen, "Introduction to computational chemistry." Wiley (2017).

[226] N. Argaman, and G. Makov, "Density functional theory: An introduction." American Journal of Physics, 68(1), 69-79 (2000).

[227] R. G. Parr, and R. G. P. W. Yang, "Density-Functional Theory of Atoms and Molecules." Oxford university press (1989).

[228] Z. Yin, "Microscopic mechanisms of magnetism and superconductivity studied from first principle calculations." Ph. D. Thesis, University of California, Davis (2009).

[229] A. D. Becke, "Density-functional exchange-energy approximation with correct asymptotic behavior." Physical review A, 38(6), 3098-3100 (1988).

[230] J. P. Perdew, "Density-functional approximation for the correlation energy of the inhomogeneous electron gas." Physical Review B, 33(12), 8822-8824 (1986).

[231] J. P. Perdew, K. Burke, and M. Ernzerhof, "Generalized gradient approximation made simple." Physical review letters, 77(18), 3865-3868 (1996).

[232] J. Tao, J. P. Perdew, V. N. Staroverov, and G. E. Scuseria, "Climbing the density functional ladder: Nonempirical meta–generalized gradient approximation designed for molecules and solids." Physical Review Letters, 91(14), 146401-146401 (2003).

[233] P. Hao, J. Sun, B. Xiao, A. Ruzsinszky, G. I. Csonka, J. Tao, and J. P. Perdew, "Performance of meta-GGA functionals on general main group thermochemistry, kinetics, and noncovalent interactions." Journal of Chemical Theory and Computation, 9(1), 355-363 (2013).

[234] B. J. Alder, and T. E. Wainwright, "Phase transition for a hard sphere system." The Journal of chemical physics, 27(5), 1208-1209 (1957).

[235] B. J. Alder, and T. E. Wainwright, "Studies in molecular dynamics. I. General method." The Journal of Chemical Physics, 31(2), 459-466 (1959).

[236] F. H. Stillinger, and A. Rahman, "Improved simulation of liquid water by molecular dynamics." The Journal of Chemical Physics, 60(4), 1545-1557 (1974).

[237] P. Steneteg, "Development of molecular dynamics methodology for simulations of hard materials." Doctoral dissertation, Linköping University Electronic Press, (2012).

[238] R. Car, and M. Parrinello, "Unified approach for molecular dynamics and density-functional theory." Physical review letters, 55(22), 2471-2474 (1985).

[239] H. C. Andersen, "Molecular dynamics simulations at constant pressure and/or temperature." The Journal of chemical physics, 72(4), 2384-2393 (1980).

[240] M. Parrinello, and A. Rahman, "Polymorphic transitions in single crystals: A new molecular dynamics method." Journal of Applied physics, 52(12), 7182-7190 (1981).

[241] M. Parrinello, "Molecular-Dynamics Simulation of Statistical-Mechanical Systems." (1986). *(ed. by G. Ciccotti and W. G. Hoover (North-Holland, 1986)*

[242] A. Sholejh, "Structural, electronic and magnetic properties of various nanosystems: molecular dynamics simulations and density functional theory calculations." PhD Thesis, Middle East Technical University, Ankara (2014).

[243] M. J. Uline, and D. S. Corti, "Molecular dynamics at constant pressure: allowing the system to control volume fluctuations via a "shell" particle." Entropy, 15(9), 3941-3969 (2013).

[244] M. L. Klein, and J. A. Venables, "Rare gas solids" Academic Press, 1, 626-627 (1976).

[245] What is Siesta?, Available online: https://www.simuneatomistics.com/products/siesta-code/

[246] E. Kaxiras, "Atomic and electronic structure of solids." Cambridge University Press, Cambridge, 696 (2003).

[247] D. Vanderbilt, "Soft self-consistent pseudopotentials in a generalized eigenvalue formalism." Physical review B, 41(11), 7892-7895 (1990).

[248] P. E. Blöchl, "Projector augmented-wave method." Physical review B, 50(24), 17953-17979 (1994).

[249] D. R. Hamann, M. Schlüter, and C. Chiang, "Norm-conserving pseudopotentials." Physical Review Letters, 43(20), 1494-1497 (1979).

[250] N. Troullier, and J. L. Martins, "Efficient pseudopotentials for plane-wave calculations." Physical review B, 43(3), 1993-2006 (1991).

[251] S. Le Roux, and V. Petkov, "ISAACS–interactive structure analysis of amorphous and crystalline systems." Journal of Applied Crystallography, 43(1), 181-185 (2010).

[252] F. Ercolessi, "A molecular dynamics primer." Spring college in computational physics, ICTP, Trieste, 19 (1997).

[253] F. D. Murnaghan, "The compressibility of media under extreme pressures." Proceedings of the National Academy of Sciences, 30(9), 244-247 (1944).

[254] F. Birch, "Finite elastic strain of cubic crystals." Physical review, 71(11), 809-824 (1947).

[255] D. M. Teter, "Computational alchemy: the search for new superhard materials." MRS Bulletin, 23(1), 22-27 (1998).

[256] X. Q. Chen, H. Niu, D. Li, and Y. Li, "Modeling hardness of polycrystalline materials and bulk metallic glasses." Intermetallics, 19(9), 1275-1281 (2011).

[257] Y. Tian, B. Xu, Z. Zhao, "Microscopic theory of hardness and design of novel superhard crystals." International Journal of Refractory Metals and Hard Materials, 33, 93-106 (2012).

[258] X. Jiang, J. Zhao, A. Wu, Y. Bai, and X. Jiang, "Mechanical and electronic properties of B12-based ternary crystals of orthorhombic phase." Journal of Physics: Condensed Matter, 22(31), 315503-315503 (2010).

[259] K. Hussain, U. Younis, I. Muhammad, Y. Qie, Y. Guo, T. Li, ... and Q. Sun, "Three-dimensional porous borocarbonitride bc 2 n with negative Poisson's ratio." Journal of Materials Chemistry C, 8(44), 15771-15777 (2020).

[260] I. N. Frantsevich, "Elastic constants and elastic moduli of metals and insulators." Reference book, (1982).

[261] S. F. Pugh, "XCII. Relations between the elastic moduli and the plastic properties of polycrystalline pure metals." The London, Edinburgh, and Dublin Philosophical Magazine and Journal of Science, 45(367), 823-843 (1954).

[262] D. S. Williams, "Elastic stiffness and thermal expansion coefficient of boron nitride films." Journal of applied physics, 57(6), 2340-2342 (1985).

[263] R. W. Trice, and J. W. Halloran, "Investigation of the physical and mechanical properties of hot-pressed boron nitride/oxide ceramic composites." Journal of the American Ceramic Society, 82(9), 2563-2565 (1999).

[264] K. Watanabe, T. Taniguchi, and H. Kanda, "Direct-bandgap properties and evidence for ultraviolet lasing of hexagonal boron nitride single crystal." Nature materials, 3(6), 404-409 (2004).

[265] W. Lei, H. Zhang, Y. Wu, B. Zhang, D. Liu, S. Qin, ... and Y. Chen, "Oxygen-doped boron nitride nanosheets with excellent performance in hydrogen storage." Nano Energy, 6, 219-224 (2014).

[266] D. S. McGregor, T. C. Unruh, and W. J. McNeil, "Thermal neutron detection with pyrolytic boron nitride." Nuclear Instruments and Methods in Physics Research

Section A: Accelerators, Spectrometers, Detectors and Associated Equipment, 591(3), 530-533 (2008).

[267] M. Zheng, Y. Liu, P. Wang, and Y. Xiao, "Synthesis and formation mechanism of cubic boron nitride nanorods in lithium bromide molten salt." Materials Letters, 91, 206-208 (2013).

[268] S. N. Mohammad, "Electrical characteristics of thin film cubic boron nitride." Solid-State Electronics, 46(2), 203-222 (2002).

[269] K. O. Obodo, R. C. Andrew, and N. Chetty, "Modification of the band offset in boronitrene." Physical Review B, 84(15), 155308-155308 (2011).

[270] J. Eichler, and C. Lesniak, "Boron nitride (BN) and BN composites for high-temperature applications." Journal of the European Ceramic Society, 28(5), 1105-1109 (2008).

[271] T. Taniguchi, T. Teraji, S. Koizumi, K. Watanabe, and S. Yamaoka, "Appearance of n-type semiconducting properties of cBN single crystals grown at high pressure." Japanese journal of applied physics, 41(2A), L109-L111 (2002).

[272] S. W. King, M. French, J. Bielefeld, M. Jaehnig, M. Kuhn, and B. French, "X-ray photoelectron spectroscopy investigation of the Schottky barrier at a-BN: H/Cu interfaces." Electrochemical and Solid-State Letters, 14(12), H478-H479 (2011).

[273] A. N. Caruso, "The physics of solid-state neutron detector materials and geometries." Journal of Physics: Condensed Matter, 22(44), 443201-443201 (2010).

[274] O. O. Kurakevych, and V. L. Solozhenko, "High-pressure design of advanced BN-based materials." Molecules, 21(10), 1399-1399 (2016).

[275] K. P. Loh, M. Nishitani-Gamo, I. Sakaguchi, T. Taniguchi, and T. Ando, "Thermal stability of the negative electron affinity condition on cubic boron nitride." Applied physics letters, 72(23), 3023-3025 (1998).

[276] L. Britnell, R. V. Gorbachev, R. Jalil, B. D. Belle, F. Schedin, M. I. Katsnelson, ... and K. S. Novoselov, "Electron tunneling through ultrathin boron nitride crystalline barriers." Nano letters, 12(3), 1707-1710 (2012).

[277] D. Akinwande, N. Petrone, and J. Hone, "Two-dimensional flexible nanoelectronics." Nature communications, 5(1), 1-12 (2014).

[278] W. H. Balmain, "Bemerkungen über die Bildung von Verbindungen des Bors und Siliciums mit Stickstoff und gewissen Metallen." Journal für Praktische Chemie, 27(1), 422-430 (1842).

155

[279] Y. Matsui, Y. Sekikawa, T. Sato, T. Ishii, S. Isakosawa, and K. Shii, "Formations of rhombohedral boron nitride, as revealed by TEM-electron energy loss spectroscopy." Journal of Materials Science, 16(4), 1114-1116 (1981).

[280] R. H. Wentorf Jr, "Synthesis of the cubic form of boron nitride." The Journal of Chemical Physics, 34(3), 809-812 (1961).

[281] F. P. Bundy, and R. H. Wentorf Jr, "Direct transformation of hexagonal boron nitride to denser forms." The Journal of Chemical Physics, 38(5), 1144-1149 (1963).

[282] V. I. Levitas, J. Hashemi, and Y. Z. Ma, "Strain-induced disorder and phase transformation in hexagonal boron nitride under quasi-homogeneous pressure: In situ X-ray study in a rotational diamond anvil cell." EPL (Europhysics Letters), 68(4), 550-556 (2004).

[283] F. R. Corrigan, and F. P. Bundy, "Direct transitions among the allotropic forms of boron nitride at high pressures and temperatures." The Journal of Chemical Physics, 63(9), 3812-3820 (1975).

[284] V. F. Britun, and A. V. Kurdyumov, "Mechanisms of martensitic transformations in boron nitride and conditions of their development." International Journal of High Pressure Research, 17(2), 101-111 (2000).

[285] T. Taniguchi, T. Sato, W. Utsumi, T. Kikegawa, and O. Shimomura, "Effect of nonhydrostaticity on the pressure induced phase transformation of rhombohedral boron nitride." Applied physics letters, 70(18), 2392-2394 (1997).

[286] C. Ji, V. I. Levitas, H. Zhu, J. Chaudhuri, A. Marathe, and Y. Ma, "Shear-induced phase transition of nanocrystalline hexagonal boron nitride to wurtzitic structure at room temperature and lower pressure." Proceedings of the National Academy of Sciences, 109(47), 19108-19112 (2012).

[287] N. Dubrovinskaia, V. L. Solozhenko, N. Miyajima, V. Dmitriev, O. O. Kurakevych, and L. Dubrovinsky, "Superhard nanocomposite of dense polymorphs of boron nitride: Noncarbon material has reached diamond hardness." Applied Physics Letters, 90(10), 101912-101912 (2007).

[288] V. L. Solozhenko, G. Will, and F. Elf, "Isothermal compression of hexagonal graphite-like boron nitride up to 12 GPa." Solid state communications, 96(1), 1-3 (1995).

[289] V. I. Levitas, Y. Ma, J. Hashemi, M. Holtz, and N. Guven, "Strain-induced disorder, phase transformations, and transformation-induced plasticity in hexagonal boron

nitride under compression and shear in a rotational diamond anvil cell: In situ x-ray diffraction study and modeling." The Journal of chemical physics, 125(4), 044507-044507 (2006).

[290] Y. Meng, H. K. Mao, P. J. Eng, T. P. Trainor, M. Newville, M. Y. Hu, ... and R. J. Hemley, "The formation of sp3 bonding in compressed BN." Nature materials, 3(2), 111-114 (2004).

[291] S. N. Dub, and I. A. Petrusha, "Mechanical properties of polycrystalline cBN obtained from pyrolytic gBN by direct transformation technique." High pressure research, 26(2), 71-77 (2006).

[292] T. Taniguchi, T. Sato, W. Utsumi, T. Kikegawa, and O. Shimomura, "In-situ X-ray observation of phase transformation of rhombohedral boron nitride under static high pressure and high temperature." Diamond and related materials, 6(12), 1806-1815 (1997).

[293] H. Lorenz, and I. Orgzall, "Influence of the initial crystallinity on the high pressure–high temperature phase transition in boron nitride." Acta materialia, 52(7), 1909-1916 (2004).

[294] V. F. Britun, A. V. Kurdyumov, N. I. Borimchuk, V. V. Yarosh, and A. I. Danilenko, "Formation of diamond-like BN phases under shock compression of graphite-like BN with different degree of structural ordering." Diamond and related materials, 16(2), 267-276 (2007).

[295] L. C. Nistor*, G. Van Tendeloo, and G. Dinca, "Crystallographic aspects related to the high pressure–high temperature phase transformation of boron nitride." Philosophical Magazine, 85(11), 1145-1158 (2005).

[296] A. V. Kurdyumov, V. F. Britun, and I. A. Petrusha, "Structural mechanisms of rhombohedral BN transformations into diamond-like phases." Diamond and related materials, 5(11), 1229-1235 (1996).

[297] R. Becker, L. Chkhartishvili, R. Avci, I. Murusidze, O. Tsagareishvili, and N. Maisuradze, "Metallic" boron nitride." European Chemical Bulletin, 4(1), 8-23 (2015).

[298] J. B. Condon, C. E. Holcombe, D. H. Johnson, and L. M. Steckel, "The kinetics of the boron plus nitrogen reaction." Inorganic Chemistry, 15(9), 2173-2179 (1976).

[299] V. L. Solozhenko, and O. O. Kurakevych, "New boron subnitride B13N2: HP-HT synthesis, structure and equation of state." In Journal of Physics: Conference Series, IOP Publishing, 121(6), 062001-062001 (2008, July).

[300] V. L. Solozhenko, and O. O. Kurakevych, "Chemical interaction in the B–BN system at high pressures and temperatures: synthesis of novel boron subnitrides." Journal of Solid State Chemistry, 182(6), 1359-1364 (2009).

[301] J. Guo, H. Wang, M. Zhu, J. Zhu, and H. Yan, "Synthesis of B50N2 nanorods by electrolysis of organic solutions." Electrochemistry communications, 8(8), 1211-1214 (2006).

[302] H. Hubert, L. A. Garvie, P. R. Buseck, W. T. Petuskey, and P. F. McMillan, "High-pressure, high-temperature syntheses in the B–C–N–O system." Journal of Solid State Chemistry, 133(2), 356-364 (1997).

[303] V. L. Solozhenko, Y. Le Godec, and O. O. Kurakevych, "Solid-state synthesis of boron subnitride, B6N: myth or reality?." Comptes Rendus Chimie, 9(11-12), 1472-1475 (2006).

[304] R. Zedlitz, M. Heintze, and M. B. Schubert, "Properties of amorphous boron nitride thin films." Journal of non-crystalline solids, 198, 403-406 (1996).

[305] J. Y. Huang, H. Yasuda, and H. Mori, "HRTEM and EELS studies on the amorphization of hexagonal boron nitride induced by ball milling." Journal of the American Ceramic Society, 83(2), 403-409 (2000).

[306] M. Durandurdu, "Hexagonal nanosheets in amorphous BN: A first principles study." Journal of Non-Crystalline Solids, 427, 41-45 (2015).

[307] J. G. Kho, K. T. Moon, G. Nouet, P. Ruterana, and D. P. Kim, D. P. "Boron-rich boron nitride (BN) films prepared by a single spin-coating process of a polymeric precursor." Thin Solid Films, 389(1-2), 78-83 (2001).

[308] C. W. Ong, K. F. Chan, and C. L. Choy, "Optical absorption and transport mechanisms of dual ion-beam-deposited boron-rich boron nitride films." Thin Solid Films, 388(1-2), 217-225 (2001).

[309] J. J. Pouch, S. A. Alterovitz, K. Miyoshi, and J. O. Warner, "Boron nitride: composition, optical properties, and mechanical behavior." MRS Online Proceedings Library (OPL), 93 (1987).

[310] P. Ordejón, E. Artacho, and J. M. Soler, "Self-consistent order-N density-functional calculations for very large systems." Physical Review B, 53(16), R10441-R10444 (1996).

[311] C. Lee, W. Yang, and R. G. Parr, "Development of the Colle-Salvetti correlation-energy formula into a functional of the electron density." Physical review B, 37(2), 785-789 (1988).

[312] K. Momma, and F. Izumi, "VESTA 3 for three-dimensional visualization of crystal, volumetric and morphology data." Journal of applied crystallography, 44(6), 1272-1276 (2011).

[313] Y. Kumashiro, "Electric Refractory Materials." CRC Press, New York, 1 (2000).

[314] R. G. Delaplane, T. Lundstrom, U. Dahlborg, W. S. Howells, D. Emin, T. L. Aselage, A. C. Switendick, B. Morosin, C. L. Beckel (Eds.), Boron-Rich Solids, AIP Conf, Proc, 231, 241–244 (1991).

[315] S. Krishnan, S. Ansell, J. J. Felten, K. J. Volin, and D. L. Price, "Structure of liquid boron." Physical Review Letters, 81(3), 586-589 (1998).

[316] N. N. Medvedev, "The algorithm for three-dimensional Voronoi polyhedra." Journal of computational physics, 67(1), 223-229 (1986).

[317] V. L. Solozhenko, and T. Peun, "Compression and thermal expansion of hexagonal graphite-like boron nitride up to 7 GPa and 1800 K." Journal of Physics and Chemistry of Solids, 58(9), 1321-1323 (1997).

[318] F. Datchi, A. Dewaele, Y. Le Godec, and P. Loubeyre, "Equation of state of cubic boron nitride at high pressures and temperatures." Physical Review B, 75(21), 214104-214104 (2007).

[319] V. L. Solozhenko, D. Häusermann, M. Mezouar, and M. Kunz, "Equation of state of wurtzitic boron nitride to 66 GPa." Applied physics letters, 72(14), 1691-1693 (1998).

[320] O. O. Kurakevych, Y. Le Godec, and V. L. Solozhenko, "Equations of state of novel solids synthesized under extreme pressure–temperature conditions." In Journal of Physics: Conference Series IOP Publishing, 653(1), 012080-012080 (2015, November).

[321] A. O. Lyakhov, and A. R. Oganov, "Evolutionary search for superhard materials: Methodology and applications to forms of carbon and TiO 2." Physical Review B, 84(9), 092103-092103 (2011).

[322] R. J. Nelmes, J. S. Loveday, D. R. Allan, J. M. Besson, G. Hamel, P. Grima, and S. Hull, "Neutron-and x-ray-diffraction measurements of the bulk modulus of boron." Physical Review B, 47(13), 7668-7673 (1993).

[323] C. Jiang, Z. Lin, J. Zhang, and Y. Zhao, "First-principles prediction of mechanical properties of gamma-boron." Applied Physics Letters, 94(19), 191906-191906 (2009).

[324] S. Aydin, and M. Simsek, "First-principles calculations of elemental crystalline boron phases under high pressure: Orthorhombic B28 and tetragonal B48." Journal of alloys and compounds, 509(17), 5219-5229 (2011).

[325] J. Qin, N. Nishiyama, H. Ohfuji, T. Shinmei, L. Lei, D. He, and T. Irifune, "Polycrystalline γ-boron: As hard as polycrystalline cubic boron nitride." Scripta Materiailia, 67, 257-260 (2012).

[326] Q. Peng, W. Ji, and S. De, "Mechanical properties of the hexagonal boron nitride monolayer: Ab initio study." Computational Materials Science, 56, 11-17 (2012).

[327] F. Zhang, Y. Guo, Z. Song, and G. Chen, "Deposition of high quality cubic boron nitride films on nickel substrates." Applied physics letters, 65(8), 971-973 (1994).

[328] S. W. King, M. French, J. Bielefeld, M. Jaehnig, M. Kuhn, G. Xu, and B. French, "Valence band offset at the amorphous hydrogenated boron nitride-silicon (100) interface." Applied Physics Letters, 101(4), 042903-042903 (2012).

[329] M. H. Manghnani, Proceedings of the 5th NIRIM International Symposium on Advanced Material (ISAM'98) Tsukuba, Japan, 73 (1998).

[330] M. Grimsditch, E. S. Zouboulis, and A. Polian, "Elastic constants of boron nitride." Journal of applied physics, 76(2), 832-834 (1994).

[331] S. Q. Wang, and H. Q. Ye, "First-principles study on elastic properties and phase stability of III–V compounds." Physica status solidi (b), 240(1), 45-54 (2003).

[332] S. Daoud, K. Loucif, N. Bioud, and N. Lebgaa, "First-Principles Study of Structural, Elastic and Mechanical Properties of Zinc-Blende Boron Nitride (B3-BN)." Acta Physica Polonica, A., 122(1), 109-115 (2012).

[333] A. R. Oganov, V. L. Solozhenko, C. Gatti, O. O. Kurakevych, and Y. Le Godec, "The high-pressure phase of boron, γ-B28: Disputes and conclusions of 5 years after discovery." Journal of Superhard Materials, 33(6), 363-379 (2011).

[334] M. Herrmann, I. Sigalas, M. Thiele, M. M. Müller, H. J. Kleebe, and A. Michaelis, "Boron suboxide ultrahard materials." International Journal of Refractory Metals and Hard Materials, 39, 53-60 (2013).

[335] I. Solodkyi, S. S. Xie, T. Zhao, H. Borodianska, Y. Sakka, and O. Vasylkiv, "Synthesis of B6O powder and spark plasma sintering of B6O and B6O–B4C ceramics." Journal of the Ceramic Society of Japan, 121(1419), 950-955 (2013).

[336] S. S. Xie, H. Chen, I. Solodkyi, O. Vasylkiv, and A. I. Tok, "Cyclic formation of boron suboxide crystallites into star-shaped nanoplates." Scripta Materialia, 99, 69-72 (2015).

[337] I. Solodkyi, H. Borodianska, T. Zhao, Y. Sakka, P. Badica, and O. Vasylkiv, "B6O ceramic by in-situ reactive spark plasma sintering of a B2O3 and B powder mixture." Journal of the Ceramic Society of Japan, 122(1425), 336-340 (2014).

[338] A. Zerr, and R. Riedel, "Introduction: Novel ultrahard materials." Handbook of ceramic hard materials, 1, 45-73 (2000).

[339] T. C. Shabalala, D. S. McLachlan, I. Sigalas, and M. Herrmann, "Hard and tough boron suboxide based composites." Ceramics International, 34(7), 1713-1717 (2008).

[340] J. Dai, and Z. Tian, "Large thermal conductivity of boron suboxides despite complex structures." Applied Physics Letters, 118(4), 041901-041901 (2021).

[341] H. Wang, and Q. An, "Band-gap engineering in high-temperature boron-rich icosahedral compounds." The Journal of Physical Chemistry C, 123(19), 12505-12513 (2019).

[342] T. Mori, T. Nishimura, K. Yamaura, and E. Takayama-Muromachi, "High temperature thermoelectric properties of a homologous series of n-type boron icosahedra compounds: A possible counterpart to p-type boron carbide." Journal of Applied Physics, 101(9), 093714-093714 (2007).

[343] Y. Chen, G. Yu, W. Chen, Y. Liu, G. D. Li, P. Zhu, ... and X. Zou, "Highly active, nonprecious electrocatalyst comprising borophene subunits for the hydrogen evolution reaction." Journal of the American Chemical Society, 139(36), 12370-12373 (2017).

[344] Z. Huang, S. Wang, R. D. Dewhurst, N. V. Ignat'ev, M. Finze, and H. Braunschweig, "Boron: Its Role in Energy-Related Processes and Applications." Angewandte Chemie International Edition, 59(23), 8800-8816 (2020).

[345] S. Satyapal, J. Petrovic, C. Read, G. Thomas, and G. Ordaz, "The US Department of Energy's National Hydrogen Storage Project: Progress towards meeting hydrogen-powered vehicle requirements." Catalysis Today ,120(3-4), 246-256 (2007).

[346] X. Y. Liu, X. D. Zhao, and W. H. Su, "High pressure synthesis of serial higher boron suboxides with cage structures." In AIP Conference Proceedings, American Institute of Physics, 309(1), 1279-1282 (1994).

[347] T. Endo, T. Sato, and M. Shimada, "High-pressure synthesis of B 2 O with diamond-like structure." Journal of Materials Science Letters, 6(6), 683-685 (1987).

[348] A. V. Nemukhin, and F. Weinhold, "Boron oxides: Ab initio studies with natural bond orbital analysis." The Journal of Chemical Physics, 98(2), 1329-1335 (1993).

[349] V. L. Solozhenko, O. O. Kurakevych, V. Z. Turkevich, and D. V. Turkevich, "Phase Diagram of the B−B2O3 System at 5 GPa: Experimental and Theoretical Studies." The Journal of Physical Chemistry B, 112(21), 6683-6687 (2008).

[350] M. P. Grumbach, O. F. Sankey, and P. F. McMillan, "Properties of B2O: An unsymmetrical analog of carbon." Physical Review B, 52(22), 15807-15811 (1995).

[351] H. Dong, A. R. Oganov, Q. Wang, S. N. Wang, Z. Wang, J. Zhang, ... and Q. Zhu, "Prediction of a new ground state of superhard compound B6O at ambient conditions." Scientific reports, 6(1), 1-6 (2016).

[352] Q. An, K. M. Reddy, H. Dong, M. W. Chen, A. R. Oganov, and W. A. Goddard III, "Nanotwinned boron suboxide (B6O): New ground state of B6O." Nano Letters, 16(7), 4236-4242 (2016).

[353] D. Music, and J. M. Schneider, "Elastic properties of amorphous boron suboxide based solids studied using ab initio molecular dynamics." Journal of Physics: Condensed Matter, 20(19), 195203-195203 (2008).

[354] M. Durandurdu, "Amorphous boron suboxide." Journal of the American Ceramic Society, 102(8), 4546-4554 (2019).

[355] M. Durandurdu, "High pressure modifications in amorphous boron suboxide: An ab initio study." Ceramics International, 46(5), 5968-5975 (2020).

[356] Z. Wang, Y. Zhao, P. Lazor, H. Annersten, and S. K. Saxena, "In situ pressure Raman spectroscopy and mechanical stability of superhard boron suboxide." Applied Physics Letters, 86(4), 041911-041911 (2005).

[357] K. M. Reddy, A. Hirata, P. Liu, T. Fujita, T. Goto, and M. W. Chen, "Shear amorphization of boron suboxide" Scripta Materialia, 76, 9-12 (2014).

[358] C. Kunka, Q. An, N. Rudawski, G. Subhash, J. Zheng, V. Halls, and J. Singh, "Nanotwinning and amorphization of boron suboxide." Acta Materialia, 147, 195-202 (2018).

[359] Materials Explorer, B2O, Available online: https://materialsproject.org/materials/mp-614006/#

[360] J. Wang, Q. Li, C. J. Pickard, C. Chen, and Y. Ma, "Computational discovery and characterization of new B2O phases." Physical Chemistry Chemical Physics, 21(5), 2499-2506 (2019).

[361] A. B. Rahane, V. Kumar, V., and J. S. Dunn, "Carbon doping in Boron suboxide: structure, energetics, and elastic properties." Journal of the American Ceramic Society, 98(7), 2223-2233 (2015).

[362] M. Kobayashi, I. Higashi, C. Brodhag, and F. Thevenot, "Structure of B6O boron-suboxide by Rietveld refinement." Journal of Materials Science, 28(8), 2129-2134 (1993).

[363] M. Durandurdu, "Liquid boron and amorphous boron: An ab initio molecular dynamics study." Journal of Non-Crystalline Solids, 417, 10-14 (2015).

[364] S. Sadaf, T. Wu, L. Zhong, Z. Y. Liao, H. C. Wang, and W. L. Wang, "Effective Mechanism of B2O3 on the Structure and Viscosity of CaO–SiO2–B2O3-based Melts." Steel Research International, 92(4), 2000531-2000531 (2021).

[365] H. Dong, A. R. Oganov, V. V. Brazhkin, Q. Wang, J. Zhang, M. M. D. Esfahani, ... and Q. Zhu, "Boron oxides under pressure: Prediction of the hardest oxides." Physical Review B, 98(17), 174109-174109 (2018).

[366] G. Voronoi, "Recherches sur les paralléloèdres primitives." Journal für die reine und angewandte Mathematik, 134, 198-287 (1908).

[367] W. Brostow, M. Chybicki, R. Laskowski, and J. Rybicki, "Voronoi polyhedra and Delaunay simplexes in the structural analysis of molecular-dynamics-simulated materials." Physical Review B, 57(21), 13448-13458 (1998).

[368] V. V. Brazhkin, Y. Katayama, K. Trachenko, O. B. Tsiok, A. G. Lyapin, E. Artacho, ... and H. Saitoh, "Nature of the structural transformations in B2O3 glass under high pressure." Physical review letters, 101(3), 035702-035702 (2008).

[369] T. Letsoalo, and J. E. Lowther, "Systematic trends in boron icosahedral structured materials." Physica B: Condensed Matter, 403(17), 2760-2767 (2008).

[370] D. R. Petrak, "Mechanical properties of hot-pressed boron suboxide and boron." Ceramic Bulletin, 53, 569-573 (1974).

[371] B. Goosey, U.S. Patent No. 3,816,586. Washington, DC: U.S. Patent and Trademark Office (1974).

[372] R. F. Zhang, Z. J. Lin, Y. S. Zhao, and S. Veprek, "Superhard materials with low elastic moduli: Three-dimensional covalent bonding as the origin of superhardness in B6O." Physical Review B, 83(9), 092101-092101 (2011).

[373] Q. An, and W. A. Goddard III, "Boron suboxide and boron subphosphide crystals: hard ceramics that shear without brittle failure." Chemistry of Materials, 27(8), 2855-2860 (2015).

[374] V. A. Mukhanov, O. O. Kurakevych, and V. L. Solozhenko, "On the hardness of boron (III) oxide." arXiv preprint arXiv: 1101(2965), (2011).

[375] Y. Guo, and W. A. Goddard III, "Is carbon nitride harder than diamond? No, but its girth increases when stretched (negative poisson ratio)." Chemical Physics Letters, 237(1-2), 72-76 (1995).

[376] G. V. Samsonov, and V. P. Latysheva, "Chemical compounds of boron with silicon." Doklady Akademii Nauk SSSR, 105, 499-499 (1955).

[377] R. F. Adamsky, "Unit cell and space group of orthorhombic SiB6." Acta Crystallographica, 11(10), 744-745 (1958).

[378] C. F. Cline, "Preliminary investigations of the silicon boride, SiB6." Nature, 181(4607), 476-477 (1958).

[379] R. Giese, "Polyhedral groups in the phase SiB6." Electron Technol, 3(1), 151-157 (1970).

[380] W. Dietze, M. Miller, E. Amberger, "Pyrolitic formation of Si-doped B and silicon borides." Electron Technol, 3, 73-79 (1970).

[381] G. V. Samsonov, and V. M. Sleptsov, "Preparation of boron-silicon alloys." Soviet Powder Metallurgy and Metal Ceramics, 3(6), 488-496 (1964).

[382] I. A. Bairamashvili, G. I. Kalandadze, A. M. Eristavi, J. S. Jobava, V. V. Chotulidi, and Y. I. Saloev, "An investigation of the physicomechanical properties of B6O and SiB4." Journal of the Less Common Metals, 67(2), 455-459 (1979).

[383] R. Tremblay, and R. Angers, "Preparation of high purity SiB4 by solid-state reaction between Si and B." Ceramics International, 15(2), 73-78 (1989).

[384] R. Tremblay, and R. Angers, "Mechanical characterization of dense silicon tetraboride (SiB4)." Ceramics international, 18(2), 113-117 (1992).

[385] D. Emin, "Icosahedral boron-rich solids as refractory semiconductors." MRS Online Proceedings Library (OPL), 97, 3-15 (1987).

[386] G. A. Slack, and K. E. Morgan, "Some crystallography, chemistry, physics, and thermodynamics of B12O2, B12P2, B12As2, and related alpha-boron type crystals." Journal of Physics and Chemistry of Solids, 75(9), 1054-1074 (2014).

[387] G. A. Slack, T. F. McNelly, and E. A. Taft, "Melt growth and properties of B6P crystals." Journal of Physics and Chemistry of Solids, 44(10), 1009-1013 (1983).

[388] H. Zhang, S. Yao, and M. Widom, "Predicted phase diagram of boron-carbon-nitrogen." Physical Review B, 93(14), 144107-144107 (2016).

[389] R. Franz, and H. Werheit, "Boron-rich Solids" (*AIP Conf. Proc. 231*), (1991). ed. by D. *Emin, T. Aselage, AC Switendick, B. Morosin and CL Beckel, AIP, NY*, 29.

[390] A. Hori, M. Takeda, H. Yamashita, and K. Kimura, "Absorption edge spectra of boron-rich amorphous films constructed with icosahedral cluster." Journal of the Physical Society of Japan, 64(9), 3496-3505 (1995).

[391] A. A. Berezin, O. A. Golikova, M. M. Kazanin, T. Khomidov, D. N. Mirlin, A. V. Petrov, ... and V. K. Zaitsev, "Electrical and optical properties of amorphous boron and amorphous concept for β-rhombohedral boron." Journal of Non-Crystalline Solids, 16(2), 237-246 (1974).

[392] H. Matsuda, T. Nakayama, K. Kimura, Y. Murakami, H. Suematsu, M. Kobayashi, and I. Higashi, "Structural and electronic properties of Li-and Cu-doped β-rhombohedral boron constructed from icosahedral and truncated icosahedral clusters." Physical Review B, 52(8), 6102-6110 (1995).

[393] S. Motozima, K. Sugiyama, and Y. Takahashi, "Chemical vapor deposition of tetraboron silicide whiskers." Bulletin of the Chemical Society of Japan, 48(5), 1463-1466 (1975).

[394] K. Murase, T. Ogino, and Y. Mizushima, "Thermal oxidation of amorphous silicon-germanium-boron alloy." Japanese journal of applied physics, 22(12R), 1771-1777 (1983).

[395] C. W. Ong, K. P. Chik, and H. K. Wong, "Effects of Si incorporation on the structural change of a-B x Si1− x alloy films." Journal of applied physics, 74(10), 6094-6099 (1993).

[396] G. R. Yang, Y. P. Zhao, and B. Y. Tong, "FTIR and uv study of amorphous silicon-boron alloys deposited by LPCVD." MRS Online Proceedings Library (OPL), 426, 83-88 (1996).

[397] A. Mostafa, and M. Medraj, "Binary phase diagrams and thermodynamic properties of silicon and essential doping elements (Al, As, B, Bi, Ga, In, N, P, Sb and Tl)." Materials, 10(6), 676-676 (2017).

[398] D. Eklöf, A. Fischer, A. Ektarawong, A. Jaworski, A. J. Pell, J. Grins, ... and U. Häussermann, "Mysterious SiB3: Identifying the Relation between α-and β-SiB3." ACS omega, 4(20), 18741-18759 (2019).

[399] A. Gali, J. Miro, P. Deák, C. P. Ewels, and R. Jones, "Theoretical studies on nitrogen-oxygen complexes in silicon." Journal of Physics: Condensed Matter, 8(41), 7711-7722 (1996).

[400] I. V. Getmanskii, R. M. Minyaev, V. V. Koval, and V. I. Minkin, "Quantum chemical modeling of solid-state B4X structures containing tetrahedral B4 units with X= B, C, Al, Si." Mendeleev Communications, 28(2), 173-175 (2018).

[401] L. Cheng, "B14: An all-boron fullerene." The Journal of Chemical Physics, 136(10), 104301-104301 (2012).

[402] N. G. Szwacki, A. Sadrzadeh, and B. I. Yakobson, "B 80 fullerene: an ab initio prediction of geometry, stability, and electronic structure." Physical review letters, 98(16), 166804-166804 (2007).

[403] M. Mukaida, T. Tsunoda, and Y. Imai, "Preparation of B-Si films by chemical vapor deposition." Eighteenth International Conference on Thermoelectrics. Proceedings, ICT'99 (Cat. No. 99TH8407), 667-670 IEEE (1999, August).

[404] T. B. Tai, P. Kadłubański, S. Roszak, D. Majumdar, J. Leszczynski, and M. T. Nguyen, "Electronic Structures and Thermochemical Properties of the Small Silicon-Doped Boron Clusters BnSi (n= 1–7) and Their Anions." ChemPhysChem, 12(16), 2948-2958 (2011).

[405] G. L. Perkins, "Boron: Compounds, Production, and Application." Nova Science Publishers (2011).

[406] J. Wang, G. Sun, P. Kong, W. Sun, C. Lu, F. Peng, and X. Kuang, "Novel structural phases and the electrical properties of Si 3 B under high pressure." Physical Chemistry Chemical Physics, 19(24), 16206-16212 (2017).

[407] R. W. Cahn, (1991). "Binary alloy phase diagrams." Advanced Materials, 3, 628-629 (1991).

[408] The Materials Project, Available online: https://materialsproject.org/

[409] R. Viswanathan, R. W. Schmude, and K. A. Gingerich, "Thermochemistry of BSi (g), BSi2 (g), and BSi3 (g)." The Journal of Physical Chemistry, 100(25), 10784-10786 (1996).

[410] W. Dietze, and E. Amberger, "Pyrolytische Darstellung von Siliciumboriden." Angewandte Chemie, 79(6), 278-278 (1967).

[411] B. G. Arabei, "Interactions in the System Si-B." Izvestia Akademii nauk SSSR. Neorganičeskie materialy, 15(9), 1589-1592 (1979).

[412] E. Colton, "On the boron-silicon reaction." Journal of Inorganic and Nuclear Chemistry, 17(1-2), 108-111 (1961).

[413] E. Arai, H. Nakamura, and Y. Terunuma, "Interface Reactions of B 2 O 3-Si System and Boron Diffusion into Silicon." Journal of The Electrochemical Society, 120(7), 980-987 (1973).

[414] V. I. Matkovich, C. Ervin, "Tetraboronsilicide." U.S. Patent No. 3,138,468. (23 Jun. 1964).

[415] E. L. Kern, and G. A. Jerome, "Coating of objects with tetraboron silicide." U.S. Patent No. 3,455,745. Washington, DC: U.S. Patent and Trademark Office (15 Jul. 1969).

[416] L. C. Mccandless, J. C. Withers, C. R. Brummett, "Reinforcing filaments comprising coated tungsten wires." U.S. Patent No. 3,549,413. (22 Dec. 1970).

[417] L. C. Mccandless, J. C. Withers, "High-strength, high-modulus, low density, boron silicide monofilaments, and method of making same." U.S. Patent No. 3,607,367. (21 Sep. 1971).

[418] J. K. Christie, "Atomic structure of biodegradable Mg-based bulk metallic glass." Physical Chemistry Chemical Physics, 17(19), 12894-12898 (2015).

[419] Materials Explorer, B2O, Available online: https://www.materialsproject.org/materials/mp-978496

[420] I. Mizushima, Y. Mitani, M. Koike, M. Yoshiki, M. Tomita, and S. Kambayashi, "Precipitation of boron in highly boron-doped silicon." Japanese journal of applied physics, 37(3S), 1171-1173 (1998).

[421] T. A. Yıldız, and M. Durandurdu, "Amorphous boron carbide from ab initio simulations." Computational Materials Science, 173, 109397-109397 (2020).

[422] R. Lazzari, N. Vast, J. M. Besson, S. Baroni, A. Dal Corso, "Atomic structure and vibrational properties of icosahedral B4C boron carbide." Physical Review Letters, 83, 3230-3233 (1999).

[423] N. Vast, J. Sjakste, and E. Betranhandy, "Boron carbides from first principles." *In Journal of Physics: Conference Series, IOP Publishing,* 176(1), 012002-012003 (2009, June).

[424] V. A. Mukhanov, O. O. Kurakevych, nd V. L. Solozhenko, "Thermodynamic model of hardness: Particular case of boron-rich solids." Journal of Superhard Materials, 32(3), 167-176 (2010).

[425] M. A. Imam, and R. G. Reddy, "A Review of Boron-Rich Silicon Borides Basedon Thermodynamic Stability and Transport Properties of High-Temperature Thermoelectric Materials." High Temperature Materials and Processes, 38(2019), 411-424 (2019).

[426] https://materialsproject.org/materials/mp-614006/#

APPENDIX

Appendix C. Rights and Permissions

- Chapter 3: "Reprinted by permission from Journal of the American Ceramic Society, Çetin Karacaoğlan, A. Ö. & Durandurdu, M. Hard boron rich boron nitride nanoglasses. (2018). Copyright 2018 Journal of the American Ceramic Society." https://doi.org/10.1111/jace.15383

- Chapter 6: "Reprinted by permission from Journal of Non-Crystalline Solids, Çetin Karacaoğlan, A. Ö. & Durandurdu, M. Amorphous silicon triboride: A first principles study. (2020). Copyright 2020 Journal of Non-Crystalline Solids." https://doi.org/10.1016/j.jnoncrysol.2020.119995

- Chapter 7: "Reprinted by permission from Journal of Materials Chemistry and Physics, Çetin Karacaoğlan, A. Ö. & Durandurdu, M. A first principles study of amorphous and crystalline silicon tetraboride. (2021). Copyright 2020 Journal of Materials Chemistry and Physics." https://doi.org/10.1016/j.matchemphys.2020.123928

CURRICULUM VITAE

EMPLOYMENT

2022-	Quality Engineer in Yataş A. Ş.

EDUCATION

2017-2023	**PhD.,** Materials Science and Mechanical Engineering
	Abdullah Gül University, Kayseri/Turkey
	Advisor: Prof. Dr. Murat Durandurdu
2013-2016	**M.Sc.** in Textile Engineering
	Erciyes University, Kayseri/Turkey
	Advisor: Prof. Dr. Abdülkadir Bilişik
2007-2011	**B.Sc.** in Textile Engineering
	Erciyes University, Kayseri/Turkey
2006-2007	**Preparatory Program** in School of Foreign Languages
	Erciyes University, Kayseri/Turkey

SCHOLARSHIP/GRANT

2019-2022	**2211-C National PhD Scholarship Program in the Priority Fields in Science and Technology**
	The Scientific and Technological Research Council of Türkiye (TÜBİTAK)
2017-2021	**100/2000 Ph.D. Scholarship Program**
	Higher Education Council (YÖK) of Turkey
2017-2020	**ARDEB 1001 Project**
	The Scientific and Technological Research Council of Türkiye (TÜBİTAK)
2016-2016	**Scientific Research Projects**
	Erciyes University
2013-2015	**Arçelik A.Ş. Project (San-Tez)**
	Ministry of Science, Industry and Technology

PUBLICATIONS

Journals That Entered SCI, SSCI, and AHCI Indexes

I. KARACAOĞLAN AYŞEGÜL ÖZLEM, DURANDURDU MURAT (2023), Possible Boron-Rich Amorphous Silicon Borides from Ab initio Simulations. (Submitted)

II. KARACAOĞLAN AYŞEGÜL ÖZLEM, DURANDURDU MURAT (2023), Boron-Rich Amorphous Boron Oxides from Ab initio Simulations, Journal of Non-Crystalline Solids, 604: 122130, Doi: 10.1016/j.jnoncrysol.2022.122130

III. KARACAOĞLAN AYŞEGÜL ÖZLEM, DURANDURDU MURAT (2021), A first principles study of amorphous and crystalline silicon tetraboride, Materials Chemistry and Physics, 258: 123928, Doi: 10.1016/j.matchemphys.2020.123928

IV. KARACAOĞLAN AYŞEGÜL ÖZLEM, DURANDURDU MURAT (2020), Amorphous silicon triboride: A first principles study, JOURNAL OF NON-CRYSTALLINE SOLIDS, 536: 119995, Doi: 10.1016/j.jnoncrysol.2020.119995

V. KARACAOĞLAN AYŞEGÜL ÖZLEM, DURANDURDU MURAT (2018), Hard boron rich boron nitride nanoglasses, Journal Of The American Ceramic Society, 101.5: 1929, Doi: 10.1111/jace.15383

International Congress Papers and Published Abstracts

I. Çetin Karacaoğlan, A.Ö., Durandurdu, M., 2019, An Amorphous B90Si10 Model From An ab Initio Molecular Dynamics Study, 6th International Conference on Materials Science and Nanotechnology For Next Generation (MSNG-2019), Niğde, Turkey.

II. Durandurdu, M., Çetin, A.Ö., Üçhöyük, T.A., 2018, Cmcm Intermediate Phase For The HCP-To-BCC Phase Transition in Magnesium, The International Conference on Material Science and Technology in Cappadocia (IMSTEC-2018), Nevşehir, Turkey.

III. Çetin, A.Ö., Durandurdu, M., 2018, A First Principles Study of Amorphous SiB4, The International Conference on Material Science and Technology in Cappadocia (IMSTEC-2018), Nevşehir, Turkey.

IV. Çetin, A.Ö., Durandurdu, M., 2018, A First Principles Study of Boron- Rich Amorphous Boron Nitride, The International Conference on Material Science and Technology in Cappadocia (IMSTEC-2018), Nevşehir, Turkey.

V. Çetin, A.Ö., Durandurdu, M., 2018, Amorphous Silicon Triboride: A First Principles Study, International Computational Science Congress (CSC-2018), Amasya, Turkey.